Arathi Pai

Computationally Efficient Modelling and Precision Position and Force Control of SMA Actuators

Rechenreffiziente Modellierung und präsize Positions- und Kraftregelung von FGL-Aktoren

Bibliografische Information Der Deutschen Bibliothek
Die Deutsche Bibliothek verzeichnet diese Publikation in der Deutschen Nationalbibliografie detaillierte bibliografische Daten sind im Internet über http://dnb.ddb.de abrufbar

Band 392 der Verlagsschriftenreihe des Heinz Nixdorf Instituts

ISSN (Print): 2195-5239
ISSN (Online): 2365-4422
ISBN: 978-3-947647-11-8

Satz und Gestaltung: Arathi Pai

Hersteller: readbox unipress in der readbox publishing GmbH
Dortmund

Printed in Germany

Computationally Efficient Modelling and Precision Position and Force Control of SMA Actuators

zur Erlangung des akademischen Grades
DOKTOR DER INGENIEURWISSENSCHAFTEN (Dr.-Ing.)
der Fakultät für Maschinenbau
der Universität Paderborn

vorgelegte
DISSERTATION

von
Arathi Pai
aus Baroda

Zusammenfassung

Formgedächtnislegierungen (FGL) sind metallische Werkstoffe, deren Formdeformationen sich durch eine Temperaturerhöhung erholen können. Diese Erholung kann gezielt genutzt werden, um einen kraft- oder positionsgeregelten FGL-Aktor zu realisieren. Allerdings ist aufgrund des stark nichtlinearen Verhaltens die Entwicklung einer Regelung nicht trivial.

Die Herausforderung einen Regler zu entwickeln wird durch Modelle erleichtert, die die Nichtlinearitäten mathematisch präzise beschreiben. In dieser Arbeit wird dazu ein phänomenologisches Modell entwickelt, welches das FGL-Verhalten abhängig von Temperatur und mechanischer Spannung beschreiben kann. Das Modell weist eine außerordentliche Korrelation zu den in den Experimenten festgestellten Daten auf. Um dieses Modell in einem geschlossenen Regelkreis effizient verwenden zu können, wurde zudem ein inverses Modell entwickelt.

Anschließend wurde eine Regelstrategie entwickelt, die aus einer Kombination von Kleinsignal- und Großsignalregelung besteht. Der Großsignalregler, welcher für die grobe Postionsregelung dient, ist ein Temperaturregler, der seine Solltemperatur aus dem inversen FGL Modell erhält. Der Kleinsignalregler dient zur Feinpositionsregelung. Die Ergebnisse weisen eine außerordentlich gute Regeleigenschaft nach.

Die Reglerstrategie wurde dann zur Kraftregelung einer industriellen Spanneinrichtung genutzt, um ein dünnwandiges Reagenzglas einzuspannen. Hier dient allerdings der Kleinsignalregler als einen Feinkraftregler. Die Regler laufen dabei in Echtzeit auf einem eingebetteten Prozessor. Die Klemmvorrichtung, hat neben der ausgesprochen guten Kraftregelung, auch eine sehr gute Störgrößenausregelung bewiesen.

Abstract

Shape Memory Alloys (SMAs) are metallic alloys that display shape recovery after deformation through an increase of temperature. These shape recovery mechanisms can be exploited to create SMA-based position or force actuators. However, due to their inherent nonlinear and hysteretic behaviour, the control of such actuators is non-trivial.

The development of control strategies for SMA actuators is alleviated by the use of models incorporating these nonlinearities. In this thesis a novel phenomenological model to predict the behaviour of SMAs for varying temperature and stress is presented. The model shows outstanding correlation with experimental data. In order to use the models within a control loop, computationally efficient inverse models are also developed.

A novel control strategy for precision control of SMA actuators is then developed by using a combination of large and small signal controllers. The large signal controller, responsible for course positioning, is a temperature controller that gets its desired temperature value online from the inverse SMA model. The small signal controller is responsible for fine positioning. The control results show robust and precise tracking control with exceptional disturbance rejection for various loads.

The control strategy is then used for force control in an industrial SMA-based clamping vice to clamp a thin-walled test tube. While the large signal controller remains unchanged, the small signal controller is used for force control rather than for position control. The control unit of the vice is an embedded processor, on which the control algorithms run in real-time. The vice shows accurate force tracking and good disturbance rejection.

Prior Publications

[2018] Pai, A.; Riepold, M.; Trächtler, A.: *Model-based precision position and force control of SMA actuators with a clamping application.* In: Mechatronics, Vol. 50. April 2018

[2017] Pai, A.; Niendorf, T.; Krooss, P.; Koke, I.; Trächtler, A.; Schaper, M.: *Modelling the Constitutive Behaviour of Martensite and Austenite in Shape Memory Alloys Using Closed-Form Analytical Continuous Equations.* In: SPRINGER Computational Methods in Applied Sciences, Smart Structures and Materials, Vol. 43 no. VII, 2017

[2016] Pai, A.; Riepold, M.; Trächtler, A.: *Precision Control of SMA Actuators with a Real Time Model-Based Controller and Extended VSC.* In: Proceedings of 7th IFAC Symposium of Mechatronic Systems and 15th Mechatronics Forum International Conference - MECHATRONICS, Loughborough, United Kingdom, 5. September - 8. September 2016

[2016] Pai, A.; Riepold, M.; Trächtler, A.: *A Model extended Temperature and Strain Controller modulated with PWM for Precision Position Control of Shape Memory Alloy Actuators.* In: Proceedings of IEEE International Conference on Advanced Intelligent Mechatronics - AIM, Banff, Canada, 12. July - 15. July 2016

[2015] Pai, A.; Trächtler, A.; Schaper, M.: *Real-Time Compatible Phenomenological Modelling of the Austenitic Phase in Shape Memory Alloys as an Example for Modelling of Materials with Repeatable Non-Linear Characteristics.* In: Proceedings of 1st IFAC Conference on Modelling, Identification and Control of Nonlinear Systems - MICNON, St. Petersburg, Russia, 24. June - 26. June 2015

[2015] Pai, A.; Niendorf, T.; Krooss, P.; Koke, I.; Trächtler, A.; Schaper, M.: *Modelling the Constitutive Behaviour of Martensite and Austenite in Shape Memory Alloys Using Closed-Form Analytical Continuous Equations.* In: Conference of 7th ECCOMAS Thematic Conference on Smart Structures and Materials - SMART, Ponta Delgada, Azores, Portugal, 3. June - 6. June 2015

[2014] Pai, A.; Krooss, P.; Niendorf, T.; Koke, I.; Trächtler, A.; Schaper, M.: *Analyses of the stress-strain behaviour of SMAs under cyclical loading conditions – implementation of a novel phenomenological constitutive model.* In: Poster ICOMAT - International Conference on Martensitic Transformations, Bilbao, Spain, 6. July - 11. July 2014

Computationally Efficient Modelling and Precision Position and Force Control of SMA Actuators

Table of Contents

Appendix

List of Acronyms

asym.	Asymmetrical.
BL	Boundary Layer.
CPS	Cyber-Physical-Systems.
CPU	Central Processing Unit.
EPWM	Extended Pulse Width Modulated (Control).
EVSC	Extended Variable Structure Control.
IoT	Internet of Things.
IQR	Interquartile Range.
MEMS	Micro-electro-mechanical systems.
NPID	Nonlinear Proportional-Integral-Derivative (Control).
NRMSE	Normalised Root Mean Square Error.
PID	Proportional-Integral-Derivative (Control).
PWM	Pulse Width Modulation.
RAM	Random Access Memory.
RMS	Root Mean Square.
RMSE	Root Mean Square Error.
SIM	Stress Induced Martensite.
SMA	Shape Memory Alloy.
SPI	Serial Peripheral Interface.
sym.	Symmetrical.
VSC	Variable Structure Control.

List of Symbols

Name	Description	Unit
A_f	Austenite finish temperature	$[°C]$
A_f^o	Austenite finish temperature at no load	$[°C]$
A_s	Austenite start temperature	$[°C]$
A_s^o	Austenite start temperature at no load	$[°C]$
A_{SMA}	Cross-sectional area of SMA wire	$\left[\mathrm{m}^2\right]$
B	Base of triangle in second jaw of vice	$[m]$
C	Cooling curve	$[-]$
D	Diameter of test tube	$[m]$
E_1	Slope (modulus) until first knee	$[Pa]$
E_1^*	Slope (modulus) until first knee of current stress-strain segment	$[Pa]$
E_1^a	Slope (modulus) until first knee for loading at $T > A_f$ (austenite)	$[Pa]$
E_1^m	Slope (modulus) until first knee for loading at $T < M_f$ (martensite)	$[Pa]$
E_2	Slope (modulus) from first to second knee	$[Pa]$
E_2^*	Slope (modulus) from first to second knee of current stress-strain segment	$[Pa]$
E_2^a	Slope (modulus) from first to second knee for loading at $T > A_f$ (austenite)	$[Pa]$
E_2^m	Slope (modulus) from first to second knee for loading at $T < M_f$ (martensite)	$[Pa]$
E_2^u	Slope (modulus) from first to second knee for unloading identified from experiments	$[Pa]$
E_3	Slope (modulus) after second knee	$[Pa]$
E_3^*	Slope (modulus) after second knee of current stress-strain segment	$[Pa]$
E_3^a	Slope (modulus) after second knee for loading at $T > A_f$ (austenite)	$[Pa]$
E_3^m	Slope (modulus) after second knee for loading at $T < M_f$ (martensite)	$[Pa]$
E_{1a}^u	Slope (modulus) unitl first knee for unloading at $T > A_f$ (austenite)	$[Pa]$
E_{1m}^u	Slope (modulus) until first knee for unloading at $T < M_f$ (martensite)	$[Pa]$
E_{2m}^u	Slope (modulus) from first to second knee for unloading at $T < M_f$ (martensite)	$[Pa]$
E_{3a}^u	Slope (modulus) after second knee for unloading at $T > A_f$ (austenite)	$[Pa]$
E_{3m}^u	Slope (modulus) after second knee for unloading at $T < M_f$ (martensite)	$[Pa]$

Name	Description	Unit
F_{SMA}	Force in the SMA wire (temperature dependant) in the vice	$[N]$
F_{act}	Actual force on test tube	$[N]$
F_{des}	Desired force on test tube	$[N]$
F_s	Spring force in the vice	$[N]$
H	Height of triangle in second jaw of vice	$[m]$
H	Heating curve	$[-]$
I_H	Maximum current through wire	$[A]$
$I_H(\sigma_{act})$	Maximum current through wire depending on wire stress	$[A]$
I_H^{max}	Maximum allowable I_H	$[A]$
I_H^{min}	Minimum allowable I_H	$[A]$
I_L	Minimum current through wire	$[A]$
K_T^P	Proportional gain in P-P^{2}P^3 temperature controller	$[N]$
K_T^{P2}	Gain for square of temperature error in P-P^{2}P^3 temperature controller	$[-]$
K_T^{P3}	Gain for cube of temperature error in P-P^{2}P^3 temperature controller	$[-]$
K_ε^D	Gain for derivative component in PD-P^{2}P^3 strain controller	$[-]$
K_ε^P	Proportional gain in PD-P^{2}P^3 strain controller	$[-]$
K_ε^{P2}	Gain for square of strain error in PD-P^{2}P^3 strain controller	$[-]$
K_ε^{P3}	Gain for square of strain error in PD-P^{2}P^3 strain controller	$[-]$
K_s	Spring constant	$[Pa]$
M_f	Martensite finish temperature	$[°C]$
M_f^o	Martensite finish temperature at no load	$[°C]$
M_s	Martensite start temperature	$[°C]$
M_s^o	Martensite start temperature at no load	$[°C]$
T	Temperature	$[°C]$
T_a	Temperature at which the SMA is fully austenite	$[°C]$
T_m	Temperature at which the SMA is fully martensite	$[°C]$
$T_{\sigma\varepsilon_2}$	Temperature at which second knee occurs at a particular stress	$[°C]$
T_{act}	Actual temperature measured in wire	$[°C]$
T_{amb}	Ambient temperature	$[°C]$
T_p	Temperature at first end point in inverse phase kinetic model	$[°C]$
T_q	Temperature at second end point in inverse phase kinetic model	$[°C]$
T_{sw}	Temperature at switching point in phase kinetic model	$[°C]$
W	Distance between one jaw and tip of triangle in second jaw	$[m]$
$\Delta\sigma_s$	Additional stress in spring when jaws are touching test tube	$[Pa]$
$\Delta\varepsilon_{min}$	Minimum strain the SMA wire has to contract to touch the test tube	$[-]$
$\Delta\varepsilon_{s0}$	Strain in spring after installation in vice	$[-]$
$\Delta\varepsilon_{ss}$	Worst case steady state error band	$[-]$
Δx_{min}	Minimum length the SMA wire has to contract to touch the test tube	$[m]$
α_S	α_S^a weighted by effect of stress	$[-]$
α_S^a	Parameter detemining height of mechanical hystersis loop	$[-]$

Name	Description	Unit
α_T	α_T^a weighted by effect of stress	$[-]$
α_T^a	Parameter detemining height of thermal hystersis loop	$[-]$
β^C	Average of martensite start and finish temperatures	$[°C]$
β_o^C	Average of martensite start and finish temperatures at no load	$[°C]$
β^H	Average of austenite start and finish temperatures	$[°C]$
β_o^H	Average of austenite start and finish temperatures at no load	$[°C]$
δ_F	Force threshold	$[N]$
δ_T	Temperature threshold	$[°C]$
δ_ε	Strain threshold	$[-]$
γ_S	Parameter detemining offset of mechanical hystersis loop	$[-]$
γ_T	Parameter detemining offset of thermal hystersis loop	$[-]$
λ	Slope of sliding surface	$[-]$
ϕ	Thickness of asymmetrical boundary layer	$[-]$
σ	Stress	$[Pa]$
σ_p^n	Stress on reloading curve at unloading strain ε_{pp} on the plateau	$[Pa]$
σ_s^n	Additional stress to create a step in the austenite plateau after partial unloading and reloading	$[Pa]$
σ_{pp}^n	Stress on original loading curve at unloading strain ε_{pp} on the plateau	$[Pa]$
σ_1	Stress-strain equation until first knee	$[Pa]$
σ_2	Stress-strain equation from first to second knee	$[Pa]$
σ_3	Stress-strain equation after second knee	$[Pa]$
σ_a	Stress at ε_a	$[Pa]$
σ_m	Stress at ε_m	$[Pa]$
σ_n	Height of stress step after partial unloading and reloading in austenite	$[Pa]$
σ_q	Stress-strain equation with parabola	$[Pa]$
σ_{SMA}	Stress on the SMA wire (temperature dependant) in the vice	$[Pa]$
σ_T	Total stress in system when jaws are impinging desired stress on test tube	$[Pa]$
$\sigma_{\varepsilon 1a}$	Stress at first knee for loading at $T > A_f$ (austenite)	$[Pa]$
$\sigma_{\varepsilon 1a}^u$	Stress at first knee for unloading at $T > A_f$ (austenite)	$[Pa]$
$\sigma_{\varepsilon 1m}$	Stress at first knee for loading at $T < M_f$ (martensite)	$[Pa]$
$\sigma_{\varepsilon 1m}^u$	Stress at first knee for unloading at $T < M_f$ (martensite)	$[Pa]$
$\sigma_{\varepsilon 1}$	Stress at first knee	$[Pa]$
$\sigma_{\varepsilon 1}^*$	Stress at first knee of current stress-strain segment	$[Pa]$
$\sigma_{\varepsilon 2a}$	Stress at second knee for loading at $T > A_f$ (austenite)	$[Pa]$
$\sigma_{\varepsilon 2a}^u$	Stress at second knee for unloading at $T > A_f$ (austenite)	$[Pa]$
$\sigma_{\varepsilon 2m}$	Stress at second knee for loading at $T < M_f$ (martensite)	$[Pa]$
$\sigma_{\varepsilon 2m}^u$	Stress at second knee for unloading at $T < M_f$ (martensite)	$[Pa]$
$\sigma_{\varepsilon 2}$	Stress at second knee	$[Pa]$
$\sigma_{\varepsilon 2}^*$	Stress at second knee of current stress-strain segment	$[Pa]$
σ_{act}	Actual stress measured on wire	$[Pa]$

Name	Description	Unit
σ_{bq}	Stress calculated from base equation that describes an s-shaped stress-strain curve	$[Pa]$
σ_{des}	Desired stress on test tube	$[Pa]$
σ_{des}^{max}	Maximum possible desired stress on test tube	$[Pa]$
σ_{m0}	Initial stress in the SMA wire after installation in vice	$[Pa]$
σ_{min}	Stress in system when jaws are touching the test tube	$[Pa]$
σ_n	Stress calculated from base equation at mid-point between the knees	$[Pa]$
σ_{pp}	Stress at start of current stress-strain segment	$[Pa]$
σ_p	Stress at end of current stress-strain segment	$[Pa]$
σ_{sw}	Stress at switching point in phase kinetic model	$[Pa]$
σ_{sw}^{-}	Stress right before switching point in phase kinetic model	$[Pa]$
σ_s	Spring stress in the vice	$[N]$
ε	Strain	$[-]$
ε_{1a}	Strain at first knee for loading at $T > A_f$ (austenite)	$[-]$
ε_{1a}^{u}	Strain at first knee for unloading at $T > A_f$ (austenite)	$[-]$
ε_{1m}	Strain at first knee for loading at $T < M_f$ (martensite)	$[-]$
ε_{1m}^{u}	Strain at first knee for unloading at $T < M_f$ (martensite)	$[-]$
ε_1	Strain at first knee	$[-]$
ε_1^*	Strain at first knee of current stress-strain segment	$[-]$
ε_1^u	Strain at first knee for unloading identified from experiments	$[-]$
ε_{2a}	Strain at second knee for loading at $T > A_f$ (austenite)	$[-]$
ε_{2a}^{u}	Strain at second knee for unloading at $T > A_f$ (austenite)	$[-]$
ε_{2m}	Strain at second knee for loading at $T < M_f$ (martensite)	$[-]$
ε_{2m}^{u}	Strain at second knee for unloading at $T < M_f$ (martensite)	$[-]$
ε_2	Strain at second knee	$[-]$
ε_2^*	Strain at second knee of current stress-strain segment	$[-]$
ε_{RMS}^{avg}	Average RMS error	$[-]$
ε_R	90% of strain step height	$[-]$
ε_{act}	Actual strain measured on wire	$[-]$
ε_a	Minimum (austenitic) strain at a particular load	$[-]$
$\varepsilon_{k\xi}$	Strain at which mechanically induced martensite is 0.5	$[-]$
ε_{m0}	Initial strain in the SMA wire after installation in vice	$[-]$
ε_{min}	Strain in system when jaws are touching the test tube	$[-]$
ε_m	Maximum (martensitic) strain at a particular load	$[-]$
ε_{pp}	Strain at start of current stress-strain segment	$[-]$
ε_p	Strain at end of current stress-strain segment	$[-]$
ε_{ra}	Residual strain for loading at $T > A_f$ (austenite)	$[-]$
ε_{rm}	Residual strain for loading at $T < M_f$ (martensite)	$[-]$
ε_r	Residual strain	$[-]$
ε_{ss}^{avg}	Average steady state error	$[-]$
ε_t	Maximum strain travel at a particular load	$[-]$
ξ	Total martensite fraction	$[-]$
ξ^H	Martensite fraction for heating curve	$[-]$
ξ_D	Detwinned martensite fraction	$[-]$
ξ_S	Mechanically induced martensite fraction	$[-]$

Name	Description	Unit
ξ_S^p	Mechanically induced martensite fraction evaluated at ε_p	$[-]$
ξ_T	Thermally induced martensite fraction	$[-]$
ξ_W	Twinned martensite fraction	$[-]$
ξ_1	Martensite fraction at first knee for inverse phase kinetic model	$[-]$
ξ_2	Martensite fraction at second knee for inverse phase kinetic model	$[-]$
ξ_{SIM}	Stress induced martensite fraction	$[-]$
ξ_{So}	Initially mechanically induced martensite fraction	$[-]$
ξ_{To}	Initial thermally induced martensite fraction	$[-]$
ξ_{act}	Actual martensite fraction in wire	$[-]$
ξ_{des}	Desired martensite fraction in wire	$[-]$
ξ_{sw}	Martensite fraction at switching point in inverse phase kinetic model	$[-]$
b	Sliding surface	$[-]$
c	Number of loading/unloading cycles	$[-]$
c_m	Slope of heating curve	$[°C/Pa]$
$d\xi_{Ta}$	Derivative of martensite fraction w.r.t. temperature at T_a	$[1/°C]$
$d\xi_{Tm}$	Derivative of martensite fraction w.r.t. temperature at T_m	$[1/°C]$
$d\xi_\beta$	Derivative of martensite fraction w.r.t. temperature at β_H	$[1/°C]$
e_F	Force error	$[N]$
e_T	Temperature error	$[°C]$
e_ε	Strain error	$[-]$
h_1	Inverse phase kinetic model upto first knee	$[-]$
h_2	Inverse phase kinetic model at plateau	$[-]$
h_3	Inverse phase kinetic model after second knee	$[-]$
i	Current from control signal	$[A]$
i_T	Current from temperature control signal	$[A]$
i_ε	Current from strain control signal	$[A]$
k^C	Slope of cooling curve	$[°C/Pa]$
k^H	Slope of heating curve	$[°C/Pa]$
k^{inv}	Slope of sigmoid function (y_2) in inverse $\sigma-\varepsilon$ curve	$[1/Pa]$
k_1	Curvature at first knee	$[-]$
k_1^*	Curvature at first knee of current stress-strain segment	$[-]$
k_1^a	Curvature at first knee for loading at $T > A_f$ (austenite)	$[-]$
k_1^m	Curvature at first knee for loading at $T < M_f$ (martensite)	$[-]$
k_2	Curvature at second knee	$[-]$
k_2^*	Curvature at second knee of current stress-strain segment	$[-]$
k_2^a	Curvature at second knee for loading at $T > A_f$ (austenite)	$[-]$
k_2^m	Curvature at second knee for loading at $T < M_f$ (martensite)	$[-]$
k_ξ	Slope of mechanically induced martensite function	$[-]$
k_b	Parameter defining curvature in inverse phase kinetic model	$[°C]$
k_s	Spring constant	$[N/m]$
l_{SMA}	Length of SMA wire	$[m]$
m	Slope after ξ_2 in inverse phase kinetic model	$[°C]$
m_1	Slope of inverse stress-strain curve upto first knee	$[-]$

Name	Description	Unit
q	Parabolic constant	$[-]$
q^*	Parabolic constant of current stress-strain segment	$[-]$
t_r	Rising time	$[s]$
t_r^{avg}	Average rising time	$[s]$
t_{sw}	Time at switching point in phase kinetic model	$[s]$
t_s	Settling time	$[s]$
t_s^{avg}	Average settling time	$[s]$
u	Control signal	$[-]$
u_F	Force control signal	$[N]$
u_T	Temperature control signal	$[^\circ C]$
u_ε	Strain control signal	$[-]$
x	Slope upto ξ_1 in inverse phase kinetic model	$[^\circ C]$
y_1	Equation adding slope m_1 to sigmoid function in inverse $\sigma-\varepsilon$ curve (inverse upto first knee)	$[-]$
y_2	Equation defining sigmoid function in inverse $\sigma-\varepsilon$ curve (plateau inverse)	$[-]$
y_3	Equation adding slope $1/E_3$ to sigmoid function in inverse $\sigma-\varepsilon$ curve (inverse after second knee)	$[-]$
z_1	Minimum of sigmoid function (y_2) in inverse $\sigma-\varepsilon$ curve	$[-]$
z_2	Maximum of sigmoid function (y_2) in inverse $\sigma-\varepsilon$ curve	$[-]$

1 Introduction

Actuators are devices that provide the driving force and motion in a system [HFA97] by conversion of electrical, chemical, thermal or flow energy into kinetic energy [Jen98]. For example, the muscles of animals are naturally occurring actuators, as they convert electrical signals from the brain to locomotion. Examples of man-made actuators are hydraulics, pneumatics, electrical motors etc. Majority of technology developments, as we know and use daily, cannot exist without actuators because they form the fundamental movement mechanism in a vast range of applications e.g. industrial equipment, transportation, electrical and consumer devices, instrumentation, health, agriculture, energy etc.

Current technological trends according to Cyber-physical systems (CPS) call for systems with embedded software and electronics that are networked with the outside world through intelligent sensors and actuators [Bro16]. The inter-networking of physical devices and systems within cyberspace is called the Internet of Things (IoT) [VF13], and together with CPS, form the basis of Industry 4.0 [MKB+16]. Industry 4.0, also called the fourth industrial revolution, aims to develop systems that are self-aware and are able to self-configure, self-organize, self-maintain and self-predict [LBK15].

The demands of Industry 4.0 has caused a rise in the complexity of various products and systems with consistent, or even decreasing, physical dimensions, and therefore a tremendous decrease in the available installation space. Further, in the past decade, there has been a continuing technological trend towards miniaturisation. For example, consumer electronic products such as cell phones, cameras, personal computers etc. have seen a stark decrease in size, with a simultaneous increase in functionality and complexity.

In keeping with these trends, actuators, which are ubiquitous in most devices, applications and industries, also have had to undergo a similar miniaturisation. This has caused the emergence of novel actuators such as piezoelectrical, electrostatical, magnetostrictive materials and shape memory alloys [TF08].

Shape memory alloys (SMAs) are metallic materials that seem to *remember* a predefined base shape. When the material is deformed from this base shape, application of an external stimulus causes macroscopic recovery of the base shape. The external stimulus can either be a change of stress or temperature[1]. The impregnation of the base shape onto the material is performed by a metallurgical process called annealing [OR05]. The shape recovery capability of SMAs can be exploited to work on a load, and SMAs can hereby be used as actuators.

In a study performed by Huber et al. [HFA97], which classified mechanical actuators based on perfomance indices, SMA-based actuators were shown to have one of the highest energy density (energy/volume) and specific actuation stress (stress/density or force/mass) as compared with conventional actuators as shown in Tab. 1-1.

[1] In the case of magnetic shape memory alloys (MSMAs), the external stimulus is a change in a surrounding magnetic field. MSMAs will not be considered in this thesis.

Table 1-1: *Comparison of conventional actuators*

Actuator	Solenoid	Electric	Pneumatic	Hydraulic	Piezo	**SMA**
Energy density (MJ/m^3)	0.05	0.0015	1	80	0.01	**80**
Specific actuation stress (MNm/Kg)	0.0005	0.0001	0.05	0.5	0.1	**1**

The high energy density combined with high specific actuation stress makes SMA actuators powerful and compact in both volume and mass, and therefore able to meet the miniaturisation demands due to Industry 4.0.
Further advantages of SMA-actuators are as follows [Sha95], [HFA97], [Hum01],[OR05]:

- high tensile strength (upto 1 GPa)
- elastic modulus in the range of 30-40 GPa
- recovery of upto 10% deformation strains
- elongation to failure of 50% strain
- significant internal damping
- smooth and silent actuation
- bio-compatibility making them attractive for bio-medical applications
- scalability (m - μm)
- reduced part counts compared to traditional alternatives
- ability to be used as a sensor and actuator simultaneously

These advantages make SMA-based actuators very attractive for a wide range of applications, most especially, where high forces are required with simultaneous constraints on installation space and weight e.g. for applications in automotive, aerospace, micro-robotics, surgical devices, micro-electro-mechanical systems (MEMS) etc.

The most commonly used SMAs are Nickel-Titanium (NiTi) alloys, whose shape memory capabilities were first accidentally discovered in the 1960s by W. J. Buehler at the Naval Ordinance Laboratory[2] [DMS90].

Since then, a number of other alloys that display shape memory have been discovered including copper based alloys such as copper zinc aluminium (CuZnAl), copper aluminium nickel (CuAlNi) or iron based alloys such as iron manganese Silicon (FeMnSi) etc. (see [AO16] for a comprehensive list of copper and iron based alloys), as well as alloys such as gold, silver, indium and platinum [Pai07]. However, these alloys are still a subject of research and NiTi, which is commercially available, is most widely used in applications in the industry today.

[2] giving the alloy alternative name NiTiNOL from NiTi **N**aval **O**rdinance **L**aboratory.

1.1 Motivation

Current applications in the industry that employ SMA actuators include door latches, locking mechanisms e.g. in the Microsoft Surface Book [Mic16], [iFi16] etc. These applications use the SMA in one of two states: hot or cold and therefore the SMA actuator is used as a temperature-controlled binary switch.

SMA actuators capable of position or force control are extremely attractive for a variety of applications. For example, in the automotive or aerospace industries, where large forces are required with extreme weight and volume constraints; in the medical field, where bio-compatible, silent actuation is desirable etc. However, the design of actuators for position or force control is non-trivial because SMAs are inherently extremely nonlinear and hysteretic in behaviour.

Precision control of SMA actuators has thus been a focus of various research efforts over the past three decades, with promising results. However, the proposed control methods are often complicated and computationally expensive. Consequently, although one of the major advantages of SMA actuators is their miniaturization, the control units that are commonly employed are large, dictated by the need for computational power.

Therefore, in order for SMA actuators to be interesting for industrial applications, a holistic approach that involves miniaturization of both the SMA actuator, its controller, sensors and other periphery is paramount. This additional requirement lends weight to the use of embedded processors or microcontrollers as the control unit of choice. To this end, the control algorithms should be 'simple' enough to run on an embedded processor, should run in real-time and should allow for precise and accurate position and/or force control.

The development of control strategies for such actuators is alleviated by incorporating models that predict the characteristic nonlinearities. While several models predicting SMA behaviour have been developed, they are either extremely complicated and computationally expensive or they are too elementary, in consequence showing poor correlation to observed behaviour. This leaves a necessity for SMA models that are accurate enough to model SMA behaviour relevant to actuator applications as well as being computationally efficient enough to be used in control algorithms. This thesis proposes to tackle the challenges mentioned above with the specific goals detailed below.

1.2 Goals

The goals of this thesis are:

- the development of **computationally efficient models** to accurately predict macroscopic SMA behaviour, relevant to their use as actuators.
- The use of these models to **design non-linear controllers**,
- that allow for **precise and robust control** of the SMA,
- while being **computationally efficient** enough to run on **embedded** processors,
- thereby **miniaturising** both the actuator and the controller and thus make them more **attractive** for **industrial applications**.

1.3 Outline

The thesis is organised as follows:

Chapter 2: Shape Memory Alloys This chapter presents an overview of SMA behaviour including the underlying cause of the shape recovery mechanisms in SMAs. The description of the SMA behaviour outlined here will be used as a basis for the development of SMA models.

Chapter 3: Literature Review and Solution Approach In this chapter, a literature review of exiting control strategies for SMAs is presented. The deficiencies and strengths of the controllers are outlined and model-based control is selected as a promising control strategy. This is followed by a literature review of existing SMA models and a discussion of their deficiencies. Finally, the solution approach to combat the deficiencies in modelling and control is presented.

Chapter 4: Stress-Strain Model at Threshold Temperatures In this chapter, a novel constitutive model for SMAs at threshold temperatures, where the SMA is completely composed of a single phase at no load, is presented. The base of the model is the analytical description of an 's-shaped' curve that is ubiquitous in the SMA stress-strain behaviour.

Chapter 5: Stress Strain Model at Arbitrary Temperatures The focus of this chapter is the extension of the constitutive model in the previous chapter to arbitrary temperatures, where the SMA is a mixture of phases.

Chapter 6: Phase Kinetics Model The phase kinetic model, which describes the evolution of the SMA phases dependant on temperature and stress is presented in this chapter. The model developed here is based on analytical equations that describe the characteristic SMA hysteresis.

Chapter 7: Inverse SMA Model In order to use the constitutive and phase kinetic models in a control loop, inverse models are required. The development of these inverses is the focus of this chapter.

Chapter 8: Model-based Position Control This chapter presents the control architecture for precise and robust position control of the SMAs. The performance of the controller for various desired strains and disturbance rejection is also shown.

Chapter 9: Embedded Force and Position Control for an Industrial Clamping Application In this chapter, an industrial SMA-based clamping vice is presented. The vice uses SMA wires to clamp a thin-walled test tube. The control architecture presented in the previous chapter is used for force control and the controller is implemented on an embedded platform. The performance of the clamping vice for various desired clamping forces and disturbance rejection is shown.

Chapter 10: Conclusions and Future Work This chapter presents concluding remarks and suggestions for future work.

2 Shape Memory Alloys

In this chapter, a brief overview of the behaviour of shape memory alloys will be presented. The shape memory behaviour is attributed to microscopic crystalline solid-solid phase transformations that occur without diffusion or plasticity [CSI09]. In Sect. 2.1, the characteristic SMA phases will be introduced, with the thermal hysteresis, stress-strain behaviour as well as the shape memory mechanisms presented in detail from Sects. 2.2 - 2.8. In Sect. 2.9, the use of SMAs as actuators will be discussed. SMAs are produced in various forms: wires, springs, strips, tubes, sheets etc. [Sae16]. For actuators, wires of various diameter are most commonly used. For the investigations in this thesis, NiTi wires with a diameter of 0.5 mm from the company SAES Group [Sae16] will be used. A good overview of SMA phenomenon can also be found in [Lag08], [CSI09].

2.1 SMA Phases

Shape memory alloys are characterised microscopically by two distinct phases: austenite and martensite, each with a different crystalline structure [GSA+01],[OR05],[FGD+10]. Phase transformations from austenite to martensite and vice versa occur under varying temperature and/or stress on the material without diffusion or plasticity [CSI09]. These transformations form the basis of the shape memory behaviour in SMAs. The crystalline structure of austenite and martensite in NiTi-based SMAs is presented below:

Austenite is the phase that occurs at simultaneously high temperatures and low stress conditions[1]. It has a highly stable cubic lattice structure. In the case of NiTi, the crystalline structure, as shown in Fig 2-1(a), consists of two interpenetrating cubic lattices of Ni and Ti, respectively [CSI09] i.e. either a Ni atom in the centre and Ti atoms at the corners or vice versa. This structures makes austenite strong with an elastic modulus of about 40-50 GPa.

Martensite is the phase that occurs at low temperatures with a crystalline structure as shown in Fig 2-1(b) and (c). The martensitic crystalline structure has lower symmetry than austenite and is stress-dependant.
In low stress conditions, martensite, in NiTi, has monoclinic symmetry, which can exist in several (12) lattice variants. These variants are reflections or rotations of each other [CSI09]. The lattices are twinned i.e. a specific atom on a so-called twin boundary, sees a coherent mirror image of the lattice along either side [CSI09], [Pai07] as shown in Fig 2-1(b). The martensite in this state is called *twinned martensite*. The application of stress causes the twin boundaries to move to variants preferentially aligned with the stress. The lattice thereby changes, in NiTi, to an oriented structure (see Fig 2-1(c)) called *detwinned martensite* [Pai07]. In comparison to austenite, both twinned and detwinned martensite are weaker with an elastic modulus of about 20-30 GPa.

[1] The definition of 'high' temperature and 'low' stress will be clear in the following sections.

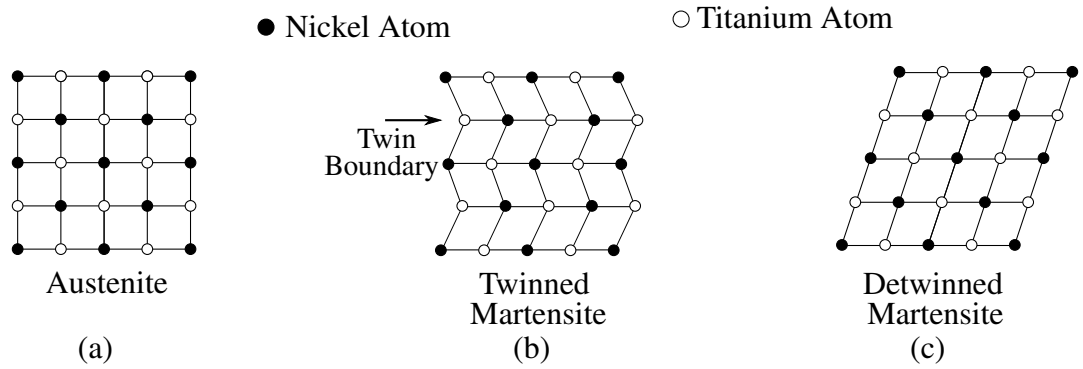

Figure 2-1: *Phases and crystal lattices in SMAs*

2.2 Stress Strain Behaviour: Austenite

The stress-strain behaviour of austenite is shown schematically in Fig. 2-2. The curve begins with an elastic portion ⓪ - ①, with a modulus of about 40-50 GPa. When the stress is sufficiently large ($> \sigma_{\varepsilon 1a}$), the austenite destabilises in favour of one or more martensite variants [CSI09] called *stress induced martensite* (SIM), which has a crystalline structure similar to detwinned martensite in 2-1(c). SIM first starts forming close to $(\varepsilon_{1a}, \sigma_{\varepsilon 1a})$ and the change of the crystalline composition of the SMA causes an abrupt change of the modulus, forming a 'knee' at $(\varepsilon_{1a}, \sigma_{\varepsilon 1a})$. After the formation of the first knee, martensite propagates rapidly, causing extensive strain with relatively low additional stress, thereby causing a 'plateau' from ② - ③. The transformation to martensite is complete at $(\varepsilon_{2a}, \sigma_{\varepsilon 2a})$. This once again causes an abrupt modulus change and the formation of a second knee, after which martensite (④ - ⑤) deforms elastically with a modulus of about 20-30 GPa. Austenite can be stretched to about 10-12% strain. Beyond that, plastic deformation (not shown in the figure) sets in.

2.2.1 Pseudoelasticity

In Fig. 2-3, loading from ⓪ to ⑤ (identical to Fig. 2-2), triggers a complete transformation from austenite to SIM. When the stress is now reduced, SIM unloads elastically (as shown exemplarily in Fig. 2-3 by the solid black line originating at ⑤ with a slope of 20 GPa). However, analysis of experimental data with NiTi wires has shown that the unloading (and reloading) behaviour of martensite follows a parabolic locus, as shown exemplary by the green dashed curve in Fig. 2-3.

Parabolic locus in unloading

The parabolic shape can be explained based on the microstructural condition of NiTi SMA wires. For improved shape memory behaviour, wires are strongly textured to allow for high transformation strains. However, minor volume fractions of grains (crystals) of all possible orientations can be expected to be found within these wires. Grain orientation corresponds to critical stress levels for phase transformation of single grains [OR05], [KNK+12], [Hor91]. Thus, small volume fractions of the wire might show a premature

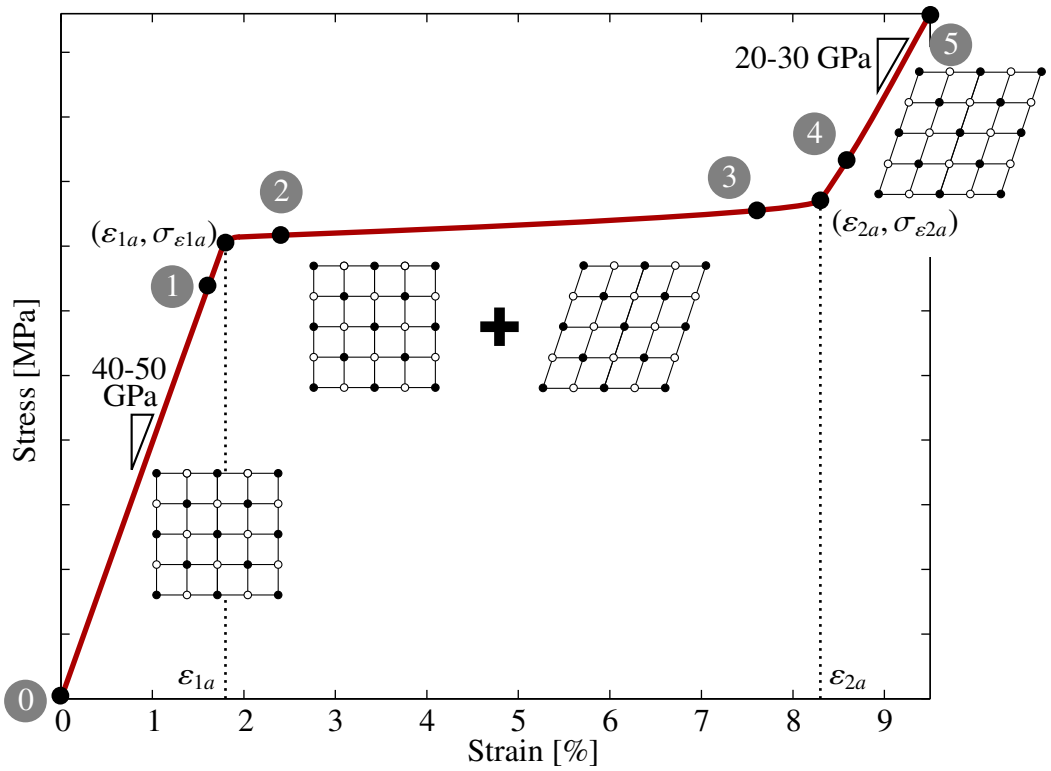

Figure 2-2: *Stress strain behaviour of austenite in NiTi wires (loading)*

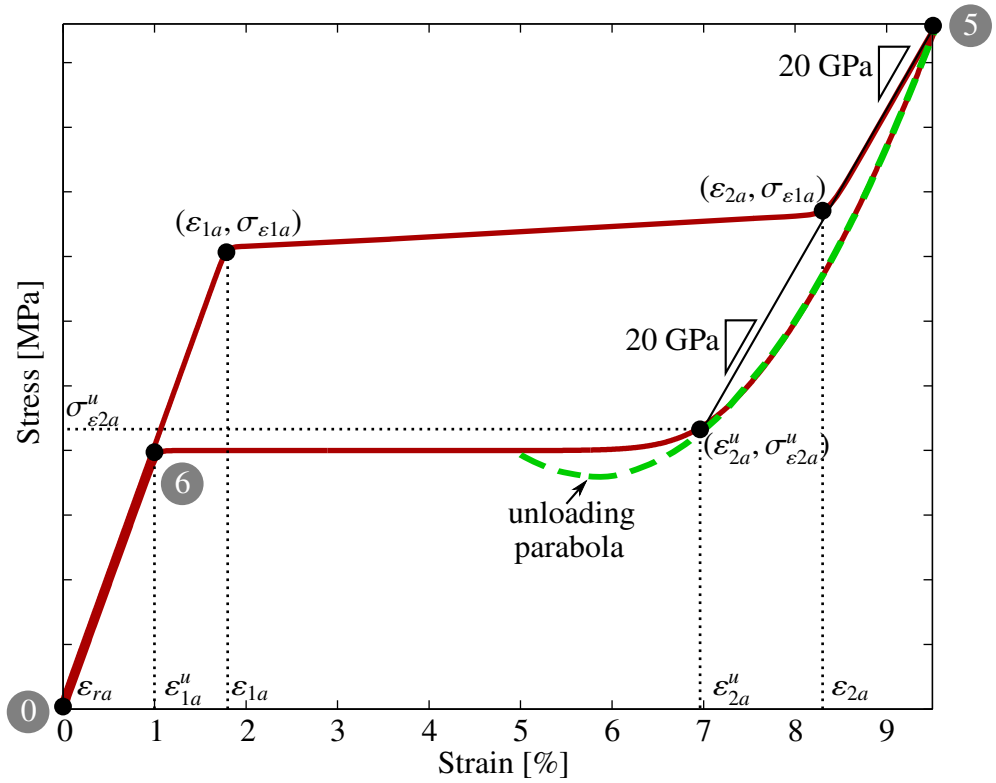

Figure 2-3: *Stress strain behaviour of austenite in NiTi wires (loading and unloading)*

and others sluggish phase transformation. As a consequence, unloading in martensite is characterized by the smooth curvatures depicted [PNK+15].

SIM starts converting back to austenite close to (ε^u_{2a}, $\sigma^u_{\varepsilon 2a}$) (see Fig. 2-3) because martensite at this stress is no longer thermodynamically stable [OR05], [CSI09]. The martensite depletion is as rapid as the propagation in the loading case. This forms an unloading plateau (ε^u_{2a} to ⑥), after which the SMA is once again, at least theoretically, 100% austenite.

Residual strain

Experimental studies such as in [RLS07] have shown that a small amount of residual strain ε_{ra} is present after unloading, showing that not all SIM has been converted back to austenite. Due to several reasons, e.g. plastic deformation of the martensite and micro-yielding effects, degradation of SMAs can be present, manifesting itself in the accumulation of irrecoverable portions of strain in the reverse transformation [GSA+01], [KNK+12].

Nevertheless, an SMA wire at these high temperatures shows a macroscopic elongation on application of stress and a strain recovery on removal of the stress, just as in an elastic material. However, due to the stress hysteresis present, this effect is called *pseudoelasticity* or *superelasticity*, and is one of the shape recovery mechanisms in SMAs.

2.2.2 Minor loop behaviour

A stress-strain profile from ⓪ - ⑤ - ⓪ (or ε_{ra}) as shown in Fig. 2-3 causes a (nearly) full transformation from austenite to martensite and back. This is called a *major loop*. A strain profile, as shown in Fig. 2-4, that consists of loading from ⓪ - ⑦, unloading from ⑦ - ⑨ and reloading from ⑨ - ⑦ (or ⑤) causes the formation of a *minor loop* (⑦ - ⑧ - ⑨ - ⑩ - ⑦). Note that when unloading, the SMA joins an unloading plateau at ⑧, when the stress reaches $\sigma^u_{\varepsilon 2a}$. Similarly, when reloading the loading plateau is joined at ⑩, where the stress is $\sigma_{\varepsilon 1a}$. A loading profile from ⓪ - ⑦, unloading from ⑦ - ⑪ and reloading from ⑪ - ⑤ also forms a minor loop (⑦-⑪-⑦). Here, the reloading is elastic. However, due to the parabolic nature of unloading, a small hysteresis is present.

2.2.3 Austenite reloading behaviour

In Fig. 2-5, the results of an experiment showing austenite reloading behaviour is shown. In this experiment, an SMA wire at high temperature was first loaded to a strain below the 1st knee, then unloaded to 25 MPa. This is the first cycle. Then, the SMA is reloaded to a strain of 1.4% and unloaded to 25 MPa (cycle 2). 7 additional loading and reloading cycles follow, with each cycle loading to 0.2% strain higher than the previous cycle, as shown in Fig. 2-5. A phenomenon exclusive to austenite reloading is the formation of 'steps' in the austenite plateau and a decrease of the plateau stress when reloading follows periods of partial unloading (partial in this case meaning unloading before the 2nd knee). They were also observed in the experimental data of [GSW10], who attribute these phenomena

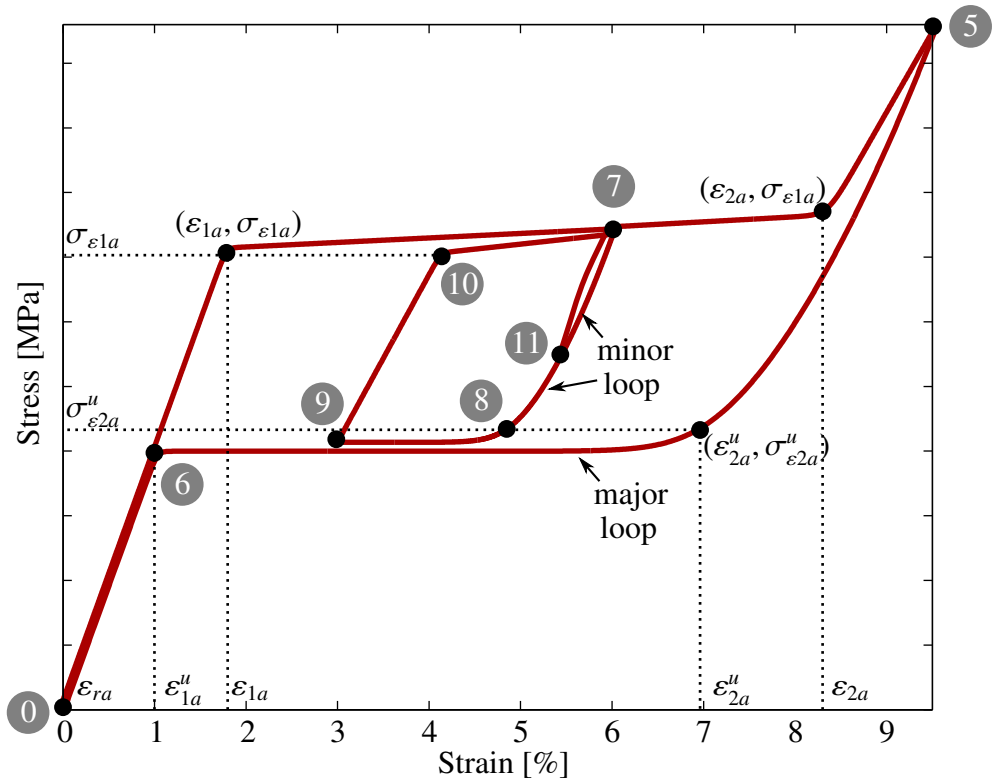

Figure 2-4: *Stress strain behaviour of austenite in NiTi wires (unloading and reloading)*

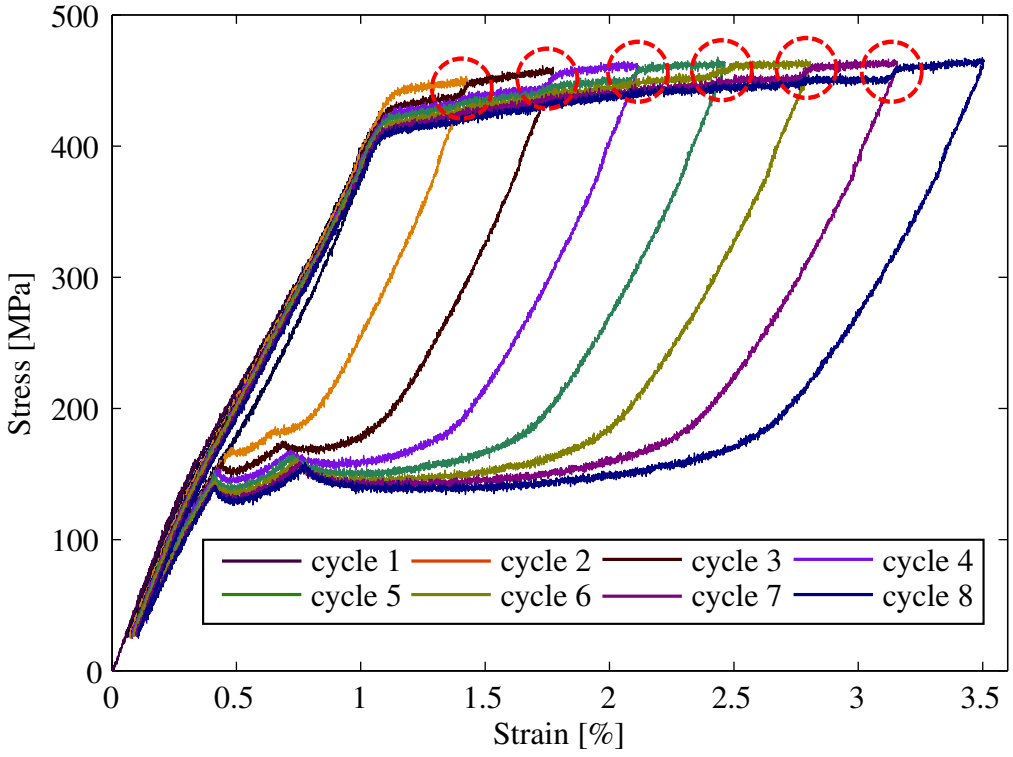

Figure 2-5: *Experimental data showing partial loading cycles in austenite with 'steps' (red dashed circles)*

to functional fatigue with the following explanation: Deformation of the austenite beyond the 1st knee is characterised by the formation and propagation of SIM bands. Outside these bands, the material is still austenitic. When the material undergoes cyclical partial reloading, then the band interfaces

> first traverse previously cycled regions. These regions are associated with a lower critical stress of interface propagation. For the interface to pass into the uncycled region, the macroscopic stress must increase. When the interfaces have completely passed into the uncycled region, the macroscopic stress reaches the level of the upper plateau [GSW10],

therefore causing the formation of 'steps' macroscopically. Should the SMA be exposed to several partial loading cycles as in Fig. 2-5, then a step occurs at each unloading point as though the material has 'memory' of the unloading positions. The most pronounced step is at the last unloading cycle (or at the absolute strain maximum of the previous loading cycles) as shown by the red dotted circles in Fig. 2-5.

2.3 Stress Strain Behaviour: Martensite

The stress-strain loading behaviour of twinned martensite, as shown in Fig. 2-6, has the same general shape of the austenite loading curve. It is also characterised by an elastic portion ⓪ - ①, the first knee, a plateau ② - ③, the second knee and a final elastic portion ④ - ⑤. Twinned martensite begins to detwinn, with a preference for martensite variants aligned to the stress, close to the first knee at $(\varepsilon_{1m}, \sigma_{\varepsilon 1m})$. Detwinned martensite propagation causes the plateau and after the second knee at $(\varepsilon_{2m}, \sigma_{\varepsilon 2m})$, the SMA is completely detwinned. After ⑤, plastic deformation sets in. The twinned martensite yield stresses and plateau are much lower than that of austenite. This is due to the fact that the austenite cubic lattice structure is much more compact and therefore stronger than the monoclinic twinned martensite lattice structure.

When the SMA is unloaded after commencement of the detwinning process, i.e. after ε_{1m}, most of the resulting macroscopic strain (from the loading process) remains since all variants are again energetically equivalent [CSI09]. This causes the presence of residual strain as shown in Fig. 2-7 for paths ⓪ - ⑥ - ⑦, ⓪ - ⑧ - ⑨ or ⓪ - ⑤ - ⑩.

Parabolic loci in unloading and reloading

The unloading behaviour also follows a parabolic locus, as shown exemplarily with the green dashed curve for unloading from ⑤ - ⑩ in Fig. 2-7.

The reloading behaviour e.g. from either ⑦, ⑨ or ⑩, is elastic, however, it also follows a parabolic locus as shown by the green dashed line in Fig. 2-7 for reloading from ⑦. In addition to the grain orientation as mentioned above in Sect. 2.2.1, the parabolic nature of the stress-strain curve can be further attributed to internal stresses present in the deformed microstructure providing the driving forces for a minor backward or forward movement of the twin boundaries [KNK+12]. Since both the unloading and reloading behaviours follow parabolic loci, minor hysteresis loops form e.g. ⑥-⑦-⑥ or ⑧-⑨-⑧.

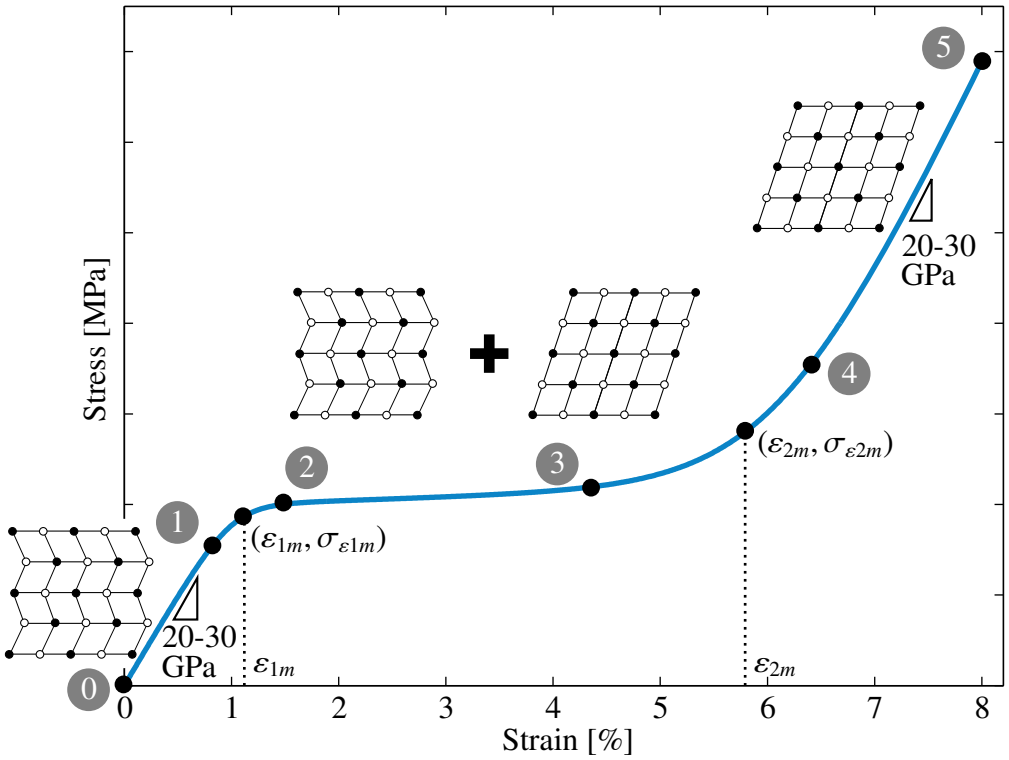

Figure 2-6: *Stress strain behaviour of martensite in NiTi wires (loading)*

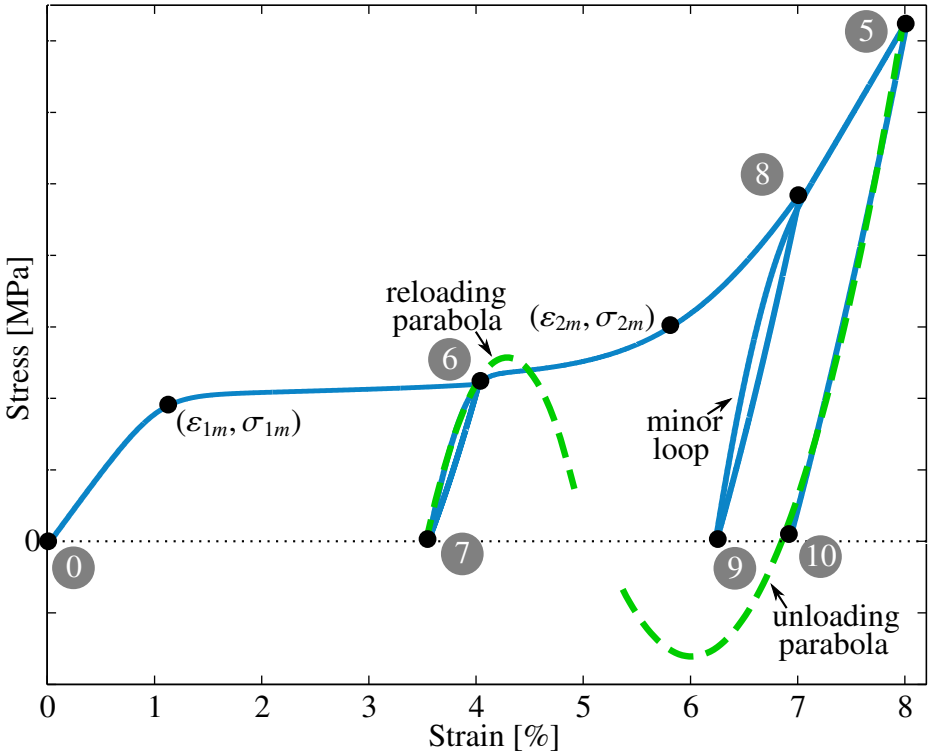

Figure 2-7: *Stress strain behaviour of martensite in NiTi wires (unloading and reloading)*

2.4 Mechanically Induced Martensite Fraction

The stress-strain behaviour of austenite and martensite in Sects. 2.2 and 2.3 are coupled with a change of the crystalline structure present at no load.

Note that both detwinned martensite and stress induced martensite have the same oriented crystalline structure, although the former is arrived at by the detwinning of martensite and the later by stressing austenite. Nevertheless, the mechanical process of increasing the stress or strain of the SMA, regardless of a twinned martensitic or austenitic start phase, causes the formation of martensite with an oriented lattice structure. In this thesis, this will be called *mechanically induced martensite*.

Defining the fraction of mechanically induced martensite ξ_S where $0 \leq \xi_S \leq 1$ as $\xi_S = 1$ when the SMA is 100% martensite, ξ_S evolves according to Fig. 2-8 with a change in strain. In the loading case, when the SMA is strained before the first knee ε_1, then $\xi_S = 0$ since no mechanically induced martensite has been formed. When the SMA is strained after the second knee ε_2, then the material is fully transformed to oriented martensite and $\xi_S = 1$. In between the knees, ξ_S propagates linearly between 0 and 1. This is true regardless of the temperature i.e. regardless of whether the SMA is twinned martensite or austenite at the origin of the $\sigma - \varepsilon$ diagram. However, since the position of the knees change with temperature (observe that the knees in Fig. 2-2 and 2-6 are at different positions), ξ_S is temperature dependant.

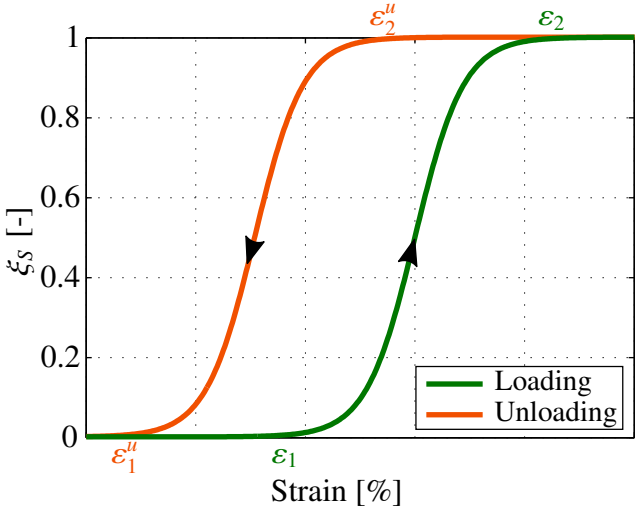

Figure 2-8: *Mechanically induced martensite fraction*

Once the SMA has been stressed beyond the second knee ($\xi_S = 1$), the reverse transformation from 100% (oriented) martensite to 0% (oriented) martensite occurs during unloading only at temperatures where austenite exists at no load. This is due to the pseudoelastic effect detailed in Sect. 2.2.1. For all other temperatures, unloading causes residual strain (see Fig. 2-7) and ξ_S remains unchanged.

2.5 Thermally Induced Martensite Fraction

The transformation from austenite to martensite and vice versa can also be triggered by a change in temperature. When austenite is allowed to cool to sufficiently low temperatures, it transforms to martensite. Likewise, when martensite is heated, a transformation to austenite occurs.

The transformations are hysteretic in nature, as shown exemplarily in Fig. 2-9, where the abscissa is the temperature (in $°C$) and the ordinate is the thermally induced martensite fraction ξ_T.

At no load, when 100% martensite ($\xi_T = 1$) is heated, at a particular temperature called the *austenite start temperature* A_s, austenite crystals will first start forming in the SMA. By the *austenite finish temperature* A_f, the SMA is fully austenite and $\xi_T = 0$. When the austenite is allowed to cool, martensite crystals first start forming at the *martensite start temperature* M_s and by the *martensite finish temperature* M_f, the SMA is again fully martensitic. Characterization of the stability of both phases is done on the basis of these four characteristic temperatures, where, generally, $M_f < M_s < A_s < A_f$[2]. The transformation temperatures are usually supplied from the SMA manufacturer, who extracts the data from Differential Scanning Calorimetry (DSC) data (see A2.3).

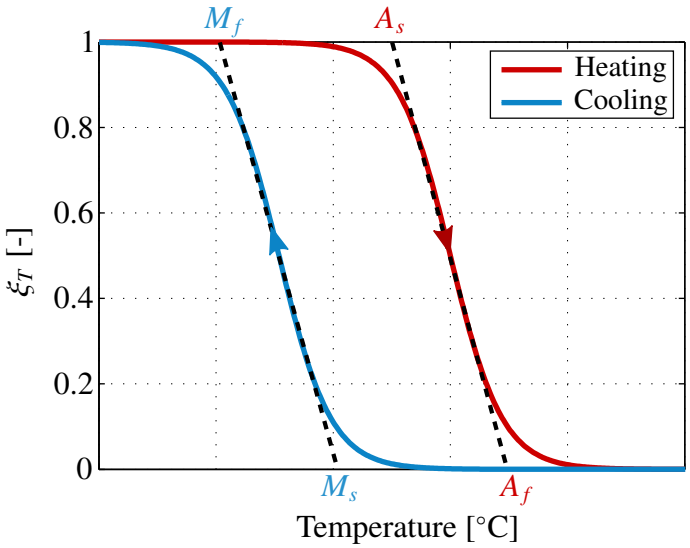

Figure 2-9: *Thermally induced martensite fraction: thermal hysteresis in SMAs*

2.6 Effect of Stress on the Hysteresis: Total Martensite Fraction

When stress is increased in the SMA, the transformation temperatures shift to higher values. In fact, the transformation temperatures are linearly dependant on the stress with a slope of c_m [MPa/K] as shown exemplarily in Fig. 2-10, where $M_f^o, M_s^o, A_s^o, A_f^o$ are the transformation temperatures at no load and $M_f^1, M_s^1, A_s^1, A_f^1$ and $M_f^3, M_s^3, A_s^3, A_f^3$ are the transformation temperatures at exemplary stresses of 100 MPa and 300 MPa, respectively.

[2] In some cases $A_s < M_s$ has also been observed.

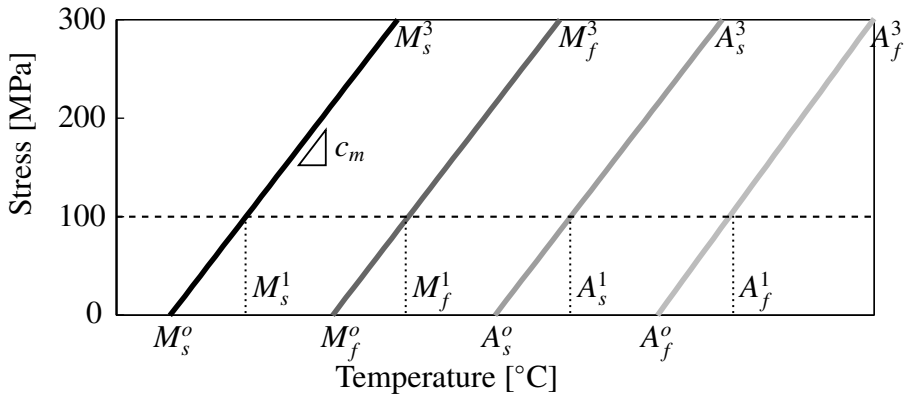

Figure 2-10: *Effect of stress on the transformation temperatures*

An increase in the SMA stress, however, also causes the formation of mechanically induced martensite (see Sect. 2.4) and thereby an increase of the strain in the SMA. Both these effects are shown (exaggerated) in Fig. 2-11(a), where the hysteresis loops are both shifted to higher temperatures, as well as being 'taller' due to an increase in the strain.

The total martensite fraction ξ, which includes both thermally and mechanically induced martensite, is often computed with the normalised strain ε_{norm} in (2-1), where ε_a is the strain when the SMA is fully austenite at $T > A_f$ (i.e. the minimum strain) and ε_m is the strain when the SMA is fully martensite at $T < M_f$ (i.e. the maximum strain), as shown in Fig. 2-11(a). Plotting ξ against temperature produces the plot in Fig. 2-11(b).

$$\varepsilon_{norm} = \frac{\varepsilon - \varepsilon_a}{\varepsilon_m - \varepsilon_a} = \xi \tag{2-1}$$

Note that the value of c_m and the transformation temperatures at a particular stress are also usually provided by the SMA manufacturers.

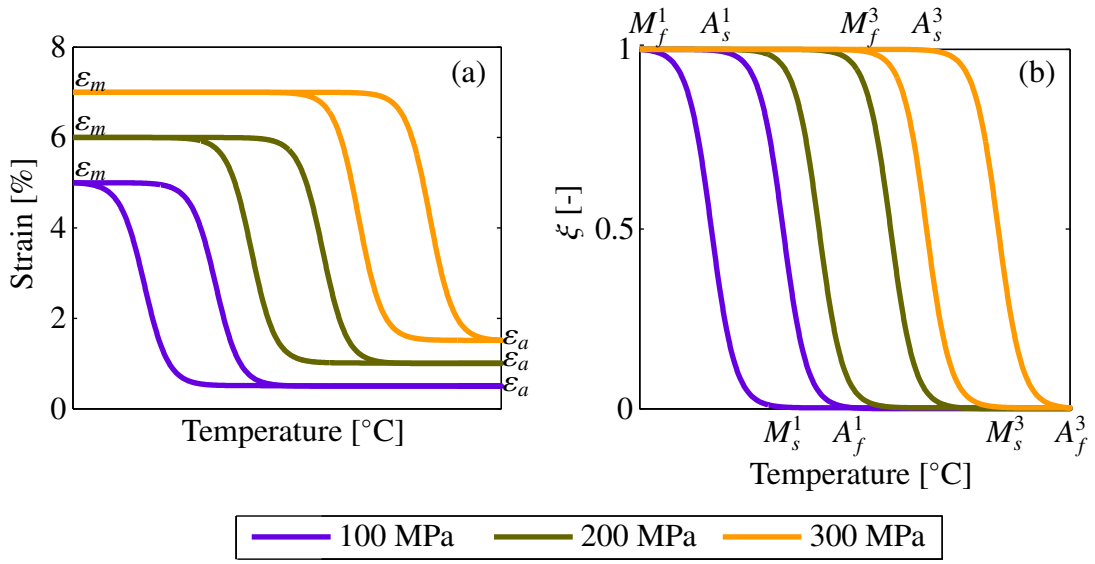

Figure 2-11: *Effect of stress on the hysteresis: Total martensite fraction*

2.7 Minor hysteresis loops

For a full transformation from austenite to martensite and vice versa, the resulting hysteresis loop is called the *major loop*.
Consider that the SMA in an initial martensitic phase is heated. If the temperature profile changes from heating to cooling before the SMA has fully converted to austenite, then it will follow a so-called *minor loop* branch as shown in Fig. 2-12(a).
Generally, if the input temperature is partially cycled between the transformation temperatures, such internal minor loops branching behaviour results (see plot(b)).

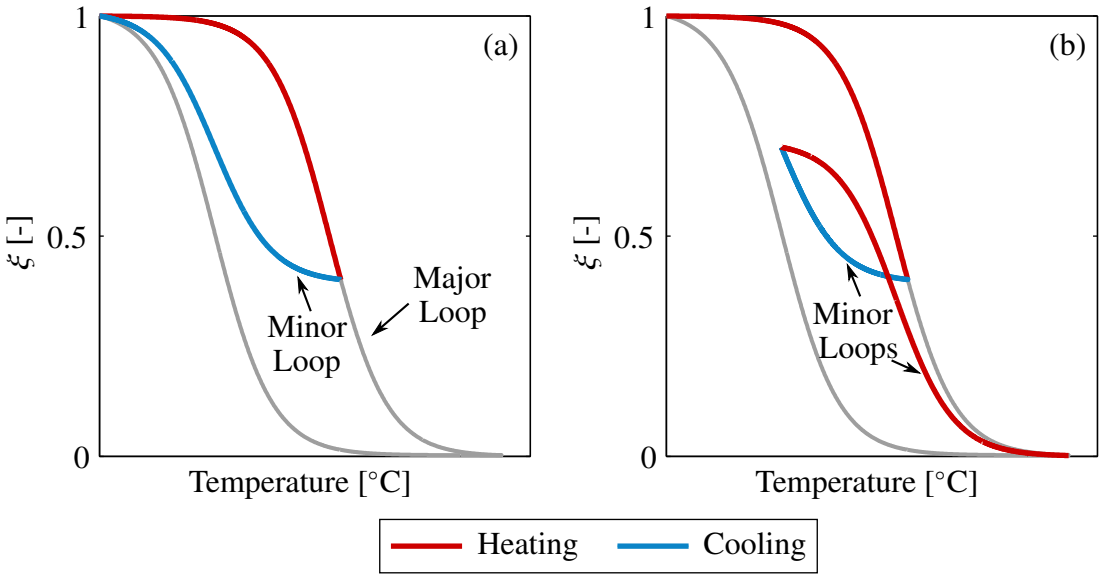

Figure 2-12: *Major and minor hysteresis loops*

2.8 Shape Memory Effect

Consider that an SMA wire at no load is in the austenite form and has length L. When the austenite is allowed to cool to below M_f^o, it transforms to twinned martensite. The twinning process is a so called *self-accommodating* process. During self-accommodation, the atoms move such that there is little or no macroscopic strain relative to the initial state [DMS90], [Sha95]. Therefore, the conversion from austenite to twinned martensite by cooling preserves the macroscopic shape of the SMA, and the wire length is still L. This is represented by ❸ - ❿ in Fig. 2-13.
Consider now that the wire is loaded from ❿ - ❶ and unloaded from ❶- ❷, causing a wire length of R, where $R > L$ due to elongation from the stress. Microscopically, the SMA is detwinned martensite (or a mixture of twinned and detwinned martensite if unloading was between the knees, such as at ❼ in Fig. 2-7). When the SMA is now heated, it follows the hysteresis curve ❷ - ❸ (cf. Fig. 2-9), the SMA

> reverts back to the cubic austenite and the strain is recovered, provided little plasticity has occurred during loading. The initial shape of the specimen [L] is recovered since the required atomic shifts are relatively small and the high-symmetry cubic structure is unique to the martensite variants [CSI09].

On cooling once again, the length L is preserved due to self-accommodation of the twinning process. This entire sequence is called the *shape memory effect*. It describes recovery of the original SMA shape after deformation on sufficient increase of the temperature. The key to this recovery is the congruence between the macroscopic dimensions of austenite and twinned martensite [DMS90], [Sha95]. This is shown in Fig. 2-13[3].

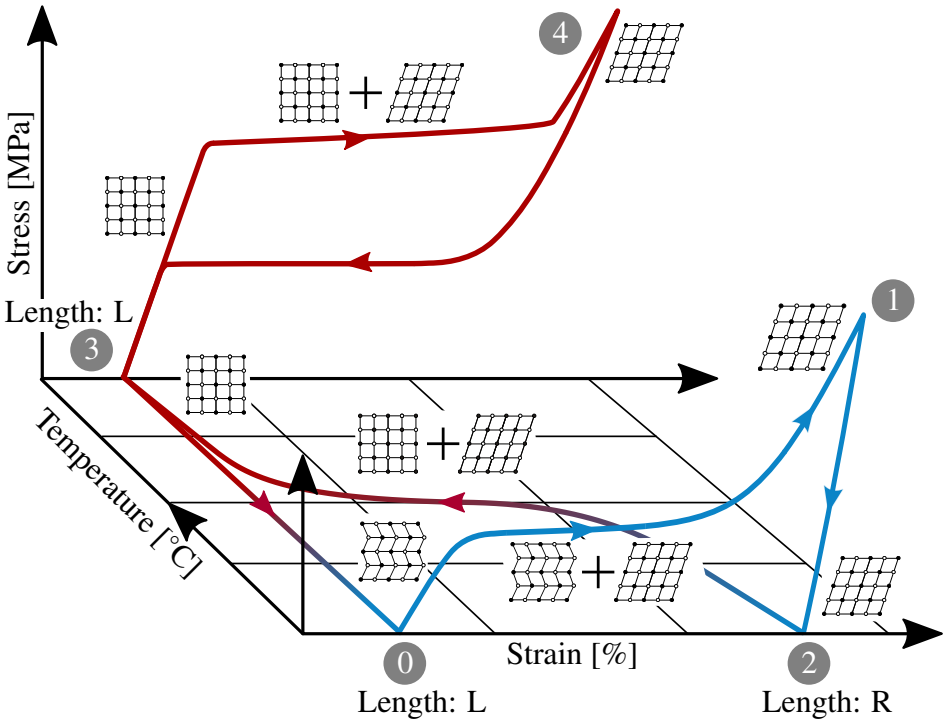

Figure 2-13: *Shape memory effect in SMAs*

2.9 SMAs as Position and Force Actuators

The shape memory effect, detailed above, can be exploited to move a load, thereby using the SMA as an actuator. For example, consider an SMA wire in its twinned martensitic form at a temperature $T < M_f^o$ (1 in Fig. 2-14(a)). As there is no load and no strain on the wire, 1 is at the origin of the stress-strain plot in Fig. 2-14(b). Further, as the SMA is fully twinned martensitic, $\xi = 1$ (1 in Fig. 2-14(c)). When the wire is attached to a constant load σ_l, it causes elongation of the wire and a strain of ε_m (2 in Fig. 2-14(a), (b)). While application of a load causes a transformation from twinned to detwinned martensite, the SMA is still fully martensite and $\xi = 1$ remains. Therefore 2 is at the same position as 1 in the hysteresis plot in Fig. 2-14(c).
Heating the wire, causes a transformation to austenite along the thermal hysteresis (path 3) and recovery of the strain to ε_a at 4. The SMA is constrained to move along 3 in the stress-strain diagram (plot (b)) due to the presence of the constant load. When the wire cools (path 5), the load elongates to 2 once again.

[3]Fig. 2-13 also shows shape recovery via pseudoelasticity i.e. when the SMA at $T > A_f^o$ and no load at 3 is stressed to 4, removal of the stress causes (almost) full recovery of the ensued strain.

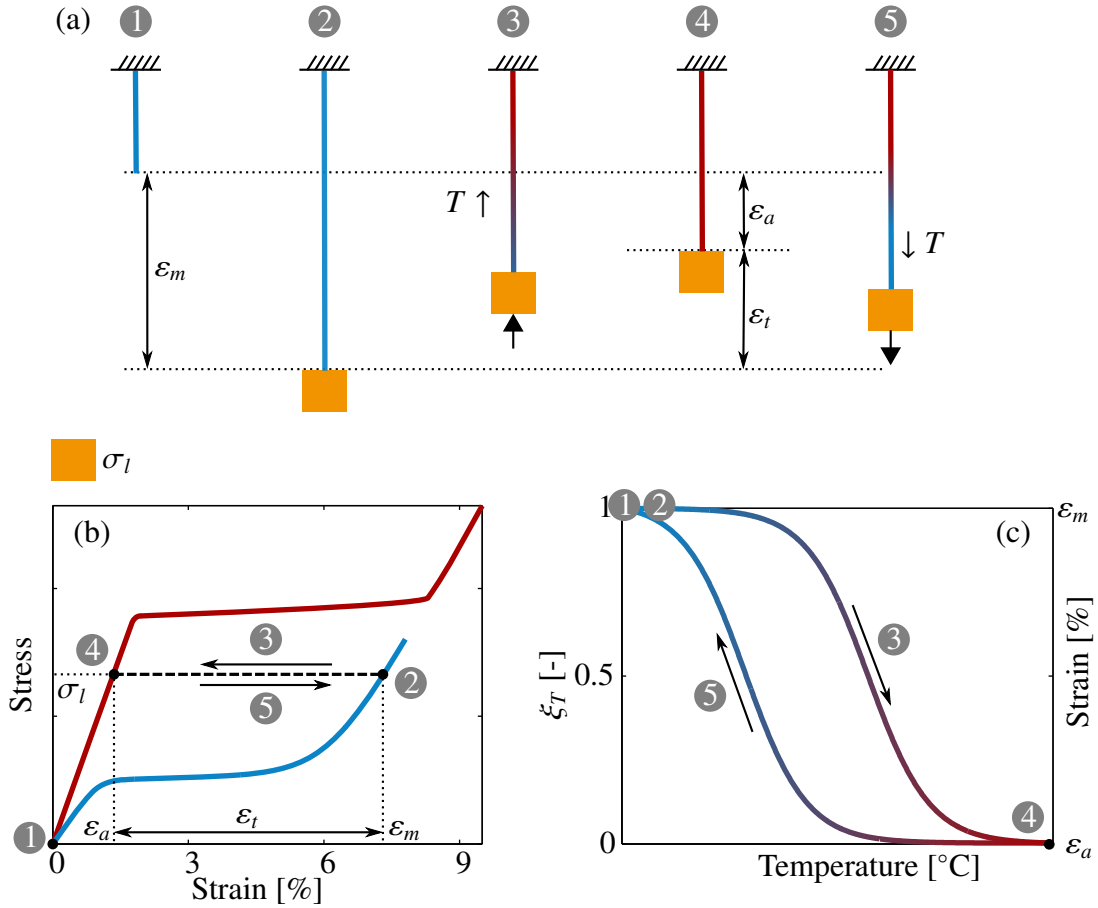

Figure 2-14: *SMAs as position actuators*

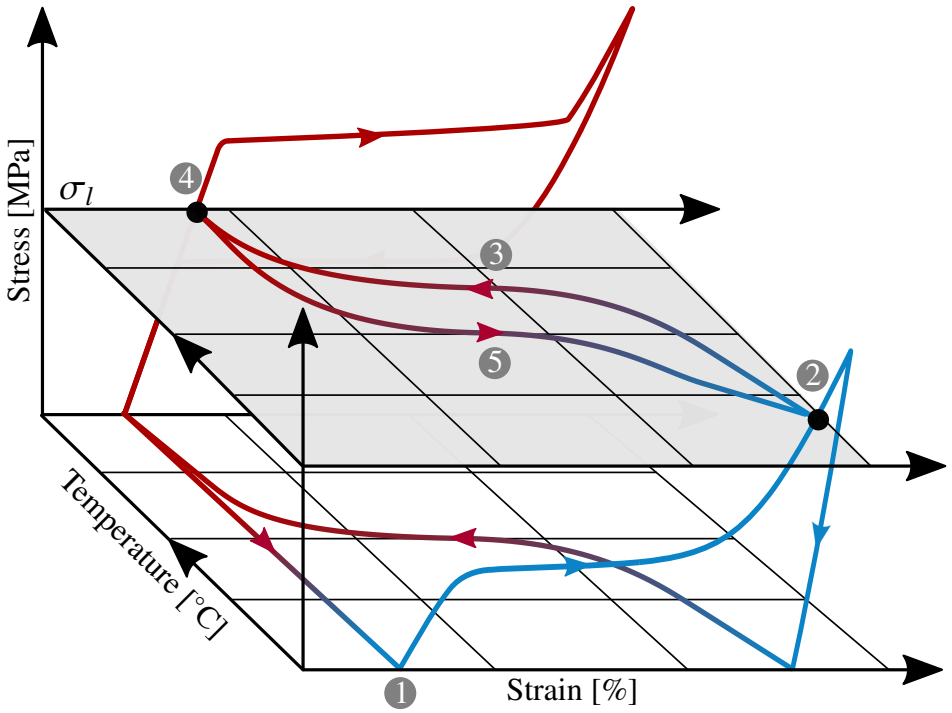

Figure 2-15: *Constant force SMA position actuator*

This process can be repeated cyclically and the SMA in this case is a thermally-activated-position-actuator, where ε_t is the maximal travel possible.
This is also shown in Fig. 2-15. Note that the hysteresis curve followed is different from the curve in Fig. 2-13 because there is a load acting on the wire and so a shifted and scaled form of the hysteresis has to be used (cf. Fig. 2-11).

The path followed by the SMA is constrained by the load acting on the wire. Should the load be a spring, then the path followed by the SMA is constrained to the black dashed line in Fig. 2-16(a). The slope of this line is the spring constant.
Should the load change dynamically, as is the case in many applications, then the path followed also changes dynamically, as shown for an exemplary case in Fig. 2-16(b).

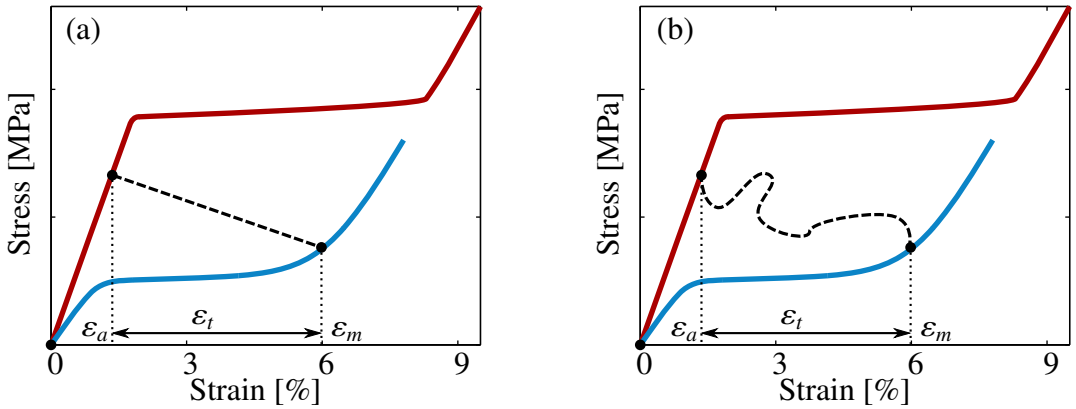

Figure 2-16: *SMA position actuators (a) spring-biased , (b) dynamically changing load*

In some applications, the SMA is used to apply force, rather than change position. Should the strain be constrained at a certain value ε_f, the force (or stress) that the SMA applies is shown by the black dashed line in Fig. 2-17(a). σ_m is the stress applied when $T < M_f$ and σ_a is the stress applied when $T > A_f$ and the σ_t is the maximum stress (force) difference between the temperature extremes.
Contrary to the position actuator, in these applications, the path followed by the SMA is constrained by the strain on the wire. If the strain changes dynamically, then the path followed by the SMA is shown in Fig. 2-17(b). The SMA used in this manner is a thermally-activated-force-actuator.

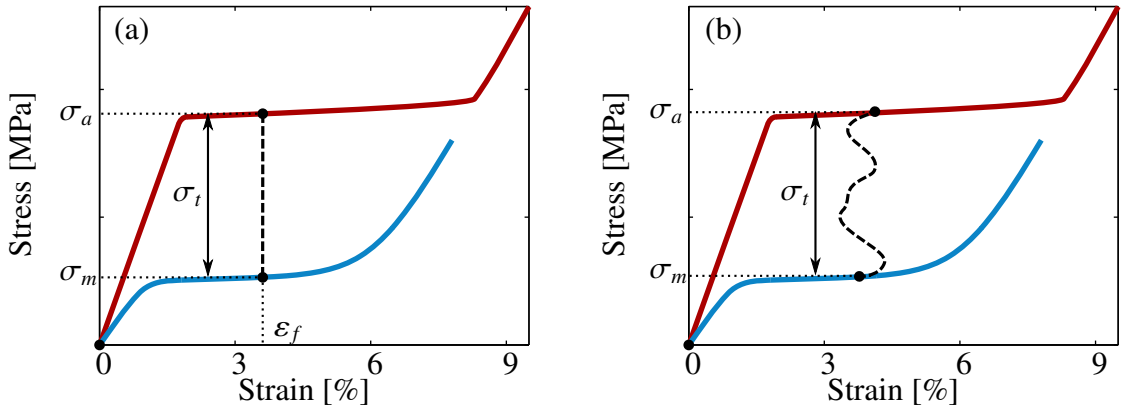

Figure 2-17: *SMA force actuators: (a) constant strain, (b) dynamically changing strain*

2.10 Summary

This chapter presents an overview of the microscopic and macroscopic behaviour of SMAs in order to give a foundation for the shape recovery mechanisms displayed by these materials. The SMA consists of two phases: austenite and martensite. Shape recovery is shown to occur due to martensitic transformations in the material: pseudoelasticity occurs from a conversion of austenite to (stress induced) martensite and back. The shape memory effect occurs due to transformation of (detwinned) martensite to austenite, assisted by the macroscopic congruence of twinned martensite and austenite. The stress-strain behaviour when starting at stress-free conditions for both austenite and twinned martensite is discussed, including the transformation to mechanically induced martensite as a function of the stress or strain in the SMA. The presence of parabolic loci for unloading and reloading of mechanically induced martensite attributed to grain orientation and internal stresses is discussed. Additionally, the presence of 'steps' in the austenite plateau due to functional fatigue is presented.

Further, the temperature hysteresis including minor hysteresis loop behaviour is shown. Finally, the total martensite fraction, which includes both thermally and mechanically induced martensite and is represented by the normalised strain, is presented. The effect of stress causes the hysteresis loop to be shifted and scaled.

The exploitation of the shape recovery mechanisms to create position and force SMA-based actuators is presented. The path followed by the actuator depends on the (dynamic) load on the wire when the SMA is used as a position actuator. Contrarily, when the SMA is used as a force actuator, the path followed by the actuator depends on the (dynamic) strain on the wire.

Due to the inherent nonlinearities and hysteresis, control of SMA actuators is challenging and the next chapter presents a review of control approaches used in literature.

3 Literature Review and Solution Approach

SMA-based actuators for position or force control, as presented in the previous chapter, have several desirable properties. The most important of these is that SMA actuators are powerful and compact in both volume and mass due to their high energy density and high specific actuation stress. Further, the actuation is smooth and silent and bio-compatibility makes them very attractive for use in medical applications. However, due to the inherent extremely nonlinear and hysteretic behaviour of SMAs, as shown in Chap. 2, the design of actuators for position or force control is non-trivial.

A review of the literature shows that in the past decades, several classes of controllers regarding position control strategies, with shape memory alloys have been proposed, as shown below[1]:

Linear controllers (PID) The most commonly used industrial controller is the PID controller and first attempts to control SMAs was with classical PID by [ITH91], [Rv94], [Da 07]. However, to track the desired strain, the P-gain needs to be quite high, which in turn causes overshoots [SZ12], [MKH01]. Overshoots in SMAs are critical since the cooling response and therefore eventual recovery is slow, causing large settling times. The I-gain that is theoretically used to reduce steady state error also cause overshoots according to [AD14] due to wind-up caused by the hysteresis and the sluggish cooling behaviour. PID with anti-windup is proposed by [SZ12], [AEGA06], [TF08], while [MSL04], [MS03], [KLH06] omit using an I-gain altogether.

Nonlinear PID A very elegant method to reduce the overshoot was first proposed by Shameli [SAS05] with a so-called PID-P^3 controller, or a quasi-linear controller. This controller appends, to the classical PID, a fourth term consisting of the cubic error amplified by a gain K_{P3} yielding the control law as shown in (3-1), where K_P, K_I, K_D are the P, I and D gains, respectively and $e(t)$ is the error. When the error is large, the $K_{P3}e^3(t)$ component causes large gains which is desirable. When the error approaches 0, so does the $K_{P3}e^3(t)$ term and the controller acts as a normal PID. The results show a reduction in the setting time and overshoot of the system when compared to a regular PID [SAS05].

$$u_{PIDP^3}(t) = K_P e(t) + K_I \int_0^t e(\tau)d\tau + K_D \dot{e}(t) + K_{P3} e^3(t) \tag{3-1}$$

The idea of a non-linear PID is extended further by Rahman [RKA08] who additionally use the quadratic error as in (3-2). Here, for small errors the cubic term vanishes but the quadratic term still produces a non-linear control effort to minimise the errors. This controller is called the NPID controller and comparisons to both a PID and PID-P^3 show superior performance with regard to rising time, overshoot and settling time [RKA08].

$$u_{NPID}(t) = K_P e(t) + K_I \int_0^t e(\tau)d\tau + K_D \dot{e}(t) + K_{P3}(e^2(t) + e^3(t)) \tag{3-2}$$

[1] A good overview of control strategies can be found in [ZS13] and [Kan11].

Model-based controllers The use of models within the control loop to overcome the stark nonlinearities is long established in the literature. The most commonly used models are inverse phenomenological hysteresis models. One of the methods frequently employed is to use the model as feedforward compensators with either a PID or PI as feedback controllers. This is used by [AK06] who use the Preisach model [Pre35] as a feedforward compensator with PID feedback, [PG07] who use Madill's model [MW98] extended to include time-varying stresses with PI feedback. [LHY09] use the Duhem model [Duh00] with PID and [SZ12] use the Prandtl-Ishlinskii model [BS96] and PI with anti-windup. Alternatively, the inverse model is applied directly between the controller output and the plant to linearise the thermal hysteresis. This method was used by [WLK99] using an adaptive Krasnosel'skil-Pokrovskii model [Voj89], [MKH01] with the Preisach and Brinson [Bri93] models and [RNTJ13] with an adaptive Prandtl-Ishlinskii model.

Knowledge-based controllers Learning systems such as neural networks or knowledge based systems such as fuzzy logic are used in order to learn the hysteresis either online or offline by [SCB03a], [MSL04], [KLH06], [AEGA08]. [KV11] use the Greedy-algorithm to learn the hysteresis and [TA12] use neural networks for model predictive control.

Explicit temperature controllers Explicit temperature control is used by [AD14], who use an NPID controller in feedback and a heat transfer model for feedforward compensation, [ZS13] who use Model Reference Adaptive Control (MRAC) as a temperature controller in addition to a PI strain controller and [VP12] who use temperature control with a PID and a current limiter to prevent overheating and thermal fatigue of the SMA wires.

Pulse Width Modulation (PWM) based controllers The use of Pulse Width Modulation (PWM) to modulate the control signal was first proposed by [MS03], who showed that the use of PWM increases robustness and saves energy compared to using the analog control signal. This method has been employed by several researchers such as [SDUS12] to modulate various adaptive controllers, and showed improved position accuracy and robustness as compared to non-modulated controllers, such as [AD14], who use a heat transfer model for feedforward compensation and modulate an NPID controller. [WSL$^+$12], who use PWM for position control of antagonistic SMAs and [NRD12] for active vibration control of a flexible structure.

Variable Structure Control (VSC) VSC controllers were proposed in [GH97], [GH00] for both position and force control of antagonistic SMA-actuators. The controller, referred to commonly in the literature as "two-stage-control"consists of a feedback that switches between the two actuators according to the sign of the displacement error. [EA02] extended the controller by adding a boundary layer and a sliding surface that is slanted in the phase plane in order to reduce chattering and increase accuracy. In [EAAT05] and [Ash06], the sliding mode controller using only position measurements is implemented. An extended Kalman filter estimates the unmeasured states that are used to avoid overheating and thereby reduce overshoots. [SCB03a] and [SCB03b] develop a VSC for position control of SMA wires using a control law within the boundary layer with a *tanh*-term, through which they claim that the hysteresis is compensated. Additionally, an inverse hysteresis model, that is developed (learned) offline with a neural network, is used as a feedforward

compensator. [RT09] implement a sliding mode controller and attempt to increase the bandwidth of the actuator through active cooling with peltier elements. [SHC+09] use VSC for an aluminium flexible beam structure in order to dampen vibrations. The control law within the boundary layer is exponential based on the error. [WSE10] use VSC for an automotive SMA-actuated mirror.

Other non-linear controllers An H_∞ controller is used by [JPNO08], [CHKC01]. [MT09] use a control Lyapunov function formulated from an SMA model. Adaptive controllers are used by [SAS05], [EE08], [SDUS12], where the latter additionally compare adaptive controllers modulated with PWM.

Although the aforementioned controllers have made good progress in position control of SMAs, force control with SMAs has been scarcely investigated, with a literature review showing only three sources: Force control of antagonistic pairs of SMA wires by [GH00] using a VSC controller. [TF08], who use a PID controller with anti-windup and a current limiter. Choi et al. [CHKC01], who use an H_∞ controller for force control of an SMA-based flexible gripper.

Deficiencies also exist with the position controllers: Other than in [TA12] and [YRHL06], the effect of various stresses on the SMA is not adequately considered in the literature. As shown in Chap. 2, the change of stress has a profound effect on the SMAs behaviour. Most of the controllers mentioned above present results only for one constant mass. Further, dynamically changing masses are considered primarily when the load is a spring, such as in [WLK99]. However, for the SMA to be used as an industrial actuator, it has to provide accurate control under various (dynamically changing) loads.

Further, since one of the major advantages of SMA actuators is their miniaturization (made possible due to their high energy density) [Hum01], it is imperative to design a controller that allows for precision control of the SMA wire, while being computationally efficient enough to run on embedded processors. In this manner both the actuator and the controller can be miniaturised, making them more attractive for the industry and smart structures. With this constraint, the use of linear, quasi-linear controllers, VSC and PWM based controllers are particularly advantageous because they are straightforward to implement onto a microprocessor.

A review of the literature cited above has shown that the performance of controllers such as PID, NPID or VSC etc. can be improved by the use of model-based controllers. Models that predict the non-linearities are useful either for linearisation or to provide the controller with *a priori* knowledge of the nonlinearities in order to enable it to react effectively. Additionally, models can be used as observers in order to either reduce the number of sensors required or to monitor states that are not measurable.

In the past several decades, models to describe SMA behaviour have been developed from various perspectives[2]: **Thermodynamics** [Duh00], [Ach89], [IP94], [BL96], [BH96], [Sha02], [SM04], [Smi05], **Phenomenological and Thermomechanical** [Bri93], [BS96], [DG05], [EA05a, EA05b],[ITH91], [MW98], [PG06], [Pre35], [Voj89], [RL97], [TKS86], **Micromechanical** [GL97], [VL98], [GHB00, HGB00], **Finite element** [ABF00], [BL93], **Constitutive** [ABSU14], [RLS07] etc.

[2]Note that all the models mentioned in the model-based control sources above can be found in this classification list of SMA models

From the classes of models listed above, the thermodynamical model from [SM04] and the thermomechanical model from [Bri93] are shown in more detail below.

The thermodynamical model from Seelecke in [See02], [SM04], [FS12] and [Hei04] etc. uses the Helholtz free-energy to compute the probability that the SMA will undergo a phase transformation. The time rate of change of the phase fractions are described by (3-3) and (3-4), where x^+ and x^- are the volume fractions of tension-induced-martensite (M^+) and compression-induced-martensite (M^-) and x^A in (3-5) is the volume fraction of austenite (A) [FS12][3]. $p^{\alpha\beta}$ represents the probability that a grain transforms from phase α to phase β i.e. p^{+A} is the probability of grain transformation from M^+ to A.

$$\dot{x}^+ = -x^+ p^{+A} + x^A p^{A+} \tag{3-3}$$

$$\dot{x}^- = -x^- p^{-A} + x^A p^{A-} \tag{3-4}$$

$$x^A = 1 - x^+ - x^- \tag{3-5}$$

The transition probabilities are in (3-6) and (3-7) for a given temperature T and stress σ (see [Hei04] and [See02] for detailed derivations) where V_{LE} is the Lattice element activation volume, τ_x is the transition attempt frequency, k_B is the Boltzmann constant, E_A and E_M are the austenite and martensite Young's moduli, respectively and σ_A and σ_M are the transformation stresses from A to M and M to A, respectively (see Fig. 3-1).

$$p^{\pm A}(\sigma, T) = \frac{1}{\tau_x} \frac{\exp\left[-\frac{V_{LE}}{2E_M k_B T}(\sigma_M \mp \sigma)^2\right]}{\operatorname{erfc}\left[\sqrt{\frac{V_{LE}}{2E_M k_B T}}(\sigma_M \mp \sigma)\right]} \tag{3-6}$$

$$p^{A\pm}(\sigma, T) = \frac{1}{\tau_x} \frac{\exp\left[-\frac{V_{LE}}{2E_M k_B T}(\sigma_M \mp \sigma)^2\right]}{\operatorname{erfc}\left[\sqrt{\frac{V_{LE}}{2E_A k_B T}}(\sigma_A + \sigma)\right] + \operatorname{erfc}\left[\sqrt{\frac{V_{LE}}{2E_A k_B T}}(\sigma_A - \sigma)\right]} \tag{3-7}$$

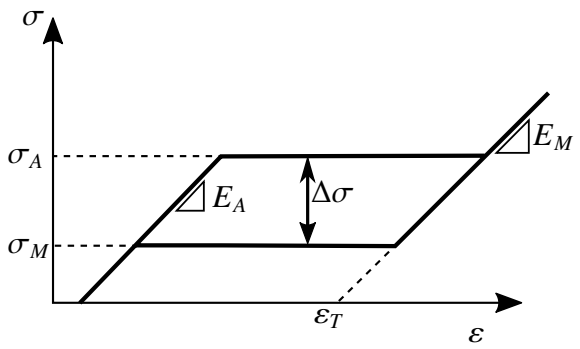

Figure 3-1: *Model parameters for stress-strain hysteresis loop. Reproduced from [FS12]*

The values of σ_A and σ_M are dependant on temperature, as shown in (3-8) and (3-9), where $\Delta\sigma$ is the width of the hysteresis in the stress-strain curve, σ_{AL} is the plateau stress at a

[3]Note that in [See02] and [Hei04], x^+ and x^- are also defined as the volume fraction of tension-preferred (M^+) and compression-preferred (M^-) martensite. The two martenite phases are based on the direction of shearing.

temperature T_L, set such that $\sigma_A < 0$ when $T < A_s$. Further $d\sigma/dT$ describes the rise of the stress-strain hysteresis with temperature.

$$\sigma_A(T) = \sigma_{AL} + \frac{d\sigma}{dT}(T - T_L) \tag{3-8}$$

$$\sigma_M = \sigma_A - \Delta\sigma \tag{3-9}$$

The stress-strain relationship is given by (3-10), where ε_T represents the maximum recoverable strain (see Fig. 3-1).

$$\varepsilon = x^A\left(\frac{\sigma}{E_A}\right) + x^+\left(\frac{\sigma}{E_M} + \varepsilon_T\right) + x^-\left(\frac{\sigma}{E_M} - \varepsilon_T\right) \tag{3-10}$$

The validation of the model under various conditions is presented in e.g. [SM04], [FS12], [FCS12] and show moderate correlation with experimental data. The major discrepancies occur due to the fact that a single crystalline is modelled in order to allow for numerical computation of the model. However SMA wires are polycrystalline and their characteristics do not display sharp corners as in the plot in Fig. 3-1 [FS12].

The phenomenological and thermo-mechnanical model according to Brinson in [Bri93] uses thermo-mechanical equations to represent the constitutive and hysteresis behaviour of the SMA. These class of models use cosine based functions to represent the SMA hysteresis, as originally proposed by [TKS86]. The martensite fraction ξ, used as an internal variable is separated into ξ_T, the purely temperature-induced martensite with multiple variants (twinned martensite) and ξ_S, the martensite transformed by stress into a single martensite variant (cf. (3-11)).

$$\xi = \xi_S + \xi_T \tag{3-11}$$

The model begins with a definition of the initial conditions as shown in (3-15), (3-16) and (3-17) using $\Delta_{T\xi}$ from (3-12) with a_M and a_A in (3-13) and (3-14).

$$\Delta_{T\xi} = \begin{cases} \frac{1-\xi_{T0}}{2(\cos(a_M(T-M_f))+1)} & (M_f < T) \text{ and } (T < M_s) \text{ and } (T < T_0) \\ 1 & T < M_f \\ 0 & \text{otherwise} \end{cases} \tag{3-12}$$

$$a_M = \frac{\pi}{M_s - M_f} \tag{3-13}$$

$$a_A = \frac{\pi}{A_f - A_s} \tag{3-14}$$

$$\xi_{T0} = \Delta_{T\xi} \tag{3-15}$$

$$\xi_{S0} = 0 \tag{3-16}$$

$$\xi_0 = \xi_{S0} + \xi_{T0} = \Delta_{T\xi} \tag{3-17}$$

Defining σ_s^{cr} and σ_s^{cf} as the critical stresses for the start and finish of the conversion of the martensitic variants, Fig. 3-2 shows that these stresses are considered constant under M_f. Above M_f, their values depend on the material constants C_M and C_A and represent both the shift of the thermal hysteresis to higher temperatures with the application of stress, as well as the shifting of yield stresses of the stress strain curves to higher values with the

increase of temperature. The algorithm starts with setting $\xi_S = \xi_{S0}$, $\xi_T = \xi_{T0}$ and $\xi = \xi_0$, as defined by the initial conditions above. These values change either due to a conversion to detwinned martensite in (3-18) or a conversion to austenite in (3-19). For the derivation of the equations, refer to [Bri93].

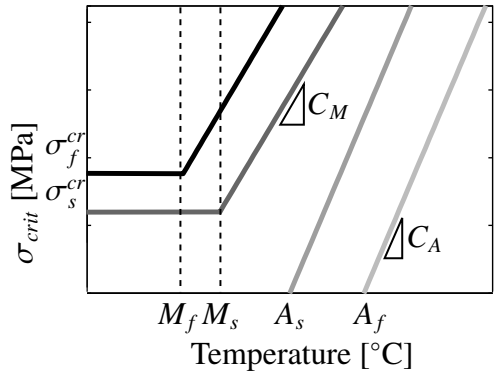

Figure 3-2: *Critical stresses for transformation or martensite twin conversion as functions of temperature. Reproduced from [Bri93]*

Conversion to detwinned martensite:

if $(T < M_s)$ and $(\sigma_s^{cr} < \sigma < \sigma_f^{cr})$:

$$\xi_S = \frac{1-\xi_{S0}}{2}\cos\left[\frac{\pi}{\sigma_s^{cr}-\sigma_f^{cr}}(\sigma-\sigma_f^{cr})\right] + \frac{1+\xi_{S0}}{2}$$

$$\xi_T = \xi_{T0} - \frac{\xi_{T0}}{1-\xi_{T0}}(\xi_S - \xi_{S0}) + \Delta_{T\xi}$$

else if $(T > M_s)$ and $((\sigma_s^{cr} + C_M(T-M_s)) < \sigma < (\sigma_f^{cr} + C_M(T-M_s))$:

$$\xi_S = \frac{1-\xi_{S0}}{2}\cos\left[\frac{\pi}{\sigma_s^{cr}-\sigma_f^{cr}}(\sigma-\sigma_f^{cr}-C_M(T-M_s))\right] + \frac{1+\xi_{S0}}{2}$$

$$\xi_T = \xi_{T0} - \frac{\xi_{T0}}{1-\xi_{T0}}(\xi_S - \xi_{S0})$$

else if $(\sigma_s^{cr} \geq \sigma$ or $(\sigma_s^{cr} + C_M(T-M_s)) > \sigma))$ and $T \leq M_f$

$$\xi_S = 0;\ \ \xi_T = 1$$

else

$$\xi_S = 1;\ \ \xi_T = \Delta_{T\xi} \tag{3-18}$$

Conversion to Austenite:

if $(T > A_s)$ and $(C_A(T-A_f) < \sigma < C_A(T-A_s))$:

$$\xi = \frac{\xi_{S0}}{2}\cos\left[a_A(T - A_s - \frac{\sigma}{C_A})\right] + 1$$

$$\xi_S = \xi_{S0} - \frac{\xi_{S0}}{\xi_0}(\xi_0 - \xi)$$

$$\xi_T = \xi_{T0} - \frac{\xi_{T0}}{\xi_0}(\xi_0 - \xi) \tag{3-19}$$

With the fractions of multi-variant martensite, single-variant martensite and austenite known, the constitutive equation is computed with (3-22), where $D(\xi)$ is the modulus of the SMA, computed as the weighted sum of the austenite modulus D_a and the martensite modulus D_m, as shown in (3-20). $\Omega(\xi)$ is considered the transformation tensor, which is calculated with (3-21), where ϵ_L is the maximum residual strain in the SMA. Θ is the thermal coefficient of expansion of the SMA. Further, (ϵ_0, σ_0) are the starting points of the SMA wire on the stress-strain plane and T_0 is the ambient temperature.

$$D(\xi) = D_a + \xi(D_m - D_a) \tag{3-20}$$

$$\Omega(\xi) = -\epsilon_L D(\xi) \tag{3-21}$$

$$\sigma - \sigma_0 = D(\xi)\epsilon - D(\xi_0)\epsilon_0 + \Omega(\xi)\xi_S - \Omega(\xi_0)\xi_{S0} + \Theta(T - T_0) \tag{3-22}$$

Similar to Seelecke's thermodynamical model presented above, Brinson's thermomechanical model also predicts SMA behaviour to have sharp corners when transforming from one phase to another due to the use of conditional statements to mark the transitions. However, what both models succeed at, is describing the general behaviour of the SMA under various conditions.

In addition to the models briefly discussed above, existing SMA models, nevertheless, show various deficiencies: the models usually have several, in some cases difficult to identify, parameters [ABSU14]. The model equations are either extremely complicated and computationally expensive or they are too elementary, in consequence showing poor correlation to observed behaviour. As mentioned earlier, the effect of stress on phase kinetics behaviour in SMAs are not adequately modelled. Constitutive models considering the stress-strain relation are usually either approximated based on linear piecewise models, implemented using a series of conditional statements, that do not fully predict observed behaviour, or with complex equations. Although, some researchers (including [ABSU14]) have published numerical solutions to such complicated equations, they are useful only for numerical simulations e.g. finite element, but are not suited to be used in real-time control algorithms.

Consequently, although model-based controllers in collaboration with other control methods have been shown to be advantageous in accurately controlling SMA-based actuators, the complexity of the models is a hindrance in fully exploiting this control strategy for industrially relevant SMA actuators.

This thesis proposes to reducing the complexity in modelling and present a novel SMA phenomenological model based entirely on closed-form continuous differentiable analytical equations that are capable of depicting the SMA constitutive and phase kinetics behaviour, including the effect of changing stresses. The model will then be used online in a control loop in combination with other controllers to achieve precision control of the SMA actuators. The modelling and control approach is presented in the next section.

3.1 Modelling Approach

The model developed in this thesis is thermomechanical in nature and the modelling method used is phenomenological. That is, equations describing phenomena observed in experiments are used as the basis of model development. To this end, the following two sets of experiments are used to investigate and subsequently model SMA behaviour:

- stress-strain ($\sigma - \varepsilon$) experiments at various constant temperatures.
- strain-temperature ($\varepsilon - T$) experiments at various constant stresses.

Using the data from the aforementioned experiments or from literature, the phenomenological modelling method can be summarised in the following steps:

1. Inspection of experimental data to identify repeatable forms (the 'base curves').
2. Mathematical description of the base curve using, if possible, analytical equations (the 'base equations').
3. Identification of required parameters in the base equation.
4. Creation of an algorithm where the equation(s) developed in step 2 and the parameters in step 3 above are used to model observed behaviour.
5. Description of a procedure to systematically calculate the model's internal parameters.
6. Validation of developed model with independent experiments.

The steps outlined above are used to develop two sets of models:

Stress-Strain (Constitutive) model This model, with a block diagram in Fig. 3-3, takes the strain ε and temperature T as the input and calculates the resulting stress σ. Chap. 4 begins with modelling the stress-strain behaviour at no load for temperatures $T < M_f$, where the SMA is fully martensitic and for $T > A_f$, where the SMA is fully austenitic. Chap. 5 then extends the model to account for intermediate temperatures where a mixture of the phases exist.

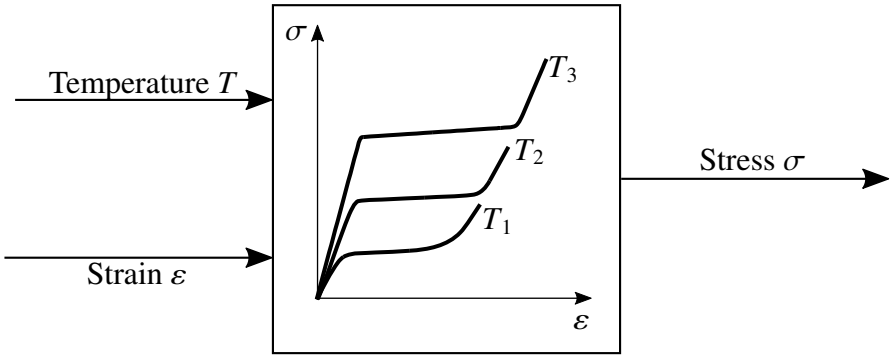

Figure 3-3: *Stress strain model*

Phase Kinetics model This model, with a block diagram in Fig. 3-4, takes the stress σ and temperature T as the input and calculates the resulting strain ε as presented in Chap. 6. The dependency of the hysteresis on the applied stress is explicitly considered.

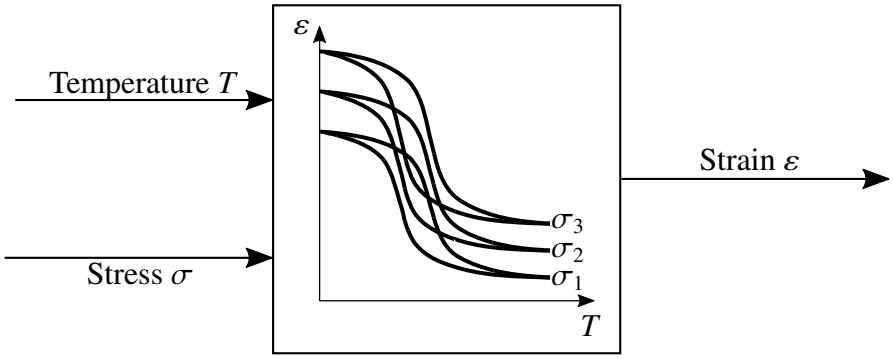

Figure 3-4: *Phase kinetic model*

The relationship between the two models is discussed in detail in Chap. 6. For control purposes, the inverse model is required, which is presented in Chap. 7.

It is important to note that the developed model focuses on modelling macroscopic phenomena observed in SMAs, as these are most relevant for actuator development. In this regard, although the model equations can be justified with hypotheses from material science, the motivation was not to describe material specific processes with the model, but to predict macroscopic SMA behaviour relevant for control and industrial applications. This modelling method has been used very successfully in the (famous) Pacejka Magic Formula for tire dynamics [PB92] which is widely used as the industrial standard in vehicle dynamic simulations.

3.2 Control Approach

The control approach used in this thesis, as presented in Chap. 8, incorporates the developed models into the controller loop as shown schematically in Fig. 3-5. The desired and measured states are fed into both the inverse model and a computationally efficient controller. The model is used both to provide the controller with knowledge of the nonlinearities in order to enable it to react effectively, as well as for linearisation of hysteresis. The controller computes the actuator commands required to achieve accurate position and force control of the SMA actuator. The controller is selected from the literature and is modified accordingly to optimise the actuator's performance.

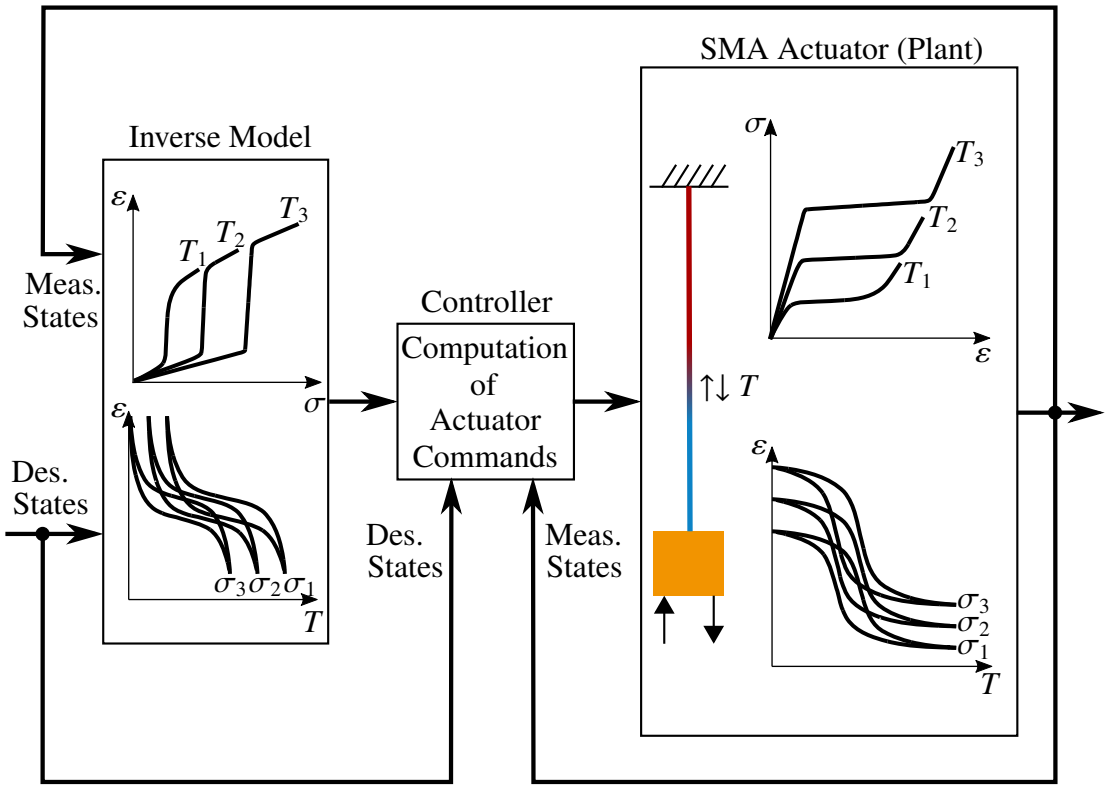

Figure 3-5: *Control approach*

Various experiments to test the controller's performance at various loads, including dynamically changing loads are carried out. Further robustness tests including disturbance rejection as well as investigations considering the limitations of the actuator in terms of bandwidth are performed.

Finally, the controller is implemented onto an embedded processor in Chap. 9 and used for force control in an industrial clamping application as the final proof-of-concept. For the prototype, SMA wires and required sensors are integrated in a commercially available clamping vice in order to clamp a test tube with a desired force. Investigations of the robustness of the SMA-based force controlled clamp are also performed.

4 Stress-Strain Model at Threshold Temperatures

This chapter presents a novel SMA constitutive phenomenological model based entirely on closed-form continuous differentiable analytical equations that are capable of depicting the smooth curvatures typical in the SMA stress-strain characteristics. The temperature of the SMA is restricted to either low temperatures ($T < M_f$) to ensure that at no load the SMA is fully (twinned) martensitic or to high temperatures ($T > A_f$) to ensure that the SMA is fully austenitic at no load. At temperatures between M_f and A_f, the SMA is a mixture of the martensitic and austenitic phases and, likewise, the stress-strain behaviour is a combination of the behaviour when the SMA is either pure martensite or pure austenite. This is shown in Chap. 5. The modelling equations and algorithms are presented in Sect. 4.1 - 4.6. Stress-strain experiments for model validation are shown in Sect. 4.7.

4.1 SMA Model Base Equation

Figure 4-1 shows typical stress-strain curves with martensite or austenite phases when starting at 0% strain and no load, for monotonic (plots (a) and (b)) and cyclical loading and unloading (plots (c) and (d)).

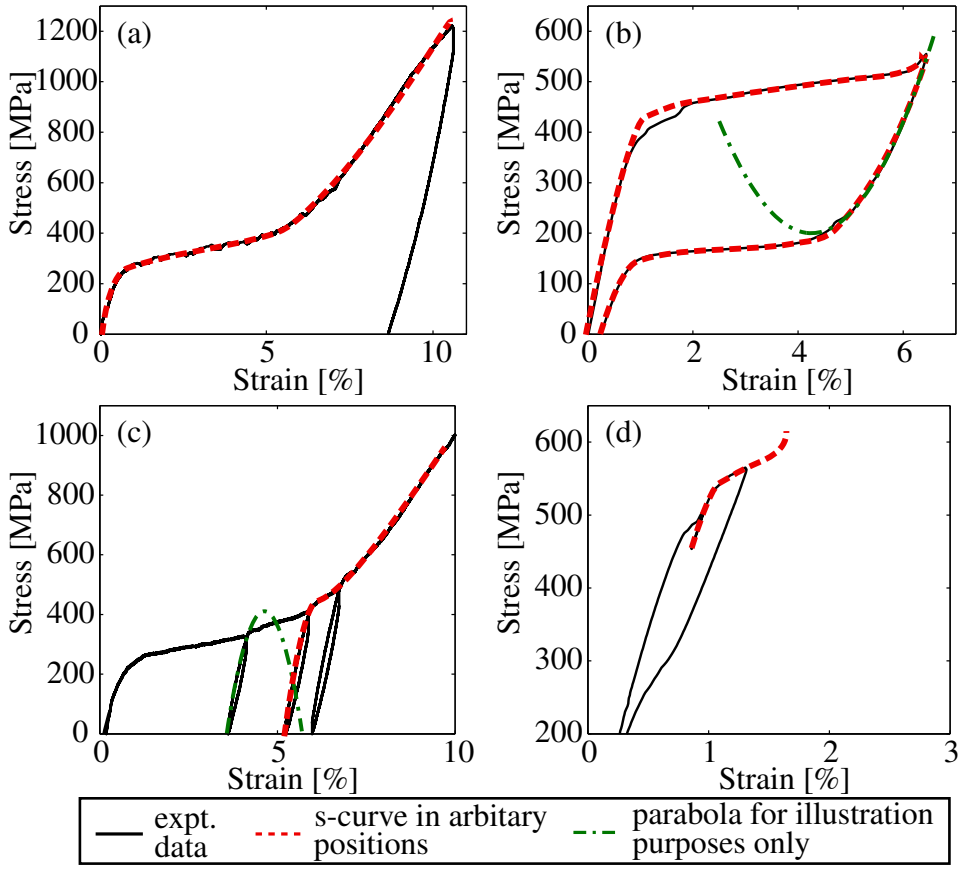

Figure 4-1: *Typical stress-strain curves for martensite and austenite: monotonic loading (plots (a) and (b)), cyclical loading (plots (c) and (d)) [Pai07]*

Inspection of the data shows a ubiquitous 's-shaped' curve (shown as red dashed curves in Fig. 4-1). Note that in plot (b), two s-shaped curves, one for loading and the other for unloading behaviour are present.

This s-curve, plotted by the red solid line on the stress-strain ($\sigma - \varepsilon$) plane in Fig. 4-2(a), is characterised by three slopes connected by two knees. It describes, physically, the evolution of phases in the SMA during an iso-thermal tensile test as described in Chap. 2: For a test done below M_f (100% martensite), twinned martensite is elastically deformed in the first segment $a - b$. Detwinning starts at ε_1 and proceeds until complete conversion to detwinned martensite at ε_2, after which the detwinned martensite is elastically deformed until plasticity (not shown) sets in. For a test conducted above A_f (100% austenite), in segment $a - b$, the austenite is elastically deformed. In segment $c - d$, austenite to stress-induced-martensite (SIM) transformation proceeds up to ε_2. Then, for the rest of $e - f$, 100% martensite is elastically deformed until plastic deformation starts.

The basis of the model is a closed form mathematical description of this s-curve in a single step, without the use of conditional statements, but including parameters to describe the curvatures present. The analytical equation is derived by first taking the partial derivative of the stress with respect to strain ($\frac{\partial\sigma}{\partial\varepsilon}$) and plotting it against the strain producing the solid red curve in Fig. 4-2(b), where E_1, E_2 and E_3 are the slopes of the σ-ε curve (moduli) in segments $a - b$, $c - d$ and $e - f$, respectively. ε_1 and ε_2 are the strains at the knees and k_1 and k_2 describe the curvatures of the function at the knees. Their values are proportional to $\frac{\partial^2\sigma}{\partial\varepsilon^2}$, evaluated at ε_1 and ε_2. With ε as the input strain, $\frac{\partial\sigma}{\partial\varepsilon}$ is mathematically described by a sum of scaled and shifted sigmoid functions, as shown in (4-1).

$$\frac{\partial\sigma}{\partial\varepsilon} = \frac{(E_1 - E_2)}{1 + e^{k_1(\varepsilon-\varepsilon_1)}} + \frac{(E_3 - E_2)}{1 + e^{-k_2(\varepsilon-\varepsilon_2)}} + E_2 \tag{4-1}$$

Taking the integral of (4-1) with $(\varepsilon_p, \sigma_p)$ as coordinates of any point on the curve yields the 'base equation', σ_{bq}, in (4-5). σ_1, σ_2 and σ_3, calculated in (4-2), (4-3) and (4-4) respectively, describe the function, roughly speaking, in segments $a - c$, $c - d$ and $d - f$, respectively. In the model, $(\varepsilon_p, \sigma_p)$ are the start coordinates of the function, but this is mathematically not required, and $(\varepsilon_p, \sigma_p)$ can be an arbitrary point on the curve. A detailed calculation of the integration is in Appendix A1.1.

$$\sigma_1 = (E_1 - E_2)\left[\varepsilon - \varepsilon_p + \frac{1}{k_1}\ln\left(\frac{1 + e^{k_1(\varepsilon_p-\varepsilon_1)}}{1 + e^{k_1(\varepsilon-\varepsilon_1)}}\right)\right] \tag{4-2}$$

$$\sigma_2 = E_2(\varepsilon - \varepsilon_p) + \sigma_p \tag{4-3}$$

$$\sigma_3 = (E_3 - E_2)\left[\varepsilon - \varepsilon_p - \frac{1}{k_2}\ln\left(\frac{1 + e^{-k_2(\varepsilon_p-\varepsilon_2)}}{1 + e^{-k_2(\varepsilon-\varepsilon_2)}}\right)\right] \tag{4-4}$$

$$\sigma_{bq}(E_{1,2,3}, \varepsilon_{1,2}, k_{1,2}, (\varepsilon_p, \sigma_p), \varepsilon) = \sigma_1 + \sigma_2 + \sigma_3 \tag{4-5}$$

As discussed in Chap. 2, analysis of the experimental data has shown that the unloading and reloading behaviour of martensite follows a parabolic locus, as shown exemplary by the green curves in Fig. 4-1 (plot (b) and (c)) and in Fig. 4-2, due to grain orientation and internal stresses.

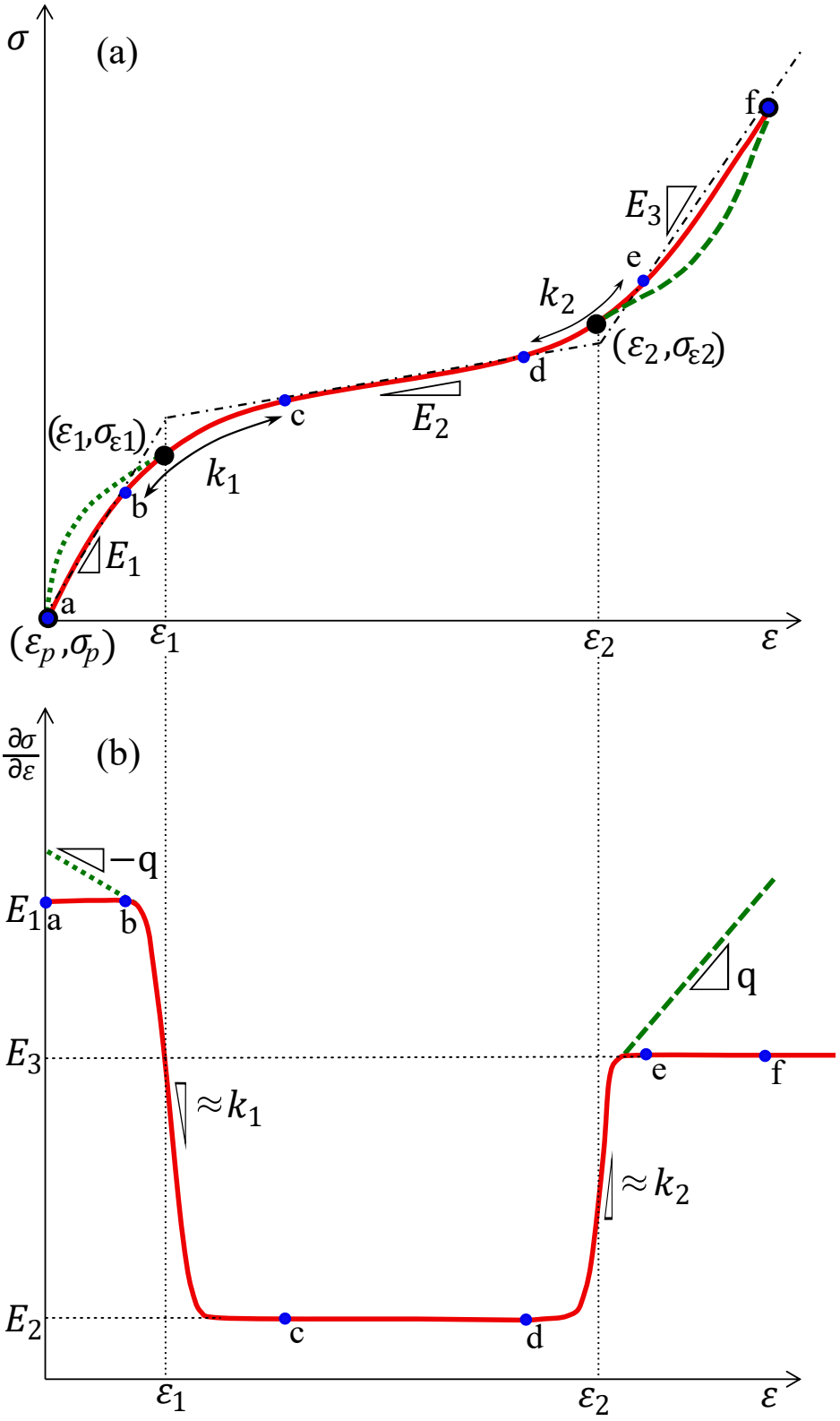

Figure 4-2: *General characteristic of SMA stress-strain behaviour*

To model this behaviour, (4-5) is augmented with σ_q in (4-6) for a parabola in segment $\varepsilon_2 - f$ (green dashed line in Fig. 4-2) or with σ_q in (4-7) for a parabola in segment $a - \varepsilon_1$ for the green dotted line in Fig. 4-2. The parameter q is the parabolic constant.

Consequently, the final base equation is given by (4-8). Note that should a parabolic locus be absent, then $q = 0$, rendering $\sigma_q = 0$ and (4-8) is identical to (4-5).

$$\begin{aligned} \text{For unloading:} \quad \sigma_q &= q(\varepsilon - \varepsilon_2)\left[\varepsilon - \varepsilon_2 + \frac{1}{k_2}\ln\left(1 + e^{-k_2(\varepsilon-\varepsilon_2)}\right)\right] \\ &\quad - q(\varepsilon_p - \varepsilon_2)\left[\varepsilon_p - \varepsilon_2 + \frac{1}{k_2}\ln\left(1 + e^{-k_2(\varepsilon_p-\varepsilon_2)}\right)\right] \end{aligned} \tag{4-6}$$

$$\begin{aligned} \text{For loading:} \quad \sigma_q &= q(\varepsilon - \varepsilon_1)\left[\varepsilon - \varepsilon_1 - \frac{1}{k_1}\ln\left(1 + e^{k_1(\varepsilon-\varepsilon_1)}\right)\right] \\ &\quad - q(\varepsilon_p - \varepsilon_1)\left[\varepsilon_p - \varepsilon_1 - \frac{1}{k_1}\ln\left(1 + e^{k_1(\varepsilon_p-\varepsilon_1)}\right)\right] \end{aligned} \tag{4-7}$$

$$\sigma_{bq}(E_{1,2,3}, \varepsilon_{1,2}, k_{1,2}, (\varepsilon_p, \sigma_p), q, \varepsilon) = \sigma_1 + \sigma_2 + \sigma_3 + \sigma_q \tag{4-8}$$

The ubiquitous s-curves in SMAs can herewith be described mathematically with one closed-form equation. With the base equation in (4-8), the entire SMA model algorithm is described in the following section.

The internal states of the system are the number of load and unload cycles, y, $(\varepsilon_p, \sigma_p)$ and $(\varepsilon_{pp}, \sigma_{pp})$ in (4-9), which saves the value of $(\varepsilon_p, \sigma_p)$ in the previous cycle.

$$(\sigma_{pp}(y), \varepsilon_{pp}(y)) = (\sigma_p(y-1), \varepsilon_p(y-1)) \tag{4-9}$$

Note that the vast majority of existing stress-strain models use the dash-dotted straight line segments in Fig. 4-2(a) as an approximation. The implementation in this case requires a series of conditional statements to distinguish between the three segments $\varepsilon \leq \varepsilon_1$, $\varepsilon_1 < \varepsilon < \varepsilon_2$ and $\varepsilon \geq \varepsilon_2$ and the curvatures at the knees in the $\sigma - \varepsilon$ function are replaced by sharp corners. Further, a description of the parabolic locus does not exist in these models, rendering inaccuracies in modelling the stress-strain behaviour.

4.2 SMA Model Algorithm

The complete model to describe SMA constitutive behaviour is characterised by the following steps, as shown graphically in Fig. 4-3:

1. **Monotonic experiments**: First, a simple monotonic experiment, as in the plots (a) and (b) of Fig. 4-1 is performed for SMA wires. In these experiments, the SMA in the 100% austenitic and 100% martensitic state at no load is loaded beyond the 2$^{\text{nd}}$ knee and unloaded to 0 stress. These experiments are not required if the SMA manufacturer provides these curves in their data sheets.
2. **Model initialisation**: The model is initialised **once**, with 7 parameters, E_1, E_2, E_3, $\varepsilon_1, \varepsilon_2, k_1, k_2$ from an identification process (Sect. 4.3) using data from step 1 above. All other parameters, $y, q, (\varepsilon_{pp}, \sigma_{pp})$, $(\varepsilon_p, \sigma_p)$ are set to 0.

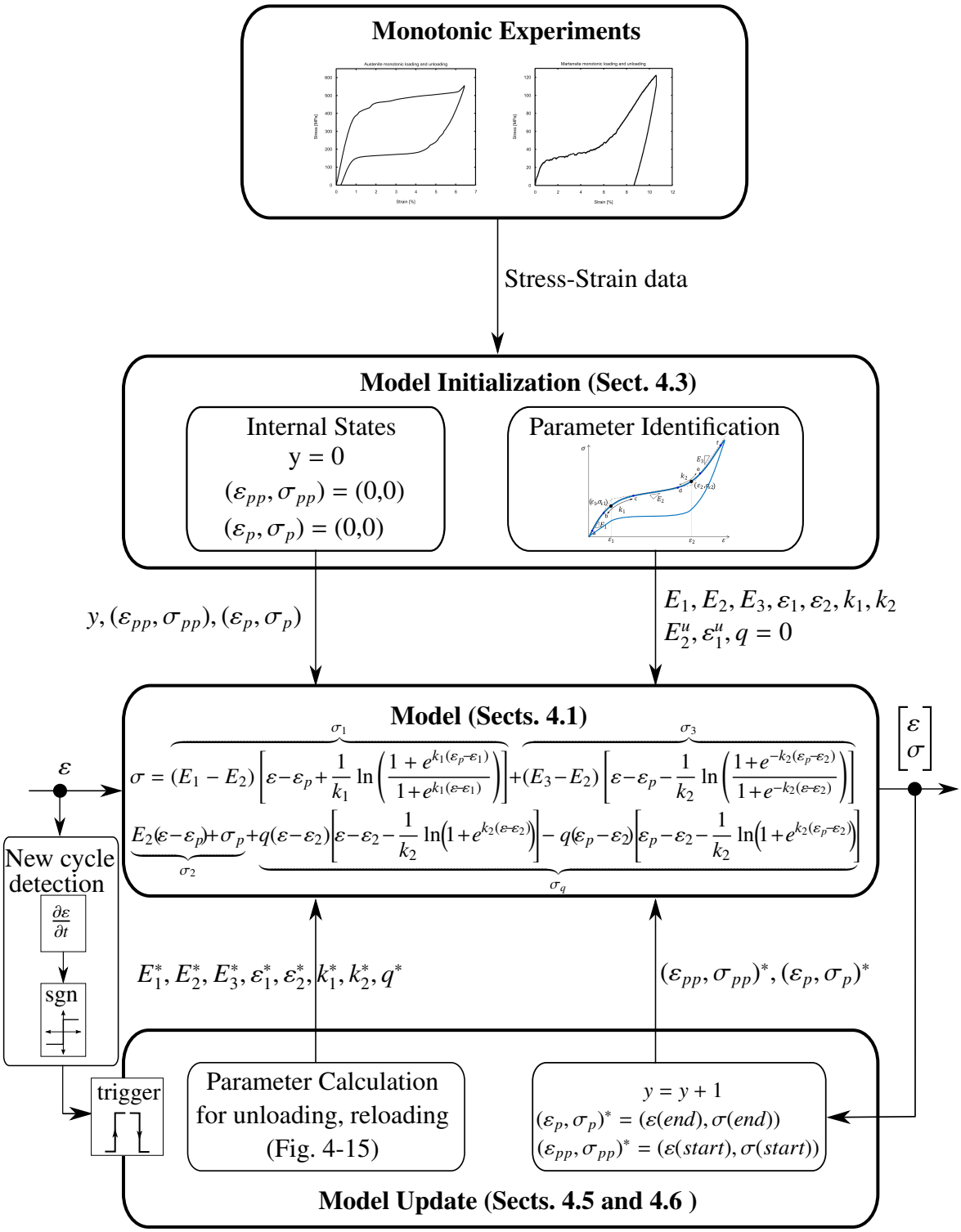

Figure 4-3: *Model algorithm*

3. **Model update**: When the input strain changes direction (from loading to unloading or vice versa), a new cycle is detected and a new s-curve is required to model the SMA behaviour. Therefore, the parameters set by the initialisation process need to be updated by a model update process (Sect. 4.5 and 4.6) to generate E_1^*, E_2^*, E_3^*, $\varepsilon_1^*, \varepsilon_2^*, k_1^*, k_2^*, q^*$, where superscript * is used to differentiate between the identified and updated parameters. The update process includes incrementing the number of cycles y by 1 ($y = y+1$). Further, for continuity, $(\varepsilon_p, \sigma_p)$ is updated to the coordinates where the new cycle is detected (end coordinates of the previous s-curve) and $(\varepsilon_{pp}, \sigma_{pp})$, according to (4-9), is updated to the previous value of $(\varepsilon_p, \sigma_p)$ (the start coordinates of the previous s-curve). This is necessary to track the stress-strain history of the material.

Consider, for example, an input strain as in Fig. 4-4, where initial loading to 4% strain is followed by unloading to 2% and reloading to 8% strain. Consider that parameters $E_1, E_2, E_3, \varepsilon_1, \varepsilon_2, k_1, k_2$ have been identified from experimental data using the procedure in Sect. 4.3. Initially, at the start of loading, $(\varepsilon_p, \sigma_p)$ and $(\varepsilon_{pp}, \sigma_{pp})$ are set to the starting coordinate $(0, 0)$, $q = 0$, $y = 0$ and the model is initialised with the identified parameters. Using exemplary parameters for the SMA in the austenitic and martensitic phase at no load, the red dashed curve in Fig. 4-5(a) and (b), respectively, are generated using (4-8).

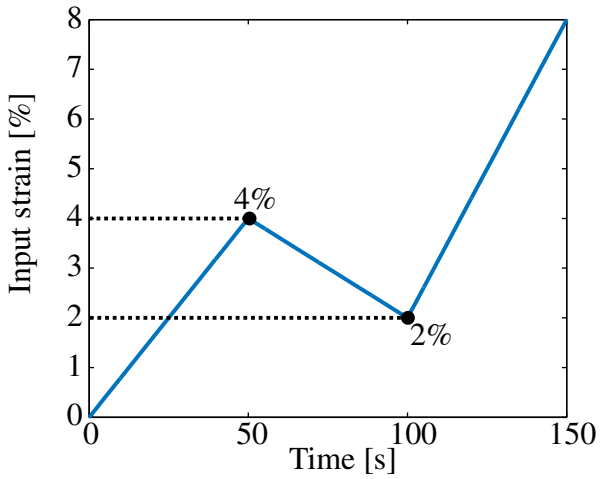

Figure 4-4: *Modelling algorithm: input strain*

As the input strain consists of 3 segments (loading, unloading and reloading), the s-curve is required 3 times to describe the SMA's complete stress strain behaviour as follows:

Loading The first s-curve is calculated with (4-8) using the identified parameters and with input strain 0% - 4% to give the *initial load s-curve* in Fig. 4-5(a) and (b) where end point of the loading curve is $(4, 470)$ for austenite and $(4, 195)$ for martensite, respectively[1].

Unloading At 4% strain, the input strain changes direction and a new s-curve, depicted by the green dash dotted curves in Fig. 4-5, is required to describe the unloading behaviour. The new parameters of this unloading s-curve, $E_1^*, E_2^*, E_3^*, \varepsilon_1^*, \varepsilon_2^*, k_1^*, k_2^*, q^*$ are **calculated** using the parameter update algorithm (see Sects. 4.5.1 and 4.6.1). Further, in order to ensure continuity, $(\varepsilon_{pp}, \sigma_{pp})$ and $(\varepsilon_p, \sigma_p)$ are updated to the start

[1] Unless explicitly mentioned, martensite and austenite in this chapter depict the phases at no load.

and end point of the previous loading curve i.e. $(0, 0)$ and $(4, 470)$ for austenite and $(0, 0)$ and $(4, 195)$ for martensite. Using these updated parameters, (4-8) is used again with input strain 4% - 2% to give the *unload s-curve* in Fig. 4-5. Note that for martensite, unloading produces residual strain ε_r (see Sect. 2.3) and decreasing the strain further has no physical effect (i.e. mathematically, stress values below 0 are cut off).

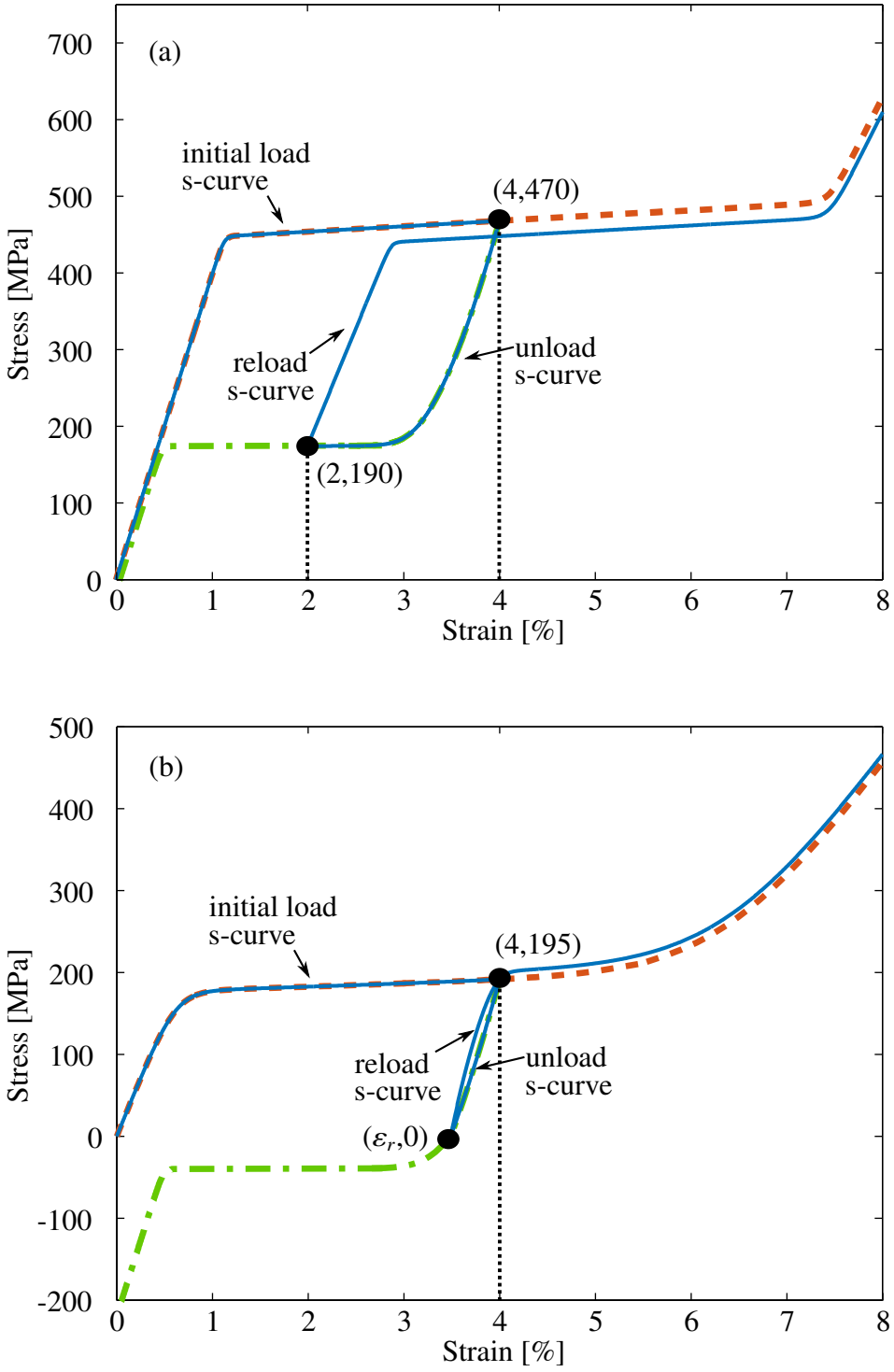

Figure 4-5: *Modelling algorithm: stress versus strain for (a) austenite, (b) martensite*

Reloading After unloading, the input strain changes direction and once again, a new s-curve with updated parameters, as calculated in Sects. 4.5.2 and 4.6.2, are required to compute the reloading behaviour. For continuity, $(\varepsilon_{pp}, \sigma_{pp})$ and $(\varepsilon_p, \sigma_p)$ are once again set to the start and end points of the unloading curve i.e. $(4, 470)$ and $(2, 190)$ for austenite and $(4, 195)$ and $(\varepsilon_r, 0)$ for martensite. These updated parameters set in (4-8) for reloading to 8% input strain produces the *reload s-curve* in Fig. 4-5.

The complete stress-strain curve corresponding to the input strain in Fig. 4-4 is the bold blue curve in Fig. 4-5(a) and (b), for austenite and martensite, respectively.

Note that for every cycle, regardless of austenite or martensite as the start phase, the stress-strain behaviour can be described by the s-curve. To this end, the s-curve parameters $E_1, E_2, E_3, \varepsilon_1, \varepsilon_2, k_1, k_2, q$, and the internal states $y, (\varepsilon_{pp}, \sigma_{pp}), (\varepsilon_p, \sigma_p)$ are sufficient to describe it analytically. The following sections present the initialization and update process in detail.

As mentioned earlier, the s-curve is implemented in other models using 3 if-statements. Therefore for a simple strain profile as in Fig. 4-4, which consists of 3 s-curves as shown in Fig. 4-5, these models require 9 if-statements. The required number of if-statements is three times the number of load-unload segments. When the strain profile consists of several of these segments, the computational capacity required can easily explode.

4.3 Model Initialization: Parameter Identification

In the model initialization process, the parabolic coefficient q is set to 0 due to the fact that the initial loading curves don't have any parabolic components. Further, the values $(\varepsilon_p, \sigma_p)$ and $(\varepsilon_{pp}, \sigma_{pp})$ are set to the initial strain and stress in the SMA. As typical experiments start with 0 MPa stress and 0% strain, $(\varepsilon_p, \sigma_p)$ and $(\varepsilon_{pp}, \sigma_{pp})$ are commonly $(0, 0)$. The remaining parameters are extracted with an automatic parameter identification algorithm that accepts the stress-strain data from a monotonic experiment as an input and produces parameters $E_1, E_2, E_3, \varepsilon_1, \varepsilon_2, k_1, k_2$ as an output. This occurs in the following steps using the data in Fig. 4-6 as an example:

1. Selection of any two points in the segments $a - b$, $c - d$, $e - f$ (see Fig. 4-2): These are called $(\varepsilon^1_{ab}, \sigma^1_{ab}), (\varepsilon^2_{ab}, \sigma^2_{ab})$; $(\varepsilon^1_{cd}, \sigma^1_{cd}), (\varepsilon^2_{cd}, \sigma^2_{cd})$; $(\varepsilon^1_{ef}\sigma^1_{ef}), (\varepsilon^2_{ef}, \sigma^2_{ef})$, as shown in Fig. 4-6.
2. Identification of slopes (moduli) E_1, E_2, E_3 using (4-10), where n is either 1, 2 or 3 and xy is either ab, cd or ef.
3. Calculation of $\varepsilon_1, \varepsilon_2$ as the intersection of the lines through the points in step 1 with slopes in step 2 using (4-11) and (4-12) (see the orange dash-dotted lines in Fig. 4-6).
4. Calculation of k_1, k_2 with (4-13) and (4-14), where σ_{ε_1} and σ_{ε_2} are the stresses at ε_1 and ε_2 (extracted from the data, as shown in Fig. 4-6). Detailed derivations of (4-13) and (4-14) are in A1.2.
5. Calculation of initial s-curve using the parameters above in (4-8), followed by optimization of all parameters to minimize the mean square error between the data and the s-curve (between the black and blue curve in Fig. 4-6) using an unconstrained, gradient-based, non-linear optimization algorithm, e.g. *fminsearch* from MATLAB®, with the values calculated in steps $2 - 4$ above as the initial values.

$$E_n = \frac{\sigma^2_{xy} - \sigma^1_{xy}}{\varepsilon^2_{xy} - \varepsilon^1_{xy}} \tag{4-10}$$

$$\varepsilon_1 = \frac{(\sigma^1_{cd} - E_2\varepsilon^1_{cd}) - (\sigma^1_{ab} - E_1\varepsilon^1_{ab})}{E_1 - E_2} \tag{4-11}$$

$$\varepsilon_2 = \frac{(\sigma^1_{cd} - E_2\varepsilon^1_{cd}) - (\sigma^2_{ef} - E_3\varepsilon^2_{ef})}{E_3 - E_2} \tag{4-12}$$

$$k_1 = -\ln(2)\left(\frac{E_1 - E_2}{\sigma_{\varepsilon_1} - \sigma^1_{ab} - E_1(\varepsilon_1 - \varepsilon^1_{ab})}\right) \tag{4-13}$$

$$k_2 = \ln(2)\left(\frac{E_3 - E_2}{\sigma_{\varepsilon_2} - \sigma^2_{ef} - E_3(\varepsilon_2 - \varepsilon^2_{ef})}\right) \tag{4-14}$$

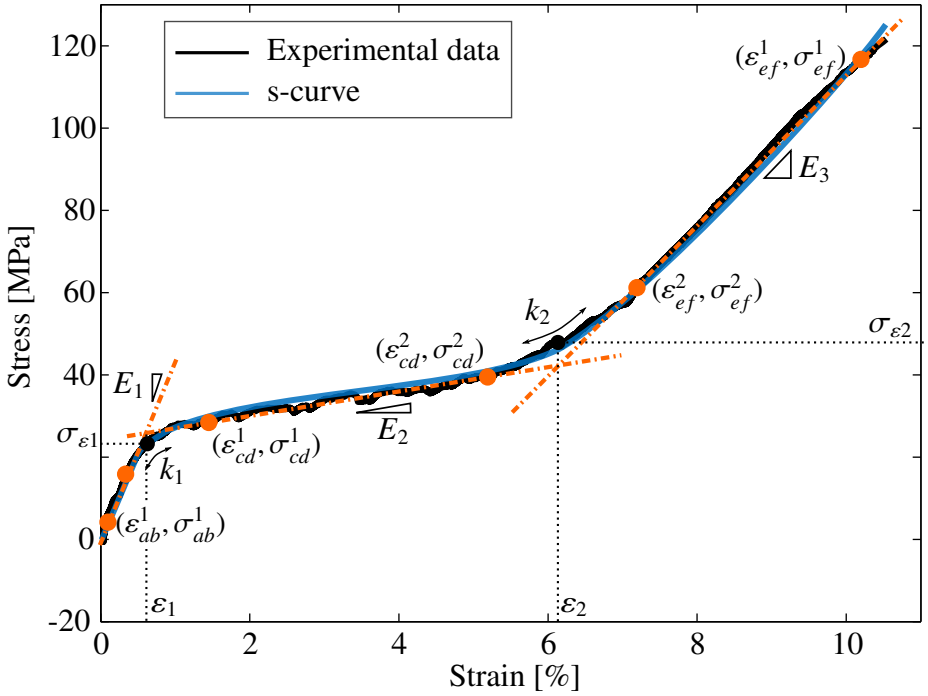

Figure 4-6: *Parameter identification using monotonic loading experimental data*

The steps above are used for the loading curve in the monotonic experiment. From the unloading curve, only two values are required (see Fig. 4-7): ε^u_1, the strain at the first unloading knee and E^u_2, the slope of the unloading plateau, with which the 'width' of the hysteresis loop is calculated. (For clarity, the parameters are named with superscript u for the unloading parameters.) Both values are extracted from the experimental data using steps 1 -3 above.

Note that when the material is martensitic at the start of the experiment, unloading is characterised by the presence of residual strain and no hysteresis loop is present. Nevertheless, the s-curve is used to model the unloading behaviour, as shown by the green dash-dotted curve in Fig. 4-5(b). When the parameters, ε^u_1 and E^u_2 are both set to 0, as they cannot be identified from experimental data, the resulting s-curve is shown by the red

curve in Fig. 4-7. This s-curve, for values of stress above 0, is still sufficient to describe unloading behaviour in martensite, as shown by the red solid curve in Fig. 4-7.

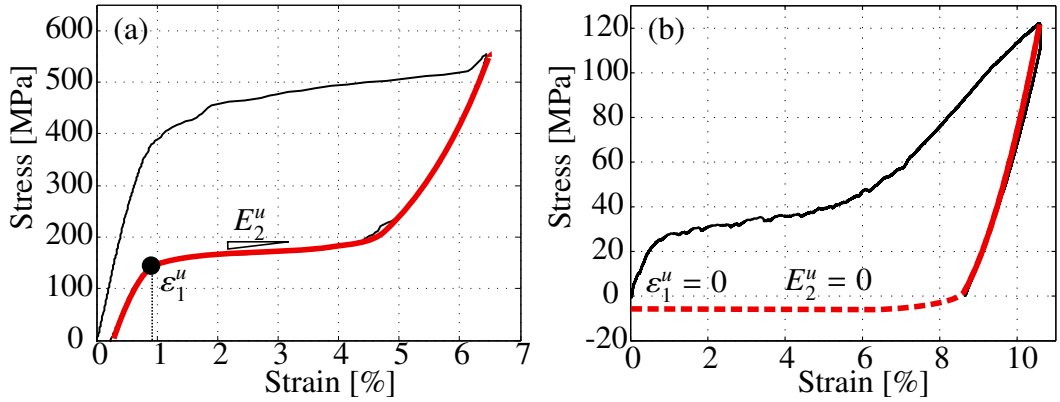

Figure 4-7: *Unloading austenite(a), martensite(b): experiment (black), s-curve (red)*

The complete set of parameters identified from monotonic experiments is in Tab. 4-1. They are used in (4-8) to compute the stress, for initial loading from the origin.

Table 4-1: *Identified model parameters*

Parameter	E_1	E_2	E_3	ε_1	ε_2	k_1	k_2	q	E_2^u	ε_1^u
Value	(4-10)	(4-10)	(4-10)	(4-11)	(4-12)	(4-13)	(4-14)	0	(4-10)	(4-11)

4.4 Modelling the Mechanically Induced Martensite Fraction

Recall from Sect. 2.4, that increasing the stress/strain of the SMA causes the formation of mechanically induced martensite ξ_S, which is hypothesised to progress according to the curve shown in Fig. 4-8. i.e. when $\varepsilon \leq \varepsilon_1$, there is no mechanically induced martensite (i.e. the SMA is austenite or twinned martensite) and $\xi_S = 0$. When $\varepsilon \geq \varepsilon_2$, the SMA is fully martensitic (SIM or detwinned martensite) and $\xi_S = 1$. For $\varepsilon_1 < \varepsilon < \varepsilon_2$, the formation of martensite progresses linearly. As the stress-strain behaviour of the SMA depends highly on the microscopic phases present, ξ_S is an important parameter that is mathematically modelled by (4-15). $\varepsilon_{k\xi}$ in (4-16) is the midpoint between the knees, where $\xi_S = 0.5$. k_ξ (in (4-18)) is proportional to the slope of the curve at $\varepsilon_{k\xi}$, which was empirically found to be proportional to the slope between the knees by a factor $n = 4$. Therefore, k_ξ is found by computing $(\frac{\partial \xi_S}{\partial \varepsilon})$ at $\varepsilon_{k\xi}$ and equating it to this slope, as in (4-17).

$$\xi_S(\varepsilon) = \frac{1}{1 + e^{-k_\xi(\varepsilon - \varepsilon_{k\xi})}} \tag{4-15}$$

$$\varepsilon_{k\xi} = \frac{\varepsilon_1 + \varepsilon_2}{2} \tag{4-16}$$

$$\frac{\partial \xi_S}{\partial \varepsilon} = \left.\frac{e^{k_\xi(\varepsilon - \varepsilon_{k\xi})} k_\xi}{(1 + e^{-k_\xi(\varepsilon - \varepsilon_{k\xi})})^2}\right|_{\varepsilon = \varepsilon_{k\xi}} = \frac{k_\xi}{4} = \frac{n}{\varepsilon_2 - \varepsilon_1} \tag{4-17}$$

$$k_\xi = \left.\frac{4n}{\varepsilon_2 - \varepsilon_1}\right|_{n=4} = \frac{16}{\varepsilon_2 - \varepsilon_1} \tag{4-18}$$

The selection of such a phase fraction profile is based on the hypothesis that the evolution of the volume fraction of martensite is directly related to the input strain. When the input strain is below ε_1, it causes elastic deformation of the phases (austenite or twinned martensite) present, but is not sufficient to cause propagation of the mechanically induced martensite. Conversely, when the input strain is above ε_2, where the material has fully been transformed to martensite, additional strain does not contribute to the evolution of more martensite but rather to elastic deformation. The propagation of martensite occurs mainly when the input strain is in between the knees (the plateau), moreover, this propagation is linearly dependant on the input strain.

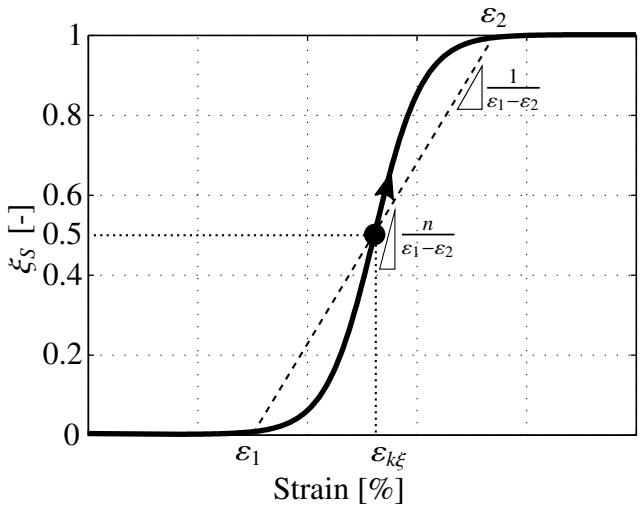

Figure 4-8: *Evolution of the mechanically induced martensite fraction*

The next sections present the model update process.

4.5 Model Parameter Update: Austenite

The initial loading curve is calculated by using the parameters $E_1, E_2, E_3, \varepsilon_1, \varepsilon_2, k_1, k_2, q$, identified in Sect. 4.3 in (4-8). When the direction of the input strain changes, which implies a switch from loading to unloading (or subsequently from unloading to reloading), the model parameter update process is triggered. This direction change is detected by using the signum (*sgn*) function to ascertain a zero crossing of the time derivative of the input strain. The parameters $(\varepsilon_{pp}, \sigma_{pp})$ and $(\varepsilon_p, \sigma_p)$ are updated first to the starting and end coordinates of the previous sequence. The rest of the parameters are calculated based on whether the material is in the martensitic or austenitic state at 0 stress, as shown in the following sections. In this section, the update process for austenite will be presented. Martensite follows in Sect. 4.6 below. In order to differentiate between the parameters identified from monotonic experiments as in Sect. 4.3 and the parameters calculated from the update process, the calculated parameter names have the superscript *. For clarity, the model update calculations are presented in the following sections for austenite unloading and reloading separately and Fig. 4-5(a) will be used for explanation. A summary of the parameter update is given in Fig. 4-15.

4.5.1 Austenite unloading

Consider that austenite at no load is loaded until a strain of 4%, as shown in Fig. 4-9. Then, the input strain changes direction to unloading. The SMA now follows a new s-curve, represented by the the green dash dotted unloading s-curve in Fig. 4-9. To this end, parameters $E_1^*, E_2^*, E_3^*, \varepsilon_1^*, \varepsilon_2^*, k_1^*, k_2^*, q^*$ are required to describe this new s-curve mathematically. The calculation of these parameters, as presented in this section, considers the behaviour of austenite, as shown in Chap. 2.

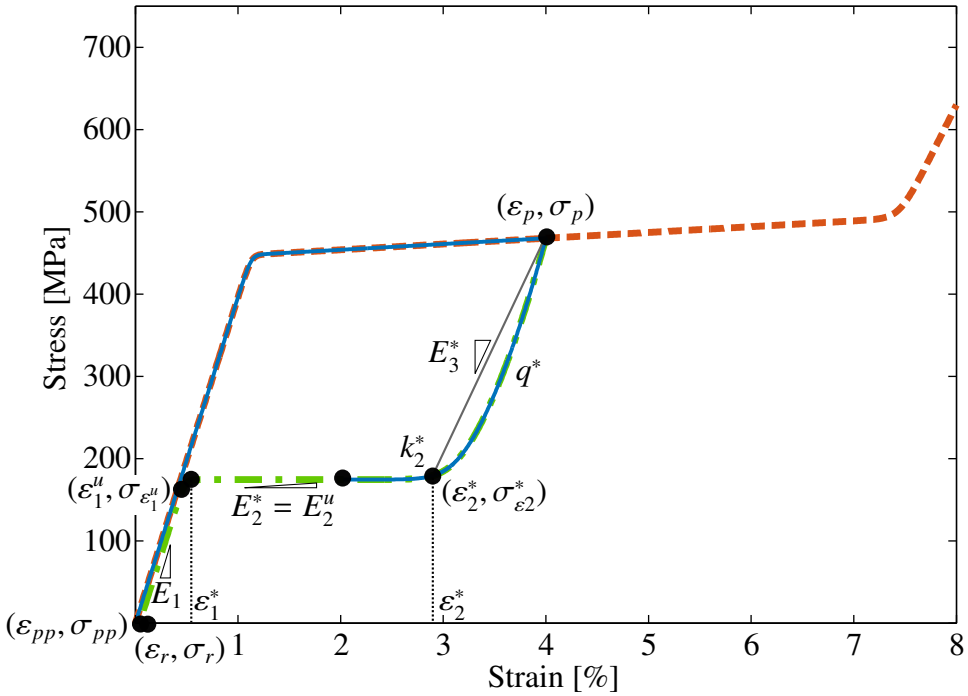

Figure 4-9: *Parameter update for unloading in austenite*

In order to model austenite unloading behaviour, a number of known phenomena have to be considered. One of these is the formation of residual strain, ε_r (see Sect. 2.2.1). The amount of residual strain saturates after about 50 cycles according to a negative exponent (cf. (4-19)[2], where y is the number of cycles[3]) due to strain hardening (training effect). This is consistent with findings available in literature, e.g. in [RLS07].

$$\varepsilon_r = (0.37)(1 - e^{-0.035(y/2-2)}) + 0.05 \tag{4-19}$$

The first step in the calculation of the required parameters for the new s-curve (see Fig. 4-9 where the green dash dotted unloading curve is considered) is to update the value of $(\varepsilon_p, \sigma_p)$ to value at which the previous loading ended and where this current unloading sequence begins. The rest of the parameters are presented in Tab. 4-2 below. A summary of the parameter calculation is given in Fig. 4-15.

[2]The values 0.37, -0.035 and 0.05 are found empirically from experimental data

[3]Note the number of cycles, y is one of the internal states of the system. Here only the number of unloading cycles is required, therefore $y/2$ appears in the equation.

Table 4-2: *Model parameter calculation for austenite unloading*

Parameter	Value and Description
E_1^*	$E_1^* = E_1$ After unloading before the 1st knee, the SMA is composed of 100% austenite, therefore the elastic modulus is identical to the loading modulus (see Fig. 4-9).
E_2^*	$E_2^* = E_2^u$ From the identification process (see Fig. 4-7(a)).
E_3^*	The calculation of E_3^* is highly dependant on the volume fraction of (mechanically induced) martensite present in the material at ε_p, the strain where unloading occurs. It is calculated with (4-20) where ξ_S^p is ξ_S evaluated at $\varepsilon = \varepsilon_p$ in (4-15). $$E_3^* = (1 - \xi_S^p)E_1 + \xi_S^p E_3 \tag{4-20}$$ Equation (4-20) implies that should unloading occur when $\xi_S^p = 0$ (100% austenite), then $E_3^* = E_1$ i.e. elastic unloading with the austenitic modulus E_1. Should unloading occur when $\xi_S^p = 1$ (100% martensite), then unloading is also elastic but with the martensitic modulus E_3. Therefore, $E_3^* = E_3$. If however, unloading occurs between the knees i.e. $0 < \xi_S^p < 1$, then the microscopic composition of the SMA is a mixture of austenite and martensite and the unloading slope E_3^* is a weighted linear combination of the slopes E_1 and E_3.
ε_1^*	The calculation of ε_1^* requires all other updated parameters and is calculated last in the algorithm. However, for consistent presentation, it is shown in this order. ε_1^* is calculated by solving for ε_1 in (4-8) yielding (4-21) where σ_2, σ_3 and σ_q are calculated with (4-3), (4-4) and (4-6), evaluated at $\varepsilon = \varepsilon_r$ and $\sigma = 0$. The calculation shows the dependency of the hysteresis loop width, which is based on ε_1^*, on ξ_S^p (through a dependence on $(\varepsilon_p, \sigma_p)$ and E_3^*); a phenomenon that is clearly observed in experiments (see Sect. 4.7). $$\varepsilon_1^* = \frac{1}{k_1^*} \ln\left(\frac{e^{k_1^* \varepsilon_p} - e^{-k_1^*\left(\frac{\sigma_3+\sigma_2+\sigma_q}{E_1^*-E_2^*} + \varepsilon_p\right)}}{e^{-k_1^*\left(\frac{\sigma_3+\sigma_2+\sigma_q}{E_1^*-E_2^*} + \varepsilon_p - \varepsilon_r\right)} - 1} \right) \tag{4-21}$$

Continued on next page

Table 4-2 – *continued from previous page*

Parameter	Value and Description
ε_2^*	The coordinate pair $(\varepsilon_2^*, \sigma_{\varepsilon_2^*})$ describes the start of the reverse transformation of martensite to austenite. It depends on the width of the hysteresis loop, that is calculated with the coordinate pair $(\varepsilon_1^u, \sigma_{\varepsilon_1^u})$ (see (4-22), recalling that ε_1^u was identified from monotonic experiments). ε_r is the residual strain, calculated with (4-19). Recall from Sect. 2.2.1 that the unloading behaviour for the SMA is elastic with a modulus E_3^*. Therefore the unloading behaviour can be modelled by a line originating at $(\varepsilon_p, \sigma_p)$ with slope E_3^*. The onset of the reverse transformation, $(\varepsilon_2^*, \sigma_{\varepsilon_2^*})$, is calculated with the intersection of the line with slope E_2^u originating at $(\varepsilon_1^u, \sigma_{\varepsilon_1^u})$ and the unloading line with (4-23) and (4-24), as shown in Fig. 4-9. $$\sigma_{\varepsilon_1^u} = E_1(\varepsilon_1^u - \varepsilon_r) \tag{4-22}$$ $$\varepsilon_2^* = \frac{E_3^*\varepsilon_p - E_2^u\varepsilon_1^u - \sigma_p + \sigma_{\varepsilon_1^u}}{E_3^* - E_2^u} \tag{4-23}$$ $$\sigma_{\varepsilon_2^*} = E_3^*(\varepsilon_2^* - \varepsilon_p) + \sigma_p \tag{4-24}$$
k_1^*	$k_1^* = k_1$ Identical to value from identification process since the transition from austenite to SIM is identical to that in the loading process.
k_2^* and q^*	In addition to the unloading moduli calculated above, the experimental data shows a parabolic locus. As mentioned earlier, this parabolic locus occurs due to sluggish behaviour of individual grains in the SMA. The material unloads elastically until $(\varepsilon_2^*, \sigma_{\varepsilon_2^*})$, calculated above, where the reverse SIM-austenite transformation starts. The calculation of the parabolic coefficient q to represent grain sluggishness then proceeds with (4-25), where the detailed derivation is shown in Appendix A1.4. k_2^* is subsequently calculated with (4-26) to ensure a smooth transition between the parabola and the rest of the curve, as shown in Appendix A1.3. $$q^* = \frac{(E_3^* - E_2^*)\sqrt{\ln(2)}}{2(\varepsilon_p - \varepsilon_2)} \tag{4-25}$$ $$k_2^* = \frac{4q}{E_3^* - E_2^*} \tag{4-26}$$

4.5.2 Austenite reloading

When the input strain changes direction again, unloading changes to reloading. Therefore, parameters for a new s-curve, the reloading curve, are required. This is shown in Fig. 4-10, where, this time, the blue solid reloading curve is considered.

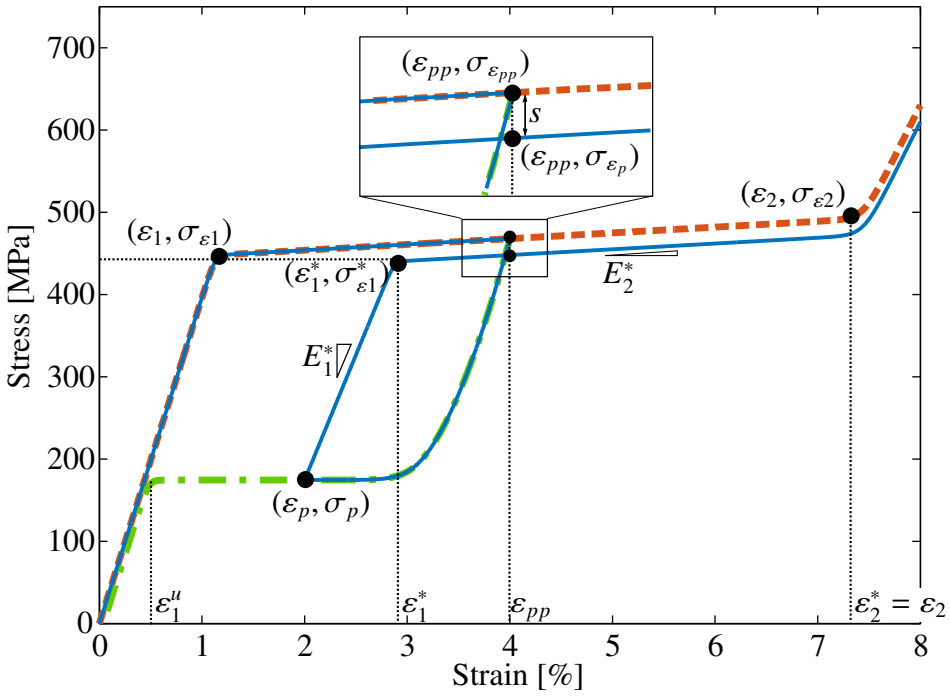

Figure 4-10: *Parameter update for reloading in austenite*

In reloading, a distinction is made between partial or complete reloading, depending on the end point of the previous unloading cycle (and therefore the reloading start point). Should the unloading end point be less than ε_1^u, then complete reloading is considered, as the material composition is 100% austenite. Conversely, partial reloading is considered when the unloading end point is greater than ε_1^u, where the material is a mixture of austenite and SIM, as is the case in Fig. 4-10 for the solid blue reloading curve.
The calculation of the parameters required for the new s-curve describing reloading is shown in Tab. 4-3. Note that the values of $E_3^*, \varepsilon_2^*, k_2^*$ are all identical to the values from the loading curve (the identified parameters). This is due to the fact that after the reloading curve reaches the plateau, further reloading continues identical to the loading curve (see Fig. 4-10).

Table 4-3: *Model parameter calculation for austenite reloading*

Parameter	Value and Description
E_1^*	The reloading modulus is dependant of the phases present at the point of reloading. Therefore, E_1^* is calculated exactly as in (4-20) and is repeated here for clarity. $$E_1^* = (1 - \xi_S^p)E_1 + \xi_S^p E_3 \quad (4\text{-}27)$$
E_2^*	For **complete reloading**: $E_2^* = E_2$ From the identification process i.e. identical to the loading curve. For **partial reloading** E_2^* is calculated with (4-28) using ε_1^* from (4-29) and the yield strengths $\sigma_{\varepsilon 1}$ and $\sigma_{\varepsilon 2}$ (see Fig. 4-10), calculated by using the identified parameters and $\varepsilon = \varepsilon_1$ and ε_2, respectively in (4-5): $$E_2^* = \frac{\sigma_{\varepsilon 2} - \sigma_{\varepsilon 1}}{\varepsilon_2 - \varepsilon_1^*} \quad (4\text{-}28)$$
E_3^*	$E_3^* = E_3$ From the identification process i.e. identical to the loading curve (see Fig. 4-10).
ε_1^*	For **complete reloading**: $\varepsilon_1^* = \varepsilon_1$ From the identification process i.e. identical to the loading curve. For **partial reloading** ε_1^* is calculated with the hypothesis that formation of SIM starts at a critical stress value, that is given by the initial yield strength, $\sigma_{\varepsilon 1}$ (see Figs. 2-4 and 4-10). Using E_1^*, calculated in (4-27), ε_1^* is given by (4-29): $$\varepsilon_1^* = \frac{\sigma_{\varepsilon_1} - \sigma_p}{E_1^*} + \varepsilon_p \quad (4\text{-}29)$$
ε_2^*	$\varepsilon_2^* = \varepsilon_2$ From the identification process i.e. identical to the loading curve (see Fig. 4-10).
k_1^*	$k_1^* = k_1$ Identical to value from identification process since the transition from austenite to SIM is identical to that in the loading process.

Continued on next page

Table 4-3 – *continued from previous page*

Parameter	Value and Description
k_2^*	$k_2^* = k_2$ From the identification process i.e. identical to the loading curve.
q^*	$q^* = q = 0$ From the identification process i.e. identical to the loading curve and since reloading in austenite does not show a parabolic locus.

Recall Sect. 2.2.3, where when reloading follows periods of partial unloading,'steps' are formed in the austenite plateau and that the most pronounced step is at the last unloading cycle (or at the absolute strain maximum of the previous loading cycles) as shown by the red dotted circles in Fig. 2-5. Modelling of these steps is important not only because they are experimentally observed phenomena but also to avoid the accumulation of model error that would occur for cyclical loading over several cycles if the steps were not modelled. To avoid unnecessary complexity, however, only the last, most pronounced step is considered.

The algorithm is as follows:

- A step of height s is calculated as the stress difference between the red dotted plateau and the solid blue plateau in Figure 4-10 at ε_{pp} using (4-30). Here, $\sigma_{\varepsilon_{pp}}$ is the stress at which unloading occurs. σ_{ε_p} is calculated with (4-5) using the $*$ parameters in Tab. 4-3 and with input $\varepsilon = \varepsilon_{pp}$ (See inset in Fig. 4-10).
- σ is calculated with (4-5) using $*$ parameters in Tab. 4-3 and ε as the input strain.
- σ_s calculated in (4-31) is then added to σ from above.

$$s = \sigma_{\varepsilon_{pp}} - \sigma_{\varepsilon_p} \tag{4-30}$$

$$\sigma_s = \frac{s}{1 + e^{-k_1(\varepsilon - \varepsilon_{pp})}} \tag{4-31}$$

The result is shown by the solid blue line in Fig. 4-11, where a 'step' at ε_{pp} is visible. Note that inclusion of the step brings the stress-strain curve back to the original loading curve (red dashed line), as is observed in experiments (cf. Fig. 2-5). This is not the case in Fig. 4-10, where the step is not modelled and a discrepancy between the reloading plateau and the original loading plateau are present. For several unloading-reloading cycles, this error accumulates considerably if the steps are not modelled.

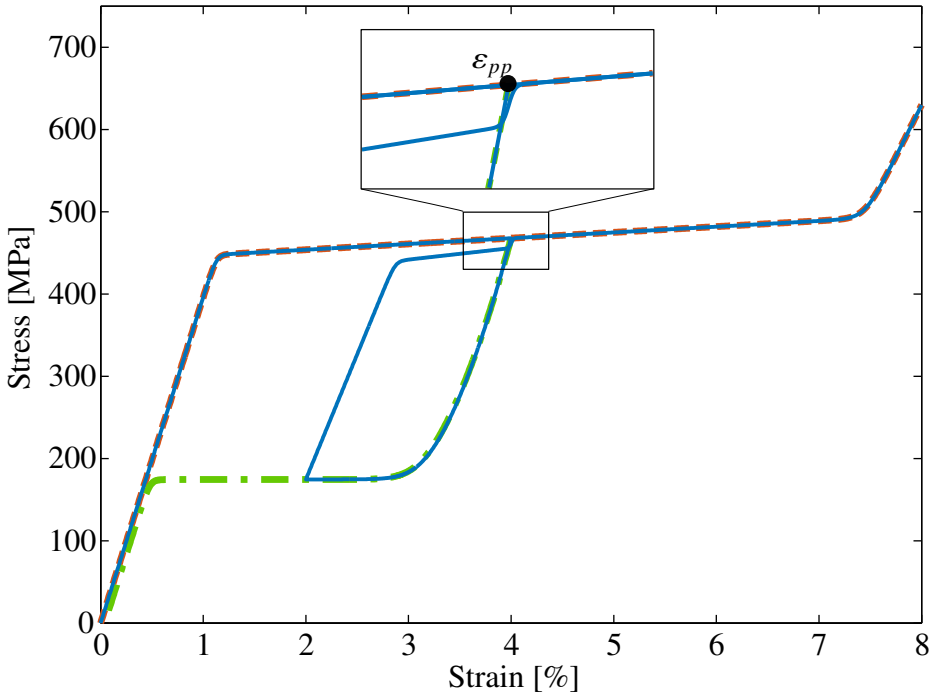

Figure 4-11: *Modelling of partial loading cycles in austenite with one step*

4.6 Model Parameter Update: Martensite

In this section, the model parameter update for martensite is presented separately for loading and reloading. The calculations are summarised in Fig. 4-15.

4.6.1 Martensite unloading

Martensite unloading is characterised by the presence of residual strain. The modelling of martensite unloading is quite simple in that only E_3^*, q^* and ε_2^* need to be calculated as shown in Fig. 4-12 for loading beyond ε_{2m} and unloading to 0 MPa of stress. The parameters E_1^*, E_2^* are set to 0 because these portions of the curve do not exist. ε_1^u is also set to 0 because loading and unloading in martensite displays no hysteresis. All other parameters remain unchanged. Table. 4-4 shows the calculation of the required parameters for the unloading s-curve. The same equations are used to calculate the required parameters when the unloading occurs from the plateau as shown exemplarily in Fig. 4-13, where experimental data from [Pai07] is taken (cf. Fig. 4-1(c)).

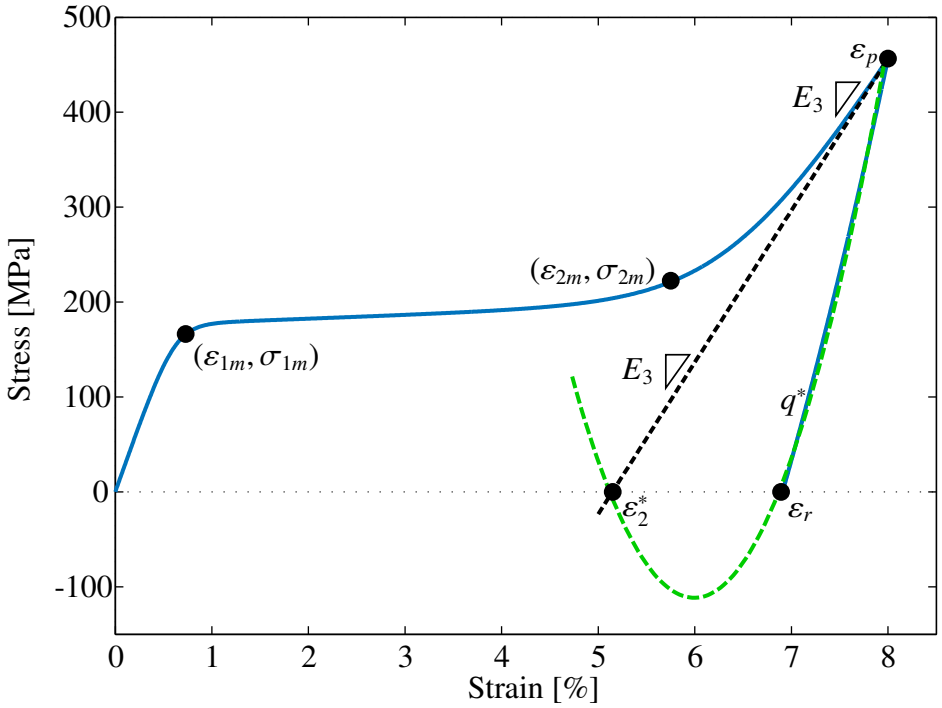

Figure 4-12: *Modelling martensite unloading*

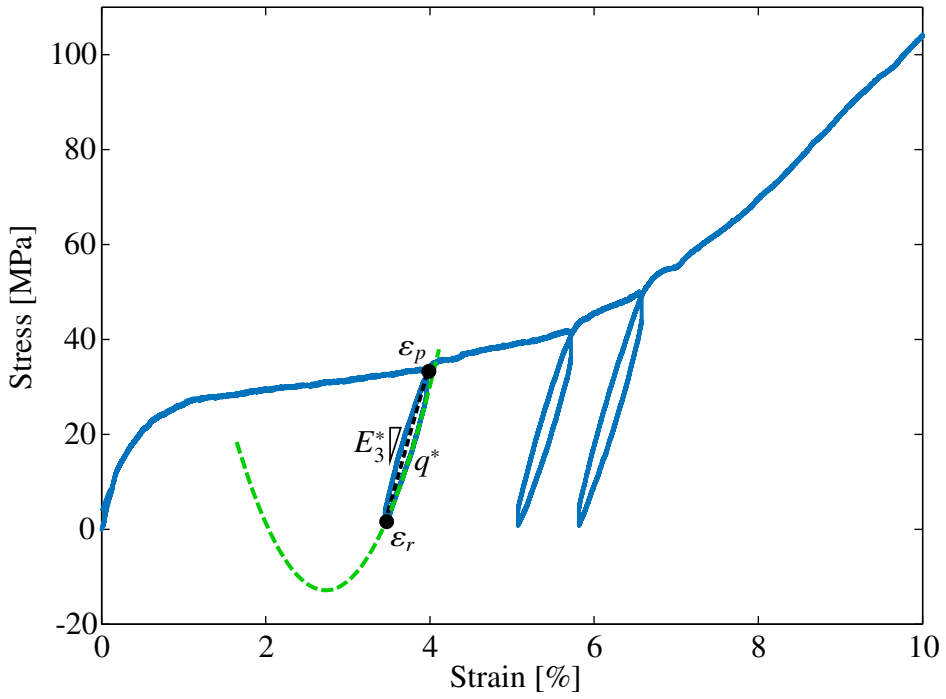

Figure 4-13: *Modelling martensite unloading from plateau*

Table 4-4: *Model parameter calculation for martensite unloading*

Parameter	Value and Description
E_1^*	$E_1^* = 0$ This portion of the s-curve does not exist.
E_2^*	$E_2^* = E_2^u = 0$ This portion of the s-curve does not exist (identified parameters as in Fig. 4-7(b)).
E_3^*	The calculation of E_3^* proceeds with the same equations (4-20) as for austenite (shown here for clarity). In this case, however, ξ_S^p refers to the fraction of detwinned martensite (instead of SIM) present in the material at the point of unloading. $$E_3^* = (1 - \xi_S^p)E_1 + \xi_S^p E_3 \tag{4-20}$$
ε_1^*	$\varepsilon_1^* = \varepsilon_1^u = 0$ This portion of the s-curve does not exist (identified parameters as in Fig. 4-7(b)).
ε_2^*	Recall from Sect. 2.3, that loading beyond ε_{2m} signifies a complete transformation to detwinned martensite where unloading is elastic. This is exploited to find ε_2^*, as shown in Fig. 4-12. The parabolic locus, characteristic of unloading (oriented) martensite, as shown by the green dashed curve in this figure, mathematically passes through the residual strain ε_r and ε_2^* (where these strains are the roots of the parabola). With $E_1 = 0$, $E_2^u = 0$ and $\varepsilon_1^u = 0$, respectively, as is the case for martensite unloading, ε_2^* can be calculated identically to the austenitic case with (4-23), which gives (4-32) as expected. $$\varepsilon_2^* = \frac{E_3^* \varepsilon_p - \sigma_p}{E_3^*} \tag{4-32}$$
k_1^*	$k_1^* = 0$ This portion of the s-curve does not exist.
k_2^*	$k_2^* = k_2$ Identical to identified parameters.

Continued on next page

Table 4-4 – *continued from previous page*

Parameter	Value and Description
q^*	q^* uses the same equation as austenite in (4-25), shown here for clarity. $$q^* = \frac{(E_3^* - E_2^*)\sqrt{\ln(2)}}{2(\varepsilon_p - \varepsilon_2)} \quad (4\text{-}25)$$

4.6.2 Martensite reloading

As mentioned in Sect. 2.3, martensite reloading is also characterised by a parabolic locus (see Figs. 2-7 and 4-1). The value of E_1, q and ε_1 are the only parameters that need updating as shown in Fig. 4-14 and in Tab. 4-5. This is due to the fact that, similar to austenite reloading, once the SMA has reloaded to the plateau, further reloading is identical to original loading therefore $E_2^*, E_3^*, \varepsilon_2^*, k_1^*, k_2^*$ are the identified (loading) parameters.

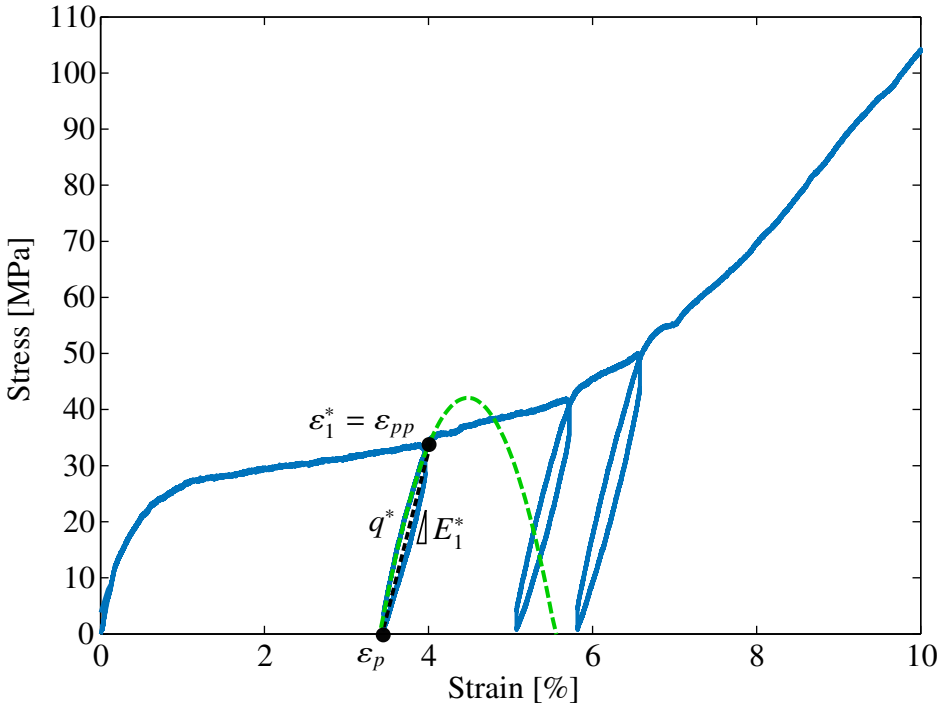

Figure 4-14: *Modelling martensite reloading*

Table 4-5: *Model parameter calculation for martensite reloading*

Parameter	Value and Description
E_1^*	E_1^* is calculated identically as in austenite reloading using (4-27), however, ξ_S^p refers to the fraction of detwinned martensite (instead of SIM) present in the material at the point of reloading. $$E_1^* = (1 - \xi_S^p)E_1 + \xi_S^p E_3 \quad (4\text{-}27)$$
E_2^*	$E_2^* = E_2$ Identical to identified parameters.
E_3^*	$E_3^* = E_3$ Identical to identified parameters.
ε_1^*	$\varepsilon_1^* = \varepsilon_{pp}$ ε_1^* is simply set to the value of ε_{pp}, the point at which the previous unloading took place. This is reasonable because detwinned martensite propagation will start again when the plateau stress is reached and this occurs at ε_{pp}.
ε_2^*	$\varepsilon_2^* = \varepsilon_2$ Identical to identified parameters.
k_1^*	$k_1^* = k_1$ Identical to identified parameters.
k_2^*	$k_2^* = k_2$ Identical to identified parameters.
q^*	The value of q^* is calculated using (4-33), where σ_1, σ_2 and σ_3 are calculated with (4-2), (4-3) and (4-4) evaluated at $\varepsilon = \varepsilon_{pp}$ and using the updated values (the * values) for the other parameters i.e. $E_1 = E_1^*$. The derivation of (4-33) is in Appendix A1.5. $$q^* = \frac{\sigma_1 + \sigma_2 + \sigma_3 - \sigma_{pp}}{(\varepsilon_{pp} - \varepsilon_p)^2} \quad (4\text{-}33)$$

The calculations are summarised in Fig. 4-15.

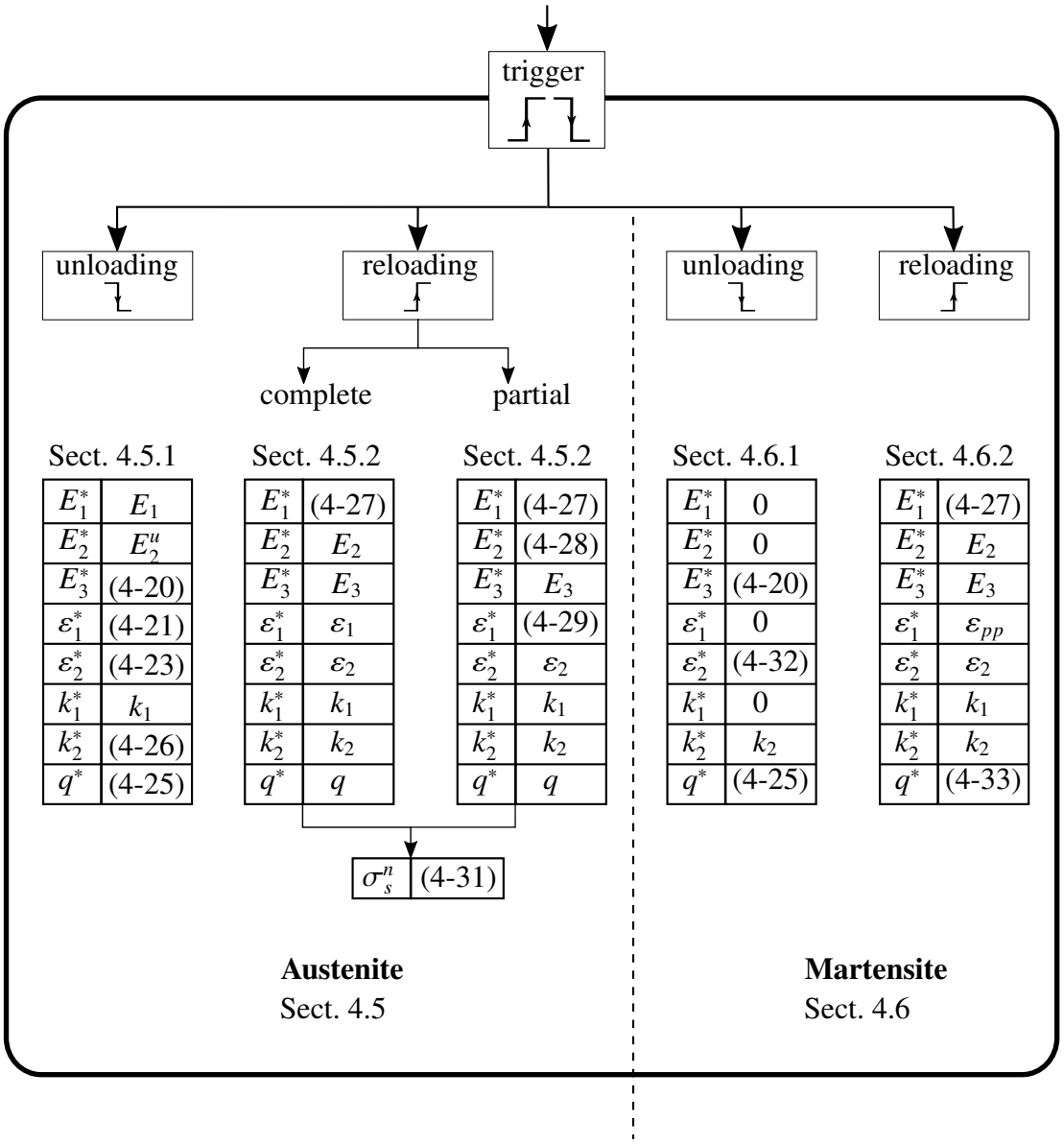

Figure 4-15: *Parameter update summary for austenite and martensite*

4.7 Experimental Validation and Discussion

In order to validate the model, a number of tensile stress-strain experiments were carried out using a servo hydraulic testing rig from MTS Systems (see Appendix A2.4). The experiments were performed at room temperature (20°C). The test specimens were two sets of 0.5 mm diameter poly-crystalline Ni-Ti SMA wires from SAES Group [Sae16], differing only in their A_f temperatures (95 °C and −25 °C). Consequently, both a 100% martensitic and a 100% austenitic initial condition at room temperature were established. The martensite wires were placed in a furnace at 400°C for 1 minute and allowed to cool to room temperature before the experiment. This ensured that all residual strains in the wire were eliminated prior to testing. The wire specimens were mounted in the testing machine using custom built fixing grips featuring grooves of appropriate diameter to facilitate installation and alignment. All geometrical dimensions were measured to enable for correct stress and strain calculation. The wire lengths were 60 mm. The tensile experiments were conducted under constant cross-head displacement velocity of 2 mm/min. Loading-unloading experiments were performed using the same set-up. For loading, the machine was run in displacement control up to the given displacement value, while unloading was conducted in displacement control up to a minimum force level of 5N (approx. 25 MPa).

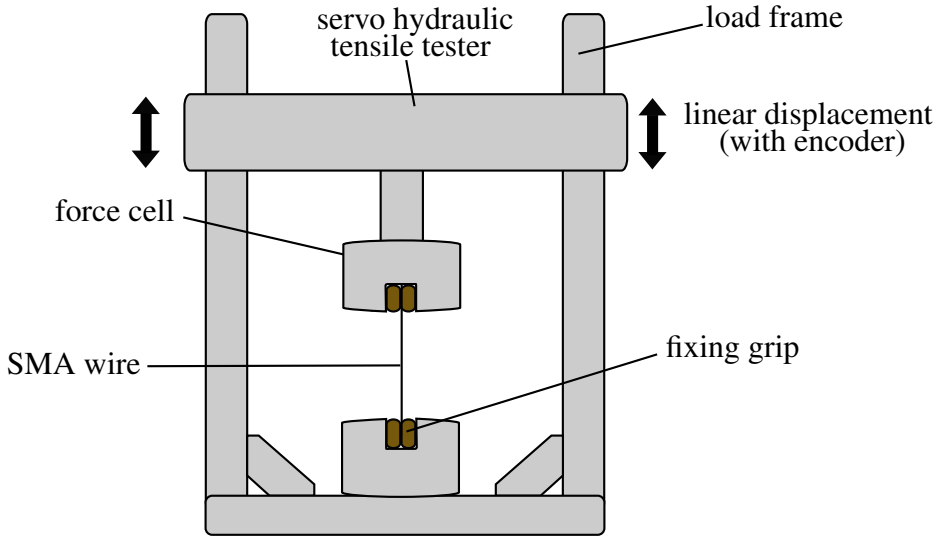

Figure 4-16: *Experimental setup for stress-strain tests at room temperature*

All experiments were carried out on wires from the same batch. The monotonic experiments were carried out on wire sample $A1$, for austenite and $M1$, for martensite. The corresponding data was used to extract the model parameters (see Sect. 4.7.1). Wire sample $A1$ was subsequently used for both austenite complete and partial cyclic loading experiments (see Sects. 4.7.2 and 4.7.3). The results for the experiments for martensite cyclic loading with wire sample $M1$ are shown in Sect. 4.7.4 and the results with other wire samples are shown in Sect. 4.7.5. Further, the *tic, toc* commands in MATLAB® were used to give a ball park value for the computational time of the model. The model was run 20 times each on a computer with an Intel Core i3-M330 processor with a CPU clock speed of 2.13 GHz and 4 GB of RAM and the average value was then documented as the computational time.

4.7.1 Monotonic loading and unloading and parameter identification

In these experiments, the wire samples were loaded up to a maximum displacement of 5 mm (approx. 8.5% strain) followed by an unloading ramp to a minimum force of 5N. The results are plotted as solid black curves in Fig. 4-17 for austenite and Fig. 4-18 for martensite. The model parameters deduced from the experimental data are shown in Tab. 4-6.

Table 4-6: *Model parameters identified from monotonic experiments.*

	E_1 GPa	E_2 GPa	E_3 GPa	ε_1 %	ε_2 %	k_1 –	k_2 –	ε_1^u %	E_2^u
Austenite	40	0.7	25	1.13	7.45	3.5e3	1.4e3	0.3	0
Martensite	29	0.39	15.8	0.58	6.43	580	170	0	0

With all the required parameters identified, the model produces the results depicted by the red dashed line in Figs. 4-17 and 4-18. The results are in good agreement with experimental data especially at the knees where most other models are not accurate enough. The root-mean-square-error (RMSE) is calculated with (4-34). σ_{expt} is the stress that is experimentally measured, σ_{model} is the stress calculated from the model and n is the number of data points. The RMSE is 6.6 MPa for austenite and 2.1 MPa for martensite. The normalised RMSE (NRMSE), calculated with (4-35), is 0.88% for austenite and 0.41% for martensite. The computational time was 29 ms for martensite and 30 ms for austenite.

$$\text{RMSE} = \sqrt{\frac{\sum_{i=1}^{n}(\sigma_{expt,i} - \sigma_{model,i})^2}{n}} \tag{4-34}$$

$$\text{NRMSE} = \frac{\text{RMSE}}{\sigma_{expt,max} - \sigma_{expt,min}} 100\% \tag{4-35}$$

Note that for the sake of simplicity, the model does not account for the ‘peaks’ at strains of about 0.5% and 5.5% for austenite unloading in Fig. 4-17. These peaks can be related to the phase transformation behaviour in SMAs. In the case of pseudoelastic behaviour, the austenite reverse transformation from the fully martensitic state can be separated into two parts: initiation of initial austenite followed by movement of band like phase fronts. Such kind of local transformation behaviour is naturally accompanied by a sudden change in stress-strain response [ACR98], [OR05], i.e. a load increase as seen in Fig. 4-17. This effect is not modelled in order to avoid complexity and thereby maintain the model’s computational efficiency.

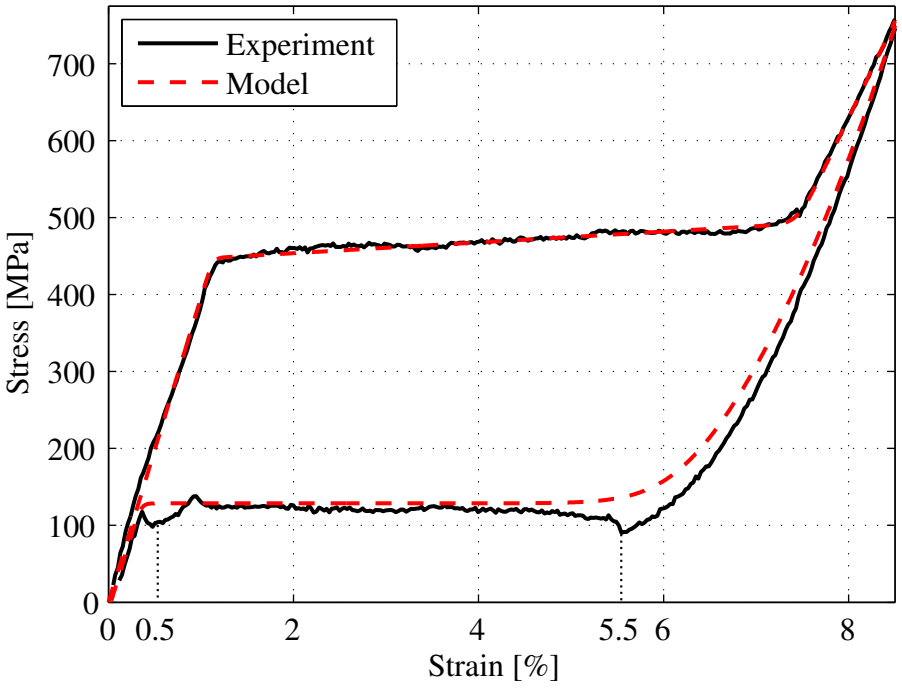

Figure 4-17: *Austenite monotonic loading, unloading on wire sample A*1

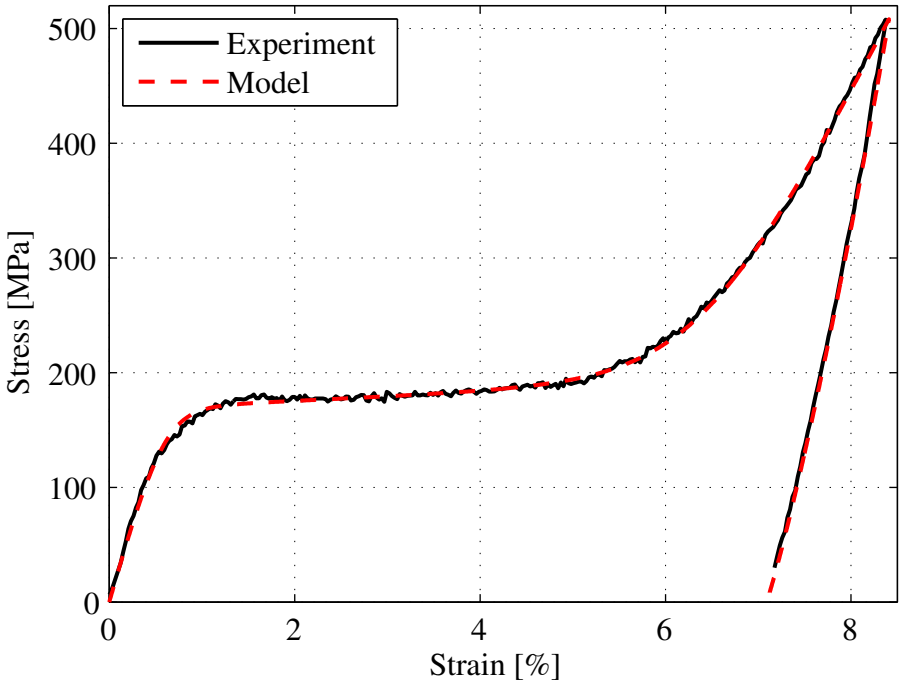

Figure 4-18: *Martensite monotonic loading, unloading on wire sample A*1

4.7.2 Austenite complete cyclic loading

In these experiments, the Ni-Ti wires having an A_f of $-25\,^{\circ}\mathrm{C}$ were loaded in displacement control with the input displacement as shown in Fig. 4-19. In the first cycle, the wire is loaded up to 0.2 mm followed by an unloading ramp down to 5 N. This was repeated for 25 cycles in a single test run, whereby the maximum displacement of the loading portion for each cycle was increased by 0.2 mm with respect to the previous cycle, i.e. the maximum displacements of cycles 2, 3 ... 25 were 0.4, 0.6 ... 5 mm, respectively. The results are plotted by the solid black curve in Fig. 4-20. With the parameters in Tab. 4-6, the model uses (4-8) multiple times, updating the required parameters, as presented in Sect. 4.5, each cycle. The model results are in Fig. 4-20 (red dash-dot line) and they show good overall correlation with experimental data with an RMSE of 7.2 MPa (NRMSE 0.9%). The computational time for the model is 120 ms.

When considering the model predictions in Fig. 4-20, the most important observations are as follows:

- Inclusion of the build up of residual strain in the model automatically causes 'shifts' of the pseudoelastic loop each cycle, a phenomenon that is clearly observed in the experiments.
- In the experiments, a further observed phenomenon is the consecutive decrease of the onset of forward transformation (the critical stress for SIM formation), which is induced by micro-plasticity in the SMA [GSA+01], [KNK+12]. Micro-plasticity leads to a slight increase in dislocation density, and thus, introduces local stress fields in the microstructure. These stress fields assist martensitic phase transformation. With respect to the Clausius-Clapeyron equation[4], phase transformation of SMAs at constant temperature is described by a constant stress value needed for transformation to SIM [OR05]. Thus, internal stress fields lower the external stress needed, as the sum of both stress values has to be considered. However, micro-plasticity and slip are characterized by irreversibility, leading to the aforementioned evolution of residual strain [KNK+12]. This consecutive reduction of the critical stress is also automatically predicted by the model.
- In addition to modelling fatigue effects such as the formation of residual strain, the model also includes load history memory i.e. steps in the austenite plateau. In the model, only 1 step is considered, although the model can easily be extended to include addition of as many (or as few) steps as required. The RMS-error when using 2 or 3 steps are both around 7.2 MPa (NRMSE 0.9%), the same RMS-error as when 1 step is used. Therefore, 1 step seems to be sufficient for predicting this behaviour without unnecessarily complicating the model.
- The model automatically predicts increase of the hysteresis loop widths with increasing strain.

[4] The Clausius-Clapeyron equation describes the relationship between the transformation of phases as a function of temperature and stress according in $\frac{d\sigma}{dT} = -\frac{\Delta H}{T_o \varepsilon}$, where ΔH is the change in enthalpy between the phases at temperature T_o [Bri93]

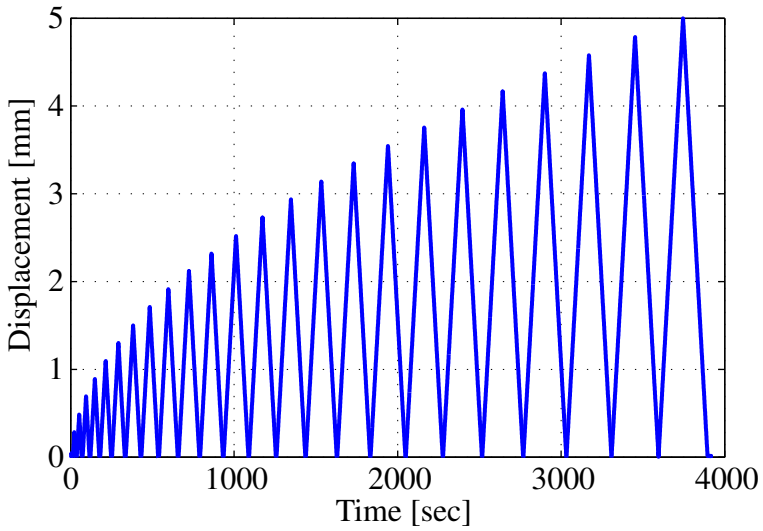

Figure 4-19: *Input displacement versus time for cyclical experiments*

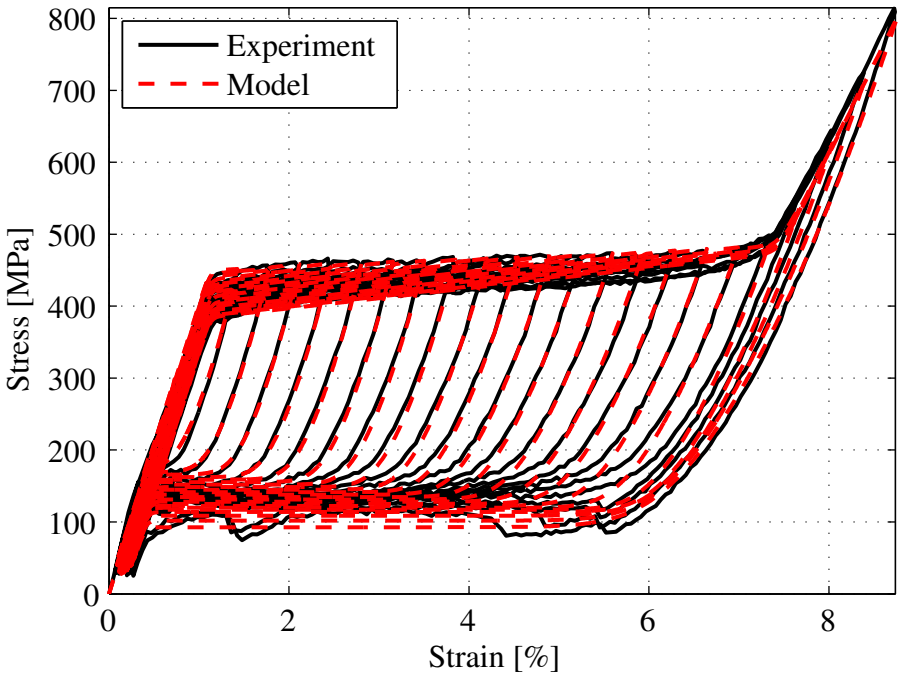

Figure 4-20: *Austenite complete cyclical loading on wire sample A*1

4.7.3 Austenite partial cyclic loading

In these experiments, two variations were performed. In the first, the Ni-Ti wires were subjected to 25 load - unload cycles, whereby the loading strain was increased by 0.4% each cycle and the wire was then partially unloaded until 3% strain recovery was achieved as shown in Fig. 4-21. The results are plotted in Fig. 4-22 with the model as the red dash-dotted line, show RMSE of 19.5 MPa, NRMSE of 1.9% and computational time of 97 ms. In the second experiment, the wire was subjected to an arbitrary input strain as shown in Fig. 4-23, with the model results plotted with the red dotted line in Fig. 4-24, with RMSE of 12.6 MPa, NRMSE of 2.2% and computational time of 75 ms. As a basis

for the development of the model, the hypothesis was made that the unloading behaviour of austenite or martensite is based on the volume fraction of either SIM or detwinned martensite, respectively, present in the SMA at the time of unloading. Using this hypothesis, the model and experiments have good correlation lending weight to its accuracy.

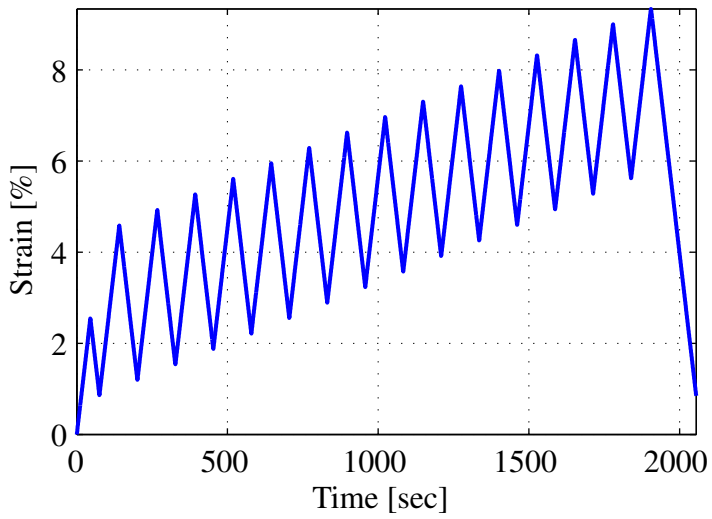

Figure 4-21: *Input strain versus time for austenite partial cyclical loading - 25 cycles*

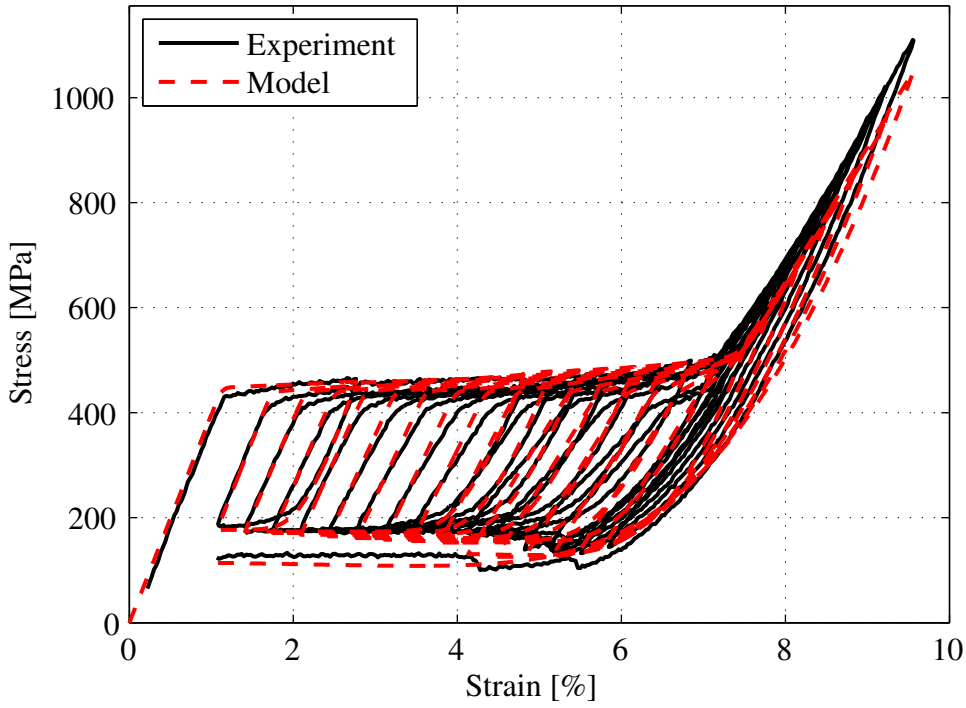

Figure 4-22: *Austenite partial cyclical loading for 25 cycles on wire sample A*1

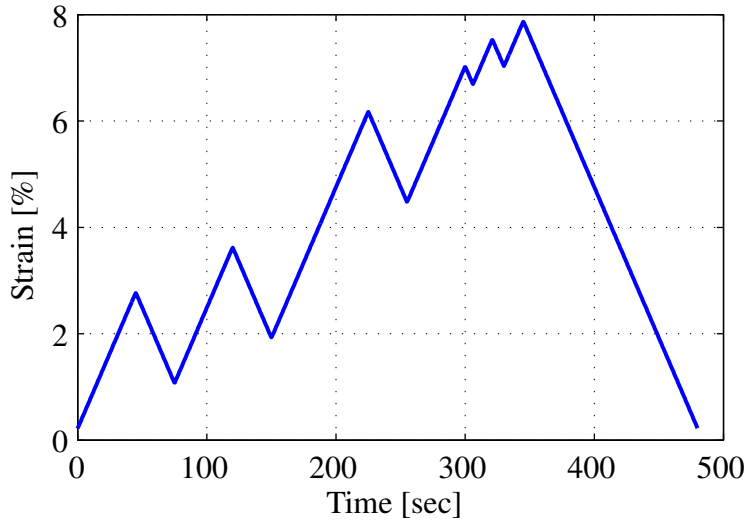

Figure 4-23: *Input strain versus time for austenite partial cyclical loading*

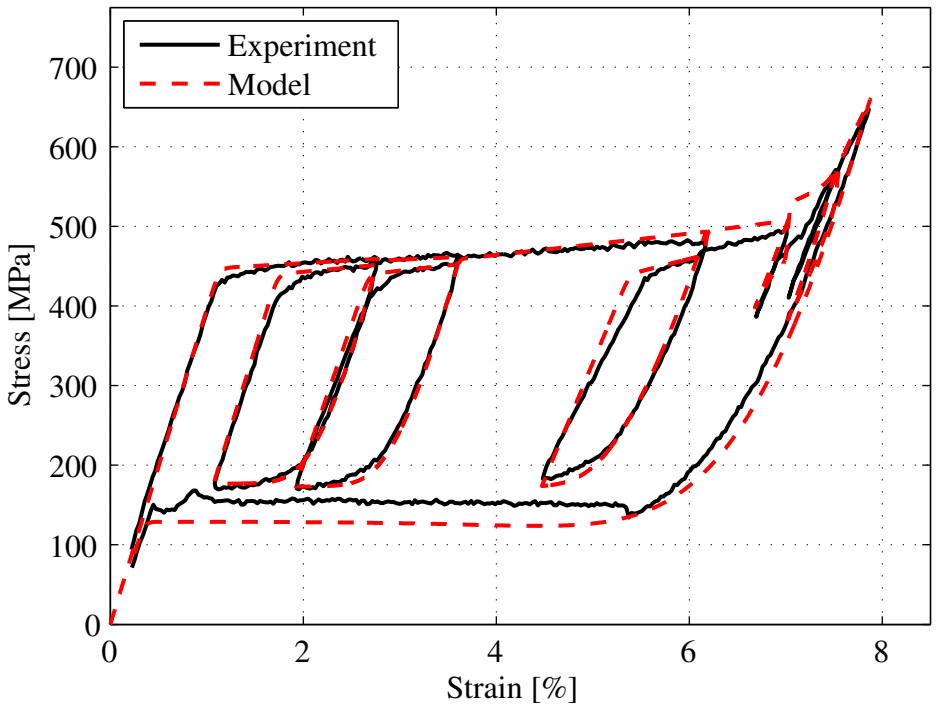

Figure 4-24: *Austenite partial cyclical loading on wire sample A*1

4.7.4 Martensite cyclic loading

The experiments evaluating the behaviour of the fully martensitic SMA were conducted in the same fashion as the experiments detailed in Sect. 4.7.2 above for the austenitic condition. The results are plotted in Fig. 4-25 showing experimental data (solid black curve) and the model (red dash-dotted curve). The RMSE is 5.8 MPa, NRMSE is 1% and the computational speed is 94 ms. Note that the model can also reproduce the minor hysteresis loops present with each unloading - reloading cycle (see inset in Fig. 4-25). As in the austenite case above, the hypothesis that the unloading behaviour of martensite is based on the volume fraction of detwinned martensite present in the SMA at the time of unloading produces good correlation between the model and experiments.

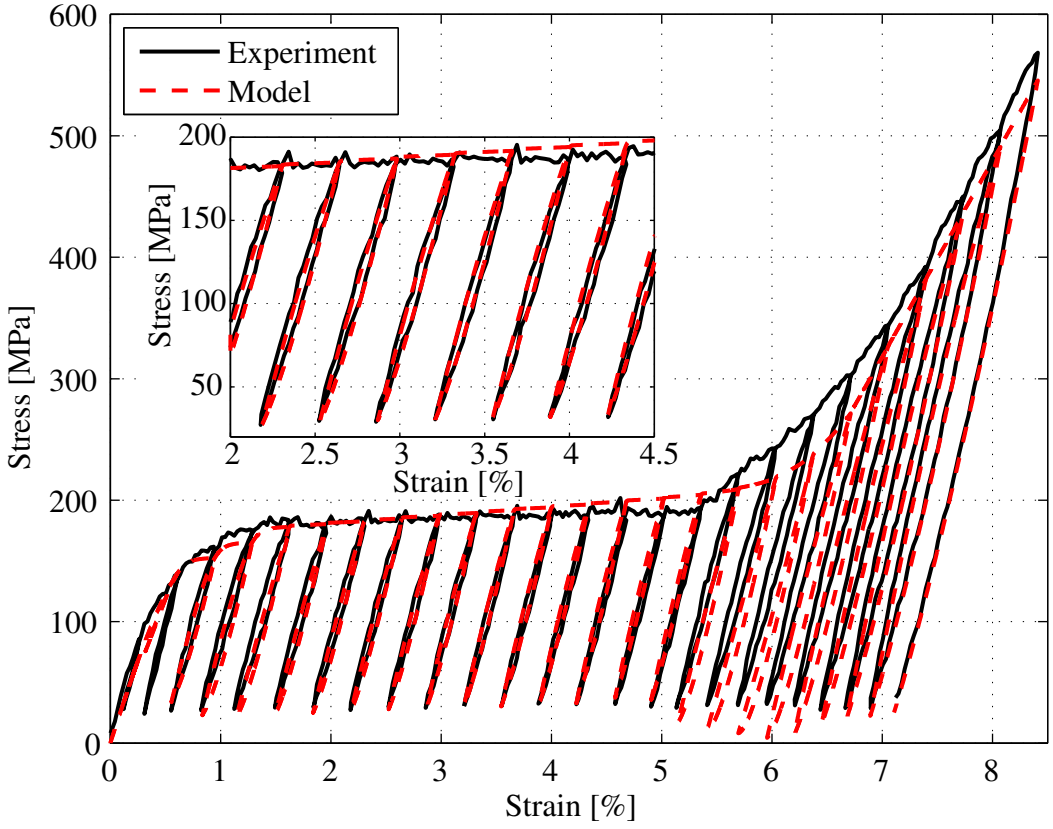

Figure 4-25: *Martensite cyclical loading on wire sample M*1

4.7.5 Experimental validation on different wire samples

The results above show extremely good correlation between experimental data and the model for wire samples $A1$ and $M1$. In order to further test the robustness of the model, the cyclical experiments were carried out for wire samples $A2$ and $A3$ in the austenitic state and for wire sample $M2$ in the martensitic state. The model is calculated using the parameters extracted from the monotonic experiments on $A1$ and $M1$. The RMSE (in MPa) and NRMSE (in %) for the experiments are summarised in Tab. 4-7 and the results are plotted in the figures below.

Table 4-7: *Root-mean-square error between experimental data and model (cc: complete cycles, pc-25: 25 partial cycles, pc: partial cycles).*

	A_1	A_2	A_3	M_1	M_2
cc [MPa]	7.2	13.3	12.0	5.8	5.5
cc [%]	0.9	1.8	1.7	1.0	0.98
(fig no.)	(*4-20*)	(*4-26(a)*)	(*4-26(b)*)	(*4-25*)	(*4-29*)
pc-25 [MPa]	19.5	15.8	23.8	–	–
pc-25 [%]	1.9	1.7	2.8	–	–
(fig no.)	(*4-22*)	(*4-27(a)*)	(*4-27(b)*)		
pc [MPa]	12.6	10.4	17.7	–	–
pc [%]	2.2	1.9	3.5	–	–
(fig no.)	(*4-24*)	(*4-28(a)*)	(*4-28(b)*)		

The results for complete cyclical loading in austenite are shown in Fig. 4-26. The plots show the model plotted with the parameters in Tab. 4-6. The model and experiment correlation is acceptable except when the strains are higher than ε_2. The value of ε_2 is very sensitive. Changing it from to 7.8 (from 7.45) produces better RMS-error values of 12.3 and 10.4 MPa, respectively (as opposed to 13.3 and 12.0 MPa). This could imply that the $A1$ was already partly transformed before the experiment, resulting in a lower value for ε_2. Figs. 4-27 and 4-28 show the model and experimental data for partial cyclical loading in austenite. The model parameters used here were also the same as in Tab. 4-6.

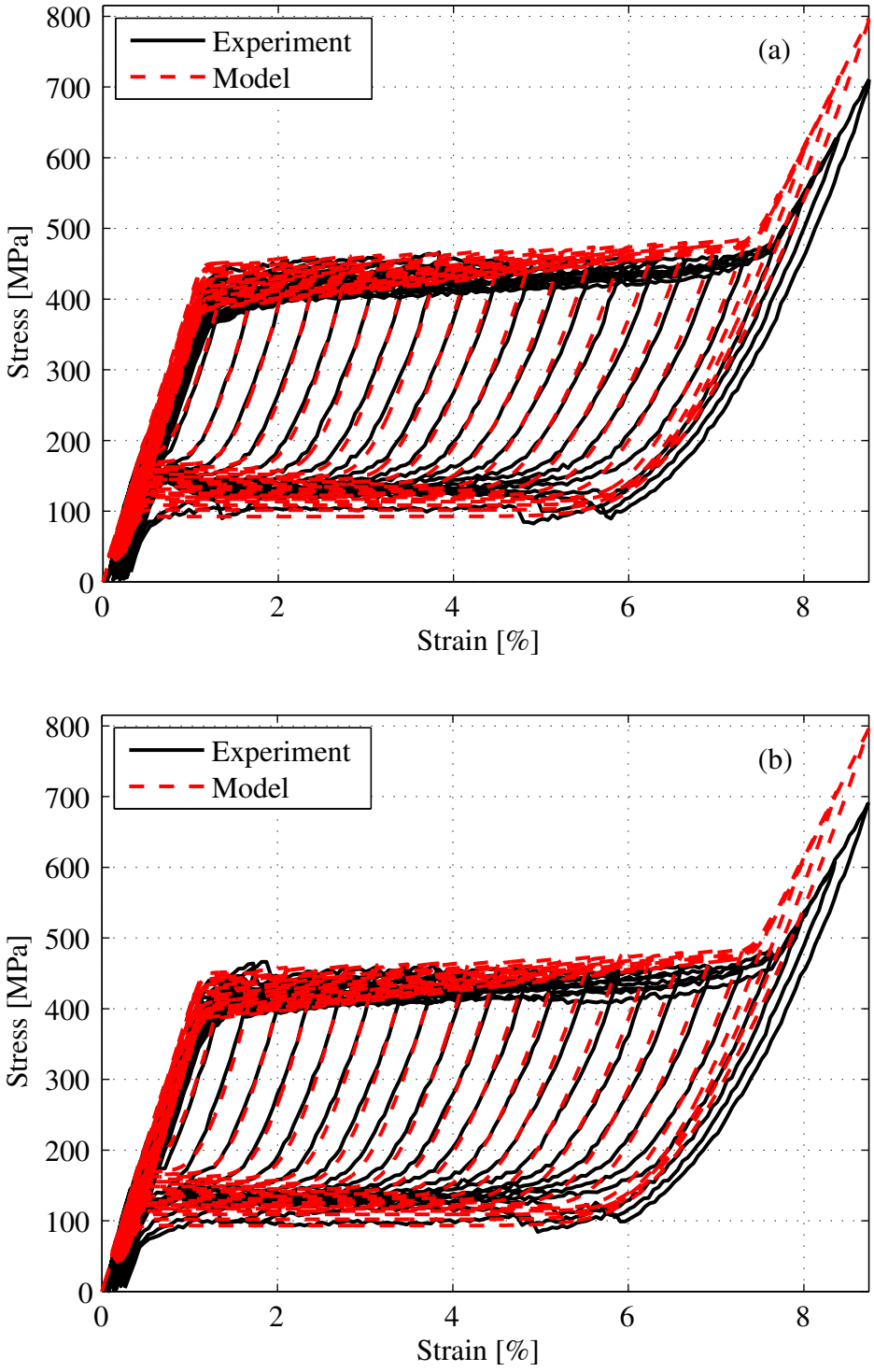

Figure 4-26: *Austenite complete cyclical loading on wire samples: A2 (a), A3 (b)*

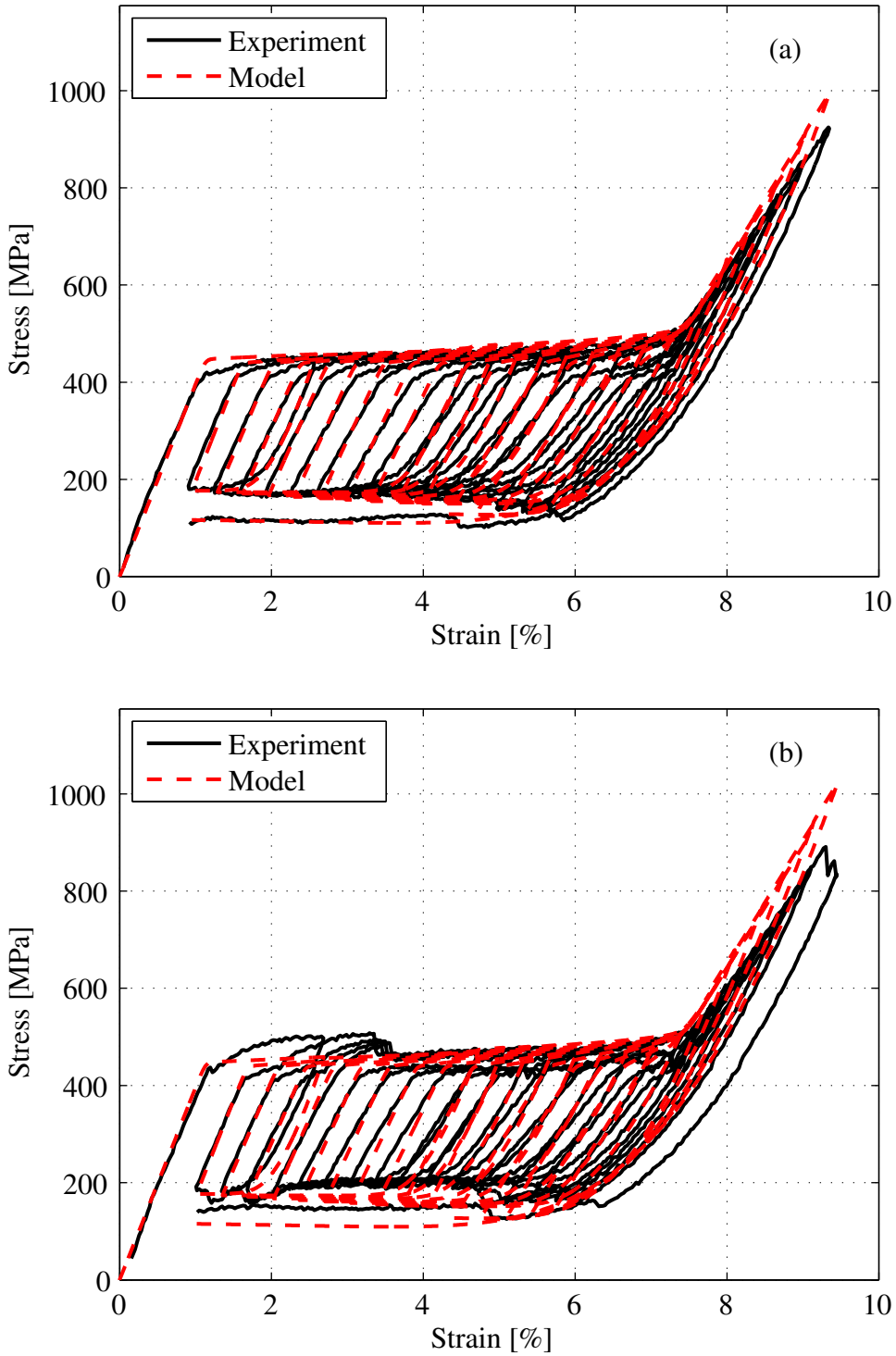

Figure 4-27: *Austenite partial cyclical loading 25 cycles on wire samples: A2 (a), A3 (b)*

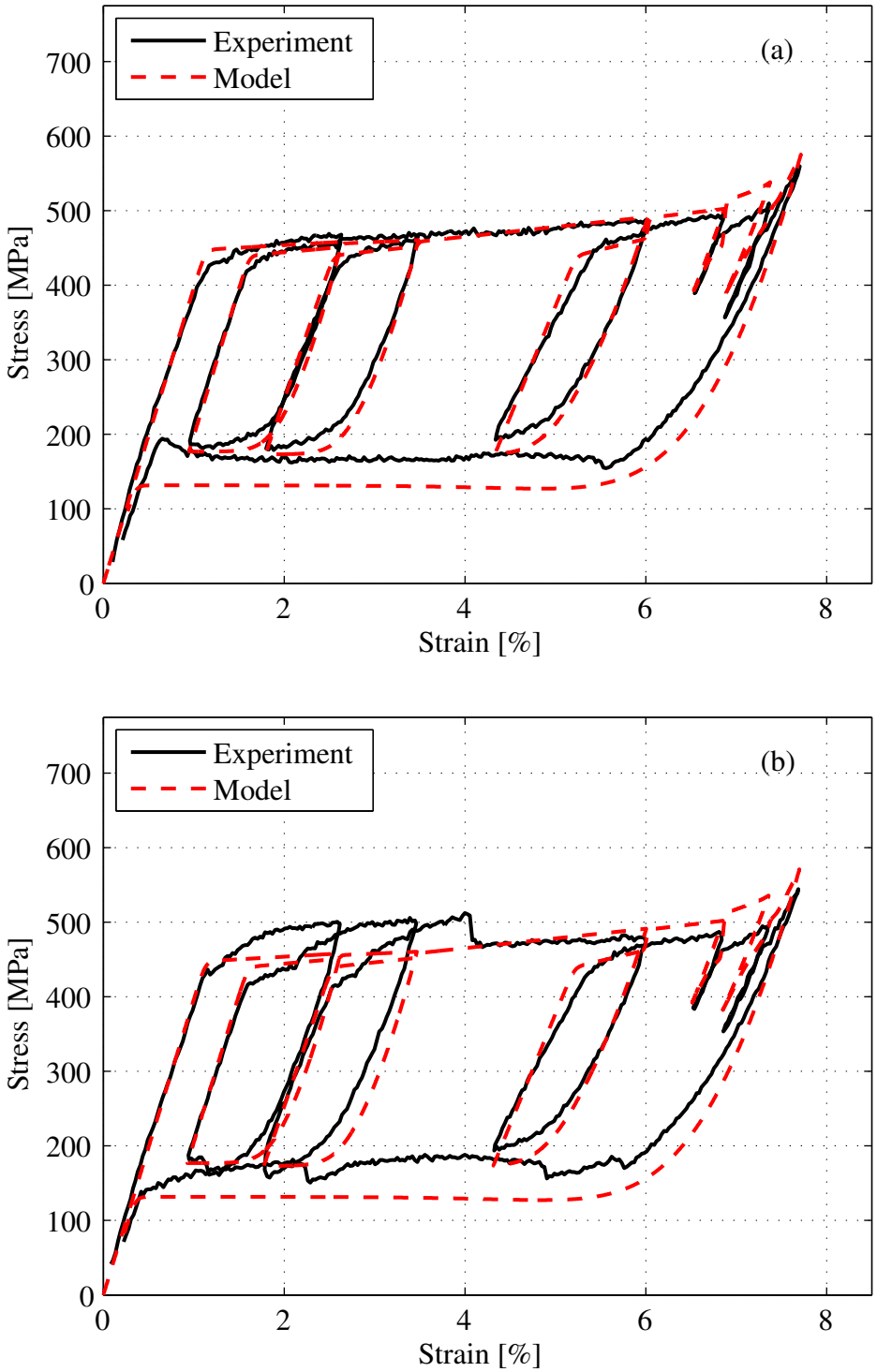

Figure 4-28: *Austenite partial cyclical loading on wire samples: A2 (a), A3 (b)*

Fig. 4-29 shows the results for a martensite cyclical experiment conducted on $M2$. The model is calculated using the parameters extracted from the monotonic experiments conducted on $M1$ and shows a similar RMSE of 5.5 MPa, NRMSE of 0.98% between the model and experiment.

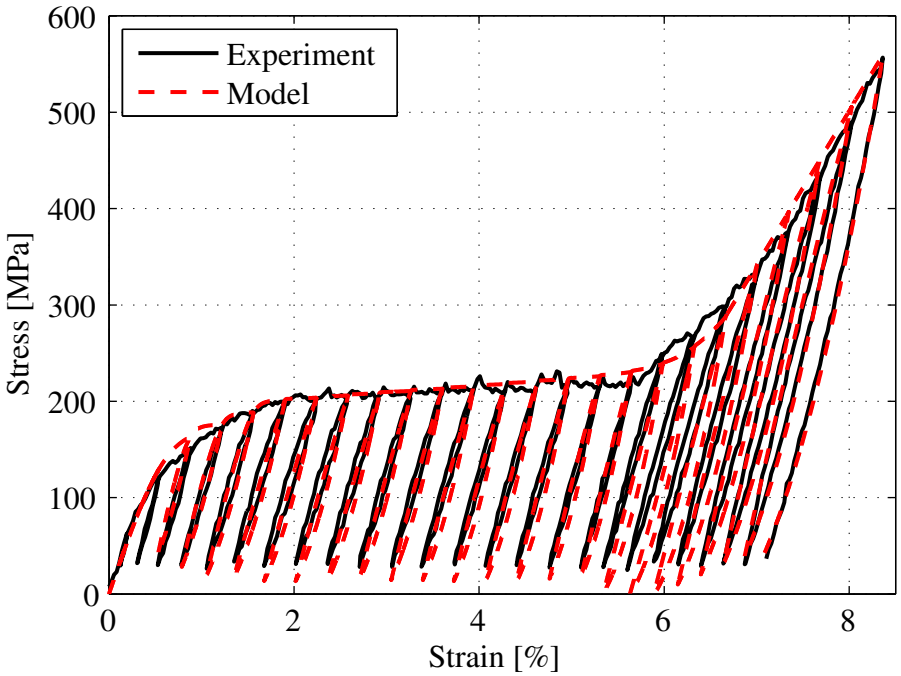

Figure 4-29: *Martensite cyclical loading on wire sample M2*

Both the austenite data and the martensite data in this chapter show reasonable correlation between the model and experiments, except for the sensitivity in ε_2 (the second knee) for the austenite complete cyclical model. The correlation is more than sufficient for the development of real-time SMA controllers.

4.8 Summary

In this chapter, a novel phenomenological constitutive model to predict the behaviour of either martensite or austenite subjected to arbitrary loading and unloading cycles is developed. The model is continuous and differentiable, with parameters that are few, physical and easy to identify and the parameter identification process has to be carried out only once for the same batch of wires. Further, the use of optimization algorithms guarantees that the identified parameters produce a minimum mean-square-error between the data and the monotonic experiments.

In addition to accurately modelling the curvature at the knees, the model includes experimentally observed phenomena such as quadratic loci for major and minor loops in both phases, the variation of the unloading slopes based on the volume fraction of the phases present and load history effects such as the build up of residual strain and ‘steps’ in the austenite plateau. Further, the maximum NRMSE between experimental data and the model for all validation experiments is shown to be 3.5%, with a majority of the results

showing an NRMSE of under 2%. This shows excellent correlation between experiments and the model.

The model's simplicity guarantees computational efficiency without compromising accuracy in predicting observed behaviour, as was verified with monotonic and cyclic loading-unloading experiments, including wires different than those used to extract the model parameters. The model can therefore form the basis for the development of real-time control algorithms for SMA actuators.

Further, although the experimental verification was carried out using NiTi wires, the phenomena that are modelled are universal for other SMAs such as iron based, copper based alloys etc. (see [CWL+14], [AO16] where stress-strain curves and shape memory phenomena described are similar to that in NiTi). To model the behaviour of these alternative SMAs, only the parameter identification step is required.

5 Stress Strain Model at Arbitrary Temperatures

The previous section presented the stress-strain model for austenite and martensite with good correlation to experimental data. The model, however, can only be used when the SMA is at the threshold temperatures when its internal crystallographic composition is either 100% martensite ($T < M_f$) or 100% austenite ($T > A_f$). When used as an actuator, the SMA is used at various temperatures between M_f and A_f where its internal phases are a combination of both martensite and austenite. The extenstion of the model to include the stress-strain behaviour for arbitrary temperatures is the focus of this section.

5.1 Experimental Set-up

In order to quantify the SMAs behaviour at various temperatures, a number of tensile stress-strain experiments were carried out using the experimental set-up in Fig. 5-1.

The wires used were 0.5 mm diameter poly-crystalline Ni-Ti SMA wires with an A_s temperature of 95°C. Similar to the experimental procedure in the previous chapter, the wires were placed in a furnace at 400°C for 1 minute and allowed to cool to room temperature before the experiment to eliminate all residual strains. The wire specimens were mounted in custom built fixtures using fixing grips featuring grooves of appropriate diameter to facilitate installation and alignment. All geometrical dimensions were measured to enable for correct stress and strain calculation. The wire lengths were 60 mm.

The fixtures and the SMA wire were submerged completely in a custom-made silicone oil bath and were attached to the same servo hydraulic tensile tester as in Sect. 4.7. The temperature of the bath was controlled by using an external cooling thermostat with level control from the company Lauda (see Appendix A2.5 and A2.6). The external cooling thermostat regulated the temperature between its internal silicone oil bath and the external bath where the wire was submerged.

The temperature of the external silicone oil bath was measured using 2 PT100 K-type thermocouples (see Appendix A2.7) at different locations in the bath. The required temperature was set in the cooling thermostat and the silicone oil in the external bath was agitated with a small hand-held mixer to ensure temperature homogeneity. When the temperature of the bath as read by both thermocouples with a digital thermometer (see Appendix A2.8) were within 1°C of each other and the required temperature, the tensile experiments were started.

The tensile experiments were conducted under constant cross-head displacement velocity of 2 mm/min. For loading, the machine was run in displacement control up to the given displacement value, while unloading was conducted in displacement control up to a minimum force level of 5 N (approximately 25 MPa). The experiments were carried out on several wire samples. The results for loading for temperatures from room temperature at 20°C to 120°C, well over the A_f temperature, is shown in Fig. 5-2.

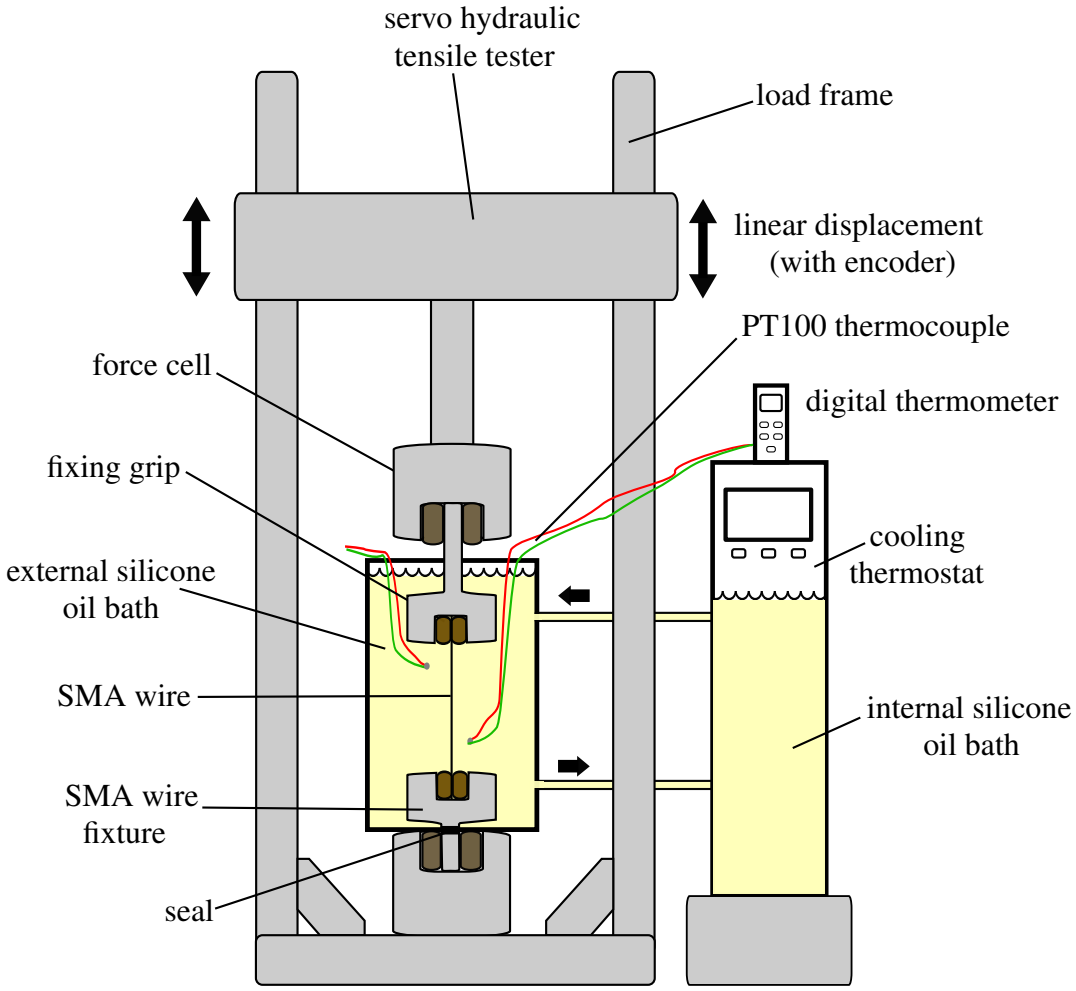

Figure 5-1: *Experimental set-up for stress-strain tests at various temperatures*

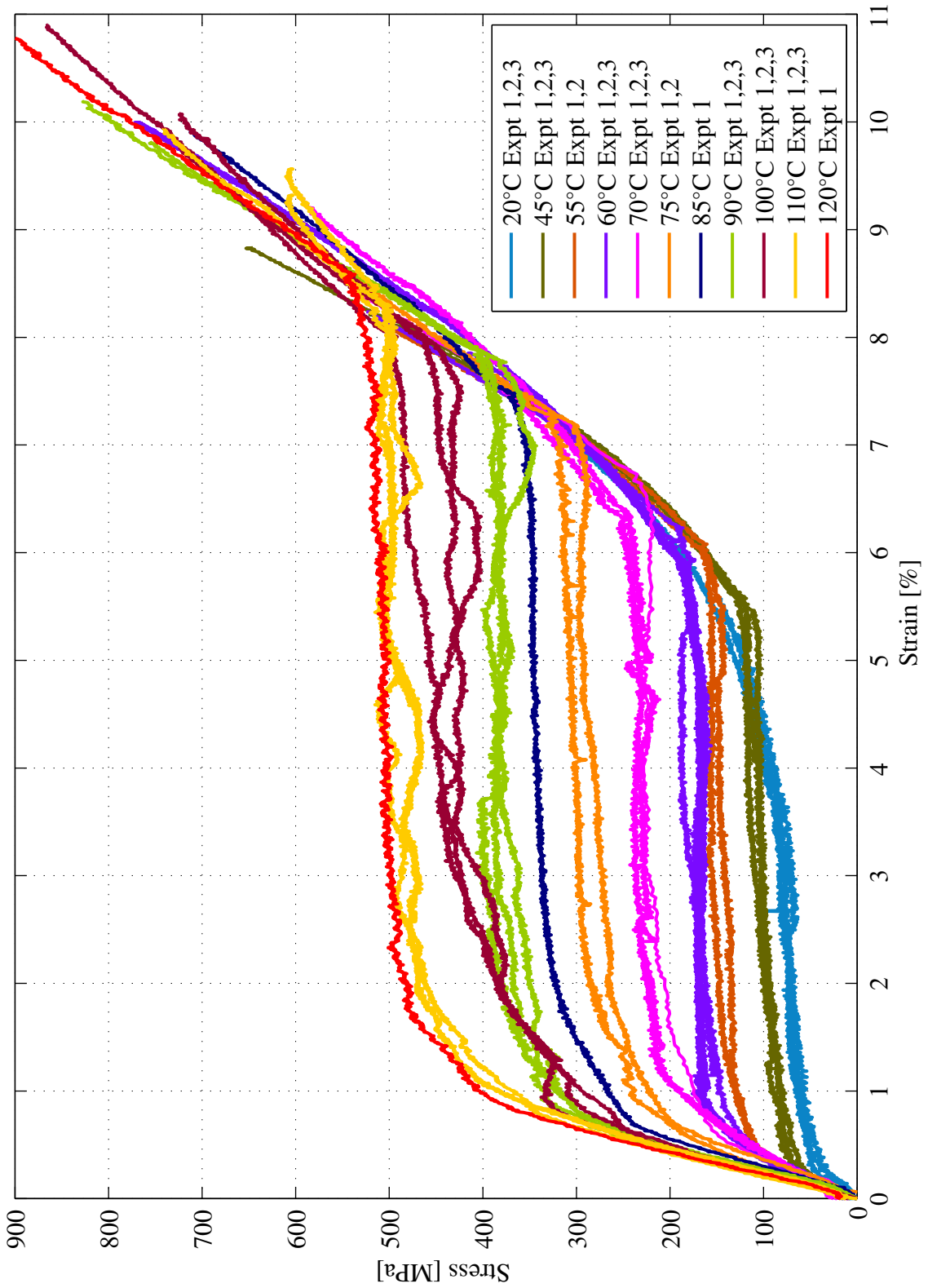

Figure 5-2: *SMA stress-strain behaviour at various temperatures*

5.2 Parallel Organisation of SMA Phases

In order to model the behaviour observed in Fig. 5-2, the volume fraction of thermal martensite ξ_T is utilised to quantify the crystallographic composition of the SMA at a given temperature, at no load and no strain. (The subscript 'T' in ξ_T signifies thermally induced martensite as opposed to mechanically induced martensite ξ_S.) $\xi_T = 0$ corresponds to 100% austenite ($T > A_f$, the red curve at 120°C in Fig. 5-2) and $\xi_T = 1$ corresponds to 100% martensite ($T < M_f$, the blue curve at 20°C in Fig. 5-2). This is shown exemplary red and blue boxes in Fig. 5-3(a) and (b).

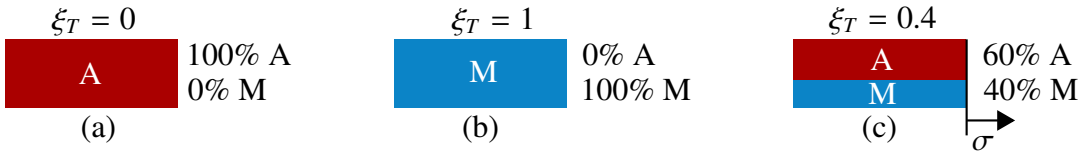

Figure 5-3: *Parallel organisation of martensite and austenite phases in SMA*

When the SMA is at an intermediate temperature between M_f and A_f, its crystallographic composition is a mixture of thermally induced martensite and austenite. It has been hypothesised in [ITH91], [Bri93], [Pai07] etc. that the two phases are organised in a parallel manner within the SMA as shown exemplary in Fig. 5-3(c) for $\xi_T = 0.4$.

The stress-strain behaviour is likewise hypothesised as a combination of the behaviours at 100% martensite and 100% austenite, weighted by martensite fraction ξ_T. To this end, the parameters required for the calculation of the stress-strain behaviour at this intermediate temperature are the austenite and martensite parameters, as shown in Fig. 5-4 and Fig. 5-5, where the subscripts 'a' and 'm' represent austenite and (twinned) martensite at no load, respectively.

The parameters for the unloading curve are appended with the superscript u. Note that $E_{1a} = E^u_{1a}$, $E_{3a} = E^u_{3a}$ and $E_{3m} = E^u_{3m}$ as shown in Chap. 4. Further, for $\xi_T = 1$, E^u_{1m}, E^u_{2m} and ε^u_{1m} are all set to 0 since these portions of the curve do not exist (cf. Fig. 4-7).

The second unloading knee $\varepsilon^u_{2a,m}$ is found by considering that unloading occurs elastically and the width of the hysteresis loop (cf. Sects. 4.5.1 and 4.6.1).

The residual strains are denoted by ε_{ra} and ε_{rm} and, as shown by the experimental data (cf. Chap. 4), 100% martensite shows considerable residual strain.

The following sections present the extension of the model to include the dependance of the stress-strain curve on temperature and the model validation. In Sect. 5.3, the modelling of the thermally induced martensite fraction ξ_T is presented, followed by the loading behaviour in Sect. 5.4, unloading behaviour in Sect. 5.5 and cyclical loading and unloading in Sects. 5.6.

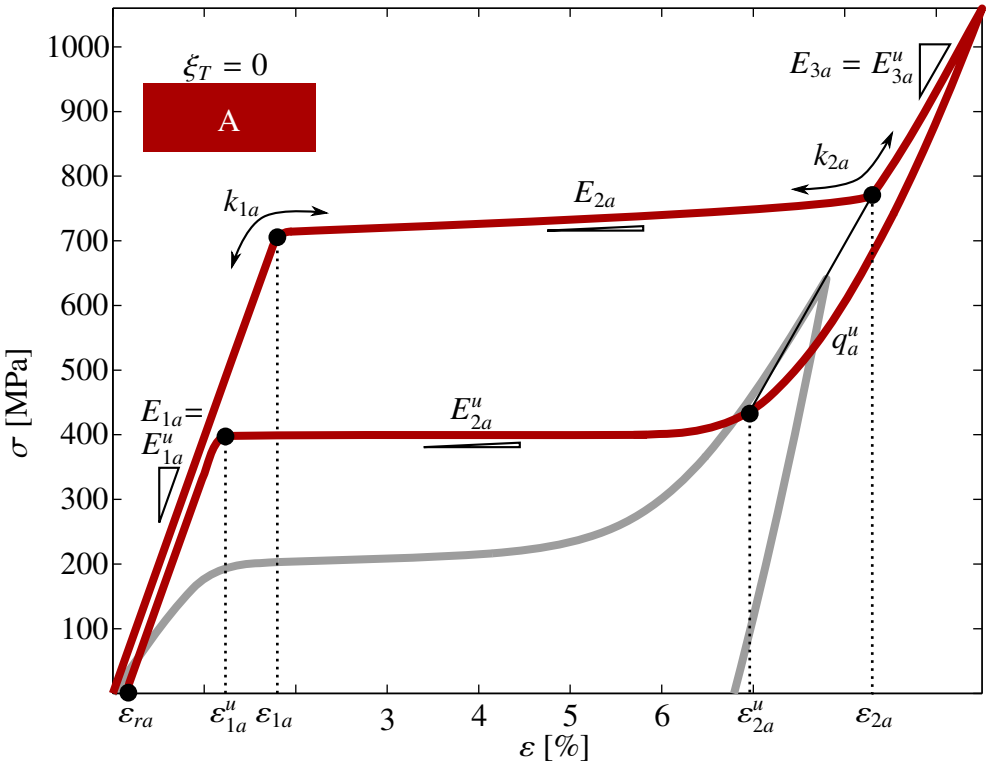

Figure 5-4: *Austenite parameters*

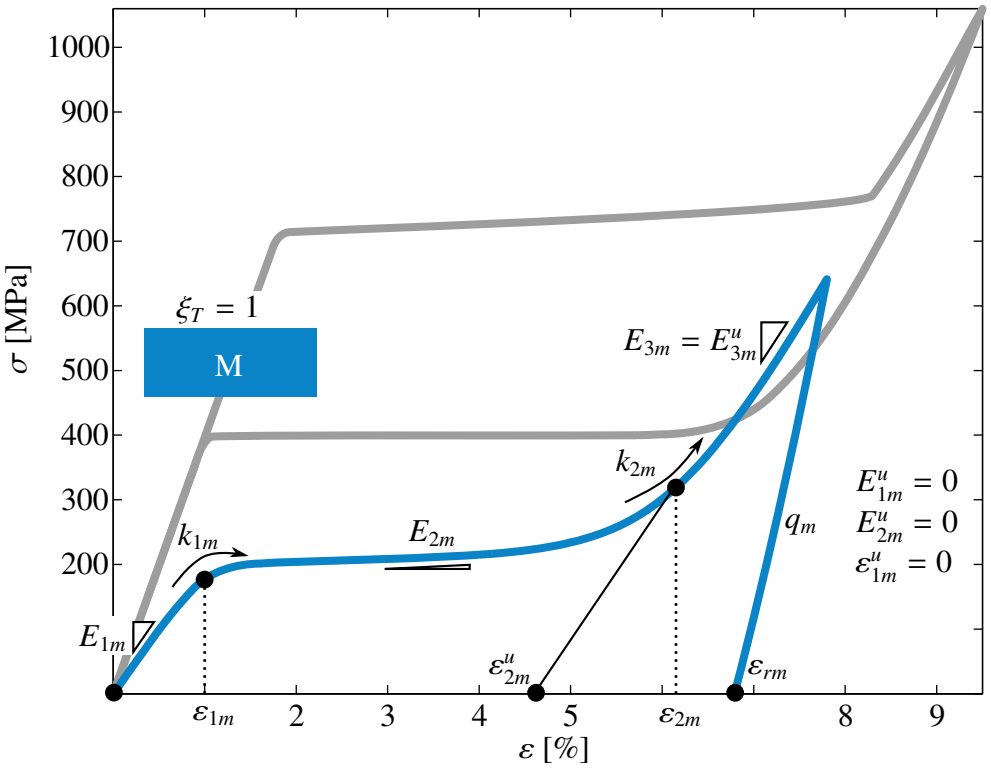

Figure 5-5: *Martensite parameters*

5.3 Modelling the Thermally Induced Martensite Fraction

This section describes the evolution of martensite from the thermal process which is therefore called thermally induced martensite. The relationship between thermally induced martensite and temperature is shown in Fig. 5-6, where A_s^o and A_f^o are the austenite start and finish temperatures, respectively and M_s^o and M_f^o are the martensite start and finish temperatures, respectively, at no load.

For the experiments carried out in this section, the SMA wire was first monotonically heated to a particular temperature at no load and then as the temperature was held constant, the strain was increased. Therefore, ξ_T is calculated only with the heating curve model (red curve in Fig. 5-6) in (5-3)[1] which is a simplified version of the thermal hysteresis equation (6-6) in Sect. 6.1.

T_m is the temperature where the SMA is fully martensite. For the wires used in the experiments, it is the ambient temperature ($T_m = T_{amb} = 20°C$). β_o^H in (5-1) is the midpoint of the transformation temperatures A_s^o and A_f^o and k^H in (5-2) is the slope of the curve at β_o^H (see Fig. 5-6).

$$\beta_o^H = \frac{A_s^o + A_f^o}{2} \tag{5-1}$$

$$k^H = \frac{1}{A_f^o - A_s^o} \tag{5-2}$$

$$\xi_T(T) = \frac{1 + e^{k^H(T_m - \beta_o^H)}}{1 + e^{k^H(T - \beta_o^H)}} \tag{5-3}$$

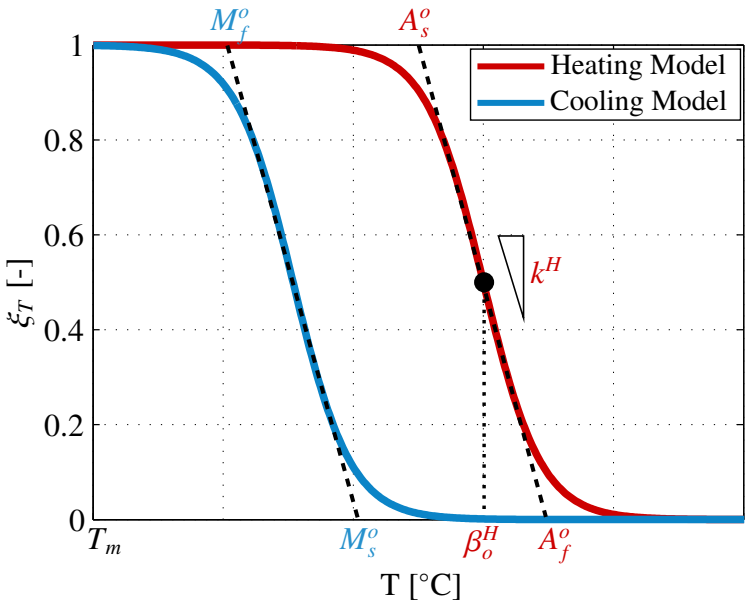

Figure 5-6: *Thermal hysteresis curve with model parameters*

[1] Note that for $T < T_m$, $\xi_T > 1$. However, using A_s^o and A_f^o from Tab. 5-1, this is negligible. Further, as the SMA is never cooled below T_m, ξ is always ≥ 1

5.4 Loading

As the SMA at intermediate temperatures is a combination of the martensitic and austenitic phases, the stress-strain loading behaviour will be in between the characteristic martensite and austenite stress-strain curves in Fig. 5-2 as shown schematically by the green curve in Fig. 5-7. The parameters that need to be calculated to describe the green curve are $E_1, E_2, E_3, \varepsilon_1, \varepsilon_2, k_1, k_2$.

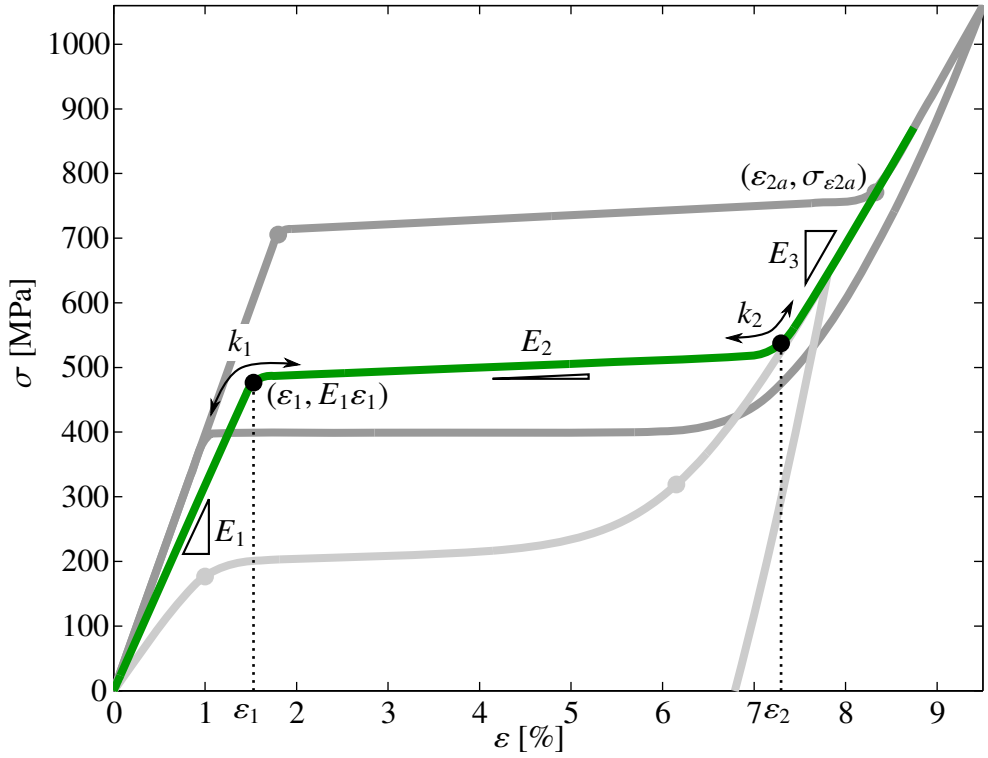

Figure 5-7: *SMA stress-strain loading behaviour at an intermediate temperature*

The third modulus, E_3, is trivially calculated when considering the following: On starting with 100% twinned martensite with a monoclinic crystalline structure, loading beyond the 2^{nd} knee ε_{2m} causes a complete conversion to detwinned martensite with an oriented crystalline structure. On starting with 100% austenite with a body centred cubic structure, loading beyond ε_{2a} causes a complete conversion to stress induced martensite, also with an oriented crystalline structure. Therefore, regardless of the temperature of the SMA, or the phases present at the origin (0% strain and 0 MPa stress), loading beyond the second knee causes the formation of oriented martensite, with identical moduli i.e. $E_{3a} = E_{3m} = E_3$. This phenomenon is observed in Fig. 5-2, where at high strains, the stress-strain behaviour follows the same slope regardless of the temperature.

Using ξ_T from (5-3) and the hypothesis that the phases are arranged in a parallel manner, the required parameters are calculated using a weighted sum of the austenite and martensite parameters as shown in (5-4) for all parameters except ε_2. Note that since $E_{3a} = E_{3m} = E_3$, the value of E_3, can also be calculated with (5-4).

ε_2 is then calculated using (5-5) as the intersection of the line going through $(\varepsilon_{2a}, \sigma_{\varepsilon_{2a}})$ with slope E_3 and the line going through $(\varepsilon_1, E_1\varepsilon_1)$ with slope E_2, as shown by the green

curve in Fig. 5-7. The new parameters are then used in (4-5) to calculate the stress-strain behaviour at the particular temperature.

$$\begin{bmatrix} E_1 \\ E_2 \\ E_3 \\ \varepsilon_1 \\ k_1 \\ k_2 \end{bmatrix} = \xi_T \begin{bmatrix} E_{1m} \\ E_{2m} \\ E_{3m} \\ \varepsilon_{1m} \\ k_{1m} \\ k_{2m} \end{bmatrix} + (1 - \xi_T) \begin{bmatrix} E_{1a} \\ E_{2a} \\ E_{3a} \\ \varepsilon_{1a} \\ k_{1a} \\ k_{2a} \end{bmatrix} \tag{5-4}$$

$$\varepsilon_2 = \frac{E_3 \varepsilon_{2a} - \sigma_{\varepsilon_{2a}} + (E_1 - E_2)\varepsilon_1}{E_3 - E_2} \tag{5-5}$$

In order to validate the model for loading for arbitrary temperatures, note that the parameters required are only the 100% austenite and 100% (twinned) martensite parameters. These parameters are easily identified using the procedure in Sect. 4.3 from the experiments at 120°C and 20°C, respectively, giving the values in Tab. 5-1. Note that the values of E_2 are the same for both phases and that the modulus of twinned, detwinned martensite and SIM (E_1 and E_3) are also identical. The fact that k_1 for martensite and k_2 for austenite are identical is coincidental. Additionally, the parameters E_2^u and ε_1^u are needed for the unloading behaviour presented in Sect. 5.5.

Using the parameters in Tab. 5-1[2], the parameters for the intermediate temperatures are calculated using (5-4) and (5-5). The stress-strain behaviour at the respective temperature is then calculated with (4-5). The results are shown in Fig. 5-8 with the grey curves for the temperatures from 20°C to 120°C and show excellent correlation with experimental data with RMS errors and normalised RMS errors (NRMSE) of the model and experiment shown in Tab. 5-2. Discrepancies exist for 85°C and 100°C, where k_1 from the model is higher than observed in the experiments. Note that the figure includes experimental data from various experiments to show repeatability of the data.

Table 5-1: *Model parameters identified from monotonic experiments*

	E_1	E_2	E_3	ε_1	ε_2	k_1	k_2	E_2^u	ε_1^u	A_s^o	A_f^o
	GPa	*GPa*	*GPa*	*%*	*%*	*–*	*–*	*GPa*	*%*	*°C*	*°C*
Austenite	50	0.5	17	1.05	8.85	430	780	1.6	1.25	58	78
Martensite	17	0.5	17	0.25	6.5	780	100	0	0		

Table 5-2: *RMSE and NRMSE between experiments and model for monotonic loading*

T [°C]	20	45	55	60	70	75	85	90	100	110	120
RMSE [MPa]	10.6	15.8	12.2	11.2	21.8	14.6	21.7	15.1	30.1	17.6	7.2
NRMSE [%]	6	2.8	2.4	2.0	4.3	2.6	3.0	2.2	3.9	2.7	0.8

[2]See Sect. 6.6 for the derivation of the transformation temperature A_s^o and A_f^o from the SMA datasheet.

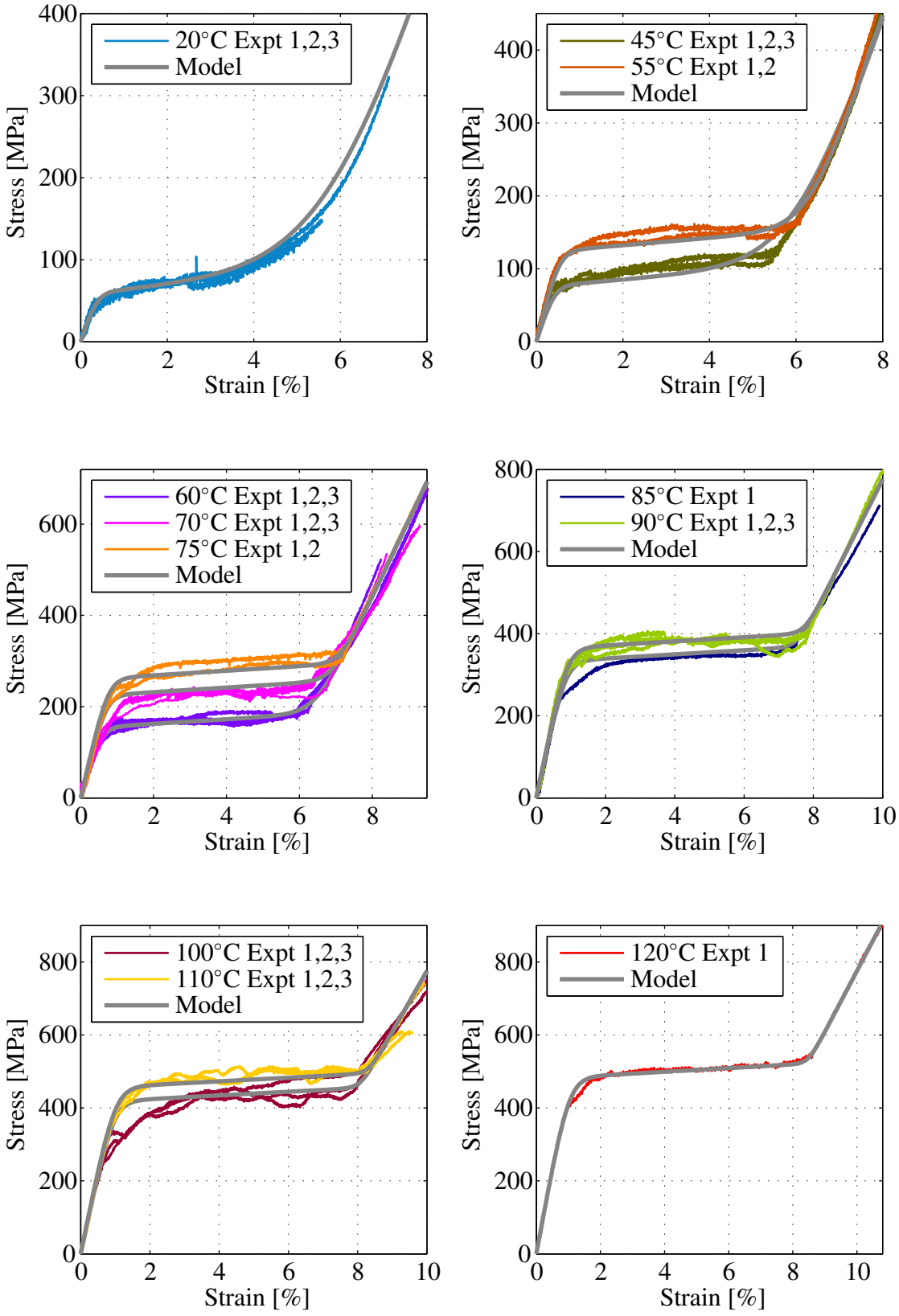

Figure 5-8: *Experiment and model for monotonic loading for* 20°C *to* 120°C

5.5 Unloading

Unloading behaviour requires the parameters as shown in Fig. 5-9.

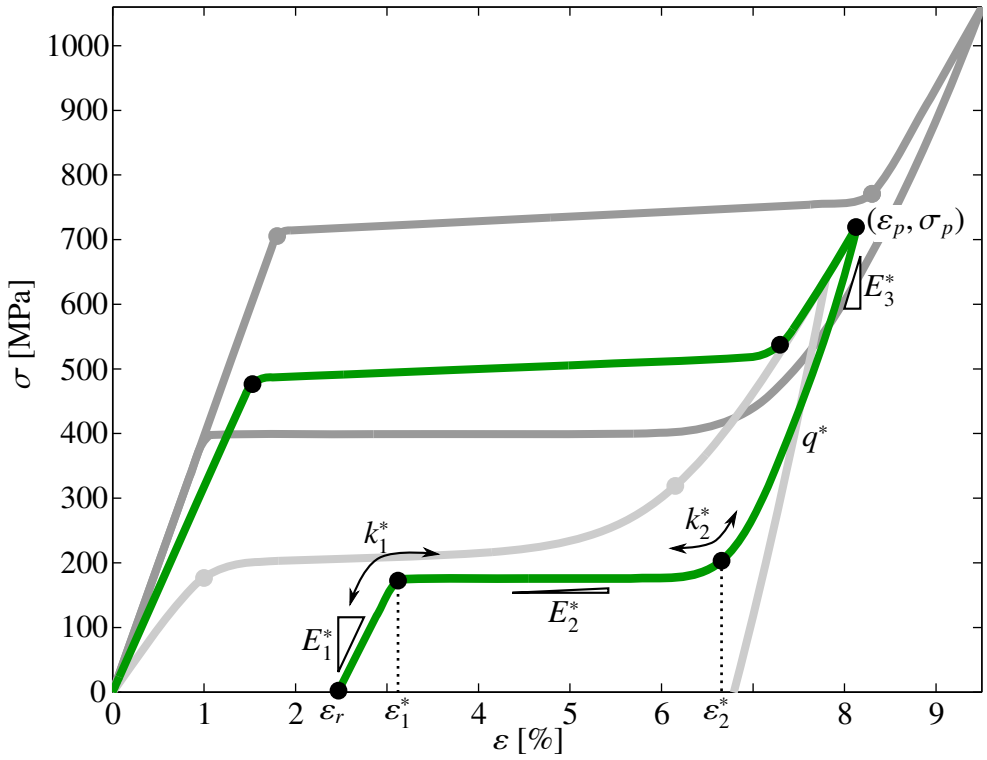

Figure 5-9: *SMA stress-strain unloading behaviour at an intermediate temperature*

To calculate the required stress-strain unloading behaviour, the equations presented in Sect. 4.5.1 are used with new parameters based on the temperature. Recall that the unloading parameters, which are recalculated during the model update process, are denoted with the superscript * and are based on $(\varepsilon_p, \sigma_p)$, which is the point of unloading.

The temperature dependence first affects the parameters, E_1, E_2, E_3, ε_1^u, which are subsequently used to calculate the * parameters. Similar to the loading case, they are calculated as the weighted sum of the austenite and twinned martensite values (see Tab. 5-4 and Figs. 5-4 and 5-5) using the identified parameters in Tab. 5-3. Recall (from Sect. 4.3) that E_{2a}^u and ε_{1a}^u need to be identified from experimental data of the austenite unloading curve.

Table 5-3: *Model parameters for unloading*

Austenite				Martensite			
E_{1a}^u	E_{2a}^u	E_{3a}^u	ε_{1a}^u	E_{1m}^u	E_{2m}^u	E_{3m}^u	ε_{1m}^u
E_{1a}	E_{2a}^u	E_{3a}	ε_{1a}^u	0	0	E_{3m}	0

Using the parameters in (5-4) and (5-5), the updated parameters are calculated as follows:

Table 5-4: *Model parameter calculation for unloading at intermediate temperatures*

Parameter	Value and Description
E_1^*	$E_1^* = \xi_T E_{1m}^u + (1-\xi_T)E_{1a}^u$ Weighted sum of austenite and twinned martensite values
E_2^*	$E_2^* = \xi_T E_{2m}^u + (1-\xi_T)E_{2a}^u$ Weighted sum of austenite and twinned martensite values
E_3^*	E_3^* is calculated with (4-20) using E_1^*, E_3 (recall that $E_3 = E_{3a} = E_{3m}$), where ξ_S^p is calculated using $\varepsilon_1, \varepsilon_2$ from (5-4) and (5-5). $E_3^* = (1-\xi_S^p)E_1^* + \xi_S^p E_3$ (4-20)
ε_1^*	ε_1^* is calculated identically to (4-21) for austenite unloading (see Tab. 4-2), using ε_r from (5-6), which is identical in form to (4-19), except for the factor +0.8, which is set empirically from experimental data. $\varepsilon_1^* = \frac{1}{k_1^*}\ln\left(\frac{e^{k_1^*\varepsilon_p} - e^{-k_1^*\left(\frac{\sigma_3+\sigma_2+\sigma_q}{E_1^*-E_2^*}+\varepsilon_p\right)}}{e^{-k_1^*\left(\frac{\sigma_3+\sigma_2+\sigma_q}{E_1^*-E_2^*}+\varepsilon_p-\varepsilon_r\right)}-1}\right)$ (4-21) $\varepsilon_r = (0.37)(1-e^{-0.035(y/2-2)}) + 0.8$ (5-6)
ε_2^*	Identical to (4-23) for austenite unloading (see Tab. 4-2) using * parameters in this table. $\sigma_{\varepsilon_1}^* = E_1^*(\varepsilon_1^* - \varepsilon_r)$ (4-22) $\varepsilon_2^* = \frac{E_3^*\varepsilon_p - E_2^*\varepsilon_1^* - \sigma_p + \sigma_{\varepsilon_1^*}}{E_3^* - E_2^*}$ (4-23)
k_1^*	$k_1^* = \xi_T k_{1m} + (1-\xi_T)k_{1a}$ Identical to k_1 from (5-4) since its value does not change for unloading.

Continued on next page

Table 5-4 – *continued from previous page*

Parameter	Value and Description
k_2^*	k_2^* also uses the same equation as austenite unloading in (4-25). $$k_2^* = \frac{4q}{E_3^* - E_2^*} \quad (4\text{-}26)$$
q^*	q^* uses the same equation as austenite unloading in (4-25). $$q^* = \frac{(E_3 - E_2)\sqrt{\ln(2)}}{2(\varepsilon_p - \varepsilon_2)} \quad (4\text{-}25)$$

Using the identified parameters in Tab. 5-1 (which include the additional parameters E_2^u and ε_1^u necessary for modelling unloading behaviour), the results for monotonic loading and unloading are given for temperatures 20°C to 120°C in Fig. 5-10. Note that for clarity, only one experiment is shown.

The temperatures 20°C to 85°C show considerable residual strain, however, with increasing temperature the unloading curve is more 'curved'. The model and experiments show very good correlation (RMSE and NRMSE between model and experiment in Tab. 5-5). However, at 85°C, the model predicts less residual strain than the experimental data.

The temperatures, 90°C to 120°C show the characteristic stress-strain hysteresis loop (pseudoelasticity). This is due to the fact that at such high temperatures, significant austenite is in the material and the unloading behaviour starts to show strain recovery.

Table 5-5: *RMSE and NRMSE between experiments and model for monotonic unloading*

T [°C]	20	45	55	60	70	75	85	90	100	110	120
RMSE [MPa]	12.2	15.3	14.4	20.6	22.7	13.0	33.8	14.6	22.2	16.5	12.1
NRMSE [%]	4.2	3.7	2.8	3.3	3.9	3.3	5.2	2.6	3.0	2.1	1.1

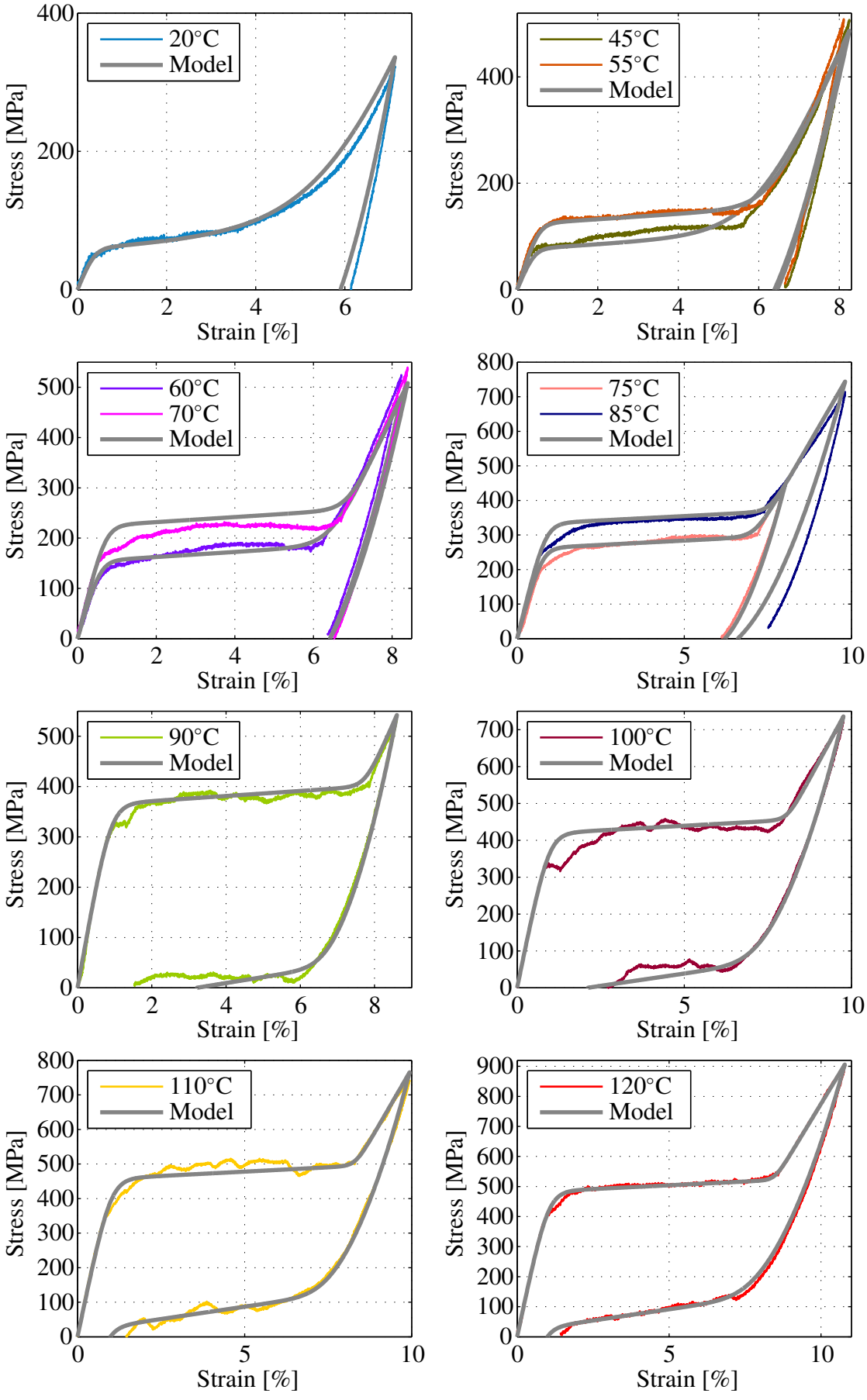

Figure 5-10: *Experiment, model for monotonic loading and unloading for* 20°C *to* 120°C

5.6 Cyclical Loading and Unloading

Experimental data has shown that the parameters for cyclical loading (or reloading) are mostly identical with the parameters in (5-4) with the exceptions of E_1^*, E_2^*, q^*, whose values are based on the temperature of the SMA.

For temperatures below the austenite start temperature A_s, the SMA is a combination of martensite with different crystallographic forms depending on the strain. The reloading behaviour is identical to Sect. 4.6.2.

For temperatures above A_s, where austenite forms in the SMA, the reloading behaviour is identical to Sect. 4.5.2. This includes the formation of steps in the plateau during cyclical loading.

For clarity, a summary of the required equations is in Tab. 5-6.

Experimental data has shown that the parameters for cyclical unloading is also identical to monotonic unloading, and no further parameters need to be identified or calculated.

Table 5-6: *Model parameter calculation for austenite complete and partial reloading*

reloading	E_1^*	E_2^*	E_3^*	ε_1^*	ε_2^*	k_1^*	k_2^*	q^*	σ_s^n
$T > A_s$ (complete)	(4-27)	E_2	E_3	ε_1	ε_2	k_1	k_2	0	(4-31)
$T > A_s$ (partial)	(4-27)	(4-28)	E_3	(4-29)	ε_2	k_1	k_2	0	(4-31)
$T < A_s$	(4-27)	(4-28)	E_3	(4-29)	ε_2	k_1	k_2	(4-33)	0

The experiment and model for cyclical loading and unloading are shown for 45°C to 80°C in Fig. 5-11[3] and from 90°C to 120°C is shown in Fig. 5-12.

For temperatures under 90°C, the experiments show increasing values of residual strain and minor hysteresis loops with every cycle. The model shows reasonable correlation to experimental data with RMSE and NRMSE in Tab. 5-7.

For temperatures higher than 90°C, the input strain (in the top left plot of Fig. 5-12) also causes the formation of minor hysteresis loops. However, since considerable austenite is present in the SMA at these temperatures, the minor loops are much wider. The model shows good correlation with the experiment, except for the final unloading sequence. Here in all three temperatures, the unloading behaviour after loading beyond the second knee has a modulus that is much lower than what the model predicts. Unloading and reloading within the plateau seems to cause shifts in the crystalline structure and therefore a much lower modulus is observed. Nevertheless, the RMSE and NRMSE in Tab. 5-7 show that the correlation is reasonable.

[3]The data for temperature higher than 80°C are not shown here because they are too crowded to distinguish individual loops. For clarity, the higher temperatures use fewer cycles (see Fig. 5-12)

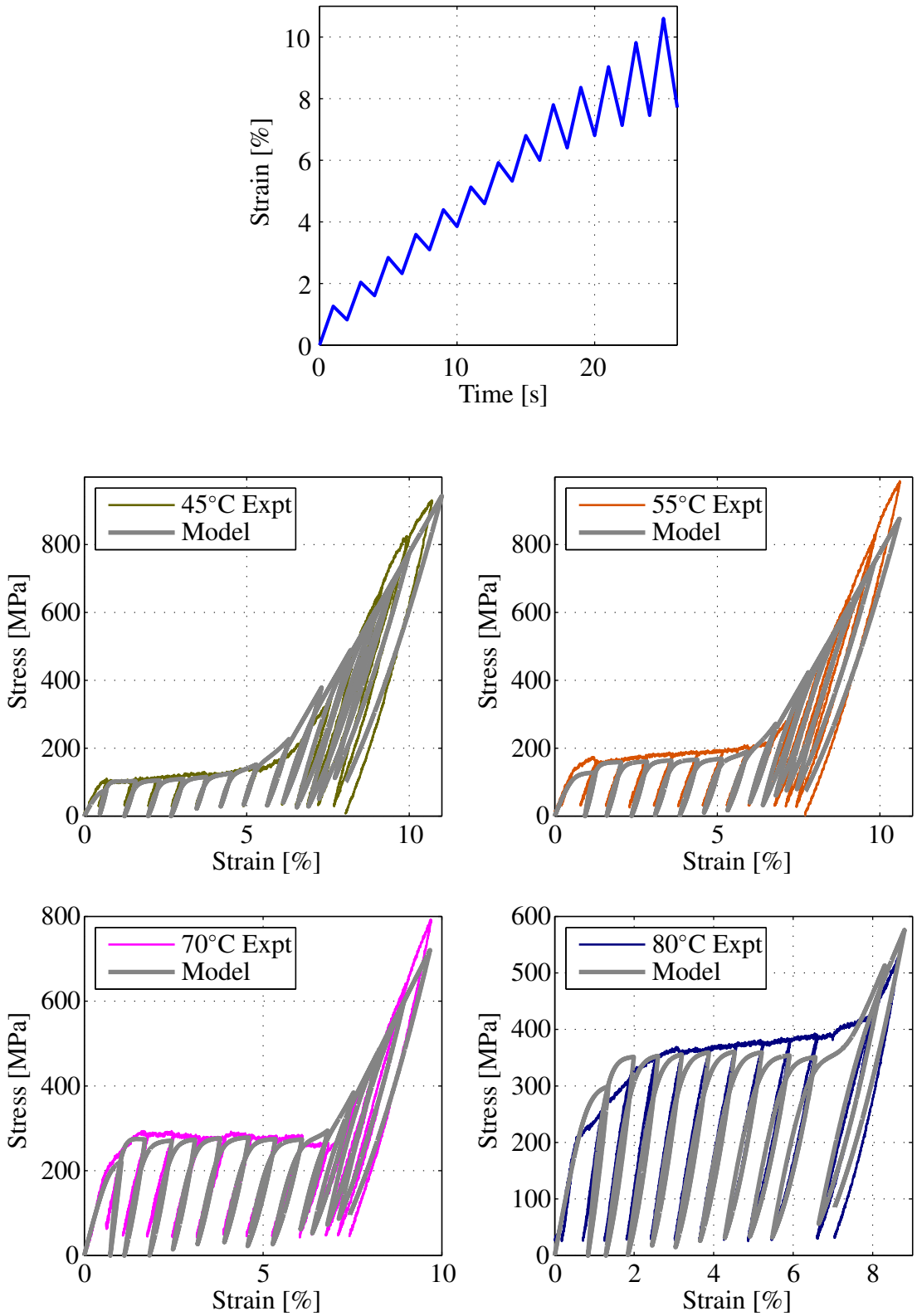

Figure 5-11: *Experiment and model for cyclical loading and unloading (minor loops) for temperatures from* 45°C *to* 80°C *with input strain in top plot*

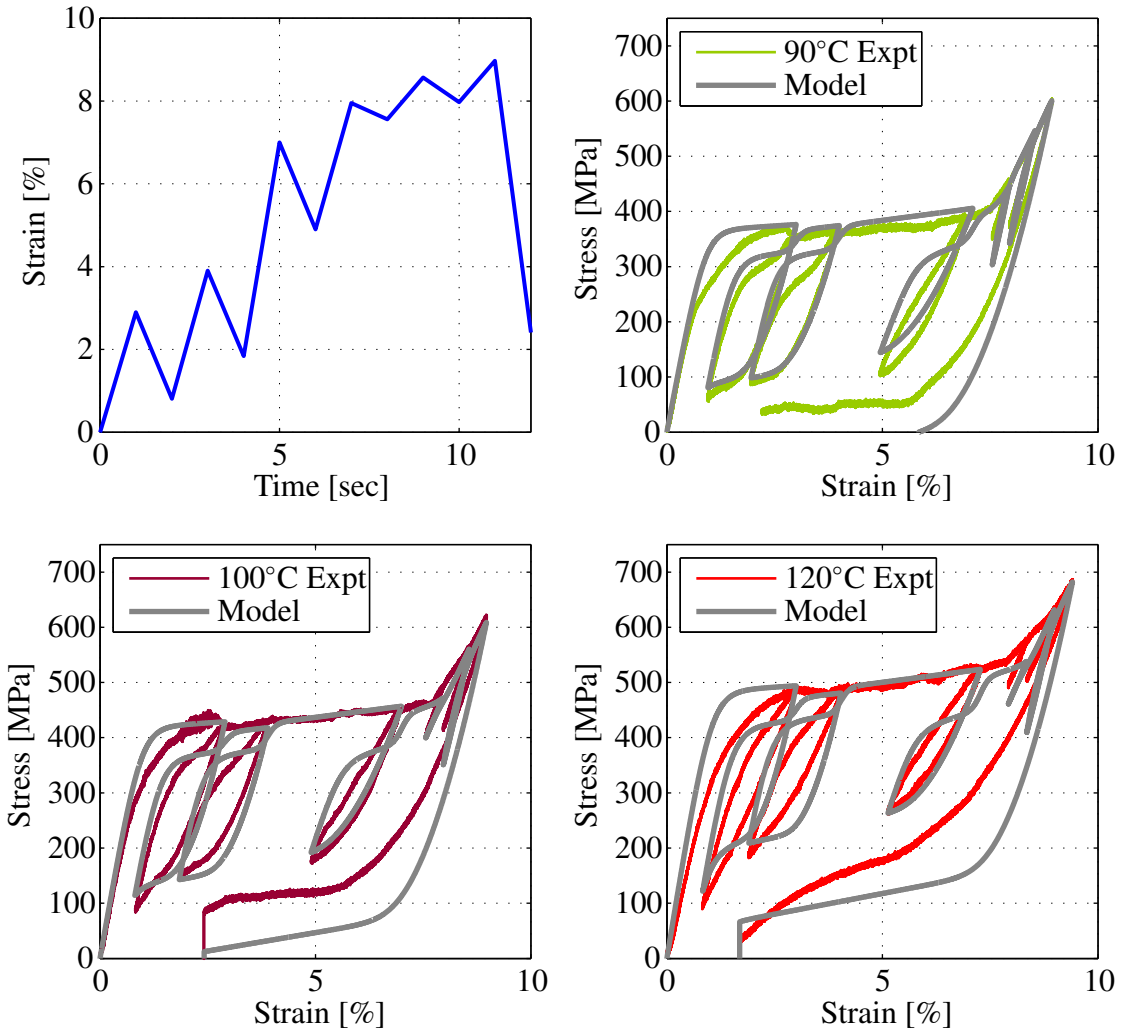

Figure 5-12: *Experiment and model for cyclical loading and unloading (minor loops) for temperatures from* 90°C *to* 120°C *with input strain in top left plot*

Table 5-7: *RMSE and NRMSE between experiments and model for cyclical loading and unloading*

T [°C]	45	55	70	80	90	100	120
RMSE [MPa]	16.9	26.9	19	39	22.4	25.4	30.2
NRMSE [%]	2.7	3.1	4.4	6.3	5.2	5.9	6.6

5.7 Summary

In this section, the constitutive model from Chap. 4 is extended in order to model the stress-strain behaviour of SMAs regardless of the temperature. The SMA at these intermediate temperatures consist of a combination of austenite and martensite.

The constitutive model is extended by combining the stress-strain behaviours when the SMA, at no load, is either purely martensite or purely austenite. The combination is based on the volume fraction of martensite present at a given temperature, and the hypothesis that the phases in the SMA are arranged in a parallel manner.

The model can be used to predict the stress-strain behaviour of SMAs subjected to arbitrary loading and unloading cycles provided that the temperature during the duration of the experiment remains constant.

As the structure of the model is the same as presented in Chap. 4, it is continuous and differentiable and no extra parameters for the same batch of wires need to be identified. Additionally, phenomena such as the quadratic loci for martensitic unloading and reloading behaviour, build up of residual strain with decreasing temperature, formation of steps in the plateau and minor hysteresis loops are also inherited. The model was validated using experimental data from various wires and showed good correlation with measured behaviour. The next section presents the modelling of the phase kinetic behaviour of SMAs.

6 Phase Kinetics Model

This chapter presents a novel SMA phase kinetics phenomenological model to describe the evolution of the phases in the SMA due to temperature hysteresis with and without mechanical loading. The phase kinetics behaviour is quantified using the normalised strain in the SMA, which is proportional to the volume fraction of martensite present in the material. Recall from Sects. 2.4 and 2.5, that the martensite fraction, however, is separated into thermally induced martensite ξ_T and mechanically induced martensite ξ_S. Thermally induced martensite is formed, as the name suggests, from temperature influences on the SMA lattice structure and is presented in Sect. 6.1. Mechanically induced martensite is formed as the stress/strain in the SMA is increased, as shown in detail in the Sect. 6.4. The total martensite fraction is then presented in Sect. 6.5.
The model can be used for arbitrary heating-cooling cycles irrespective of the phases present. The modelling equations and algorithm are presented in Sects. 6.2 and 6.3. Thermal experiments at various loads are subsequently used for validation as shown in Sect. 6.6.

6.1 Thermal Hysteresis Modelling

This section describes the evolution of martensite from the thermal process and is therefore called thermally induced martensite. The relationship between thermally induced martensite and temperature is shown in Fig. 6-1, where A_s and A_f are the austenite start and finish temperatures, respectively and M_s and M_f are the martensite start and finish temperatures, respectively.

The modelling of this characteristic thermal hysteresis in SMAs is taken from [MW98], [PG06], [Pai07] and is shown in (6-6), where ξ_T^H describes the heating curve (red curve in Fig. 6-1) and ξ_T^C describes the cooling curve (blue curve in Fig. 6-1)[1].

T_m is the temperature where the SMA is fully martensite. For the wires used in the experiments in Chaps. 4 and 5, it is the ambient temperature, therefore $T_m = T_{amb} = 20°\text{C}$.

Variables $\alpha_T^a(T)$ and $\gamma_T(T)$ are temperature dependant piecewise continuous functions with values between 0 and 1, inclusive. They are initialised at $\alpha_T^a(T_m) = 1$ and $\gamma_T(T_m) = 0$ to describe the hystereis from 1 to 0.[2].

β_o^H and β_o^C in (6-1) and (6-2), respectively, are the midpoints of the transformation temperatures M_s^o, M_f^o, A_s^o and A_f^o at no load (stress = 0 MPa). As mentioned in Chap. 2, increasing the load on the SMA causes an increase of the transformation temperatures. Consequently, the hysteresis shifts to the right with increasing load. This shift is linear [Lag08], [Pai07] with slope c_m [K/Pa] and is modelled by introducing a stress dependency to β as shown in (6-3).

$k^{H,C}$ in (6-4) and (6-5) are the slopes of the curves at $\beta^{H,C}$, as shown in Fig. 6-1.

[1] The superscripts H and C signify heating and cooling.
[2] This defines the major loop. For the minor loops, $\alpha_T^a(T)$ and $\gamma_T(T)$ take on different values as shown in Sect. 6.2 and Tab. 6-1.

Note that in addition to T_m and the load σ, which are known, the only parameters required for the model are the four transformation temperatures at no load, and c_m. They are typically standard values that are part of the SMA data sheet from the supplier.

$$\beta_o^H = \frac{A_s^o + A_f^o}{2} \tag{6-1}$$

$$\beta_o^C = \frac{M_s^o + M_f^o}{2} \tag{6-2}$$

$$\beta^{H,C}(\sigma) = \beta_o^{H,C} + c_m\sigma \tag{6-3}$$

$$k^H = \frac{1}{A_f^o - A_s^o} \tag{6-4}$$

$$k^C = \frac{1}{M_s^o - M_f^o} \tag{6-5}$$

$$\xi_T^{H,C}(T) = \frac{\overbrace{\alpha_T^{aH,C}(T)(1 + e^{k^{H,C}(T_m - \beta^{H,C}(\sigma))})}^{\alpha_T^{H,C}}}{1 + e^{k^{H,C}(T - \beta^{H,C}(\sigma))}} + \gamma_T^{H,C}(T) \tag{6-6}$$

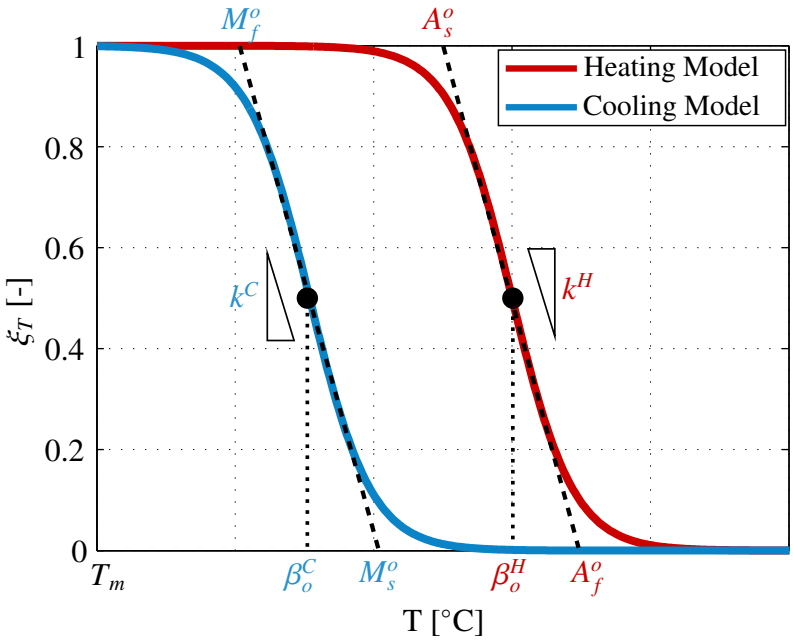

Figure 6-1: *Thermal hysteresis curve with model parameters*

6.2 Modelling of Minor Loops

The hysteresis loop defining the martensite fraction in Fig. 6-1 spans from a minimum of 0 to a maximum of 1. This loop is called the '*major loop*'. In SMAs, however, so called '*minor loops*', which have a maximum less than 1 and a minimum greater than 0 can also form. To fully model the phase kinetic behaviour, it is imperative to model these minor loops. In ξ_T from (6-6), the modelling of either major or minor loops is based on the parameters α^a and γ (the superscripts H and C are omitted for simplicity).
Generally, α^a represents the 'height' (maximum - minimum) of the hysteresis and γ represents the offset. Additionally $0 \leq \alpha^a + \gamma \leq 1$ has to hold. In Fig. 6-2, three curves with various heights and offsets are shown, with their α^a and γ parameters in Tab. 6-1.

Table 6-1: *Parameters for major and minor loops*

Curve colour (Fig. 6-2)	Curve height α^a	Curve offset γ	Loop type
grey	1	0	major
purple	0.4	0	minor
grey	0.4	0.6	minor

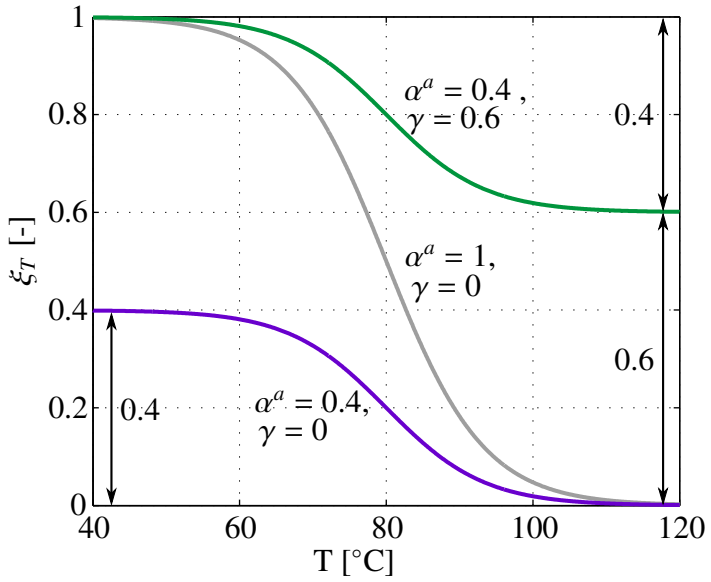

Figure 6-2: *Parameters for minor loop modelling*

6.3 Modelling Algorithm

The first step in the algorithm is the **initialisation**, where at $t = 0$, $T = T_m$ and it is assumed that the wire is fully martensite ($\xi_T = 1$). Therefore the variables in (6-8) for the major loop are set in (6-6). From this starting point, the SMA can be heated as shown in Fig. 6-3(a), where the heating curve (red curve), described by $\xi_T^H(T, \sigma)$ follows the heating curve of

the hysteresis major loop (grey curve). This is regarded as **monotonic heating** and the variables in (6-9) are used.

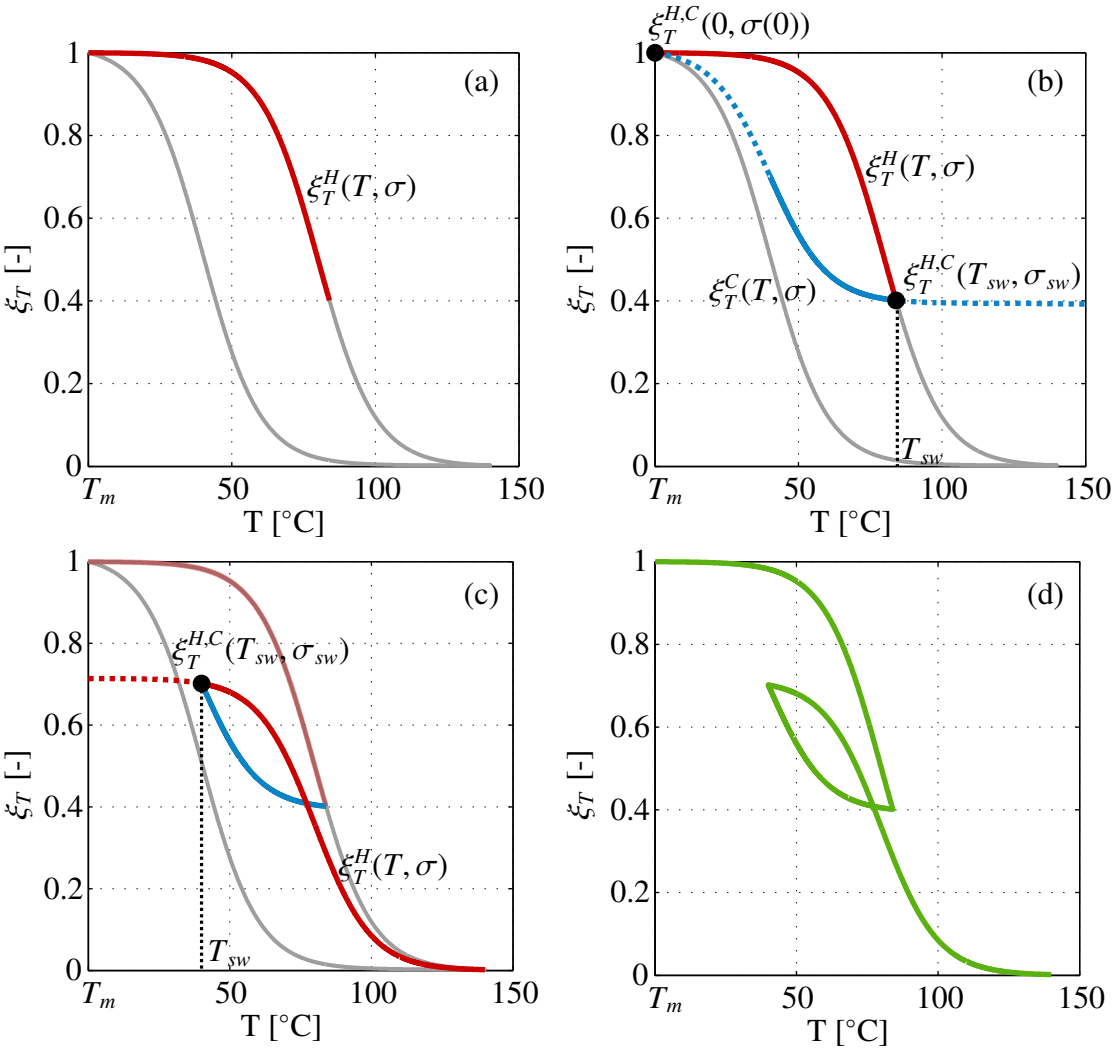

Figure 6-3: *Algorithm for calculation of martensite fraction*

Consider, that the temperature increases until a certain temperature, T_{sw}, before ξ_T is 0, at which the temperature profile changes from increasing to decreasing. Let the stress at this 'switching point' be σ_{sw}. When the temperature changes direction, so does ξ_T since input reversal causes immediate output reversal [Pai07]. The SMA now has to follow a minor cooling curve shown as the dotted curve in Fig. 6-3(b). In order to define this minor cooling curve, its α^a and γ values need to be determined. **Switching conditions** are used to provide two equations to solve for these two unknowns.

In order to ensure continuity in ξ_T, the value of the original heating curve, ξ_T^H, and the value of the subsequent cooling curve, ξ_T^C, must be identical at $T = T_{sw}$. This is called the *continuity condition*, shown mathematically in (6-7). In Fig. 6-3(b), it is observed that the major loop heating and cooling curve, and the minor loop cooling curve all originate at the same point, i.e. at $T = T_m$. This condition, called the *common origin condition* in (6-7), must be satisfied since the SMA major loop is closed. These conditions are used to update the values of α^a and γ according to (6-10) to give the solid blue curve in Fig. 6-3(b).

Consider now that before the temperature reduces down to T_m, the temperature profile switches from cooling to heating at certain temperature, T_{sw}. The material will now follow a minor heating curve as shown by the red dotted curve in Fig. 6-3(c). Similarly to the cooling case, the α^a and γ values need to be determined to define this minor heating curve. The continuity condition still holds at the switching point. However, as $T \to \infty$, it is observed that the major loop heating and cooling curve and the minor loop heating curve all terminate at the same point. This is called the *common limit condition*, written mathematically in (6-7). The continuity and common limit conditions are used to find the parameters for the minor heating curve ξ_T^H as shown in (6-11) and by the red minor heating curve in Fig. 6-3(c). The complete hysteresis curve for the temperature profile described above is in Fig. 6-3(d).

$$\begin{aligned}
&\text{Continuity} \quad : \quad \xi_T^C(T_{sw}, \sigma_{sw}) = \xi_T^H(T_{sw}, \sigma_{sw}) \\
&\text{Common Origin} \quad : \quad \xi_T^C(T_m, \sigma_{sw})\Big|_{\substack{\alpha_T^{aC} = \alpha_T^{aC}(T_{sw}) \\ \gamma = \gamma(T_{sw})}} = \xi_T^{H,C}(T_m, \sigma)\Big|_{\substack{\alpha_T^a = \alpha_T^a(T_m) = 1 \\ \gamma = \gamma(T_m) = 0}} \\
&\text{Common Limit} \quad : \quad \lim_{T\to\infty} \xi_T^H(T, \sigma_{sw})\Big|_{\substack{\alpha_T^{aH} = \alpha_T^{aH}(T_{sw}) \\ \gamma = \gamma(T_{sw})}} = \lim_{T\to\infty} \xi_T^{H,C}(T, \sigma)\Big|_{\substack{\alpha_T^a = \alpha_T^a(T_m) = 1 \\ \gamma = \gamma(T_m) = 0}}
\end{aligned} \tag{6-7}$$

Initial conditions

$$\begin{aligned}
\alpha_T^{aH}(T_m) &= 1 \\
\alpha_T^{H,C}(T_m) &= \alpha_T^{aH}(T_m)(1 + e^{k^H(T_m - \beta^H(\sigma))}) \\
\gamma_T^{H,C}(T_m) &= 0
\end{aligned} \tag{6-8}$$

Monotonic heating or cooling When either monotonically heating or cooling, $\alpha_T^{aH,C}$ and $\gamma^{H,C}$ retain their previous values. Therefore, at $t = 0$, α_T^{aH} and γ values are those set by the initial conditions (6-8).

$$\begin{aligned}
\alpha_T^{H,C}(T) &= 1 + e^{k^H(T_m - \beta^H(\sigma))} \\
\gamma_T^{H,C}(T) &= 0
\end{aligned} \tag{6-9}$$

Switching: heating to cooling Using T_{sw}^-, T_{sw}^+ and σ_{sw}^-, σ_{sw}^+ to specify the temperature and stress at instants before and after switching, respectively, the updated values are as follows (derivation is in Appendix A1.6):

$$\begin{aligned}
\alpha_T^{aH}(T_{sw}^+) &= (\xi_T^H(T_{sw}^-, \sigma_{sw}^-) - 1)\left[\frac{1 + e^{k^C(T_{sw}^+ - \beta^C(\sigma_{sw}^+))}}{e^{k^C(T_m - \beta^C(\sigma_{sw}^+))} - e^{k^C(T_{sw}^+ - \beta^C(\sigma_{sw}^+))}}\right] \\
\alpha_T^C(T_{sw}^+) &= \alpha_T^{aH}(T_{sw}^+)(1 + e^{k^C(T_m - \beta^C(\sigma_{sw}^+))}) \\
\gamma_T^C(T_{sw}^+) &= 1 - \alpha_T^{aH}(t_{sw}^+)
\end{aligned} \tag{6-10}$$

Switching: cooling to heating Using the same nomenclature as above, the updated values are as follows (derivation is in Appendix A1.7):

$$\begin{aligned}
\gamma_T^H(T_{sw}^+) &= 0 \\
\alpha_T^H(T_{sw}^+) &= \xi_T^C(T_{sw}^-, \sigma_{sw}^-)(1 + e^{k^H(T_{sw}^+ - \beta^H(\sigma_{sw}^+))})
\end{aligned} \tag{6-11}$$

6.4 Mechanical Hysteresis Modelling

Recall from Sect. 2.4, that mechanically induced martensite ξ_S forms (or depletes) through the application (or removal) of stress[3]. In addition to this stress dependency, ξ_S also has a temperature dependency, as presented for the rest of this section.

Fig. 6-4(a) shows the stress-strain curves predicted by the stress-strain model from Chap. 5 for 7 temperatures $T = [20, 50, 60, 65, 70, 75, 120]°\text{C} + T_m$ (where $T_m = T_{amb} = 20\,°\text{C}$)[4]. Consider that the SMA is loaded with a stress σ of 200 MPa. This stress causes a strain of ε_m [%], as shown in Fig. 6-4(a) at ❶.When the wire is heated such that $T > A_f(\sigma)$, it will eventually contract to a strain of ε_a at ❼, while passing through strains ❷ to ❻ in Fig. 6-4. Plotting the strain against temperature yields the plot in Fig. 6-4(b). Normalising this plot by using the maximum and minimum strains i.e. ε_m and ε_a as the normalisation constants, as shown in (6-12), and plotting it against temperature produces Fig. 6-4(c).

$$\varepsilon_N = \frac{\varepsilon - \varepsilon_a}{\varepsilon_m - \varepsilon_a} \tag{6-12}$$

Recall from Sect. 4.4 that in a stress-strain curve, at constant temperature, ξ_S is 0 below the first knee, 1 after the second knee and linear in between (cf. Fig. 4-8), as in (4-15) (shown in (6-13) below for ease of reading), where the knees ε_1 and ε_2 are temperature dependant and computed with (5-4) and (5-5) from Sect. 5.4, respectively.

$$\xi_S(\varepsilon(T)) = \frac{1}{1 + e^{-\frac{16}{\varepsilon_2(T) - \varepsilon_1(T)}\left(\varepsilon - \frac{\varepsilon_2(T) + \varepsilon_1(T)}{2}\right)}} \tag{6-13}$$

Consider that at the start, the SMA at 40°C has a strain at ❶ that is well over the second knee for the $\sigma - \varepsilon$ curve at this temperature (blue curve in Fig. 6-4(a)) and therefore $\xi_S = 1$. When the temperature is increased to 80°C, the SMA contacts to ❸, which is close to the second knee of the 80°C-purple-curve. A slight increase of the temperature by only 5°C to 85°C, causes the strain to be well in the middle of the stress-strain plateau, (green 85°C-curve at ❹) and therefore the value of ξ_S, as expected, drops sharply after the second knee at ❸. Similarly, at ❺, the strain is close to the first knee (pink curve at 90°C), after which ξ_S tends to 0. The procedure above is repeated for stresses 250 MPa and 350 MPa as shown in Fig. 6-5, generating corresponding ε_N curves. The value of $\xi_S(\varepsilon)$ is plotted with the solid brown line in Fig. 6-4(c). It is found by computing the values of the knees ε_1 and ε_2 for every temperature $(T - T_m)$ at which the family of stress-strain curves in Fig. 6-4(a) was generated and then setting ε to the corresponding strain at $\sigma = 200$ MPa in (6-13). From Fig. 6-4(c), it is noticeable that $\xi_S(\varepsilon)$ calculated in this manner is almost identical to ε_N. The value of ξ_S therefore has not only a stress but also a temperature dependency, through the temperature dependency of the knees. In order to calculate temperature dependant ξ_S (or $\xi_S(T)$) using the aforementioned procedure, it is necessary to use the inverse of the stress-strain model from Chap. 5 to find the value of ε that coincides with the applied stress at the given temperature. While the inverse can be calculated (see Chap. 7), it is more computationally efficient to approximate $\xi_S(T)$ using a sigmoid function similar to the modelling of ξ_T in Sect. 6.1. $\xi_S(T)$ is approximated with (6-18)[5], where $\beta^{H,C}$ is calculated with (6-3).

[3] Depletion through the removal of stress occurs only at $T > A_s$

[4] This is necessary because of the definition of ξ_S in (6-18).

[5] Note that $\xi_S(T)$ has the same form as (6-6). Further, due to the fact that T_m appears in the exponential, it is added to the measured temperature to generate the family of curves in Figs. 6-4 and 6-5.

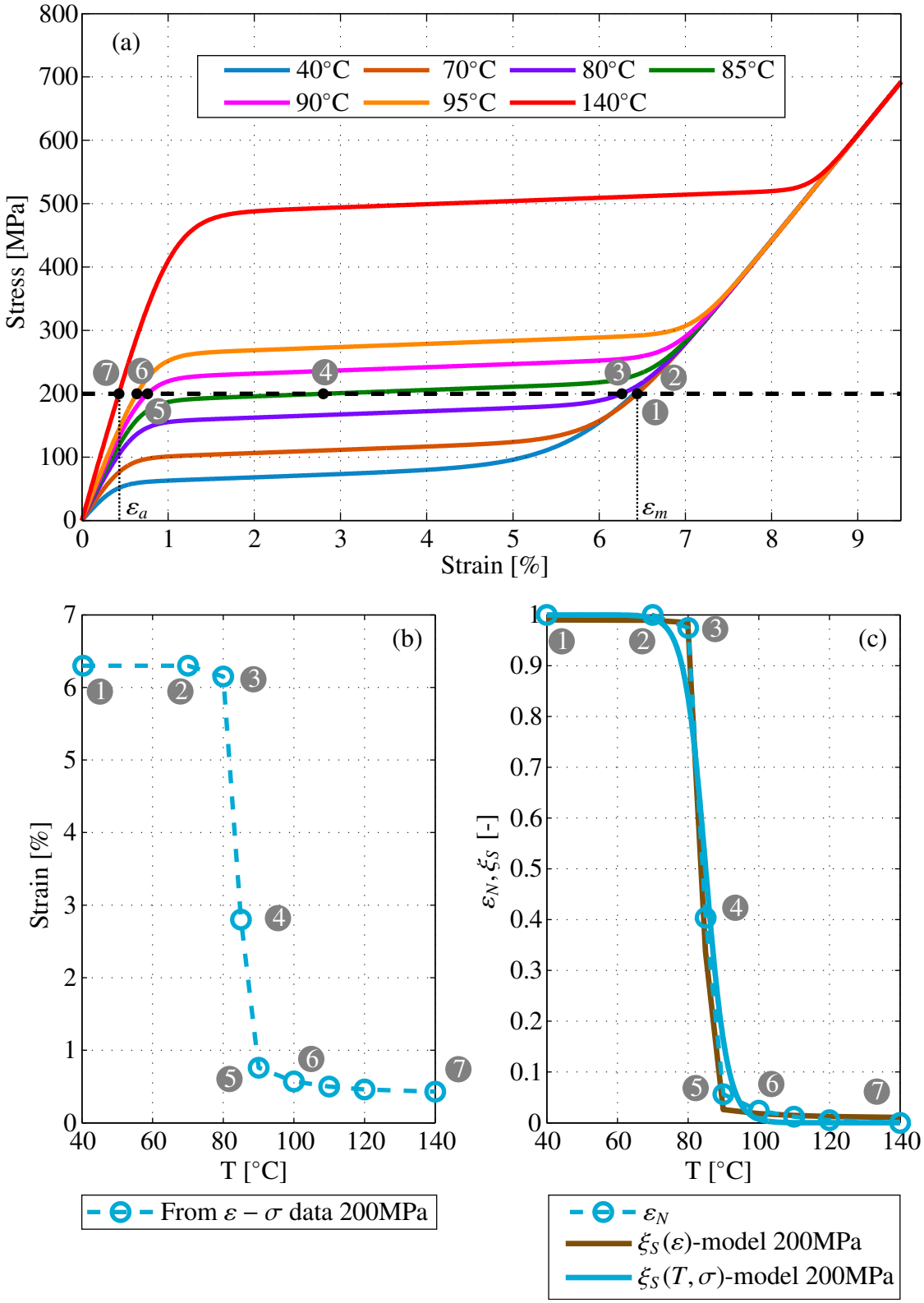

Figure 6-4: *Stress strain curves for temperatures over ambient from* 40 °C *to* 140 °C *and Strain and* ξ_S *versus temperature for 200 MPa*

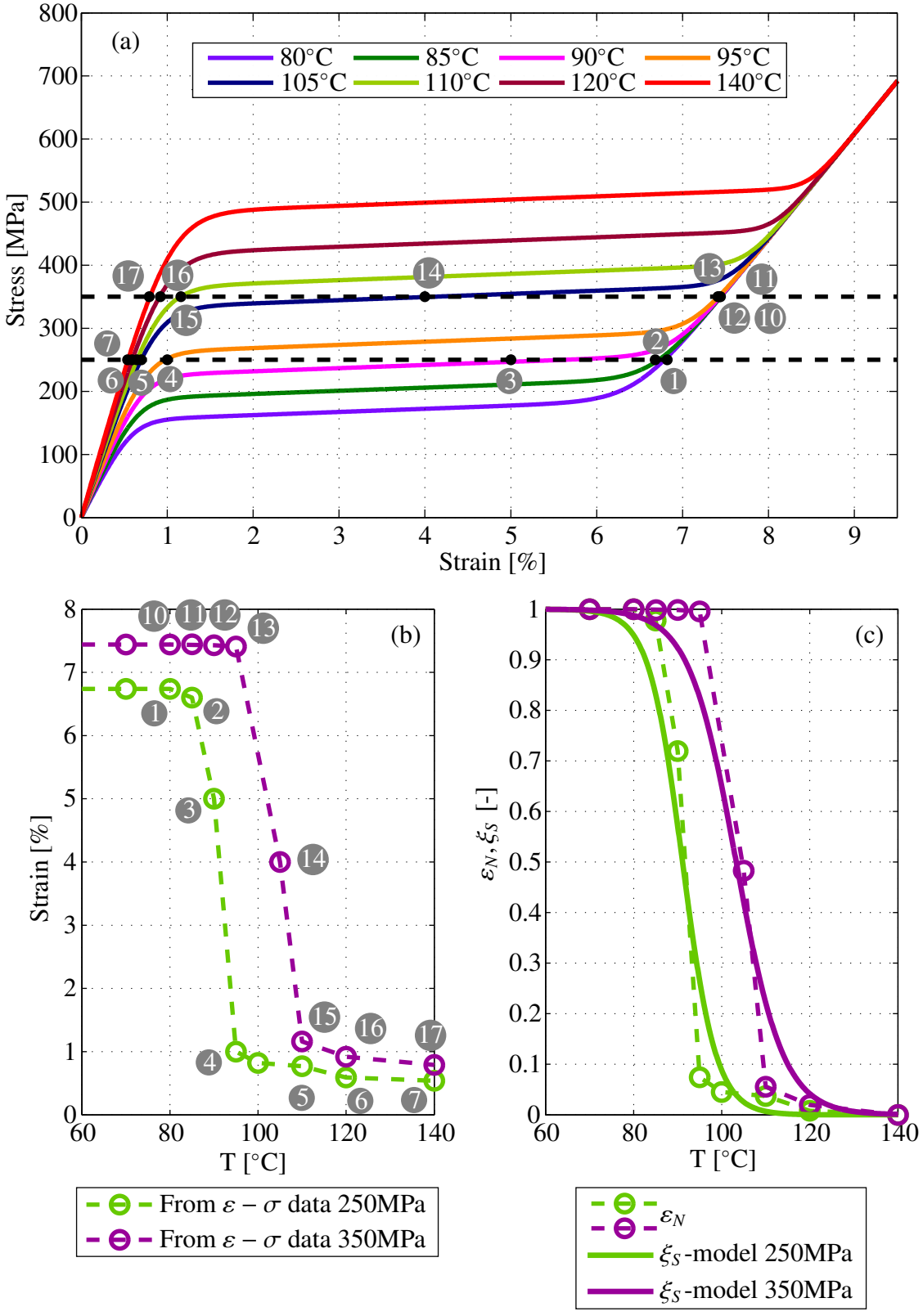

Figure 6-5: *Stress strain curves for temperatures over ambient from* 80 °C *to* 140 °C *and Strain and* ξ_S *versus temperature for 250 and 350 MPa*

k_S^H is calculated with (6-15) where $T_{\sigma\varepsilon_2}$ is the temperature at which the second knee $\varepsilon_2(T)$ coincides with the stress at which the hysteresis is considered. For example, when considering the hysteresis at a stress of 200 MPa, $T_{\sigma\varepsilon_2} \approx 80°C$ because this is the temperature at which the $\sigma - \varepsilon$ curve is at a second knee (3 in Fig. 6-4). $T_{\sigma\varepsilon_2}$ is found by solving (5-5) for ξ_T and then solving for T in (6-6). Using this method, $k^{H,C}$ simplifies to approximately $8/c_m\sigma$.

Identical to the ξ_T model, variables α_S^a and γ_S represent the height and offset of the function. They are dependant on $\xi_S(\varepsilon)$ when $T < M_f$ and $T > A_f$ i.e. ξ_S at the maximum and minimum strains ε_m and ε_a at the stress being considered, as shown in (6-16) and (6-17). For the curves in Figs. 6-4 and 6-5, $\xi_S(\varepsilon_m) = 1$ (at positions 1, 10, 11, 12) and $\xi_S(\varepsilon_a) = 0$ (at positions 7, 17). For the constant load actuator configuration shown in Fig. 6-6(a), $\xi_S(\varepsilon_m) = 0.9$ and $\xi_S(\varepsilon_a) = 0$. In Fig. 6-6(b), $\xi_S(\varepsilon_m) = \xi_S(\varepsilon_a) = 0$, therefore, as expected, (6-18) predicts $\xi_S = 0$ since mechanically induced martensite cannot form, as the load is below the 1st austenitic and martensitic knees.

When the load is changing, then the maximum and minimum strains ε_m and ε_a change as the stress changes. Consider for example a spring-biased actuator in Fig. 6-6(c). At high temperature, where the load is σ_a, $\xi_S(\varepsilon_a) = 0.1$ and $\xi_S(\varepsilon_m) = 1$. For a random stress σ, α_S^a and γ_S are dependant upon $\xi_S(\varepsilon_a)$ and $\xi_S(\varepsilon_m)$ at the stress σ being considered, as shown in Fig. 6-6(c). In fact, this also holds for a varying stress position actuator as in Fig. 6-6(d) or even for the force controlled actuator in Fig. 6-6(e). In this actuator, which operates at a constant strain ε_f, at high temperature, $\sigma = \sigma_a$ and $\xi_S(\varepsilon_a) = 0.3$, $\xi_S(\varepsilon_m) = 1$, while at low temperature $\sigma = \sigma_m$ and $\xi_S(\varepsilon_a) = 0$ and $\xi_S(\varepsilon_m) = 0.5$ and likewise at intermediate temperatures. This also holds for a force controlled actuator where the strain is not constant, as shown in Fig. 6-6(f). For all the actuators ξ_S^a and ξ_S^m are defined as in (6-14)[6].

$$\begin{cases} \xi_S^a = \xi_S(\varepsilon_a^{\sigma_a}) & \text{where } \varepsilon_a^{\sigma_a} \text{ is } \varepsilon \text{ at } \sigma_a,\ T > A_f \text{ (red curves in Fig. 6-6)} \\ \xi_S^m = \xi_S(\varepsilon_m^{\sigma_m}) & \text{where } \varepsilon_m^{\sigma_m} \text{ is } \varepsilon \text{ at } \sigma_m,\ T < M_f \text{ (blue curves in Fig. 6-6)} \end{cases} \tag{6-14}$$

The modelling algorithm in Sect. 6.3 is shown for thermally induced martensite to model the hysteresis, including minor looping behaviour. The algorithm for ξ_S is identical to that with ξ_T with only the T changed to S.

$$k_S^{H,C} = \frac{8}{\beta^H(\sigma) - T_{\sigma\varepsilon_2}} \approx \frac{8}{c_m\sigma} \tag{6-15}$$

$$\gamma_S^{H,C} = \xi_S(\varepsilon_a) \tag{6-16}$$

$$\alpha_S^{aH,C} = |\xi_S(\varepsilon_m) - \gamma_S^{H,C}| = |\xi_S(\varepsilon_m) - \xi_S(\varepsilon_a)| \tag{6-17}$$

$$\xi_S^{H,C}(T,\sigma) = \frac{\overbrace{\alpha_S^{aH,C}(1 + e^{\frac{8}{c_m\sigma}(T_m - \beta^{H,C}(\sigma))})}^{\alpha_S^{H,C}}}{1 + e^{\frac{8}{c_m\sigma}(T - \beta^{H,C}(\sigma))}} + \gamma_S^{H,C} \tag{6-18}$$

Using (6-18) for the constant load actuators in Figs. 6-4 and 6-5 produces the solid curves in plot(c) in both both figures.

[6]Note that for a constant force actuator, $\varepsilon_a^{\sigma_a} = \varepsilon_a$ and $\varepsilon_m^{\sigma_m} = \varepsilon_m$ since $\sigma = \sigma_a = \sigma_m$.

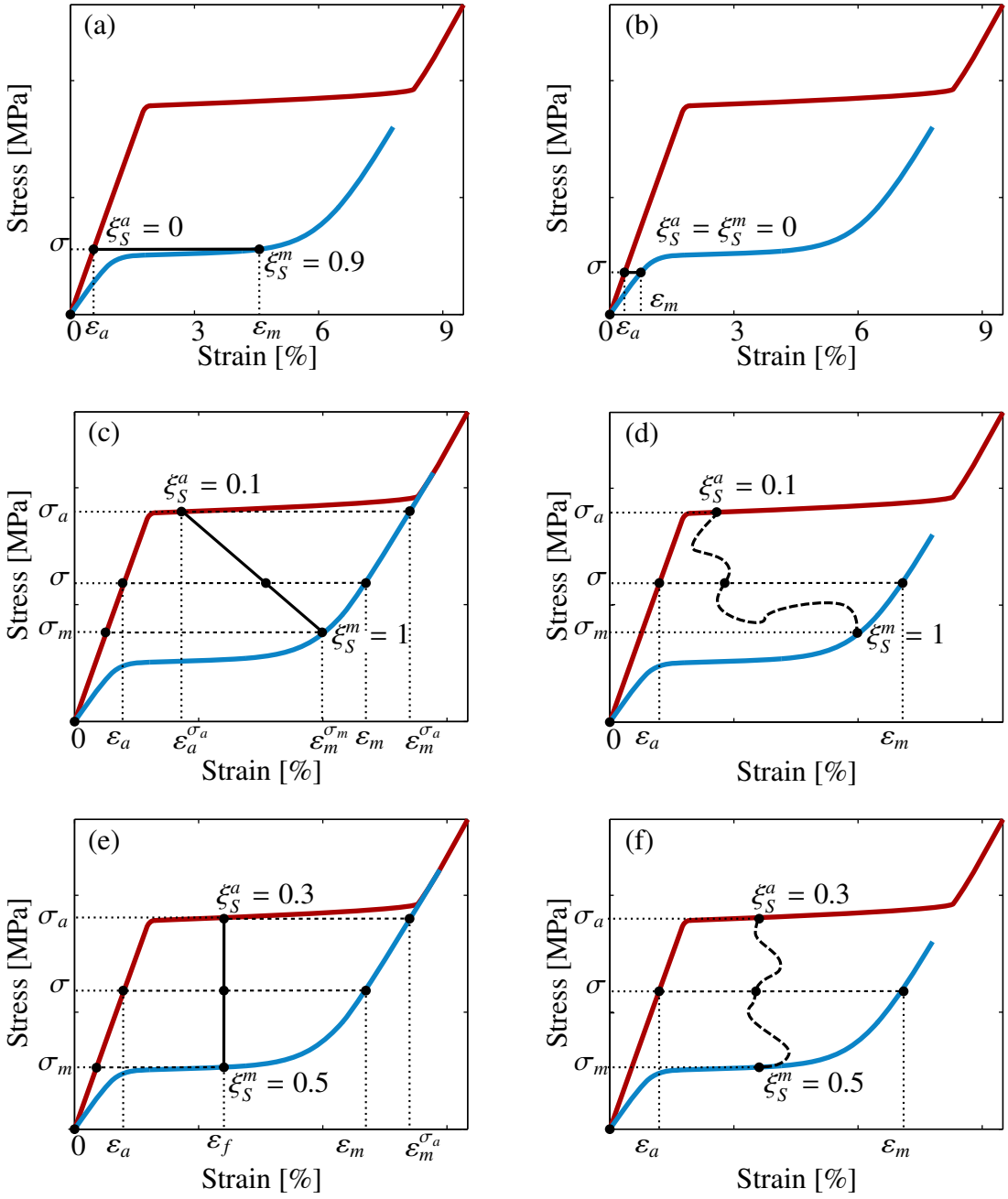

Figure 6-6: *Stress strain curves for various actuator configurations*

6.5 Total Martensite Fraction

For an SMA at no load, consider a temperature $T > A_f^o$, where the SMA is fully austenitic, as shown schematically by ❶ in the hysteresis in Fig. 6-7(a). Likewise, consider a temperature $T < M_f^o$, where the SMA is fully martensitic i.e. at ❸ and an intermediate temperature $A_s^o < T < A_f^o$, such that $\xi_T = 0.6$, where the SMA is a mixture of phases, such as at ❹. Now consider that at each of these temperatures, the strain is increased (while the temperature stays constant) to produce the three stress-strain curves in Fig. 6-7(b), (c) and (d), respectively[7]. At $T < M_f^o$, twinned martensite transforms to detwinned martensite (plot (c)) and at $T > A_f^o$, austenite transforms to stress induced martensite (plot (b)). At $A_s^o < T < A_f^o$, the twinned martensite portion transforms to detwinned martensite and the austenite portion transforms to stress induced martensite (plot (d)).

The total martensite fraction ξ is dependant on the martensite formed from the thermal process ξ_T and the mechanical process ξ_S. The mechanical process produces oriented martensite, which can be formed from two paths: the formation of detwinned martensite and the formation of stress induced martensite. Since detwinned martensite can only form when thermal martensite is initially present, it is written as $\xi_T\xi_S$. Twinned martensite is calculated as the component of thermal martensite that is not detwinned as $\xi_T - \xi_T\xi_S$. Therefore, ξ_T represents twinned martensite only when the mechanical load/strain on the SMA is below the 1st knee, as expected [OR05]. Stress induced martensite is weighted by the amount of austenite present at no load (i.e. $1 - \xi_T$) since it can only form when austenite is first present in the SMA and is written as $(1 - \xi_T)\xi_S$. Therefore ξ is the sum of twinned martensite $\xi_T(1 - \xi_S)$, detwinned martensite $\xi_T\xi_S$ and stress induced martensite $(1 - \xi_T)\xi_S$, as shown in (6-19). The total martensite fraction (6-19) simplifies to (6-20)[8].

$$\xi = \overbrace{\xi_T(1-\xi_S)}^{\text{twinned martensite}} + \overbrace{\overbrace{\xi_T\xi_S}^{\text{detwinned martensite}} + \overbrace{(1-\xi_T)\xi_S}^{\text{stress induced martensite}}}^{\text{mechanically induced martensite}} \tag{6-19}$$

$$\xi = \xi_T + \xi_S - \xi_T\xi_S \tag{6-20}$$

The austenite fraction ξ_A is in (6-21), which, as expected, is identical to $1 - \xi$.

$$\xi_A = (1 - \xi_T)(1 - \xi_S) = 1 - (\xi_T + \xi_S - \xi_T\xi_S) = 1 - \xi \tag{6-21}$$

The validity of (6-20) to describe the total martensite fraction is shown with the following scenarios, also shown graphically in Fig. 6-7.

The first four scenarios show the total martensite fraction at no load for various temperatures. Thermal martensite progression or depletion follows the hysteresis in Fig. 6-7(a) (where the transformation temperatures are the no load temperatures). The SMA stays at the origin of the stress-strain diagram in Fig. 6-7(b)-(d) and $\xi_S = 0$ due to the absence of a load to produce mechanically induced martensite:

[7] Note that in plot (c), a blurred version of the curve at $T > A_f^o$ is shown for reference and in plot (d), both $T > A_f^o$ and $T < M_f^o$ curves are shown

[8] Note that for $0 \le \xi_T \le 1$ and $0 \le \xi_S \le 1$, ξ in (6-20) is, as expected, always $0 \le \xi \le 1$. Similarly, ξ_A in (6-21) is also $0 \le \xi_A \le 1$

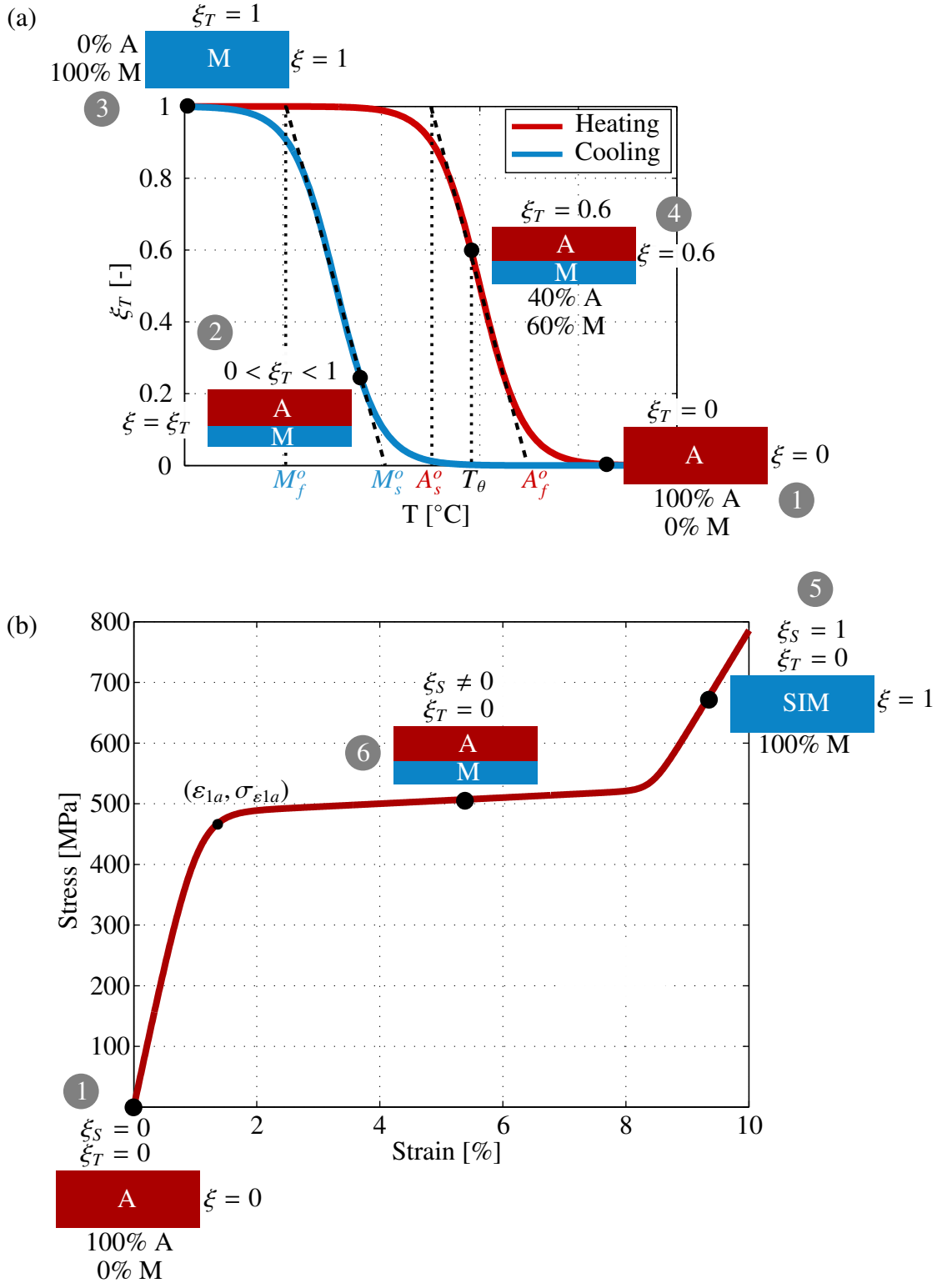

Figure 6-7: *Total martensite fraction: (a) Thermally induced martensite at no load (b) Mechanically induced martensite at $T > A_f^o$*

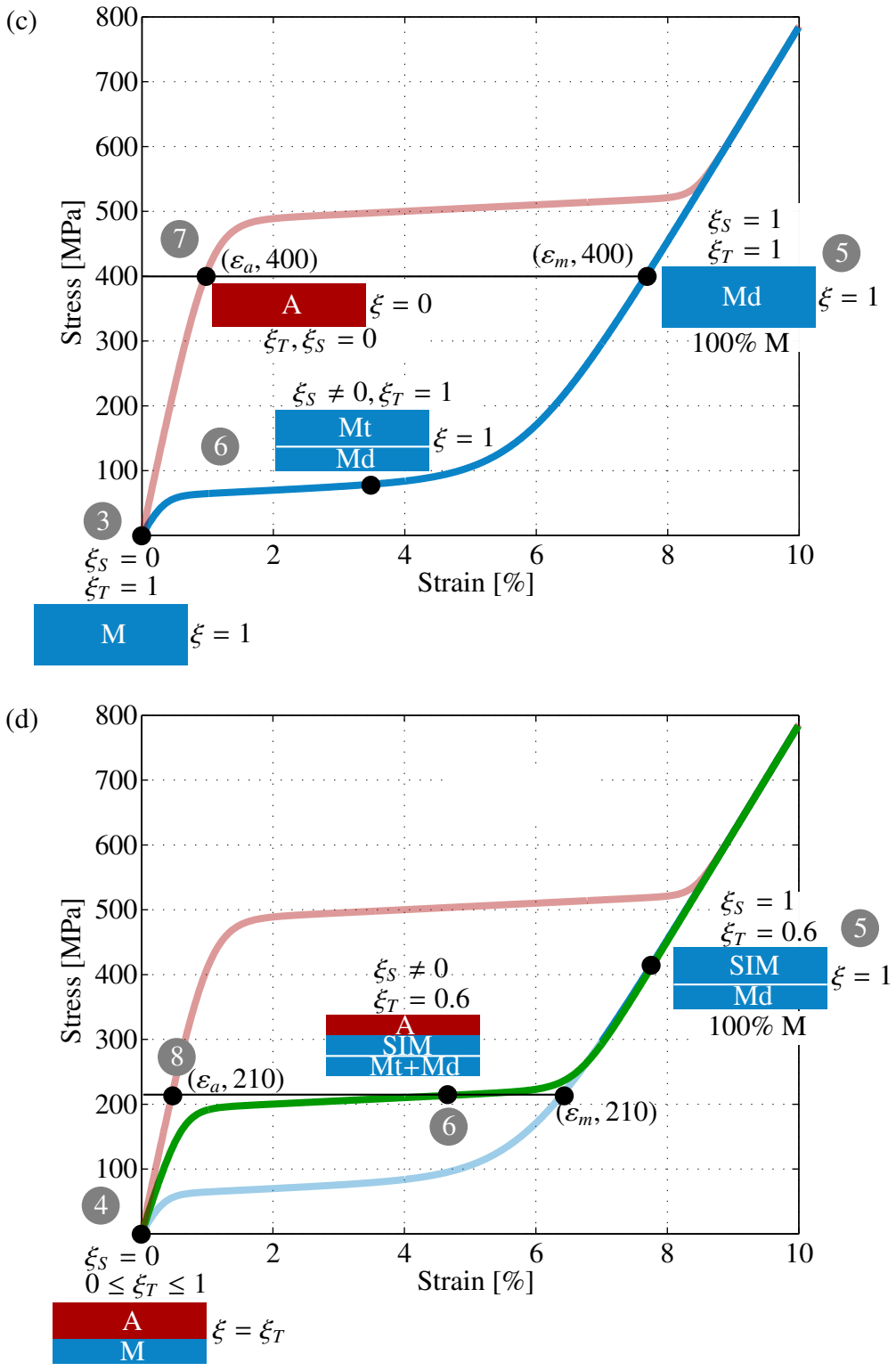

Figure 6-7: *Total martensite fraction: (c) Mechanically induced martensite at $T < M_f^o$ (d) Mechanically induced martensite at $A_s^o < T < A_f^o$ or $M_f^o < T < M_s^o$*

Scenario ⓧ→❶ No load, the SMA at an unknown state x at room temperature is first heated so that $T > A_f^o$: Initially, the SMA is at room temperature, therefore fully martensitic. However, there is no knowledge about the amount of residual strain in the SMA. Nevertheless, heating the SMA beyond A_f^o ensures a complete transformation to austenite i.e. $\xi_T = \xi = 0$, which is predicted by (6-20), with parameters $\xi_T = 0, \xi_S = 0$, as shown in (6-22) and Fig. 6-7(a).

$$\xi = \xi_T + \xi_S - \xi_T\xi_S = 0 + 0 - 0 = 0 \tag{6-22}$$

Scenario ❶→❷ No load, the SMA from scenario ❶ is allowed to cool to some arbitrary temperature $M_f^o < T < M_s^o$: ξ_T is calculated from (6-6) (temperature dependant). $\xi_S = 0$ due to no load. Using (6-20) gives, as expected, $\xi = \xi_T$ as shown in (6-23).

$$\xi = \xi_T + \xi_S - \xi_T\xi_S = \xi_T + 0 - 0 = \xi_T \tag{6-23}$$

Scenario ❶→❸ No load, the SMA from scenario ❶ is allowed to cool to $T < M_f^o$: This is a special case of scenario 2 above where the SMA transforms completely to martensite ($\xi_T = 1$). Using (6-23) gives $\xi = 1$ as shown in (6-24) and Fig. 6-7[9].

$$\xi = \xi_T + \xi_S - \xi_T\xi_S = 1 + 0 - 0 = 1 \tag{6-24}$$

Scenario ❸→❹ No load, from the SMA from scenario ❸, T increased such that $A_s^o < T < A_f^o$ and $\xi_T = 0.6$: Here, thermal martensite makes up 60% of the SMA and austenite makes up 40% of the SMA. $\xi_S = 0$ due to absence of mechanical loading. Using (6-20), with parameters $\xi_T = 0.6, \xi_S = 0$, gives $\xi = 0.6$ as expected (see (6-25)). More generally, $\xi = \xi_T$ as calculated from (6-6). So e.g. when the temperature is increased such that $T > A_f^o$, then the material is fully austenite and $\xi = \xi_T = 0$ (❶ in Fig. 6-7a).

$$\xi = \xi_T + \xi_S - \xi_T\xi_S = 0.6 + 0 - 0 = 0.6 \tag{6-25}$$

The next scenarios show the effect of keeping the temperature constant while increasing the strain. Here, the SMA moves away from the origin of stress-strain diagram, as shown in Fig. 6-7(b)-(d) and ξ_S is no longer 0:

Scenario ❺ After any of the scenarios ❶-❹, T is held constant. The SMA is initially at no load and no strain. Then, it is strained beyond second knee. In this case, $\xi_S = 1$ since mechanical loading beyond the second knee causes a full transformation to oriented martensite. Using (6-20), with parameters $\xi_S = 1$, gives $\xi = 1$ as expected (see (6-26)) regardless of the temperature i.e. regardless of the value of ξ_T. Therefore, all three stress-strain curves in Fig. 6-7(b),(c) and (d) have $\xi = 1$ at the end of loading.

$$\xi = \xi_T + \xi_S - \xi_T\xi_S = \xi_T + 1 - \xi_T = 1 \tag{6-26}$$

[9] Recall that for the stress-strain experiments in Chaps. 4 and 5, the SMA wire was heated in a furnace and allowed to cool to room temperature before any experiment. The reason was to bring the SMA into a state where all residual strains are eliminated and the initial SMA state is known as described by scenarios ⓧ→❶ and then ❶→❸

Scenario 6 After any of the scenarios 1-4, T is held constant. The SMA initially at no load and no strain. Then, it is strained to a particular value of ξ_S where $0 < \xi_S < 1$ since the strain is between the knees (see Fig. 6-7). The total martensite fraction is given by (6-27). Note that if $\xi_T = 1$, then the material is fully martensitic before mechanical loading and $\xi = 1$ regardless of ξ_S since mechanical loading causes only a transformation from twinned to detwinned martensite (see (6-28)). If $\xi_T = 0$, then the material is fully austenitic at no load and martensite can only form by loading i.e. $\xi = \xi_S$ (see (6-29)).

$$\xi = \xi_T + \xi_S - \xi_T \xi_S \tag{6-27}$$

$$\xi_T = 1 : \xi = 1 + \xi_S - \xi_S = 1 \tag{6-28}$$

$$\xi_T = 0 : \xi = 0 + \xi_S - 0 = \xi_S \tag{6-29}$$

Generally speaking a change in the total martensite fraction can be trigged either by a change in temperature, as shown in scenarios 1-4 above, or a change in strain (or stress) as shown in scenarios 5-6 above and (6-20) is shown to be valid when either ξ_T is constant and ξ_S is changing or vice versa.

In order to test the model where a load is present and the temperature is changing (a typical SMA actuator scenario), an experiment where the SMA at $T < M_f$ is loaded with a stress of 250 MPa and then heated to $T > A_f$ and cooled to $T < M_f$ is performed. The experimental data, ξ_T and ξ_S are shown in Fig. 6-8(a). In Fig. 6-8(b), the results of using (6-20) is plotted over the experimental results. The model shows very poor correlation to experimental data, therefore showing that (6-20) is not sufficient to describe the SMA's behaviour when both a load is present and the temperature is changing.

In order to model this behaviour, consider that if the SMA is loaded to beyond the 2$^{\text{nd}}$ knee at $T < M_f$, then $\xi_T = 1$ and $\xi_S = 1$. Using (6-20) gives $\xi = 1$. In an attempt to model the SMA actuator's behaviour, ξ is rewritten as the average of the thermal and mechanically induced martensite fractions (6-30), which for $\xi_T = 1$ and $\xi_S = 1$ gives $\xi = 1$ as in (6-20).

$$\xi = \frac{\xi_T + \xi_S}{2} \tag{6-30}$$

Using the average of the thermal and mechanically induced martensite fractions gives surprisingly good results for modelling ξ when the SMA is used as an actuator, as shown in Fig. 6-9(b), where the results of using (6-30) are plotted over the same experiment as in Fig. 6-8 above. Observe that neither ξ_T nor ξ_S alone are sufficient to describe the hysteresis behaviour at 250 MPa accurately (Fig. 6-9(a)). As the phase transformation under these conditions is quite complex, using the average of the thermal and mechanically induced martensite fractions seems reasonable, however, a sound hypothesis from materials science could not be found in the literature.

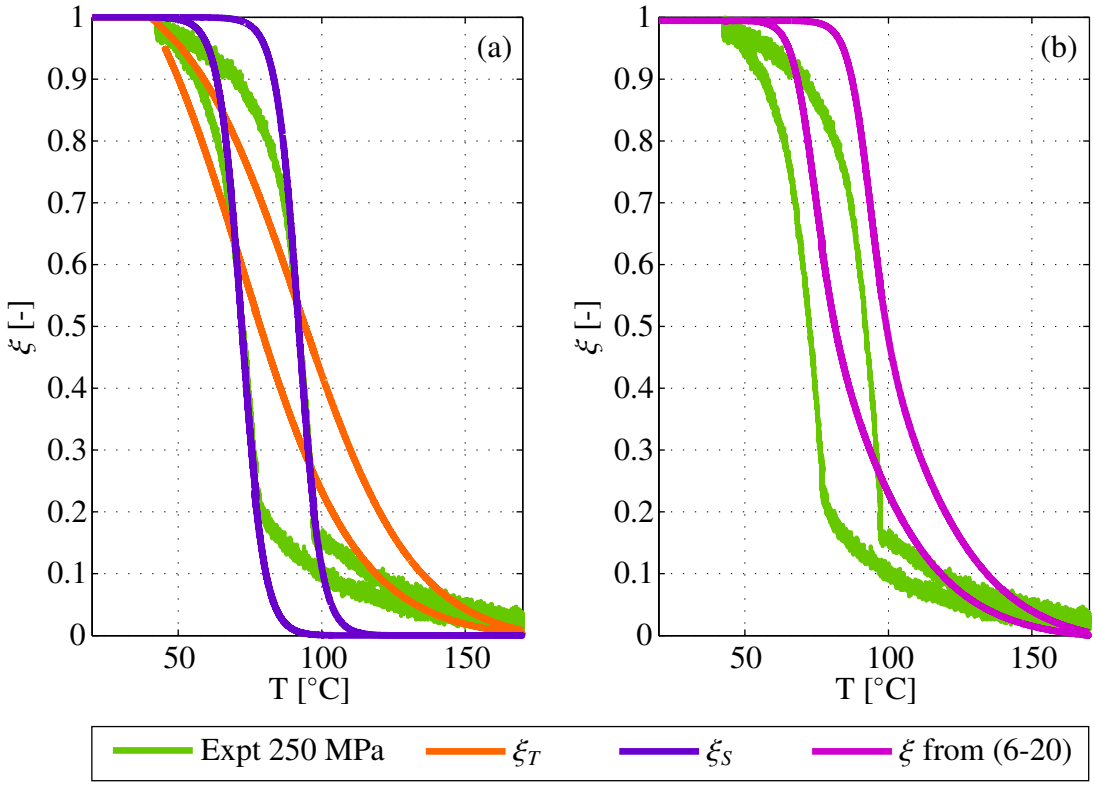

Figure 6-8: *Phase kinetic model for stress of 250 MPa, showing ξ_T, ξ_S and ξ using the 1st attempt at modelling the hysteresis.*

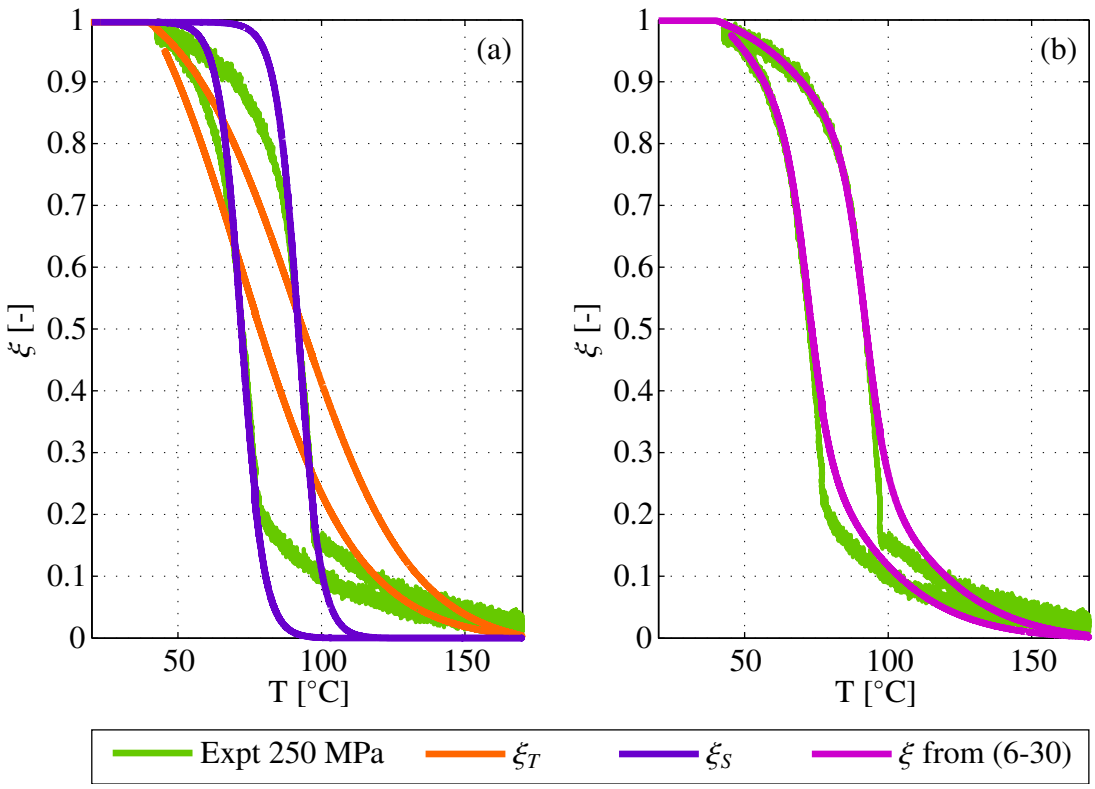

Figure 6-9: *Phase kinetic model showing ξ_T, ξ_S and ξ for stress of 250 MPa*

In order to incorporate temperature changes while $\sigma > 0$, initial and boundary conditions that account for the actuator's travel and continuity in ξ were used as in (6-31)[10], with $\xi_S(T, \sigma)$ from (6-18)[11]. Note that for the constant load actuators in Figs. 6-8 and 6-9, $\xi_S(\varepsilon_m) = 1$ and $\xi_S(\varepsilon_a) = 0$ and (6-31) is identical to (6-30).

$$\xi = \frac{\overbrace{\xi_T(2 - \xi_S(\varepsilon_m)) + (1 - \xi_T)\xi_S(\varepsilon_a)}^{\text{actuator travel from temperature changes}} + \xi_S(T, \sigma)}{2} \tag{6-31}$$

In order to demonstrate that (6-31) computes the correct values of ξ at the boundaries, consider the actuators in Fig. 6-6. Consider that the SMA is at the threshold temperature $T < M_f$, where $\xi_T = 1$ (blue curves in the Figure). The SMA is then loaded such that $\xi_S = \xi_S^m$, as shown in the Figure. The total martensite fraction should always be 1 because the SMA is always martensitic at this temperature (cf. (6-28)). Conversely, when $T > A_f$, where $\xi_T = 0$ (red curves in the Figure), and the SMA is loaded to $\xi_S = \xi_S^a$, then ξ should be identical to ξ_S^a, since at this temperature, the total martensite fraction is based only on the amount of SIM present in the SMA (cf. (6-29)). Consider now that the SMA is loaded at $T < M_f$ to ξ_S^m and then heated along the various actuator paths in Fig. 6-6(a)-(f) such that $T > A_f$ and $\xi_S = \xi_S^a$. In this case, ξ is computed with (6-31) since the temperature changes at the presence of a load. For continuity, the same values for ξ as when using (6-20), i.e. $\xi(T < M_f) = 1$ and $\xi(T > A_f) = \xi_S^a$, have to be guaranteed.

Consider the first case where $T = T_m$ ($T_m < M_f$ by defintion) and $\xi_T = 1$. Here ξ reduces to (6-32). However, at this temperature, ξ_S in (6-18) is given by (6-33). Then $\xi(T < M_f) = 1$ (cf. (6-34)), as expected.

$$\xi = \frac{2 - \xi_S(\varepsilon_m) + \xi_S}{2} \tag{6-32}$$

$$\xi_S(T < M_f) = \alpha_S^a + \gamma_S = \xi_S(\varepsilon_m) = \xi_S^m \tag{6-33}$$

$$\xi(T < M_f) = \frac{2 - \xi_S(\varepsilon_m) + \xi_S(\varepsilon_m)}{2} = 1 \tag{6-34}$$

At the other extreme, where $T > A_f$ and $\xi_T = 0$, ξ reduces to (6-35). At this temperature, ξ_S in (6-18) is given by (6-36) and $\xi(T > A_f) = \xi_S(\varepsilon_a) = \xi_S^a$ (cf. (6-37)), as expected.

$$\xi = \frac{\xi_S(\varepsilon_a) + \xi_S}{2} \tag{6-35}$$

$$\xi_S(T > A_f) = \gamma_S = \xi_S(\varepsilon_a) = \xi_S^a \tag{6-36}$$

$$\xi(T > A_f) = \frac{\xi_S(\varepsilon_a) + \xi_S(\varepsilon_a)}{2} = \xi_S(\varepsilon_a) = \xi_S^a \tag{6-37}$$

Note that using (6-31) requires no *aprior* knowledge of the actuator path and the value of ξ for random paths such as in Fig. 6-6(d) and (f) can also be computed.

[10] Note that the only values for which ξ>1 when using (6-31) is when $\xi_T = \xi_S = 1$ and $\xi_S(\varepsilon_m) = 0$. This is however, physically not possible because when $\xi_S = 1$, $\xi_S(\varepsilon_m)$ must also be 1.

[11] Superscripts H, C are omitted here for simplicity.

The total martensite fraction can then be computed by (6-38), where $\xi_S(\varepsilon(T))$ is in (6-13) and $\xi_S(T,\sigma)$ is in (6-18)[12]. Note that at the absence of a load, $\xi_T(T,\sigma) = \xi_T(T,0)$.

$$\xi = \begin{cases} \dfrac{\xi_T(T,\sigma)[2-\xi_S(\varepsilon_m)] + [1-\xi_T(T,\sigma)]\xi_S(\varepsilon_a) + \xi_S(T,\sigma)}{2} & \sigma>0 \text{ and } |\frac{dT}{dt}|>0 \\ \xi_T(T,0) + \xi_S(\varepsilon(T)) - \xi_T(T,0)\xi_S(\varepsilon(T)) & \text{otherwise} \end{cases} \tag{6-38}$$

Consider now scenario 7 in Fig. 6-7(c), where $\sigma > 0$ and $|\frac{dT}{dt}| > 0$. This is a typical constant load SMA actuator scenario:

Scenario 7 The SMA at no load is heated beyond A_f^o, allowed to cool to $T < M_f^o$ (scenario 1→3) and is therefore 100% martensite, as shown in (6-39). The SMA is then loaded by a stress of σ [Pa], lower than the 1st knee (yield stress) of austenite $\sigma_{\varepsilon 1a}$. This is shown exemplarily in Figs. 6-7(c) for $\sigma = 400$ MPa, which causes strain ε_m. ξ remains at 1, as shown in (6-40) because of a transformation from twinned to detwinned martensite during loading. Now the SMA is heated such that $T > A_f(\sigma)$. Here, $\xi_S(\varepsilon_m) = 1$ and $\xi_S(\varepsilon_a) = 0$ due to the constant load. ξ progresses according to (6-41). In the stress-strain diagram in Fig. 6-7(c), the SMA contracts along the constant stress line at 400 MPa since the load during heating does not change. At the end of heating, when $T > A_f(\sigma)$, ξ is 0 as shown in (6-42) and the strain is ε_a. Note that $\xi_S = 0$ because σ is lower than $(\varepsilon_{1a}, \sigma_{\varepsilon 1a})$, therefore no SIM is generated. When the SMA is now allowed to cool, the 400 MPa stress stretches the wire and the martensite fraction during and at the end of cooling is given by (6-43) and (6-44).

Scenario 7 :

Start $T < M_f^o$, no load 1 → 3 :

$\xi_T = 1$, $\xi_S = 0$:

$$\xi = \xi_T + \xi_S - \xi_T\xi_S = 1 + 0 - 0 = 1 \tag{6-39}$$

Loading to σ load at $T < M_f^o$ 3 → 5 :

$\xi_T = 1$, $\xi_S = 1$:

$$\xi = \xi_T + \xi_S - \xi_T\xi_S = 1 + 1 - 1 = 1 \tag{6-40}$$

Heating with σ load to $T > A_f(\sigma)$ 5 → 7 :

ξ_T , ξ_S , $\xi_S(\varepsilon_m) = 1$, $\xi_S(\varepsilon_a) = 0$:

$$\xi = \frac{\xi_T(2-\xi_S(\varepsilon_m)) + (1-\xi_T)\xi_S(\varepsilon_a) + \xi_S}{2} = \frac{\xi_T + \xi_S}{2} \tag{6-41}$$

[12] $\xi_S(\varepsilon(T))$ and $\xi_S(T,\sigma)$ actually give similar values for ξ_S, but when only loading at a constant temperature, it is more computationally efficient to use $\xi_S(\varepsilon(T))$ in (6-13)

Heating complete $T > A_f(\sigma)$ with σ load ❼ :

$\xi_T = 0$, $\xi_S = 0$, $\xi_S(\varepsilon_m) = 1$, $\xi_S(\varepsilon_a) = 0$:

$$\xi = \frac{\xi_T + \xi_S}{2} = \frac{0+0}{2} = 0 \tag{6-42}$$

Cooling with σ load to $T < M_f(\sigma)$ ❼ → ❺ :

ξ_T , ξ_S , $\xi_S(\varepsilon_m) = 1$, $\xi_S(\varepsilon_a) = 0$:

$$\xi = \frac{\xi_T(2 - \xi_S(\varepsilon_m)) + (1 - \xi_T)\xi_S(\varepsilon_a) + \xi_S}{2} = \frac{\xi_T + \xi_S}{2} \tag{6-43}$$

Cooling complete with σ load, $T < M_f(\sigma)$ ❺ :

$\xi_T = 1$, $\xi_S = 1$, $\xi_S(\varepsilon_m) = 1$, $\xi_S(\varepsilon_a) = 0$:

$$\xi = \frac{\xi_T + \xi_S}{2} = \frac{1+1}{2} = 1 \tag{6-44}$$

The actuator scenarios considered above show that using (6-38) guarantees continuity and accounts for actuator travel when the SMA is either fully martensite or fully austenite at no load, the SMA is then loaded at either $T < M_f$ or $T > A_f$, respectively, to a particular stress and then the temperature changes, thereby utilising the SMA as an actuator. The model also accounts for dynamically changing stresses during the actuator's travel [13].

The model validation is presented in the next section.

6.6 Model Validation: Experimental Set-Up

In order to validate the model, various experiments were conducted using the custom built test set-up in Fig. 6-10. Several experiments were performed to record data of the major and minor hysteresis loop at various loads. The test samples were 0.5 mm diameter poly-crystalline NiTi SMA wires with an A_s of 95 °C (at 300 MPa) i.e. the same wire type from the stress-strain experiments in Chap. 5. The experimental set-up, with data sheets of all components in Appendix A2 is as follows:

Frame The frame was built from aluminium profiles, with a stiffness that is several orders of magnitudes larger than the SMA wire, with a construction as shown exemplarily in Fig. 6-10.

Clamps The wire was attached to the frame via two clamps. In order to thermally and electrically isolate the SMA from the rest of the set-up, the ends of the wire were

[13] There is a rare case shown exemplarily in scenario ❽ in Fig. 6-7(d). Here, the SMA at no load is heated to temperature T_θ at ❹, where when the SMA is a mixture of phases, and then with the temperature held constant, the SMA is loaded to a stress of 210 MPa to ❻ (green curve in the Figure) which is lower than the second knee. When now, the temperature is changed, the current model needs to be extended to guarantee continuity. The extension of the model to cover this case is presented separately in Appendix A1.8, as this situation is very rare when the SMA is used as an actuator, where loading is typically performed when the SMA is either fully martensitic or fully austenitic.

sandwiched between two pieces of cork before being secured by the clamps. One of the clamps was attached to a force cell to measure the forces on the wire, the other was attached to a reference plate that was mounted perpendicular to the wire.

Force measurement The forces on the wire were measured with a force cell *S2M 1000N* from Hottinger Baldwin Messtechnik GmbH (see A2.9). It can be used to measure forces from 10N to 1000N with an accuracy of 0.02%. The force signals were amplified by a signal amplifier *VM 151* from ATR Industrie-Elektronik GmbH (see A2.10).

Distance/Strain measurement In order to measure the strain of the wire, a laser distance sensor *OADM 12U7460/S35A* from Baumer Elektrik AG (see A2.11) was used. It can measure distances from 16 to 120 mm with a resolution of 0.002 to 0.12 mm depending on the nominal distance measured. The sensor measured the distance between a set point on the frame and a reference plate that was attached to one of the wire clamps and mounted perpendicular to the wire. In such a manner, the strain on the wire could be measured.

Temperature measurement The temperature of the wire was measured by a Type K fine gauge thermocouple from RS Components Ltd (see A2.12). The thermocouple has a bead diameter that is 0.075 mm and therefore about 7 times smaller than the diameter of the wire[14]. The measurement temperature range is -75°C to 260°C. The signals from the thermocouple were sent to a converter *MAS Thermo-K* with galvanic isolation from Weidmüller Interface GmbH & Co. KG (see A2.13).

Load The SMA wire could be loaded with a set of slotted weights from 1 kg to 10 kg (excluding 6 kg, which was not available).

Current supply The temperature in the wire was controlled through resistive (joule) heating by passing a current through it. The current in the wire was regulated using a constant controlled current source from MyTinySun® (see A2.14) that outputs an analog current upto 3A when triggered.

Data acquisition In order to interface between the computer that controls the experiment and the sensors and current source, a data acquisition card *PCI-DAS6014* from Measurement Computing Corporation (see A2.15) was installed in the PCI (Peripheral Component Interconnect) bus of the computer. The card has 16 analog inputs, 2 analog outputs and 8 digital I/O with a 16 Bit resolution. It is compatible with Simulink Real-Time Windows Target.

Control unit and software The experiment was controlled with a Windows based personal computer with Simulink Real-Time Windows Target from MathWorks® that gave out trigger signals to the current source to control the wire temperature. The measurement data was also collected and archived.

[14] If the thermocouple bead were too large, then it would act as a heat sink and the temperature measurements would be distorted.

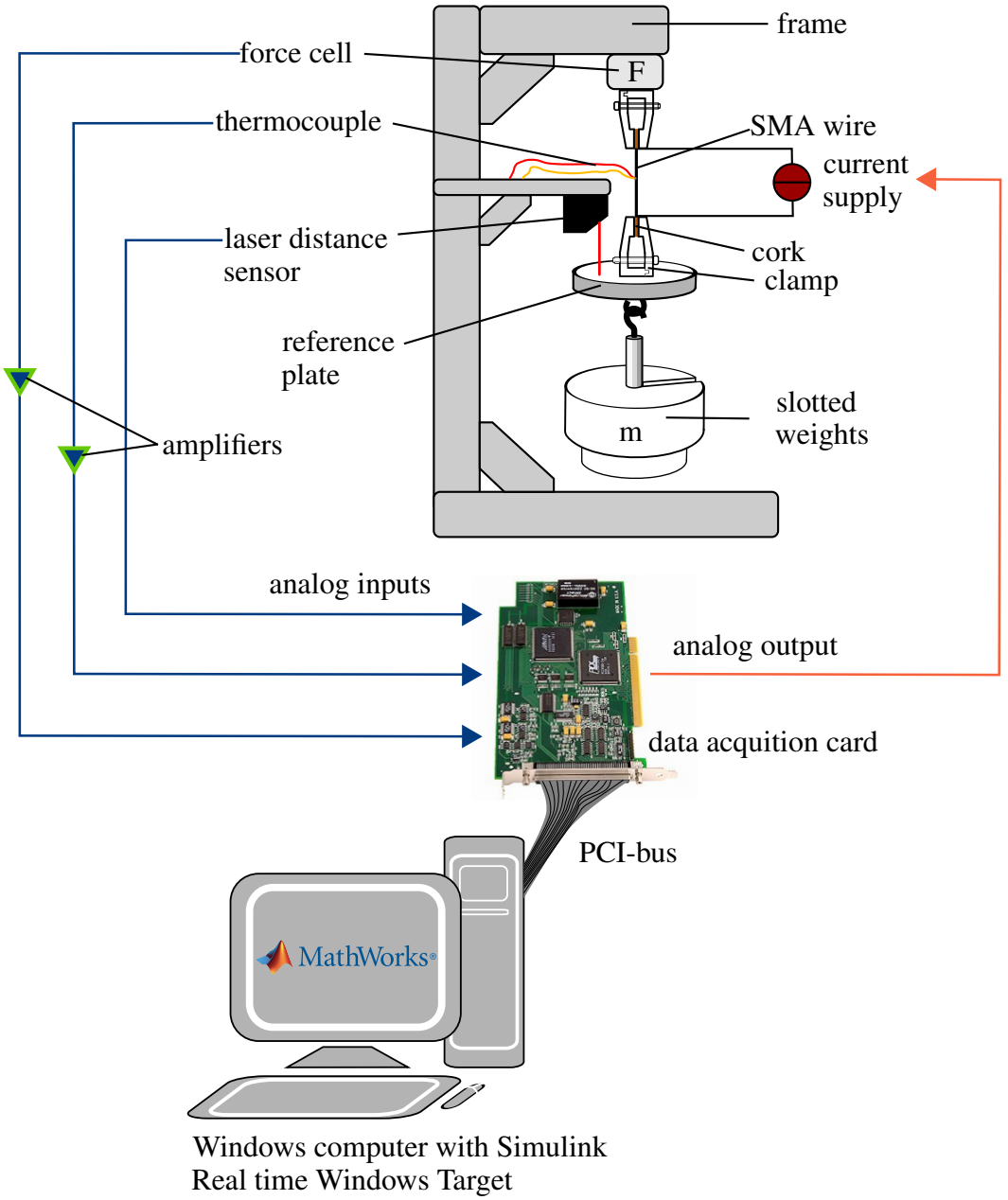

Figure 6-10: *Experimental set-up*

The parameters for the model are in Tab. 6-2. The transformation temperatures are in the SMA datasheets in A2.3 where the Differential Scanning Calorimetry (DSC) data shows $M_f \approx 65°C$, $M_s \approx 85°C$, $A_s \approx 95°C$ and $A_f \approx 115°C$. The stress at which this test was performed is taken from the *Transformation temperatures* plot in the SMA datasheets in A2.2, where the stress corresponding to these temperatures is 300 MPa. Further, the value of c_m [°C/MPa] can also be read off as $c_m = 1/8.2 = 0.122$. The transformation temperatures at no load are then calculated as shown exemplarily for A_s^0 in (6-45)[15].

$$A_s^o = A_s^{\sigma=300} + c_m(0 - \sigma) = 95 - (0.122)(300) = 58°C \tag{6-45}$$

The correlation between the model and experiments are shown in the following sections.

Table 6-2: *Parameters for hysteresis model*

M_f^o	M_s^o	A_s^o	A_f^o	β_o^C	β_o^H	T_m	c_m
28^oC	48^oC	58^oC	78^oC	38^oC	68^oC	25^oC	0.122^oC/MPa

6.7 Model Validation: Major Hysteresis Loop at Various Stresses

In these experiments, the wire was first heated with a current pulse of 3A until all residual strains were recovered, and subsequently allowed to cool, after which the wire length was measured and recorded. The wire was then loaded with a mass of 2 kg, followed by heating with a current of 1.5 - 1.8A until no change in strain was observed, after which the current was cut off and the wire was allowed to cool by natural convention. This procedure was repeated at least 2-5 times depending on the repeatability of the data. The wire strain, stress and temperature were measured during the experiment. This procedure was repeated for all masses from 2 - 10 kg, with the experimental results in Fig. 6-11 (which show the experimental data for 3 experiments excluding 3 kg, which shows only 2 experiments[16]).

The temperature data was input into the model and the results, using the parameters from Tab. 6-2, are shown in Fig. 6-11 with the grey curves. The model prediction shows good correlation to the experimental data. Note that the changing slope of the hysteresis curve as well as the changing hysteresis width is predicted automatically by the model due to the separation (and combination) of thermal and mechanical induced martensite.

The heating curve shows good correlation to experimental data at lower temperatures, but at higher temperatures, the model and experiment deviate. The observation is vice versa for the cooling curve: high temperatures shown good correlation but deviations are present at lower temperatures. The maximum error is approximately 10°C. This is most pronounced for masses less than 5 kg. Further, at masses 9 and 10 kg, the model predicts a wider hysteresis than the experimental data.

The average RMS error between the model and experimental correlation for each mass is in Tab. 6-3. The deviation between the model and experiment is less than 7.5%. Note that the NRMSE and RMSE are identical because the normalization factor (difference between maximum and minimum of experimental data) is 1.

[15] cf. This equation has the same form as (6-3).

[16] The data from the third experiment for 3 kg was corrupted

Table 6-3: *RMS Error between phase kinetic model and experiments*

Mass [kg]	2	3	4	5	7	8	9	10
RMSE [%]	7.7	7.3	7.5	7.1	5.6	5.7	6	7.1

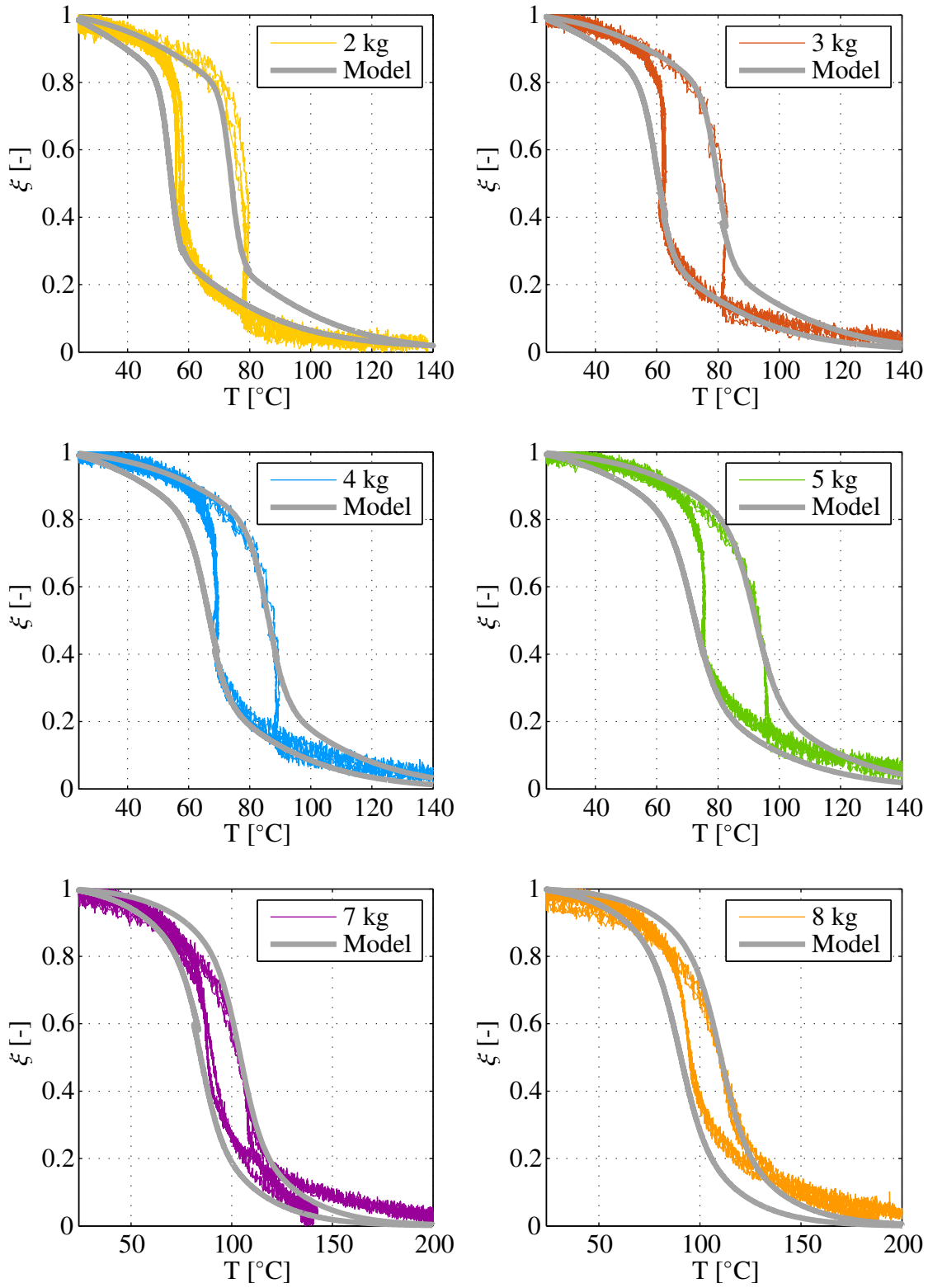

Figure 6-11: *Experiment and model for major hysteresis loops for 2 - 8 kg (3 expts each except for 3 kg (2 expts))*

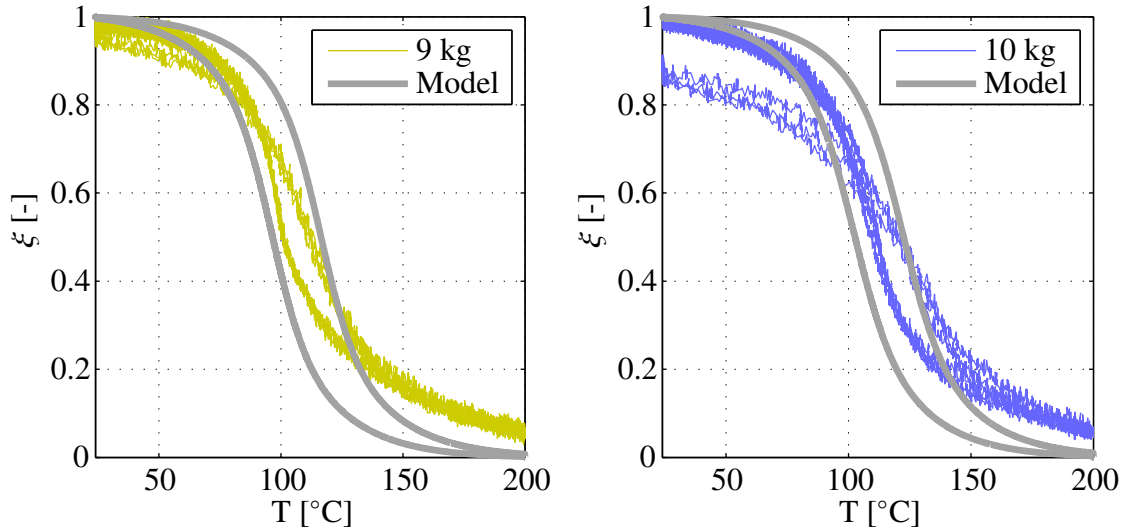

Figure 6-11: *Experiment and model for major hysteresis loops for 9 - 10 kg (3 expts each)*

In the next experiments, the wire was heated with a sinusoidal current with a minimum of 0.5A, a maximum of 2A and a period of 200s, which causes a change in the temperature of the wire, as shown Fig. 6-12. This allowed controlled heating and cooling of the wire. The wire was loaded with masses 2 - 8 kg. The experiment per mass was repeated thrice, with excellent reproducibility. The average value for all 3 experiments, along with the model prediction is in Fig. 6-13.

The model and experimental correlation is exceptional, except when ξ values are low. The predicted curve for the 8-kg mass has the right hysteresis shape, however, $\beta^{H,C}$ values are about 4°C higher than is observed in the experiments.

Note that the model is able to adjust to the changing current input, due to the fact that the actual measured temperature is fed into the model as an input. The RMSE are in Tab. 6-4.

Table 6-4: *RMS Error between phase kinetic model and experiments with sinus current*

Mass [kg]	2	3	4	5	7	8
RMSE [%]	4.9	3.9	3.4	3.9	4.2	5.8

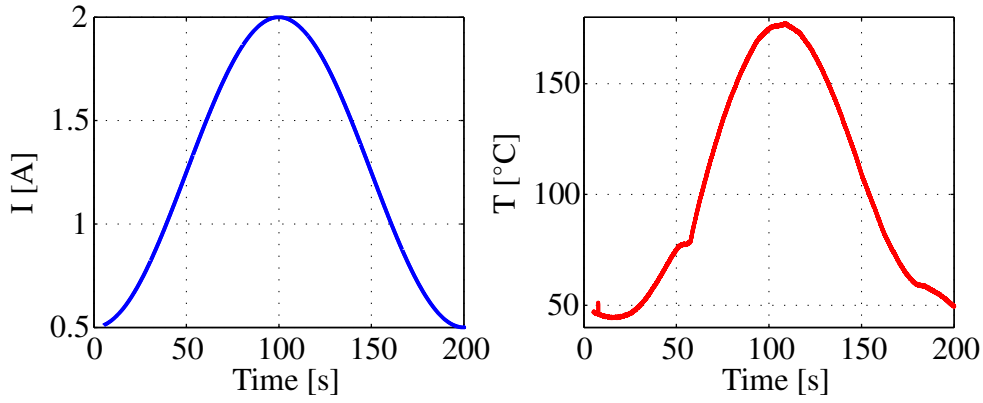

Figure 6-12: *Sinusoidal input current and resulting temperature*

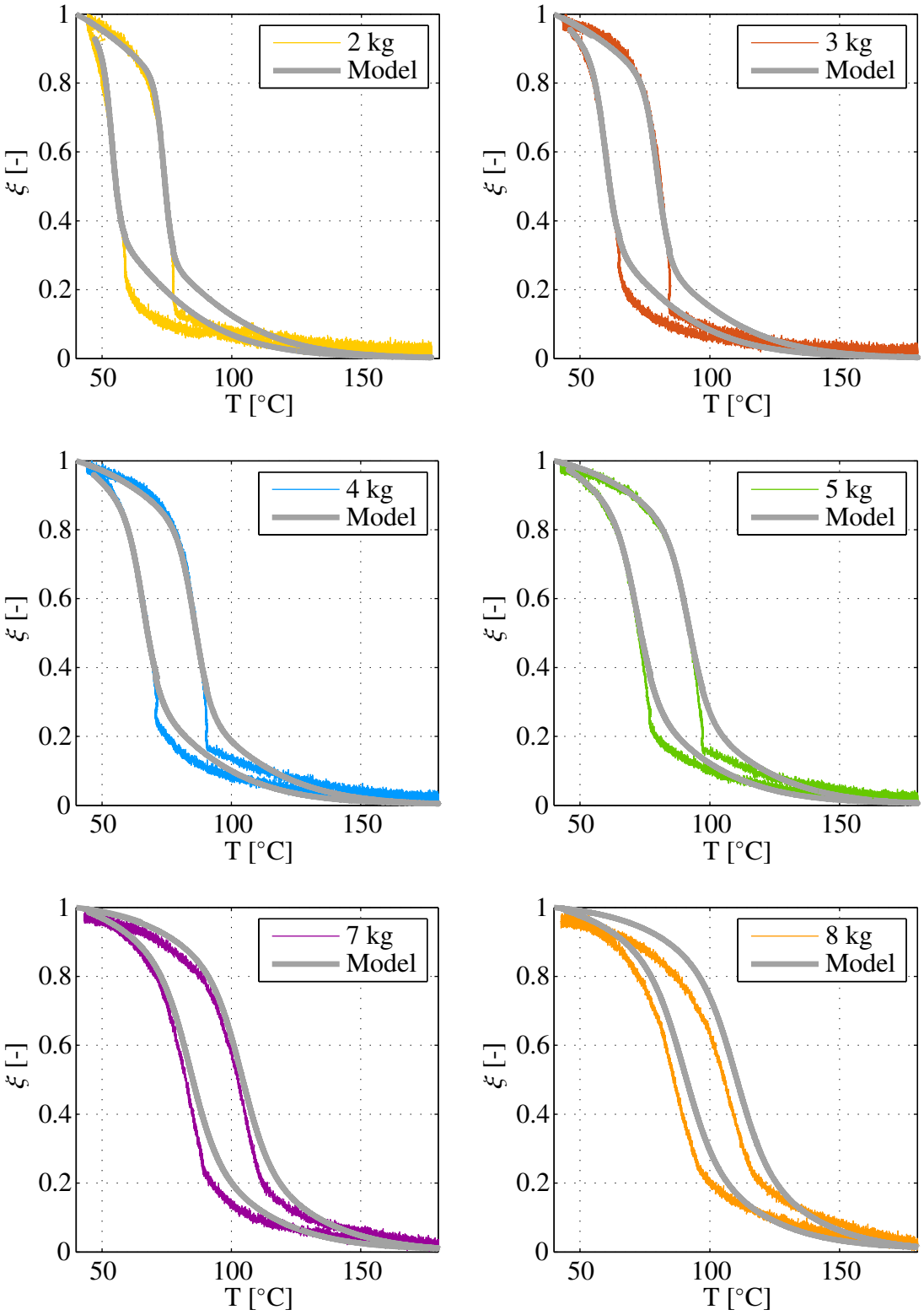

Figure 6-13: *Major hysteresis loop at various stresses with sinusoidal input current*

6.8 Model Validation: Minor Hysteresis Loop at Various Stresses

In order to generate minor loops, the wire was heated with a decaying sinusoidal current as shown in the top left plot of Fig. 6-14. The resulting wire temperature is in the top right plot. The wire was loaded with masses 3, 4 and 5 kg. The results of the experiment with the model prediction is shown in Fig. 6-14, with RMS errors in Tab. 6-5.

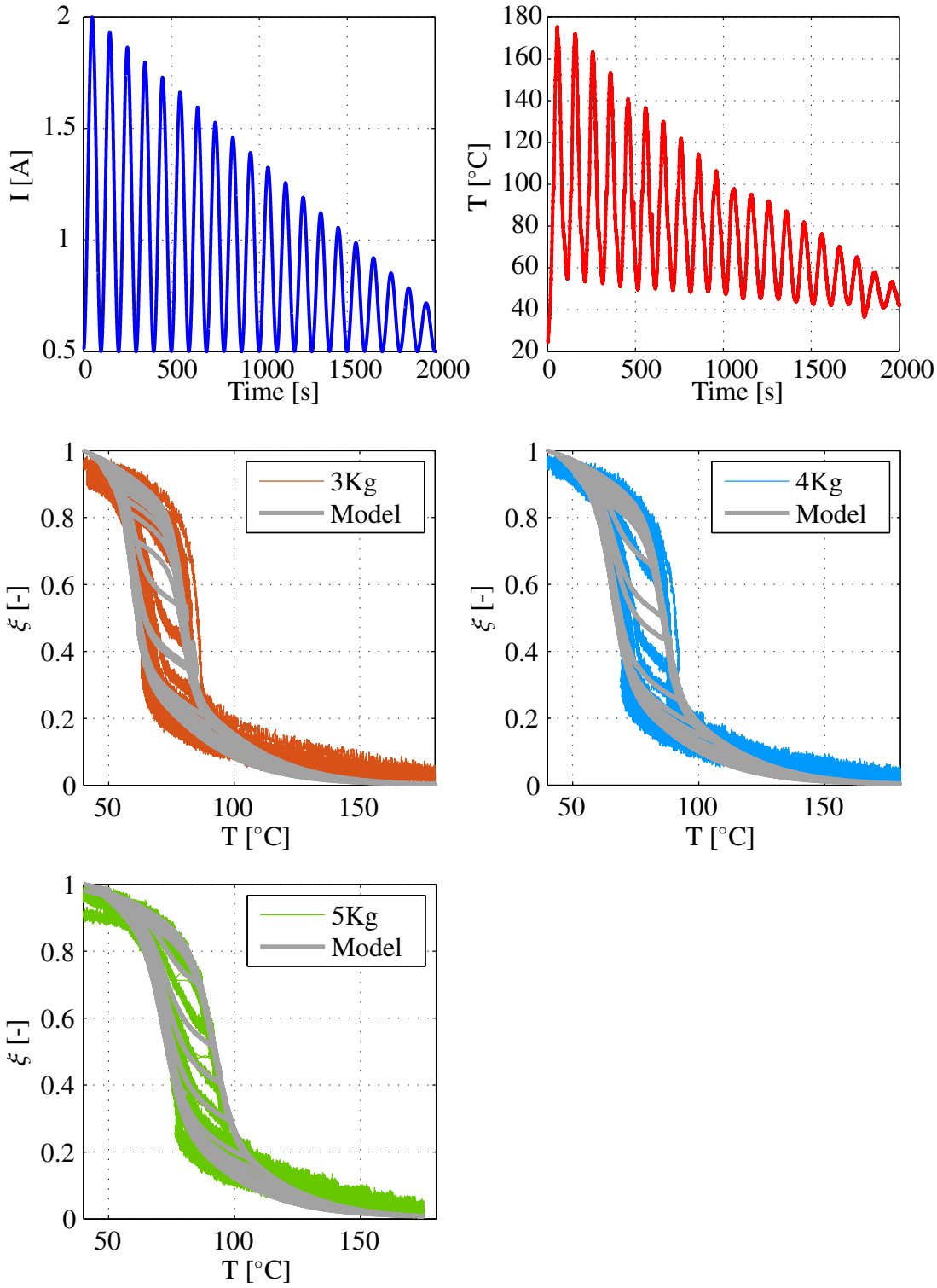

Figure 6-14: *Experimental and model correlation for minor hysteresis loop behaviour*

Table 6-5: *RMS Error between phase kinetic model and experiments for minor loops*

Mass [kg]	3	4	5
RMSE [%]	9.4	9	9

Note that due to the input current in the experiment above, the minor loops converge towards $\xi = 1$. In order to generate minor loops that converge towards $\xi = 0$, the changing sinusoidal in the top left plot of Fig. 6-15 is used. The resulting wire temperature is in the top right plot. The experimental results and model prediction are in Fig. 6-15 with an RMS error of 7%. All of the above minor loop experiments show good correlation with experimental data.

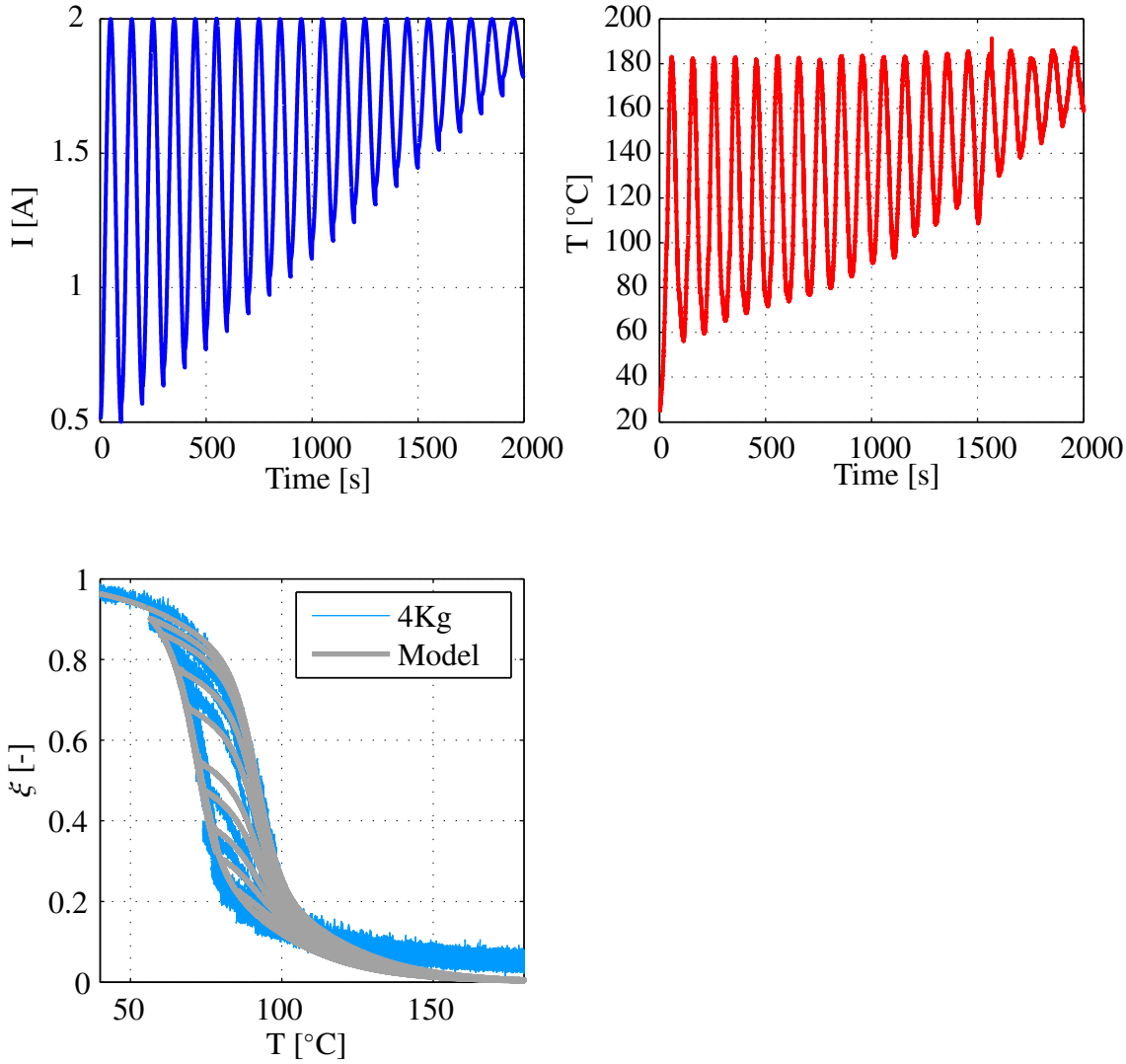

Figure 6-15: *Experimental and model correlation for reverse minor hysteresis loop behaviour*

6.9 Summary

In this section, the phase kinetic model for SMAs is presented. The model describes the evolution of the martensite fraction, and therefore the strain, based on the temperature of the SMA, regardless of the stress on the wire.

The model is developed by separately considering thermally and mechanically induced martensite that allow the calculation of the total martensite fraction evolution with varying stress and temperature. When the SMA is used as an actuator, the model predicts that the total martensite fraction is an average of the thermal and stress-induced martensite fractions. The good correlation between the model and experiments give weight to the accuracy of this hypothesis.

The model predicts the phase kinetic behaviour for SMAs for arbitrary temperature cycles, including minor loop behaviour and the shifting of the hysteresis to higher temperatures with increasing stress. Model validation using experiments with various temperature inputs at various (discrete) stresses shows exceptional correlation with measured data.

7 Inverse SMA Model

The previous chapters presented the stress-strain and phase kinetics models for SMAs. As both these models are computationally efficient and accurate enough to model SMA behaviour under various conditions, they can form the basis for the development of real-time control algorithms for SMA actuators. In order to be used online in a control loop, however, it is necessary to compute the inverse model. As both models are not analytically invertible, the derivation of the inverse is required and is the focus of this chapter.

7.1 Stress-Strain Model Inverse

In order to calculate the inverse of the stress-strain model, it is sufficient to invert the 's-shaped' curve in (4-5) as the entire algorithm is based on the definition of this curve (cf. Sect. 4.1). A schematic of the 's-shaped' curve and its inverse is in Fig. 7-1(a) and (b), respectively.

Recall from Sect. 4.1 that in order to generate the s-curve, first the partial derivative of the stress with respect to strain $\frac{\partial\sigma}{\partial\varepsilon}$, as shown by the blue curve in Fig. 7-1(c) is described with a sigmoid function (cf. (4-1)) and subsequently integrated to give (4-5), which produces the blue curve in Fig. 7-1(a). The ideal inverse is plotted by the blue curve in Fig. 7-1(b) and (d) by switching the abscissa and ordinate axes. The first attempt at computing the inverse was to use the same procedure as above, however with the slopes in the inverse curve as the reciprocals of the slopes from the forward curve. The partial derivative is therefore 'flipped' (Fig. 7-1(d)). The knees are $\sigma_{\varepsilon 1}$ and $\sigma_{\varepsilon 2}$ (see Fig. 7-1(b)) and the values of k_1 and k_2 are selected to match the slopes of ideal inverse in Fig. 7-1(d). Using these values, (4-5) is used to calculate the inverse curve with ε replaced with σ (and vice versa) and ε_p and σ_p swaped as shown in (7-1).

$$\begin{aligned}\varepsilon \;=\; &\left(\frac{1}{E_1}-\frac{1}{E_2}\right)\left[\sigma-\sigma_p+\frac{1}{k_1}\ln\left(\frac{1+e^{k_1(\sigma_p-\sigma_{\varepsilon 1})}}{1+e^{k_1(\sigma-\sigma_1)}}\right)\right] \;+\; \frac{1}{E_2}(\sigma \;-\; \sigma_p) \;+\; \varepsilon_p \;+\\ &\left(\frac{1}{E_3}-\frac{1}{E_2}\right)\left[\sigma-\sigma_p-\frac{1}{k_2}\ln\left(\frac{1+e^{-k_2(\sigma_p-\sigma_2)}}{1+e^{-k_2(\sigma-\sigma_2)}}\right)\right]\end{aligned} \tag{7-1}$$

The results are plotted with the red dashed curve in Fig. 7-1 and show very poor correlation with the forward s-curve. The discrepancy comes about in the inability to accurately compute the location of the knees and the curvature to accurately replicate the ideal inverse.

Therefore the inverse stress-strain model has to be approximated. This is done with the following procedure, using the segments a - b, b - e and e - f as shown in Fig. 7-2 below.

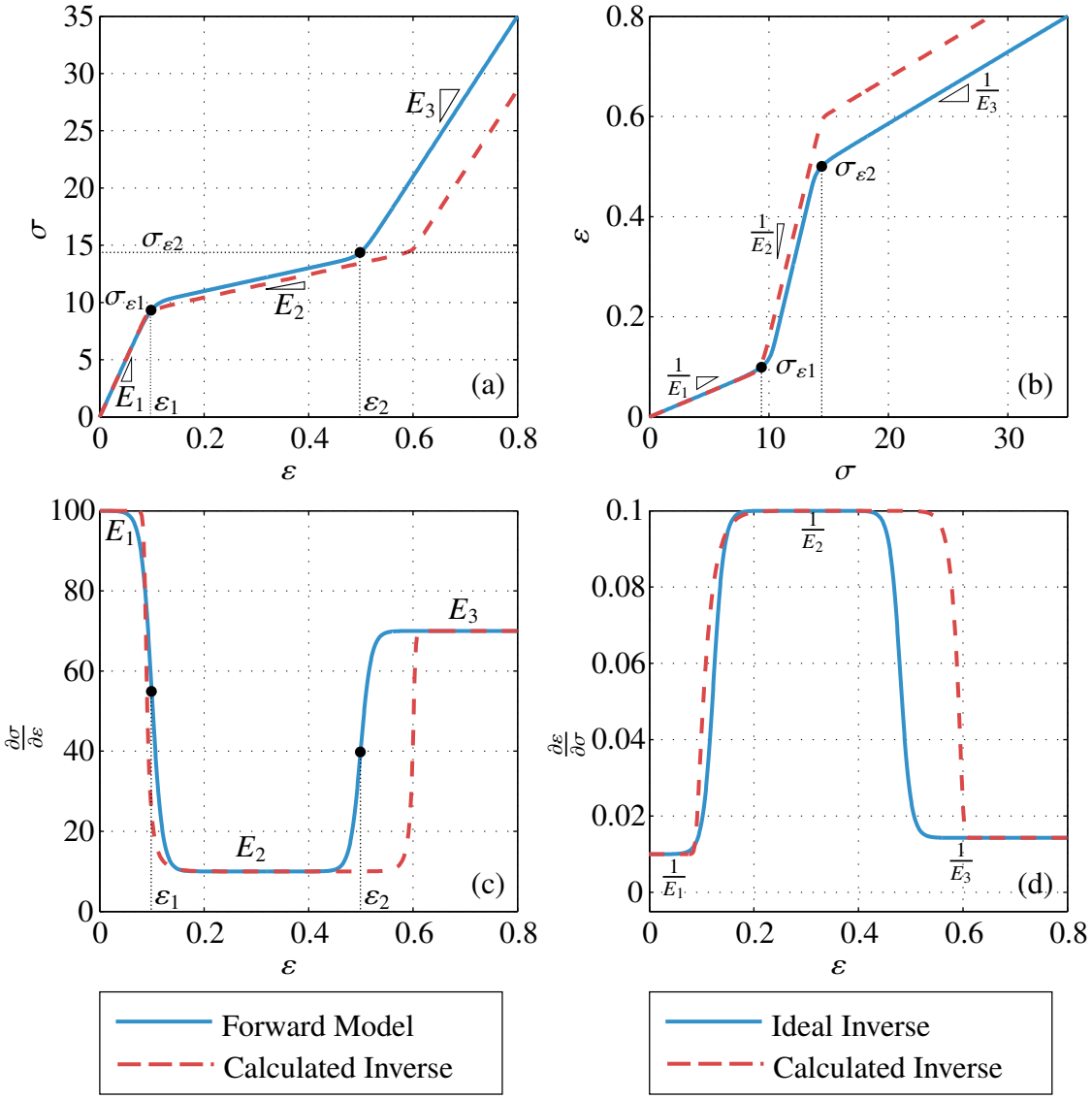

Figure 7-1: *Forward (a) and ideal inverse (b) s-shaped curve, (c) $\frac{\partial\sigma}{\partial\varepsilon}$ and (d) $\frac{\partial\varepsilon}{\partial\sigma}$ for ideal and calculated inverse stress-strain model)*

Segment b - e This segment is inverted with the sigmoid function y_2 in (7-3) as shown in Fig. 7-3. σ_n in (7-2) is the midpoint between the knee stresses $\sigma_{\varepsilon 1}$ and $\sigma_{\varepsilon 2}$. z_1 and z_2 are the maximum and minimum of the sigmoid. Their values are in (7-9) and (7-10), respectively, following the derivation of the rest of the inverse. The slope of the sigmoid at σ_n, given by k^{inv}, is proportional to $\frac{1}{E_2}$. It is calculated using the partial derivative of y_2 with respect to σ ($\frac{\partial y_2}{\partial\sigma}$) and setting $z_1 = \varepsilon_1$ and $z_2 = \varepsilon_2$ as shown in (7-4). Setting $\frac{\partial y_2}{\partial\sigma}$ to $\frac{1}{E_2}$ when $\sigma = \sigma_n$ gives k_{inv} in (7-5).

$$\sigma_n = \sigma_{bq}((\varepsilon_1 + \varepsilon_2)/2) \tag{7-2}$$

$$y_2 = \frac{z_2 - z_1}{1 + e^{-k^{inv}(\sigma - \sigma_n)}} + z_1 \tag{7-3}$$

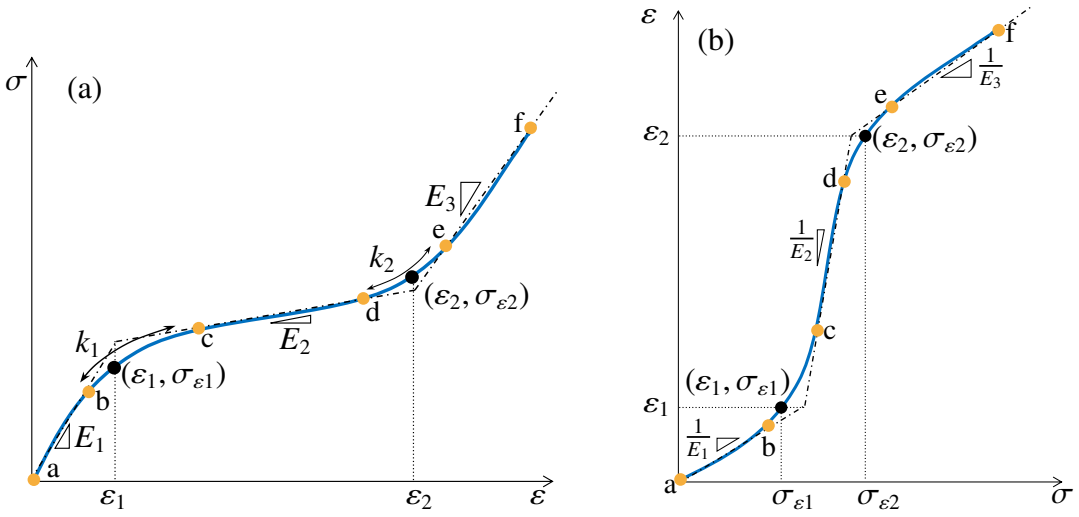

Figure 7-2: *Forward (a) and inverse (b) s-shaped curve for stress-strain model*

$$\frac{\partial y_2}{\partial \sigma} = \frac{k^{inv}(\varepsilon_2 - \varepsilon_1)e^{-k^{inv}(\sigma-\sigma_n)}}{\left(1 + e^{-k^{inv}(\sigma-\sigma_n)}\right)^2} \tag{7-4}$$

$$\frac{1}{E_2} = \frac{k^{inv}(\varepsilon_2 - \varepsilon_1)}{4}$$

$$k^{inv} = \frac{4}{E_2(\varepsilon_2 - \varepsilon_1)} \tag{7-5}$$

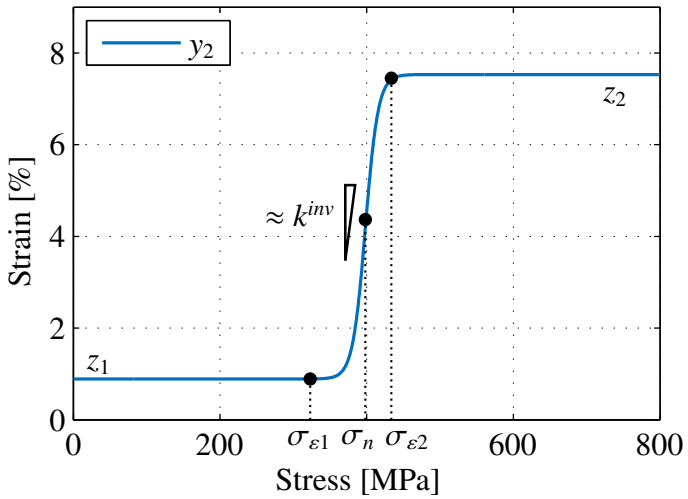

Figure 7-3: *Inverse equation for segment b-e*

Segment a - b This segment consists of a straight line with a slope $\frac{1}{E_1}$. It is modelled with the line y_1 in (7-6) with a slope m_1. Although m_1 is close in value to $\frac{1}{E_1}$, it is used instead because it allows better approximation of the curvature at the first knee. $y_2 + y_1$ results in the blue curve in Fig. 7-4.

$$y_1 = \overbrace{\frac{\varepsilon_1}{\sigma_{\varepsilon 1}}}^{m_1} (\sigma - \sigma_{\varepsilon 1}) \tag{7-6}$$

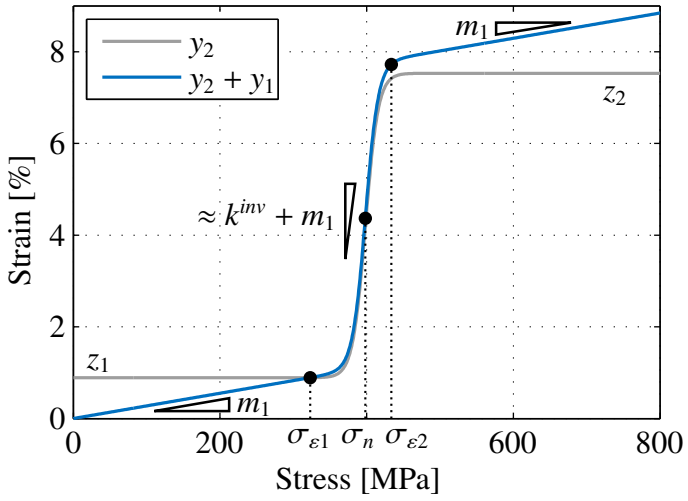

Figure 7-4: *Inverse equation for segment a-b*

Segment e - f This segment consists of a straight line with slope $\frac{1}{E_3}$ (see Fig. 7-2(b)). However, as adding y_1 to y_2 from the step above causes a slope m_1 to arise in this segment, the slope is corrected with y_3 in (7-7), shown by the black dashed curve in Fig. 7-5. Adding y_3 to $y_2 + y_1$, cancels out the slope m_1 and sets the correct slope $\frac{1}{E_3}$, as required.

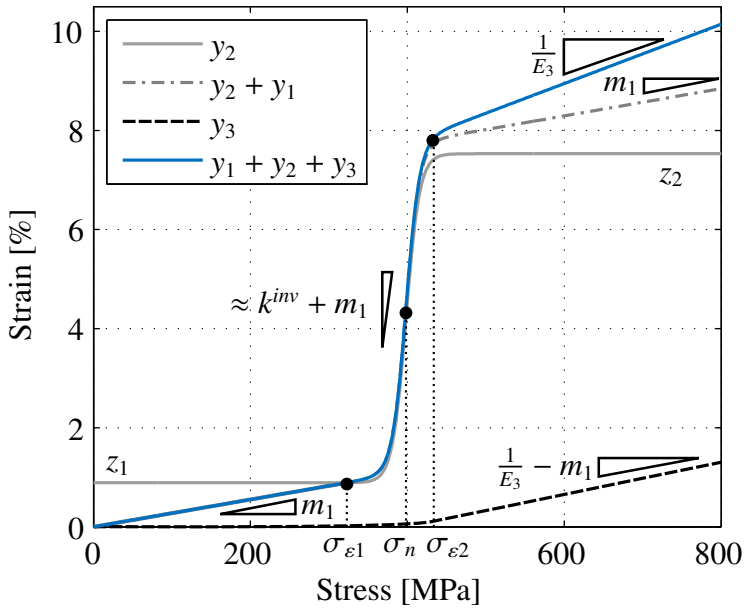

Figure 7-5: *Inverse equation for segment e-f*

$$y_3 = \left(\frac{1}{E_3} - m_1\right)\frac{\ln\left(1 + e^{k^{inv}(\sigma-\sigma_n)}\right)}{k^{inv}} \tag{7-7}$$

In y_3, when $\sigma \ll \sigma_n$, then $e^{k^{inv}(\sigma-\sigma_n)}$ is very small and $\ln\left(1 + e^{k^{inv}(\sigma-\sigma_n)}\right) \approx 0$, rendering $y_3 = 0$. Conversely, when $\sigma \gg \sigma_n$, then $e^{k^{inv}(\sigma-\sigma_n)} \gg 1$, and $\ln\left(1 + e^{k^{inv}(\sigma-\sigma_n)}\right) \approx k^{inv}(\sigma - \sigma_n)$. Here, $y_3 = \left(\frac{1}{E_3} - m_1\right)(\sigma - \sigma_n)$.

The final inverse is given by (7-8), using y_1, y_2, y_3 from above.

$$\varepsilon = \overbrace{m_1(\sigma - \sigma_{\varepsilon 1})}^{y_1} + \overbrace{\frac{z_2 - z_1}{1 + e^{-k^{inv}(\sigma-\sigma_n)}} + z_1}^{y_2} + \overbrace{\left(\frac{1}{E_3} - m_1\right)\frac{\ln\left(1 + e^{k^{inv}(\sigma-\sigma_n)}\right)}{k^{inv}}}^{y_3} \tag{7-8}$$

The value of z_1 is simply ε_1. To find z_2, σ in (7-8) is set to $\sigma_{\varepsilon 2}$ and ε is equated to ε_2. Consider that, in this case, the denominator of y_2, $\left(1 + e^{-k^{inv}(\sigma_{\varepsilon 2}-\sigma_n)}\right) \approx 1$, therefore $y_2 \approx z_2$ (see Fig. 7-3), and z_2 can be calculated using (7-10).

$$z_1 = \varepsilon_1 \tag{7-9}$$

$$z_2 = \varepsilon_2 - m_1(\sigma_{\varepsilon 2} - \sigma_{\varepsilon 1}) - \left(\frac{1}{E_3} - m_1\right)\frac{\ln\left(1 + e^{k^{inv}(\sigma_{\varepsilon 2}-\sigma_n)}\right)}{k^{inv}} \tag{7-10}$$

To test the inverse against the forward model, the monotonic loading model at various temperatures from Sect. 5.4 was plotted with both the forward (black) and inverse (red dashed) models in Fig. 7-6, with the NRMSE in Tab. 7-1.

Table 7-1: *NRMS Error between stress-strain forward and inverse models*

Temperature [°C]	25	45	55	75	100	120
NRMSE [%]	2.4	0.98	0.44	0.27	0.25	0.23

Note that the curvatures at the knees, set by parameters k_1 and k_2, cannot be explicitly defined with (7-8). Therefore correlation between the forward and inverse will be worst at the knees. For example, using the stress-strain model in Sect. 5.4 for temperatures 25°C and 45°C produce curves (see Fig. 7-6) where k_2 is approximately 170 and 260, respectively. For these temperatures, the inverse model shows discrepancies at the second knee and the NRMSE is 2.4% and 0.98%, respectively. At 55°C, the forward model has $k_2 \approx 330$, and there is reasonable correlation between the forward and inverse models (NRMSE of 0.44%). For all temperatures higher than 55°C, $k_2 > 400$ and they show good correlation between forward and inverse models with NRMSE under 0.27%. Therefore, the discrepancies are highest when the values k_2 are lower than 300 (i.e. the curve is long). Although this occurs for temperatures lower than 50°C, the errors between the forward and inverse models are still considerable low, with NRMSE values under 2.4%.

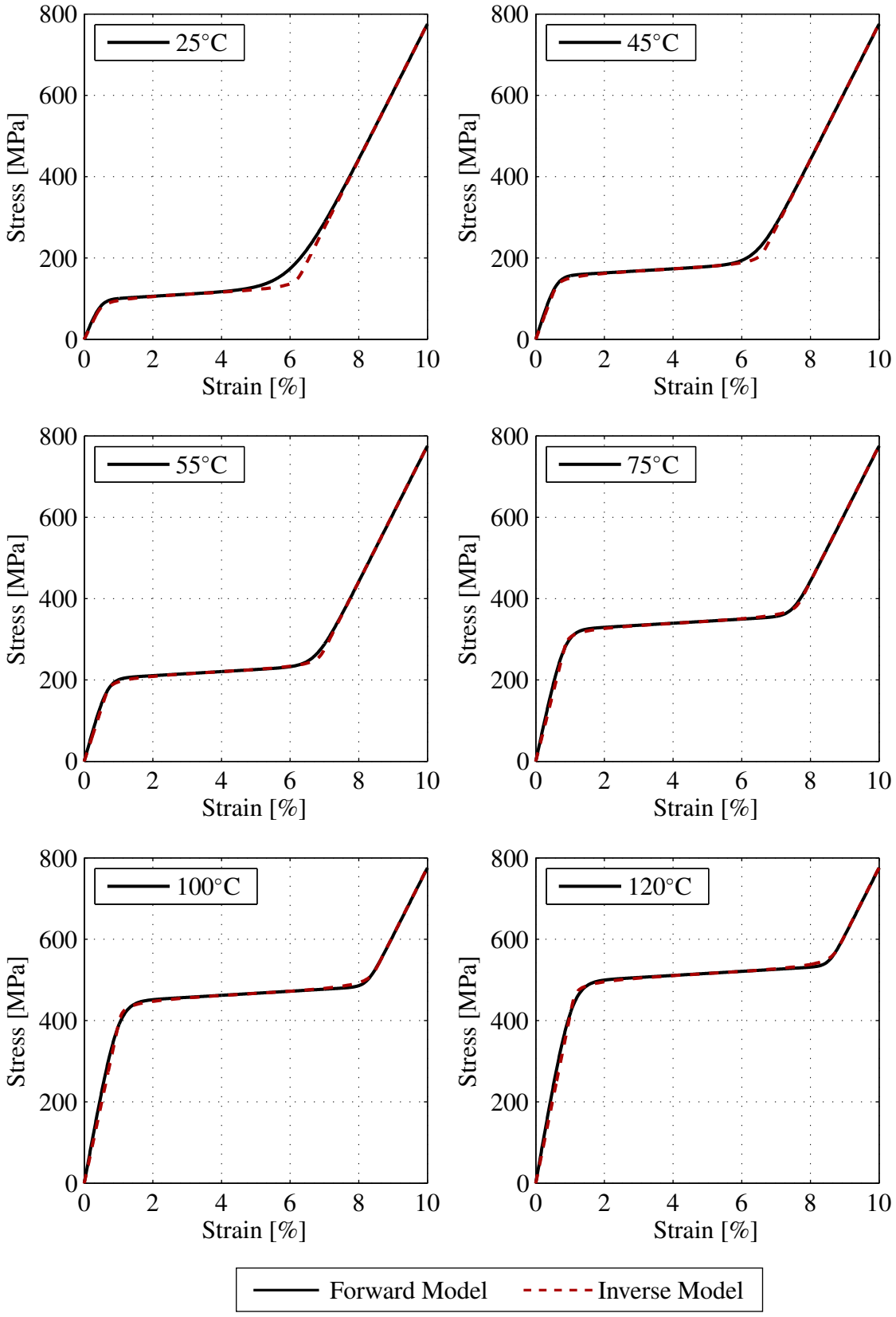

Figure 7-6: *Forward and inverse for stress-strain model for various temperatures*

7.2 Phase Kinetics Model Inverse

The forward and inverse phase kinetics model are in Fig. 7-7(a) and (b), respectively. As the forward model is not analytically invertible, a similar method as used for the stress-strain model above is used to derive the inverse model.

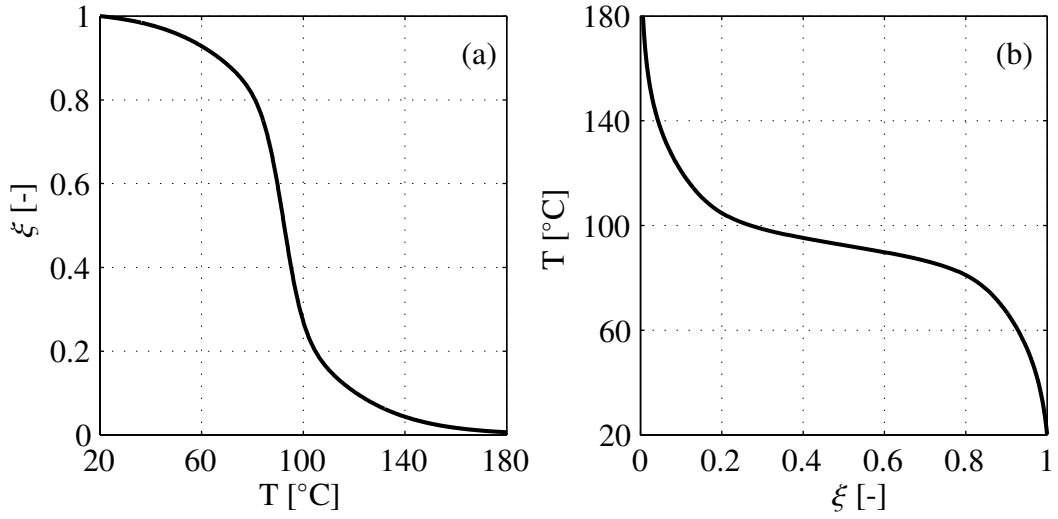

Figure 7-7: *Forward (a) and inverse (b) for phase kinetic model*

The heating curve is shown in (7-11), which is the expanded form of (6-31) using (6-6) and (6-18). Taking the derivative of ξ^H w.r.t. temperature T gives (7-12). The cooling curve is identical with superscript H changed to C for all the calculations in this section.

with $\iota = 2 - \xi_S(\varepsilon_m) - \xi_S(\varepsilon_a)$

$$\xi^H = \frac{\overbrace{\iota\alpha_T^a\left(1+e^{k^H(T_m-\beta^H)}\right)}^{\alpha_T^H}}{2\left(1+e^{k^H(T-\beta^H)}\right)} + \frac{\iota\gamma_T^H + \xi_S(\varepsilon_a)}{2} + \frac{\overbrace{\alpha_S^a\left(1+e^{(8/c_m\sigma)(T_m-\beta^H)}\right)}^{\alpha_S^H}}{2\left(1+e^{(8/c_m\sigma)(T-\beta^H)}\right)} + \frac{\gamma_S^H}{2} \tag{7-11}$$

$$\frac{\partial\xi^H}{\partial T} = \frac{-\alpha_T^H k^H e^{k^H(T-\beta^H)}}{2\left(1+e^{k^H(T-\beta^H)}\right)^2} - \frac{4\alpha_S^H e^{(8/c_m\sigma)(T-\beta^H)}}{c_m\sigma\left(1+e^{(8/c_m\sigma)(T-\beta^H)}\right)^2} \tag{7-12}$$

Consider T_m and T_a to be the temperatures at which ξ is 1 and 0, respectively (see (7-13) and (7-14)) as shown in Fig. 7-7.

$$T_m = T(\xi = 1) = 20°\text{C} \tag{7-13}$$

$$T_a = T(\xi = 0) = 180°\text{C} \tag{7-14}$$

Defining the derivative at three temperatures: $T = \beta^H$, T_m, T_a, gives (7-15), (7-16) and (7-17), respectively.

$$d\xi_\beta = \left.\frac{\partial \xi^H}{\partial T}\right|_{T=\beta_H} = \frac{-\alpha_T^H k^H}{8} - \frac{\alpha_S^H}{c_m \sigma} \tag{7-15}$$

$$d\xi_{Tm} = \left.\frac{\partial \xi^H}{\partial T}\right|_{T=T_m} \tag{7-16}$$

$$d\xi_{Ta} = \left.\frac{\partial \xi^H}{\partial T}\right|_{T=T_a} \tag{7-17}$$

The tangents of the inverse curve at $T = \beta^H$, $T = T_m$ and $T = T_a$ are related to the reciprocal of $d\xi_\beta$, $d\xi_{Tm}$ and $d\xi_{Ta}$, respectively, as shown in Fig. 7-8.

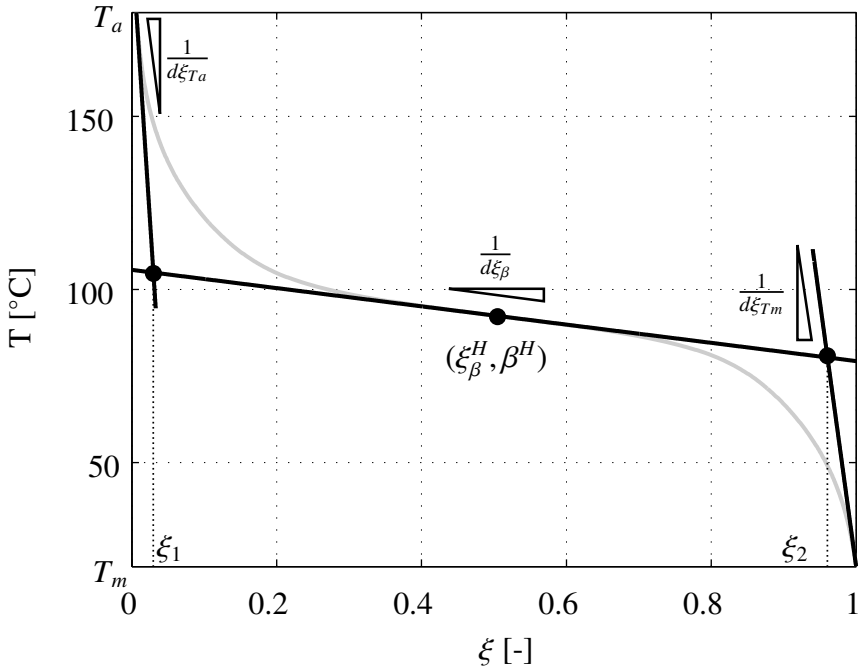

Figure 7-8: *Phase kinetic model inverse with tangents at T_m, β^H and T_a*

The intersection of the tangents are used to find the location of the 'knees' ξ_1 and ξ_2 according to (7-19) and (7-20), where γ^H is defined in (7-18). ξ_β^H is ξ from (7-11), evaluated at temperature $T = \beta_H$.

Recall that for the forward model γ ($0 \leq \gamma \leq 1$) represents the 'offset' of the hysteresis (see Fig. 6-2). The same values γ are used for the inverse, however in this case, it represents the shift of the inverse to the right (to higher ξ values).

$$\gamma^H = \frac{\iota\gamma_T^H + \xi_S(\varepsilon_a) + \gamma_S^H}{2} \tag{7-18}$$

$$\xi_1 = \frac{\frac{\gamma^H}{d\xi_{Ta}} - T_a - \frac{\xi_\beta^H}{d\xi_\beta} + \beta_H}{\frac{1}{d\xi_{Ta}} - \frac{1}{d\xi_\beta}} \tag{7-19}$$

$$\xi_2 = \frac{\frac{1+\gamma^H}{d\xi_{Ta}} - T_m - \frac{\xi_\beta^H}{d\xi_\beta} + \beta_H}{\frac{1}{d\xi_{Tm}} - \frac{1}{d\xi_\beta}} \tag{7-20}$$

The inverse is described by h_1, h_2 and h_3, as shown in Fig. 7-9 and in (7-24). The values of the slopes x and m are found by considering the start and end-points of the inverse, defined by (ξ_p, T_p) and (ξ_q, T_q). For the major loop in Fig. 7-9 (7-21) follows:

$$\begin{aligned} \text{Start:} \quad (\xi_p, T_p) &= (0, T_a) = (\xi_a, T_a) \\ \text{End:} \quad (\xi_q, T_q) &= (1, T_m) = (\xi_m, T_m) \end{aligned} \tag{7-21}$$

When considering the start point where ξ values are low, setting $(\xi, T) = (\xi_p, T_p)$ in (7-24) renders $h_3 \approx 0$. This can also be observed in Fig. 7-9, where the black dashed line that represents h_3 is 0 except when ξ values are close to 1. x is then calculated by solving (7-24) for x with (7-22). Similarly, when the end-point is considered, $(\xi, T) = (\xi_q, T_q)$ and $h_1 \approx 0$ as shown by the dark grey line for h_1 in Fig. 7-9. m is then calculated with (7-23).

$$x = \frac{k_b(T_p - \overbrace{\frac{\xi_p - \xi_\beta}{d\xi_\beta} - \beta}^{-h_2(\xi_p)})}{\ln\left(1 + e^{-k_b(\xi_p - \xi_1)}\right)} = \frac{k_b(d\xi_\beta^H(T_p - \beta^H) - \xi_p + \xi_\beta^H)}{d\xi_\beta^H \ln\left(1 + e^{-k_b(\xi_p - \xi_1)}\right)} \tag{7-22}$$

$$m = \frac{k_b(T_q - \overbrace{\frac{\xi_q - \xi_\beta}{d\xi_\beta} - \beta}^{-h_2(\xi_q)})}{\ln\left(1 + e^{k_b(\xi_q - \xi_2)}\right)} = \frac{k_b(d\xi_\beta^H(T_q - \beta^H) - \xi_q + \xi_\beta^H)}{d\xi_\beta^H \ln\left(1 + e^{k_b(\xi_q - \xi_2)}\right)} \tag{7-23}$$

Note that the values of m and x are different from the slopes $\frac{1}{d\xi_{Ta}}$ and $\frac{1}{d\xi_{Tm}}$ (see Fig. 7-8). It is necessary to adjust these slopes in order to ensure that the end-points of the inverse and forward models are congruent, which is imperative for minor loop branching.

The inverse is then described mathematically with (7-24) (see Fig. 7-9).

$$T = \overbrace{\frac{x}{k_b} \ln\left(1 + e^{-k_b(\xi^H - \xi_1)}\right)}^{h_1} + \overbrace{\frac{\xi^H - \xi_\beta^H}{d\xi_\beta} + \beta}^{h_2} + \overbrace{\frac{m}{k_b} \ln\left(1 + e^{k_b(\xi^H - \xi_2)}\right)}^{h_3} \tag{7-24}$$

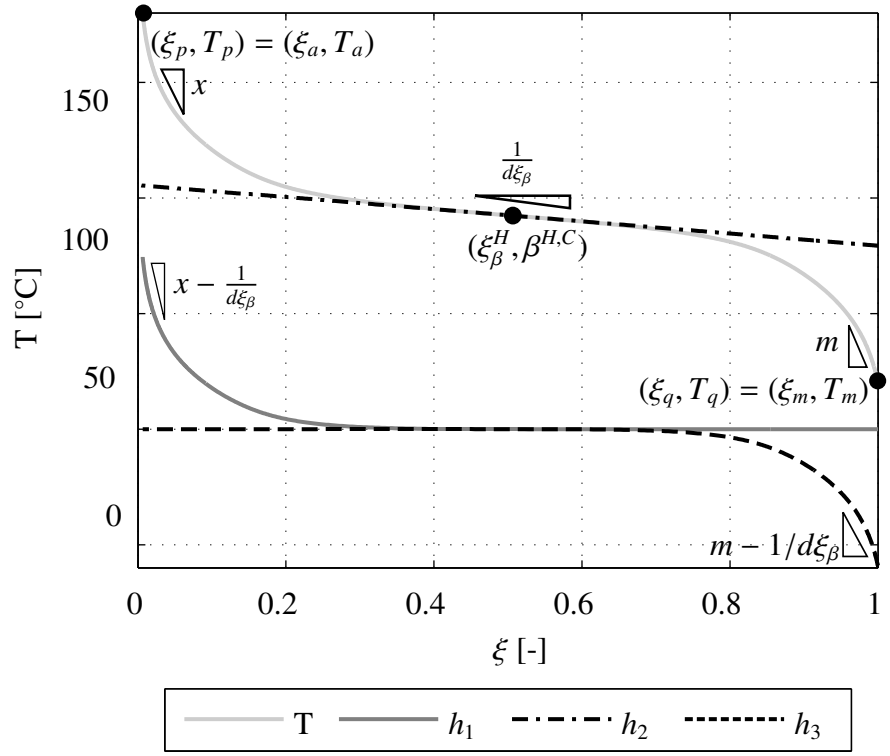

Figure 7-9: *Calculation of inverse phase kinetic model*

In order to model minor loop behaviour in the inverse model, the same algorithm as in Sect. 6.3 is used to calculate the γ parameters (required for the calculation of ξ_1 and ξ_2). However, rather than the change in temperature T, the change in martensite fraction ξ triggers minor loop branching. Further, the values of T_p, T_q and ξ_p, ξ_q (required for the calculation of x and m in (7-22) and (7-23), respectively) are initialised according to (7-25). Their values are updated (and held) when the martensite fraction (and therefore temperature) changes direction as in (7-26) and (7-27), where ξ_{sw} and T_{sw} are the values of ξ and T at the switching point.

Initialisation

$$\begin{aligned} \gamma &= 0 \\ (\xi_p, T_p) &= (0, T_a) \\ (\xi_q, T_q) &= (1, T_m) \end{aligned} \tag{7-25}$$

Switching: decreasing ξ to increasing ξ (heating to cooling)

$$\begin{aligned} \gamma &= (\iota\gamma_T^C + \gamma_S^C + \xi_S(\varepsilon_a))/2 \quad \text{(6-31)} \\ (\xi_p, T_p) &= (\xi_{sw}, T_{sw}) \\ (\xi_q, T_q) &= (1, T_m) \end{aligned} \tag{7-26}$$

Switching: increasing ξ to decreasing ξ (cooling to heating)

$$\begin{aligned} \gamma &= (\iota\gamma_T^H + \gamma_S^H + \xi_S(\varepsilon_a))/2 \quad \text{from (6-31)} \\ (\xi_p, T_p) &= (0, T_a) \\ (\xi_q, T_q) &= (\xi_{sw}, T_{sw}) \end{aligned} \tag{7-27}$$

In order to test the inverse model, the temperature profile in Fig. 7-10(a) is input into the forward model in (6-30). The resulting ξ, shown with the black solid curve in Fig. 7-10(b) is then input into the inverse model in (7-24).

The result, shown by the red dashed curve in both Figs. 7-10(a) and (b), shows good correlation to the forward model other that at the lowest and highest temperatures where the inverse deviates from the forward model. This is due to the assumption that at $T = T_a$, $\xi = 0$ and at $T = T_m$, $\xi = 1$. However, since the forward model used exponential functions, $\xi = 0$ and $\xi = 1$ occur in the limits as the temperature $T \to \infty$ and $T \to -\infty$, rather than at the absolute values T_a and T_m.

The procedure to test the inverse is repeated for a more complicated temperature profile as shown in Fig. 7-10(c), which causes the formation of several minor loops. The forward and inverse models shown in Fig. 7-10(c) and (d) display good correlation to one another, with the lowest and highest temperatures once again showing the worst correlation. For both tests, the forward to inverse model correlation is within 2%.

7.3 Summary

This chapter presents the inverse for the stress-strain and phase kinetics SMA models from the previous chapters. As both models are not analytically invertible, the inverse is calculated by developing analytical equations that approximate the forward models.

The stress-strain inverse is developed for the base s-curve and shows good correlation between the forward and inverse models. The exception to this is when the k_2 values which describe the curvature of the stress-strain curves at the second knee is less than 300 i.e. when the curve at the knee is long. This occurs only for temperatures less than 50°C, whereby the correlation between the forward and inverse models is still acceptable with a maximum NRMSE deviation of 2.4%.

The phase-kinetics inverse also shows good correlation between the forward and inverse models except at very high or very low temperatures due to the use of exponential functions. The NRMSE is shown to be 2%.

Nevertheless, the inverse for both the stress-strain model and phase kinetics model are sufficient and as they are also computationally efficient, they can be used online in a control loop.

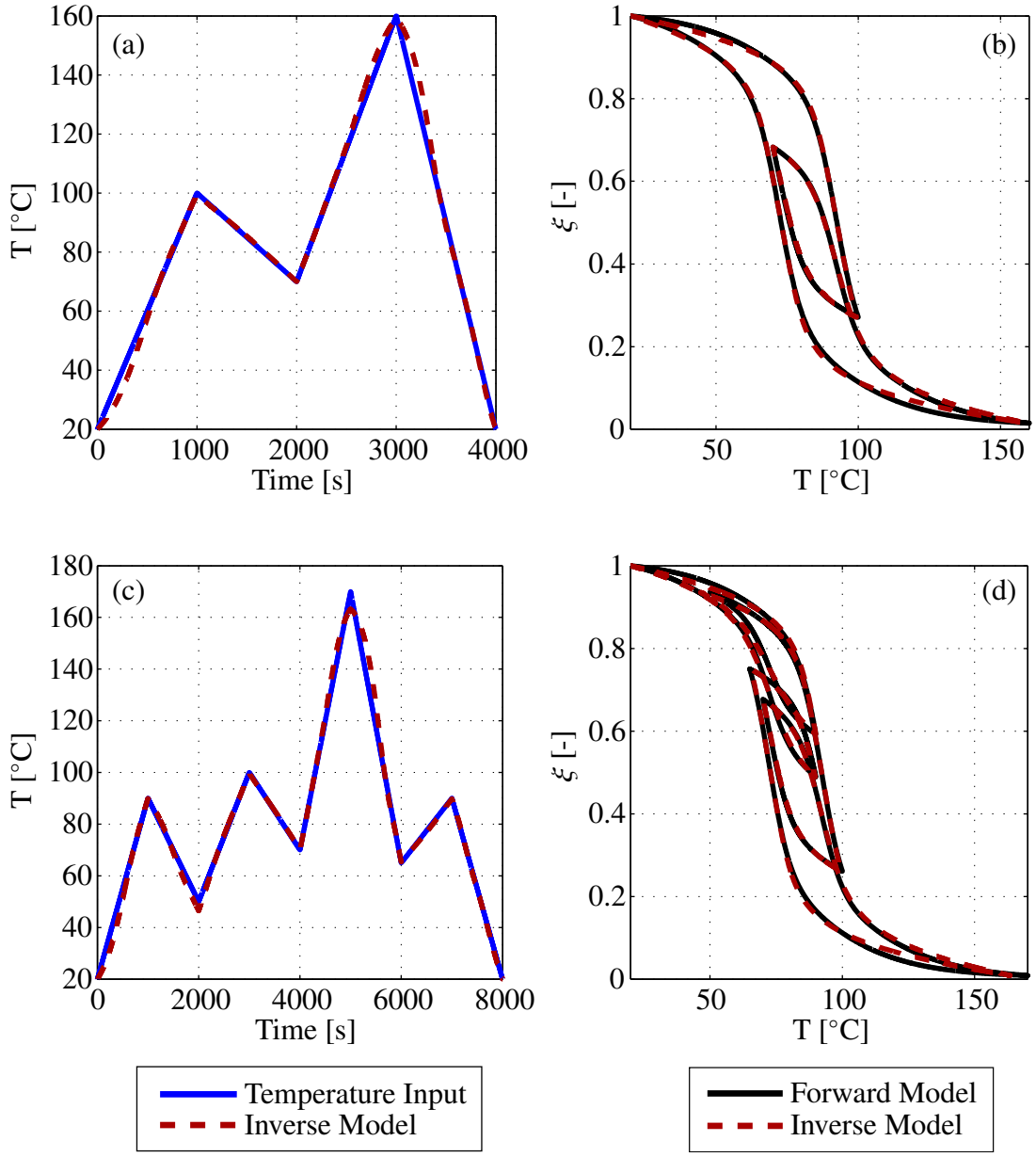

Figure 7-10: *Forward and inverse phase kinetic model*

8 Model-based Position Control

The shape memory effect was modelled and validated in Chaps. 4 - 6. It describes shape recovery of SMAs after deformation by increasing the SMA temperature. The shape memory effect can be exploited to work on a load, and SMAs can hereby be used as actuators. Such SMA actuators have attractive properties such as high energy density, smooth and silent actuation, scalability etc. However, due to the inherent extremely nonlinear and hysteretic behaviour of SMAs, the design of actuators for position control, for example, is non-trivial.

In this chapter, the results for position control with various controllers is presented. The focus of the controller design was to ensure precision control of the SMA wire, with controller algorithms that are computationally efficient enough to be implemented on an embedded processor. To this end, the controllers investigated are non-linear controllers, VSC and PWM based controllers. In addition to showing promising results in controlling SMAs, they are straightforward to implement onto a microprocessor (cf. Chap. 3). Further, as the model developed in the previous chapters fulfils the demand of computational efficiency, it is used online within the control loop to increase controller precision.

The SMA wire used is of the same type as in Chaps. 5 and 6[1]. The experimental set-up, shown in Fig. 8-1, was the same as in Chap. 6 (cf. Fig. 6-10). The SMA wire is loaded with a set of slotted weights from 2 kg to 10 kg. Position and force control of SMAs can be achieved by controlling the temperature of the wire. This is often performed by resistive heating (joule effect), where current is used to increase the wire temperature. Cooling is performed via natural convection. The wire current is therefore the control input. For feedback control purposes, three sensors were used: a laser distance sensor to measure the strain, a force sensor to measure loads on the wire and a thermocouple to measure the wire temperature.

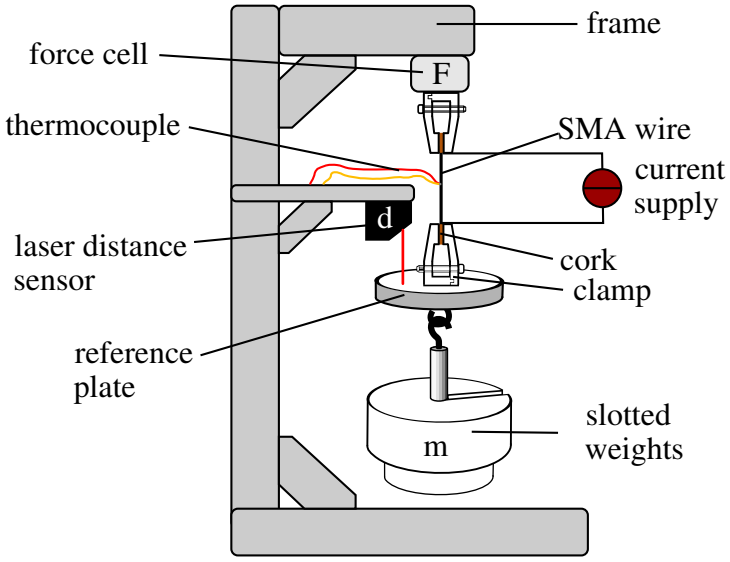

Figure 8-1: *Experimental set-up*

[1]Wire from SAES Getters with a diameter of 0.5 mm and A_s of 95°C.

The first control strategy proposed in this thesis is a model-based temperature controller in Sect. 8.1. Based on the desired strain, a desired temperature is calculated online from the computationally efficient SMA constitutive and phase kinetics models, as presented in Chaps. 4 - 7. Two types of controllers are investigated:

- A model-based, nonlinear temperature controller with control signals modulated with PWM.
- A model-based, nonlinear temperature controller with control signals sent directly to the wire.

While the aforementioned controllers give satisfactory results for coarse positioning of the wire, precision is increased by using an additional strain controller for fine positioning (Sect. 8.2). To this end, two types of controllers are investigated:

- A model-based, nonlinear temperature and strain controller with control signals modulated with PWM (Sect. 8.3).
- A model-based, nonlinear temperature controller and VSC strain controller with control signals sent directly to the wire (Sect. 8.4).

The performance of the controllers for a series of steps (Sect. 8.5) and sinusoids (Sect. 8.6) for various constant masses show good tracking. The bandwidth of the SMA actuator without active cooling is investigated in Sect. 8.7. Additionally, the robustness of the control law when the SMA is exposed to varying loads and disturbances is shown in Sect. 8.8.

8.1 Position Control via Temperature Control

The first attempt at controlling the SMA wire position is by using model-based temperature control with a control architecture as shown in Fig. 8-2. The inverse thermomechanical model, developed in Chap. 7 predicts a desired wire temperature T_{cal} to achieve a desired strain ε_{des}. A feedback temperature controller is subsequently used to increase the wire temperature T_{act} to the desired T_{cal}. The controller output u_T is then sent to a current driver, that either routes u_T directly to the wire (1 in Fig. 8-2), or first modulates the signal with PWM and then sends it to the wire (2 in Fig. 8-2).

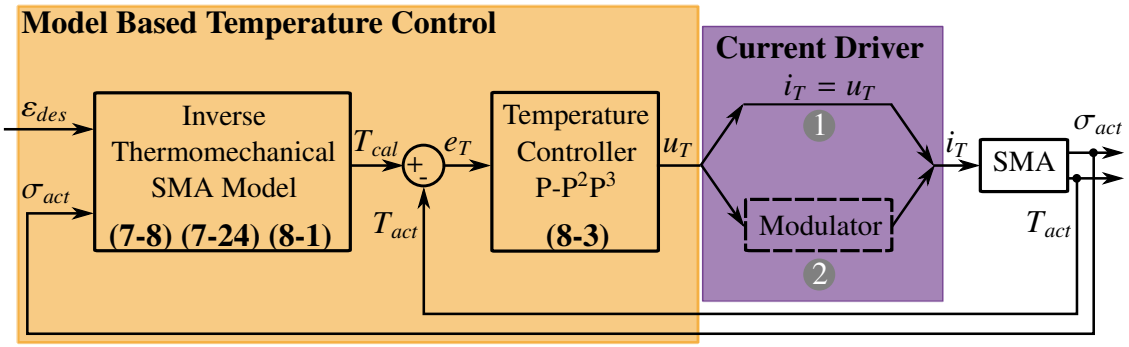

Figure 8-2: *Model-based temperature controller structure*

The inputs to the inverse model are the desired strain ε_{des} and the measured stress on the wire σ_{act}. Recall that the hysteresis in SMAs is dependant on the stress acting on the wire (cf. Sect. 2.6). The models presented in the previous chapters include this stress dependance. Therefore, in order to calculate T_{cal} for a given ε_{des}, the wire stress σ_{act} is required. At a given σ_{act}, the maximum and minimum strains possible are calculated by the constitutive inverse model in (7-8). This is shown exemplarily in Fig. 8-3 for a constant stress σ_{act} of 400 MPa, where ε_a and ε_m are the strains at 100% martensite ($T < M_f$) and 100% austenite ($T > A_f$). These strains are the strain limits achievable by the SMA wire at σ_{act}. They are used to normalise ε_{des} to calculate ξ_{des} using (8-1), as shown schematically by the green dot in Fig. 8-3(a). The desired temperature T_{cal} is then calculated using the phase kinetics inverse model in (7-24) as shown by the green dot in Fig. 8-3(b). Note that the red and blue dots in Fig. 8-3(a), which represent ε_a and ε_m, are at $\xi = 0$ and $\xi = 1$ in Fig. 8-3(b).

$$\xi_{des} = \frac{\varepsilon_{des} - \varepsilon_a}{\varepsilon_m - \varepsilon_a} \tag{8-1}$$

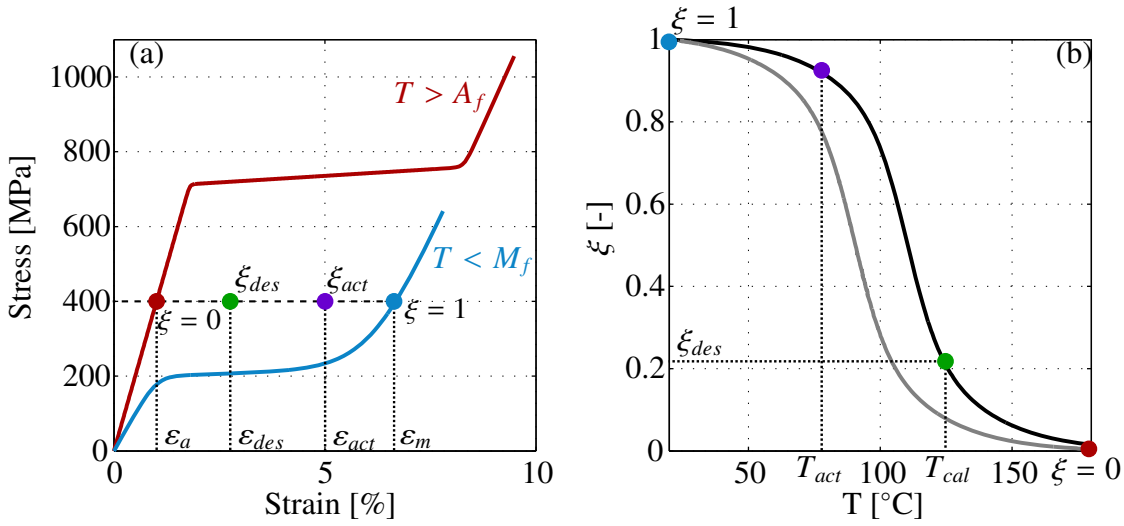

Figure 8-3: *Calculation of desired temperature with inverse model*

The temperature controller is based on a nonlinear NPID controller in (8-2), as proposed by Rahman in [RKA08]. It consists of a conventional PID controller appended with a nonlinear component $K_T^N(e_T^2 + e_T^3)$, where $e_T = T_{cal} - T_{act}$ is the temperature error. When the error is large, the nonlinear term causes large gains, which is desirable. When the error approaches 0, this nonlinear term almost vanishes and the controller acts as a normal PID. The feedback signal is the wire temperature, measured with a thermocouple.

$$u_T(t) = K_T^P e_T + K_T^I \int e(\tau)d\tau + K_T^D \dot{e}_T + K_T^N(e_T^2 + e_T^3) \tag{8-2}$$

As mentioned in the literature review in Chap. 3, the I-gain K_T^I, that is theoretically used to reduce the steady state error, causes overshoots due to wind-up caused by the hysteresis and the sluggish cooling behaviour [AD14]. To this end, the I-gain is often omitted when controlling SMAs as in [MSL04], [MS03], [KLH06] and is therefore set to 0 here. The D-gain K_T^D is also set to 0 because the temperature signal from the thermocouple is noisy

and a D-gain would undesirably amplify this noise [FKL+13]. In fact the D-gain is often omitted in PID controllers. Since both the I-gain and the D-gain are set to 0, the controller is called P-P^{2}P^3 (using the naming convention adopted by [SAS05]). The gain K_T^N is also split into two gains K_T^{P2} and K_T^{P3} for the cubed and squared error, respectively.

Consider that when the error is negative ($T_{act} > T_{cal}$), the wire needs to be cooled and therefore $u_T(t)$ should also be negative. However, since e_T^2 is always positive, the value of u_T could become positive based on the relative values of K_T^P, K_T^{P3} and K_T^{P2} and the wire would be heated rather than cooled. In order to avoid this, a $sgn(e_T)$ term is added to the quadratic error to ensure that $u_T(t)$ is negative, when the error is negative. The final control law is shown in (8-3).

$$u_T(t) = K_T^P e_T + K_T^{P2}(sgn(e_T)e_T^2) + K_T^{P3} e_T^3 \tag{8-3}$$

The output of the controller u_T is applied to the SMA wire using two methods. In the first method, the controller outputs current values that are directly sent to the SMA i.e. $u_T = i_T$, as shown by branch ❶ in Fig. 8-2.

In the second method, as shown by branch ❷ in Fig. 8-2, the u_T is first modulated via Pulse Width Modulation (PWM), according to Ma and Song in [MS03]. Their proposed modulator is shown in Fig. 8-4. The controller signal u_T is added to a triangular wave u_Δ, with amplitude a_Δ and frequency f_Δ. The resulting signal u_s is then sent into a saturation block that is 'ON' when u_s is above a threshold g_{thr}, and 'OFF' otherwise[2]. The required parameters, shown in Tab. 8-1, were selected after iterative experiments that were performed to ensure that the maximum possible current was sent to the SMA when fast heating was required and $i_T = 0$ when cooling was required. Using this modulation, a series of current pulses i_T based on the controller output is generated, as shown in Fig 8-5, and sent to the SMA.

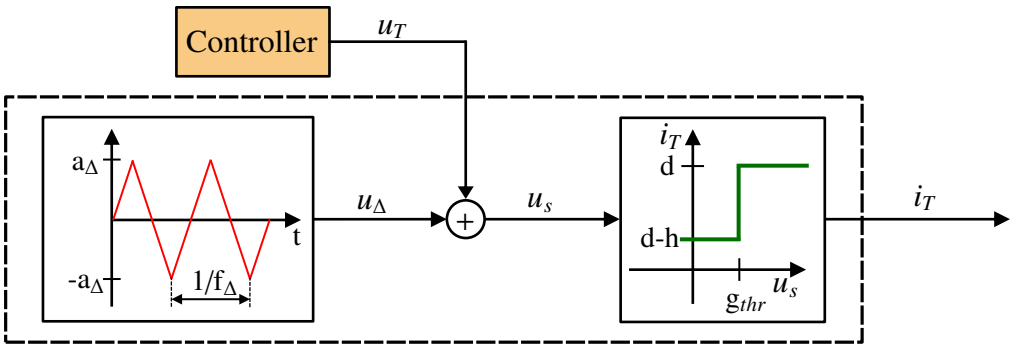

Figure 8-4: *Modulation of controller output with Pulse Width Modulation*

Table 8-1: *PWM parameters*

f_Δ	a_Δ	d	$d-h$	g_{thr}
25 Hz	1.2 A	3 A	0 A	1.2 A

[2] 'ON' signifies that 3A is sent to the wire. When u_s is below g_{thr}, a minimum current based on $d-h$ could be sent to the wire. As $d-h$ is 0A (see Tab. 8-1), the output is 'OFF'.

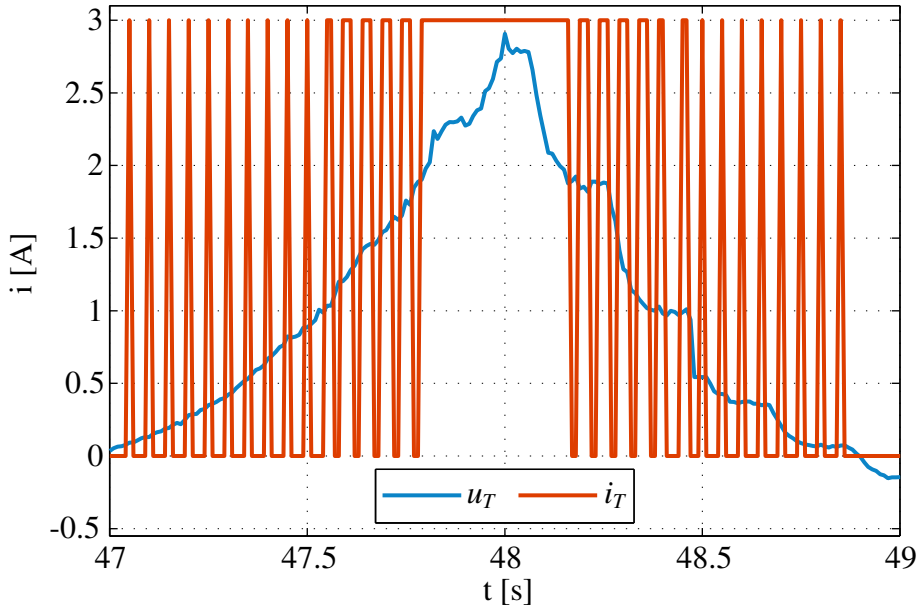

Figure 8-5: *Pulse Width Modulation pulses based on controller output*

To test the control law, a desired strain with a step height of -4% strain is set (see Fig. 8-7). Note that a strain of 0% is defined when the wire is loaded and at room temperature (T_{amb} = 20°C), as shown schematically by (a) in Fig. 8-6[3]. When the SMA is heated, it contracts and the strain is therefore negative. When the desired strain steps to -4%, as at t = 2s in Fig. 8-7, the SMA is at (b) in Fig. 8-6, where the wire is 4% shorter than at (a). The controller architecture in Fig. 8-2 is then used to heat the SMA wire accordingly in order to track the desired strain step using both the direct control signal and a PWM control signal, as described by branches (1) and (2) in Fig. 8-2. The parameters using both methods are in Tab. 8-2. They were selected iteratively to achieve the best tracking performance for the SMA. The position control results are shown in Fig. 8-7 with the solid red and green curves for the direct and PWM control signals, respectively.

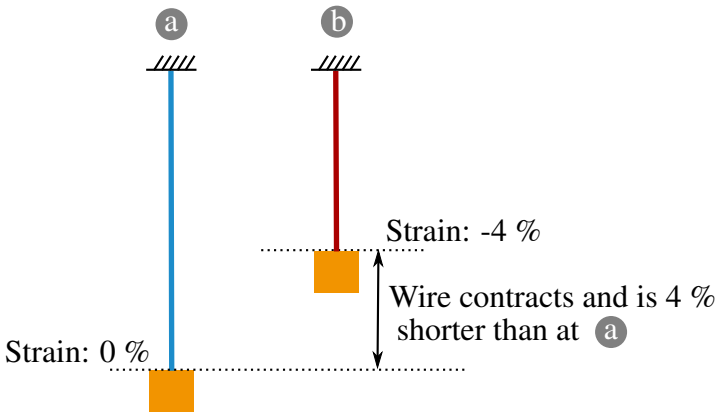

Figure 8-6: *Desired strain of -4% for SMA actuator*

[3]For the experiments in Chaps. 4 to 6, 0% strain is defined (differently) as the strain at no load.

Table 8-2: *Model based temperature control parameters*

	Direct control signal Branch ❶	PWM control signal Branch ❷
K_T^P	0.1	0.04
K_T^{P2}	3e-4	1e-4
K_T^{P3}	3e-4	1e-4

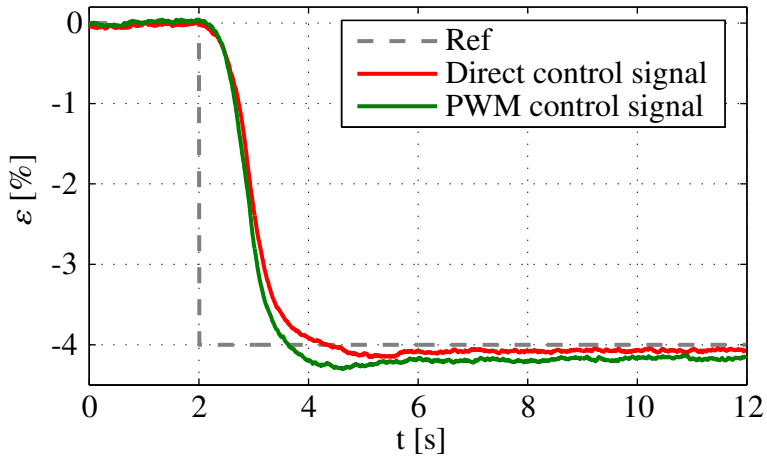

Figure 8-7: *Step response with model-based temperature controller using direct control signal and PWM modulated control signal*

While the controller is able to achieve coarse positioning of the wire, the presence of overshoots and poor steady state error makes it unsuitable for precision positioning. The poor response can be attributed to model and parameter uncertainties and due to the fact that the I-gain, which is traditionally used to reduce steady state error, is omitted here.

In order to improve tracking performance at steady state, a strain controller that is active only in the small signal areas is appended to the control structure. Details of this controller are in the next section.

8.2 Position Control via Temperature and Strain Control

Figure 8-8 shows the revised and novel control structure, consisting of a large signal and a small signal component.

The large signal component is the model-based temperature controller from the previous section and is responsible for coarse positioning of the wire. The controller is used when the desired strain ε_{des} is far from the actual strain ε_{act}, which in SMAs, implies that temperature error e_T is large, therefore the term *large signal*.

The small signal component consists of a position (strain) feedback controller and is responsible for fine positioning. The controller is used when the desired strain is within a small strain band $\pm\delta_\varepsilon$ of the actual strain, therefore the term *small signal*. Two different

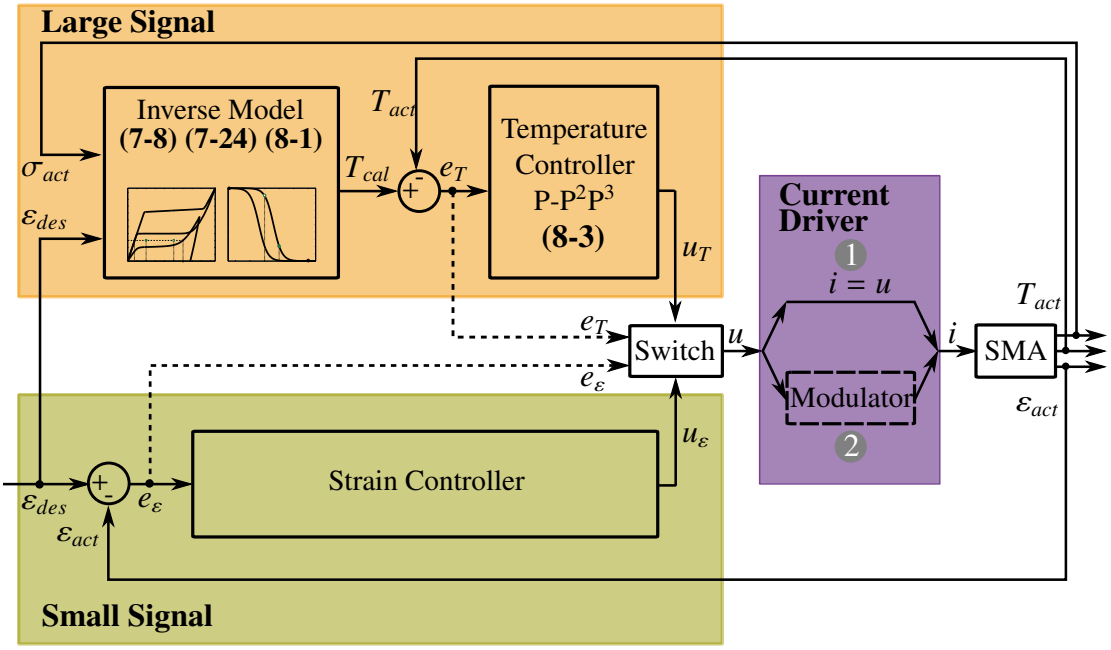

Figure 8-8: *Controller structure with large and small signal components*

types of small signal controllers are implemented, based upon whether the control signal is routed directly to the SMA along branch 1 in Fig. 8-8 or whether the control signal is modulated with PWM along branch 2.

The switch in Fig. 8-8 decides between the large and small signal controllers based on the values of the temperature error e_T and the strain error e_ε. The large signal controller is selected when $|e_T|$ is larger than a threshold value δ_T. When the large signal controller has driven the temperature such that either the temperature error is within δ_T or the absolute strain error $|e_\varepsilon|$ is within a threshold value δ_ε, then the small signal controller is selected and remains as such until a new desired strain or a disturbance pushes it outside δ_ε. This is shown mathematically in (8-4)[4]. Selecting suitable values for δ_T and δ_ε are a part of the controller design.

$$u = \begin{cases} u_T & |e_T| > \delta_T \\ u_\varepsilon & |e_T| \leq \delta_T \\ u_\varepsilon & |e_\varepsilon| \leq \delta_\varepsilon \end{cases} \tag{8-4}$$

The controllers are presented in detail in Sect. 8.3 and 8.4, with performance results for steps and sinusoidal desired strains in Sects. 8.5 and 8.6.

When investigating the performance of the controllers, it is imperative to carry out experiments at several masses for various step heights. The selection of step height is critical in SMAs. Consider Fig. 8-9, where the hysteresis for an SMA loaded with 3 and 4 kg is shown. The required temperature to achieve a desired (normalised) strain for a small step height of $\xi_{des} = 0.6$ is 80°C and 85°C at 3 and 4 kg, respectively (see Fig. 8-9). As the slope of the hysteresis ($\frac{\delta\xi}{\delta T}$) around these temperatures is very steep, small deviations of a few degrees cause large normalised strain deviations. Therefore, these steps are prone to

[4]Note that when $|e_T|$ is large, $|e_\varepsilon|$ is automatically also large. This is not explicitly written in (8-4)

overshoots due to the challenges incurred from the steepness of the hysteresis loop. Contrarily, for a large step height e.g. when $\xi_{des} = 0.1$, the required temperature is 100°C and 111°C for 3 and 4 kg, respectively (see Fig. 8-9). As this temperature is located on the tail end of the hysteresis loop, where the slope is low, control for these step heights is easier than for a small step height. Therefore, when testing the performance of the SMA controllers, it is imperative to test both large and small step heights, at various masses.

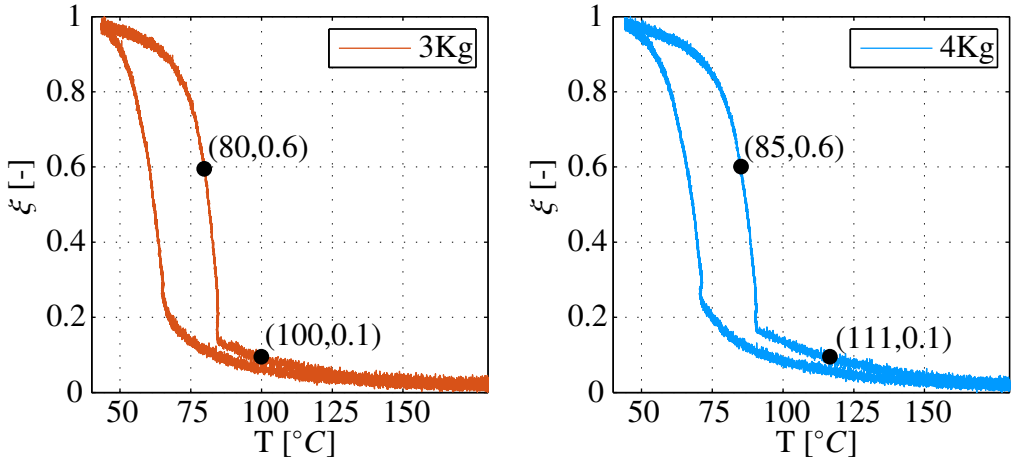

Figure 8-9: *Extended PWM controller structure*

8.3 Extended PWM based Controller

In this section, a PWM based controller with a control architecture in Fig. 8-10 is presented[5]. The large signal controller is as described in Sect. 8.1. The small signal controller is an PD-P^{2}P^3 controller with a control law in (8-5). This controller will henceforth be called the Extended PWM based controller (EPWM).

$$u_\varepsilon(t) = K_\varepsilon^P e_\varepsilon + K_\varepsilon^D \dot{e}_\varepsilon + K_\varepsilon^{P2} sgn(e_\varepsilon) e_\varepsilon^2 + K^{P3} e_\varepsilon^3 \tag{8-5}$$

Note that, contrary to the temperature controller, a D-gain is used in this controller, because the strain measurement is not as noisy as the temperature measurement. The presence of a D-gain was shown to be advantageous in improving the tracking error. However, the I-gain is still 0 for the same reasons as for the temperature controller.

To test this controller, several experiments at various loads and step heights were performed. The controller parameters were determined experimentally and are shown in Tab. 8-3.

Table 8-3: *Control Parameters for PWM and EPWM controllers*

K_T^P	K_T^{P2}	K_T^{P3}	K_ε^P	K_ε^D	K_ε^{P2}	K_ε^{P3}	δ_T	δ_ε
0.04	1e-4	1e-4	160	140	2e4	2e4	1°C	0.3%

Two examples are shown in Fig. 8-11. Plot (a) shows the SMA wire with a load of 3 kg, exposed to a heating step of height 4% strain and plot (b) shows the SMA wire with a

[5]Note that to avoid cluttering the figure, the actual stress on the wire is shown only as an input and not as a feedback as in Fig. 8-2 and Fig. 8-8.

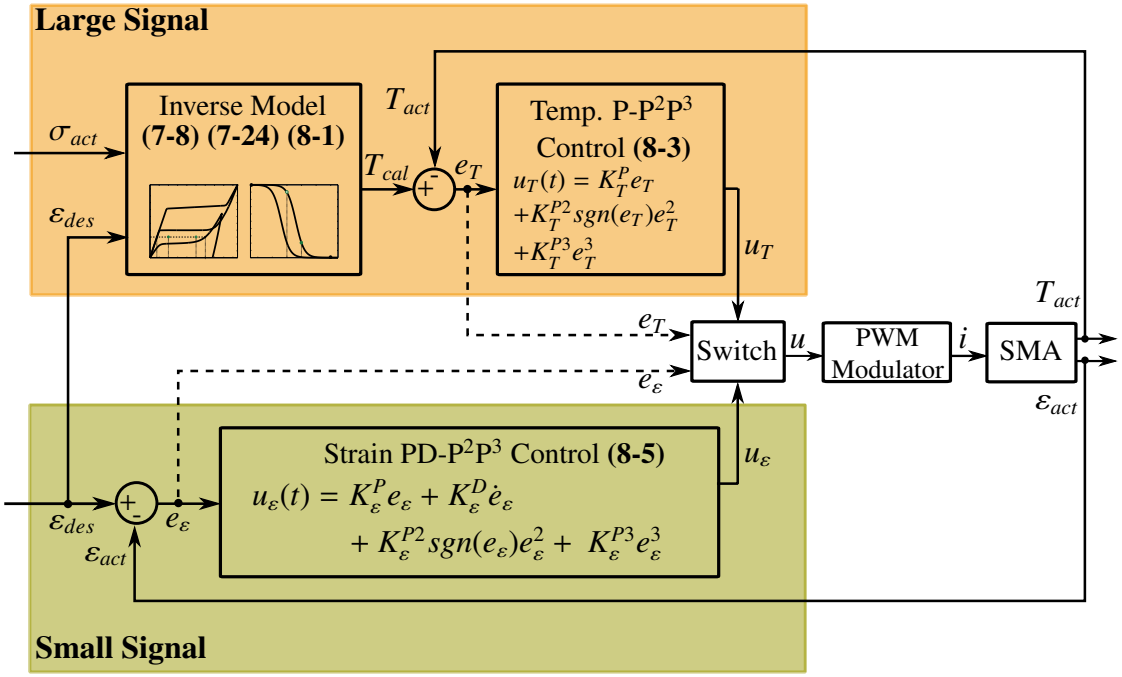

Figure 8-10: *Extended PWM controller structure*

load of 4 kg, exposed to a heating step of height 1.2% strain. In order to investigate the performance of the controller, first only the PWM based strain controller was used. The result was the red curve in Fig. 8-11(a) and (b). Subsequently, the EPWM controller was used. The result was the green curve in Fig. 8-11(a) and (b).

The response with both controllers for the larger step height is shown in Fig. 8-11(a). When compared to the model-based temperature controller alone, as presented in the previous section, the PWM based controller alone (red curve) shows better steady state error (cf. Fig. 8-7).

However, using the the EPWM controller with a control architecture in Fig. 8-10, produces the response depicted by the green curve in Fig. 8-11(a). At the start of the step at $t = 1s$, where the strain, and therefore the temperature, difference is large, the model-based large signal temperature controller is selected. It increases the temperature of the wire until the point depicted by the black circle in Fig. 8-11(a), where the strain is within a threshold value $\delta_\varepsilon = 0.3\%$. At this point the small signal PWM based controller is selected. The results for this EPWM controller show faster rising times and settling times as with only the PWM strain controller.

The controller response for the smaller step height is shown in Fig. 8-11(b). The PWM strain controller alone (red curve) shows good rising time, however, with a significant overshoot. As mentioned previously, this is attributed to the steepness of the hysteresis curve at these small steps. Overshoots are critical in SMAs due to the slow cooling response and this is shown in the long settling time. Conversely, using the EPWM controller produces the response as shown by the solid green curve in Fig. 8-11(b), which involves a switch of the large and small signal controllers based on the strain and temperature error. It shows no overshoot, faster settling time and lower steady state error, albeit with a slightly lower rising time. The performance of the proposed controller with step and sinusoidal desired strains with various constant masses will be discussed in Sects. 8.5 and 8.6 and

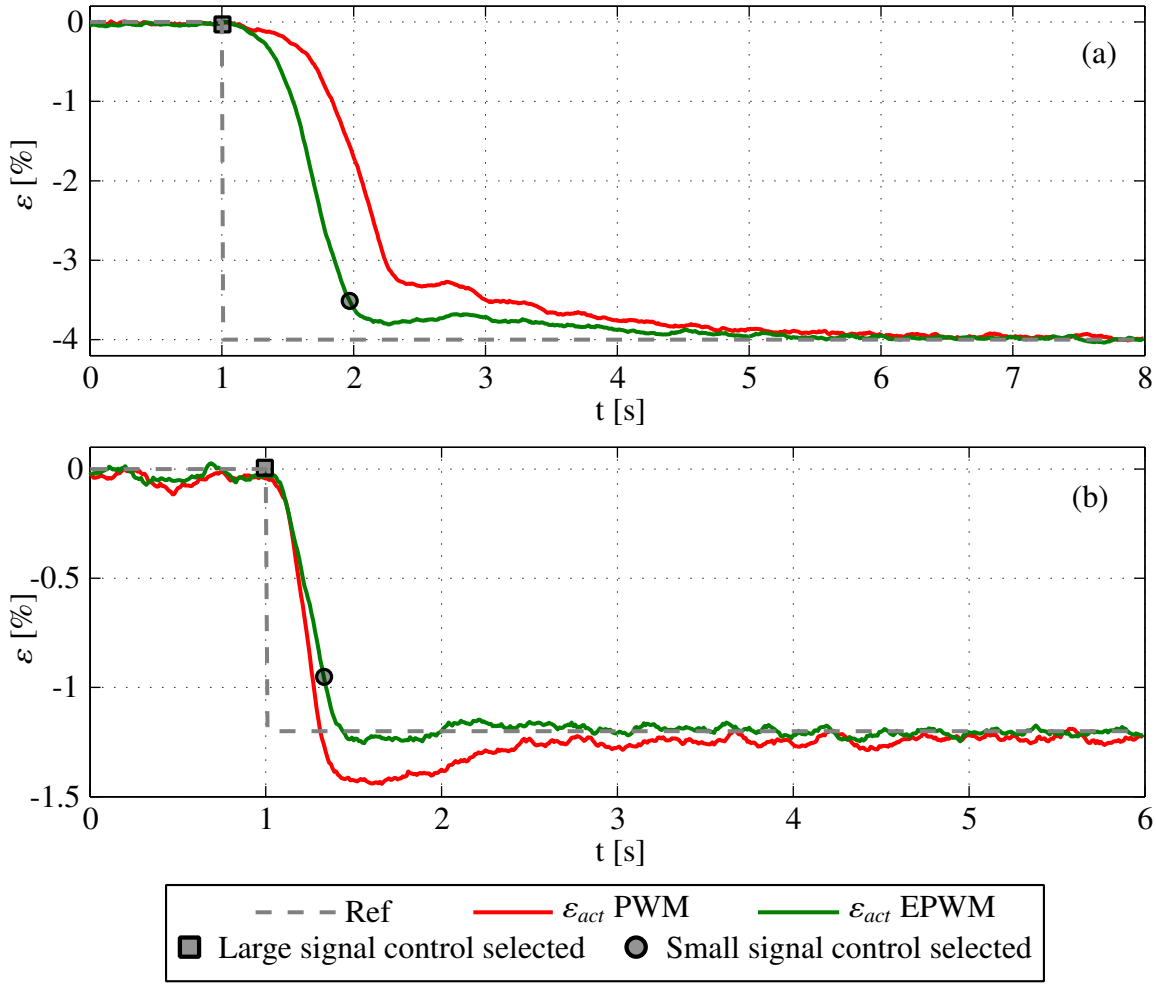

Figure 8-11: *Tracking response with PWM and EPWM controllers with, (a) large step with 3 kg mass, (b) small step with 4 kg mass*

with dynamic masses and disturbances in Sect. 8.8.

8.4 Extended Variable Structure Controller

In this section, an Extended Variable Structure Controller (EVSC) with a control architecture as in Fig. 8-12 is presented[6]. The large signal controller is identical to the model-based temperature controller in Sect. 8.1. The small signal controller consists of a variable structure controller (VSC) based on [EA02] with modifications to improve the controller performance as shown in the next couple of sections.

[6]Here, similar to Fig. 8-10, the actual stress on the wire is shown only as an input and not as a feedback as in Fig. 8-2 and Fig. 8-8.

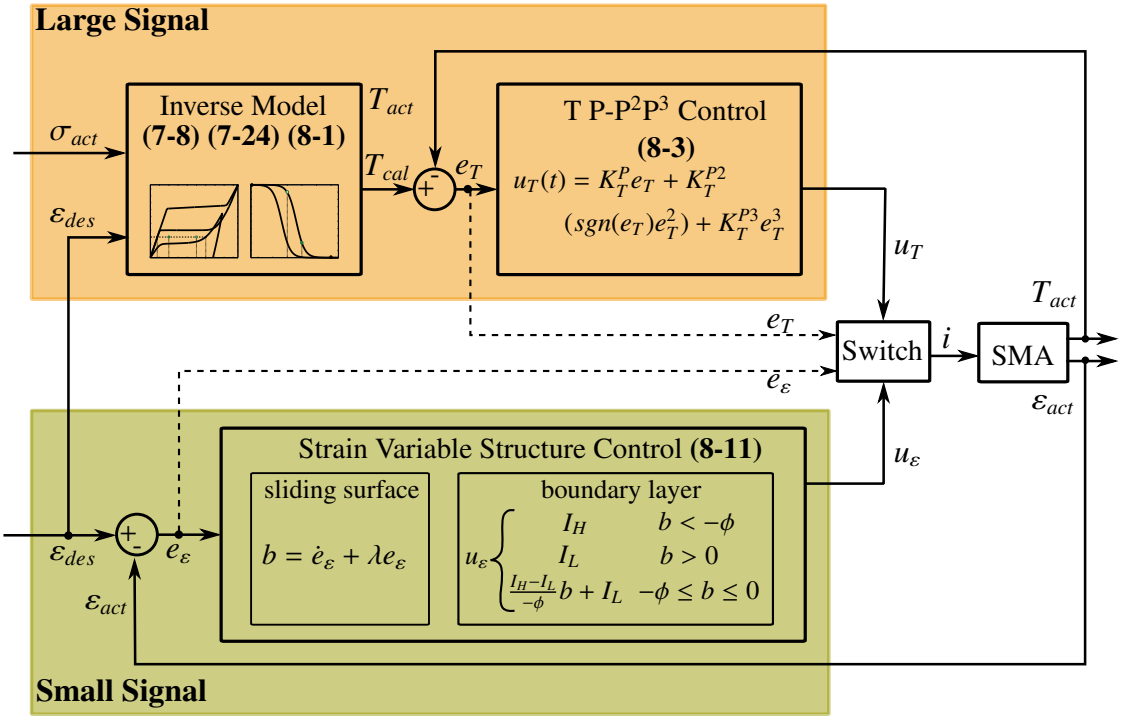

Figure 8-12: *Extended Variable Structure Controller structure*

8.4.1 Variable Structure Controller according to [EA02]

The variable structure controller used in this section is taken from Elahinia and Ashrafiuon [EA02]. Here, the phase plane is defined as $\dot{e}_\varepsilon$ versus e_ε, where $e_\varepsilon = \varepsilon_{des} - \varepsilon_{act}$ is the strain error. The trajectory b is defined by (8-6) in the phase plane, where the sliding surface at $b = 0$ is a slanted line with a slope given by $-\lambda$. Further, the controller has a boundary layer given by 2ϕ, that is symmetrical about the sliding surface as shown in Fig. 8-13.

$$b = \dot{e}_\varepsilon + \lambda e_\varepsilon \tag{8-6}$$

The control law in (8-7) calculates the required current i_ε based on the trajectory b with respect to the sliding surface and boundary layer. When $b < -\phi$, the wire needs to be heated and I_H, the maximum current, flows through the wire. When $b > \phi$, the wire needs to be cooled and I_L, the minimum current, flows through the wire. Within the boundary layer, the current through the wire is a a linear combination of I_H and I_L as shown in (8-7) and Fig. 8-13.

$$i_\varepsilon = \begin{cases} I_H & b < -\phi \\ I_L & b > \phi \\ \frac{I_H - I_L}{-2\phi} b + \frac{I_H + I_L}{2} & -\phi \le b \le \phi \end{cases} \tag{8-7}$$

Consider the VSC when the trajectory has reached the origin ($e_\varepsilon = 0$, $\dot{e}_\varepsilon = 0$). In this case, $b = 0$, as shown in (8-8), and current i_ε is calculated in (8-9).

$$b = \dot{e}_\varepsilon + \lambda e_\varepsilon = 0 \tag{8-8}$$

$$i_\varepsilon = \frac{I_H - I_L}{-2\phi} b + \frac{I_H + I_L}{2} = \frac{I_H + I_L}{2} \tag{8-9}$$

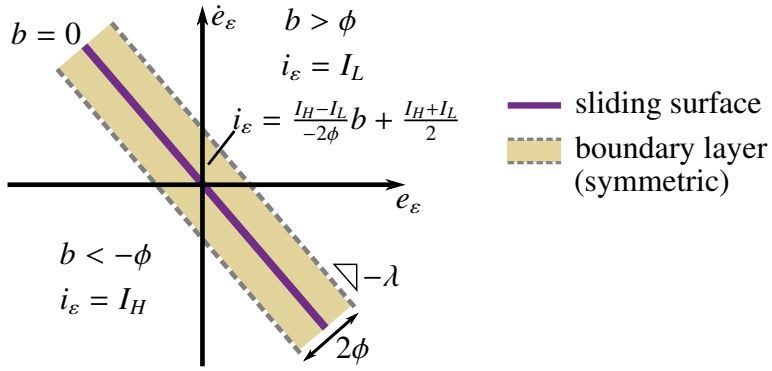

Figure 8-13: *Phase plane showing sliding surface, symmetrical boundary layer*

Since in this case, the control law calls for a current of $(I_H + I_L)/2$, regardless of the fact that the desired strain has been reached, it causes a small steady state error due to overheating of the wire. Given the slow cooling response of SMAs, unnecessary heating of the wire would cause an unnecessary drop in (an already low) bandwidth.

8.4.2 Asymmetric boundary layer

In order to avoid unnecessary heating of the wire as is the case with Elahinia's VSC, the first modification is to use an asymmetrical boundary layer as shown in Fig. 8-14. In this case, the wire is heated higher than I_L only when the trajectory is smaller than $b = 0$ as shown mathematically in (8-10).

$$i_\varepsilon = \begin{cases} I_H & b < -\phi \\ I_L & b > 0 \\ \frac{I_H - I_L}{-\phi} b + I_L & -\phi \leq b \leq 0 \end{cases} \tag{8-10}$$

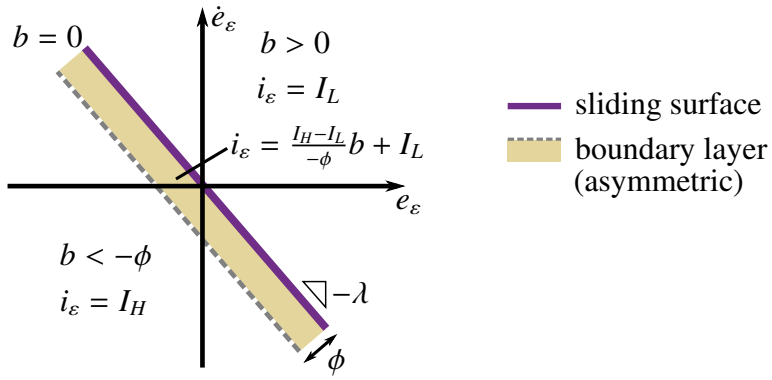

Figure 8-14: *Phase plane showing sliding surface, asymmetrical boundary layer*

In order to test this control law, the SMA wire with a load of 3 kg is exposed to a heating step of height -2.7% strain[7]. The controller parameters are shown in Tab. 8-4 and are found experimentally.

[7]The step height was selected randomly.

Table 8-4: *Control Parameters for VSC controller with symmetric and asymmetric boundary layers*

ϕ	λ	I_L	I_H
6e-3	10	0.05 A	3 A

The steady state portion of the step response is in Fig. 8-15, where it is observed that, as hypothesised, the control law with an asymmetric boundary layer (green curve) has lesser steady state error than with a symmetric boundary layer (red curve). Note that with a symmetrical boundary layer, the steady state error is caused by overheating rather than underheating.

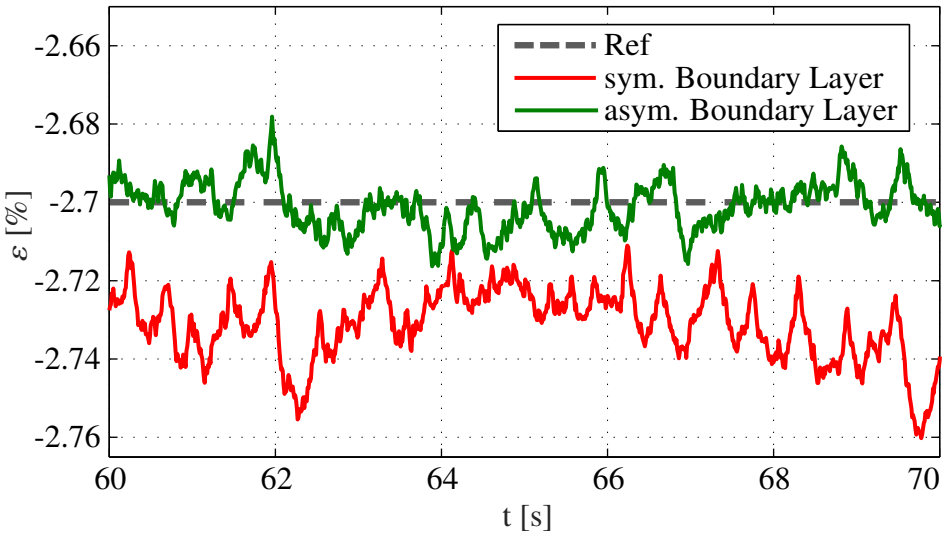

Figure 8-15: *Steady state error with symmetric and asymmetric boundary layer*

The phase plot of the step response with an asymmetrical boundary layer is shown in Fig. 8-16. The controller successfully directs the trajectory of the SMA actuator to the origin of the phase plane along the sliding surface, while ensuring that, for the most part, it remains within the asymmetrical boundary layer.

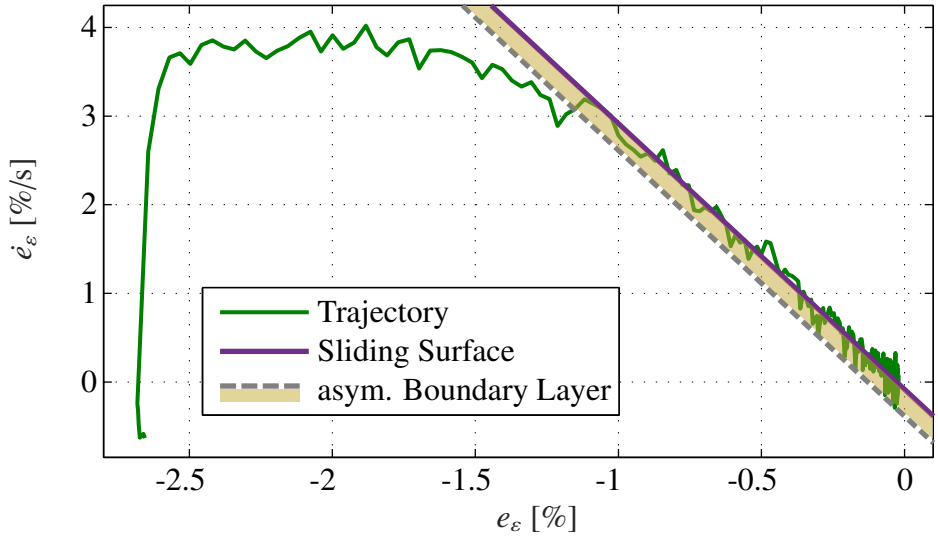

Figure 8-16: *Sliding surface and asymmetric boundary layer for VSC*

8.4.3 Adaptive control current

The second modification is the adaptation of I_H to the stress on the wire. As mentioned in Chap. 6, lower stresses require lower temperatures i.e. lower current for the martensitic to austenitic transformation. Therefore, the value of I_H is modified according to the load on the wire such that I_H^{min}, 60% of I_H flows for stresses below 200 MPa (4 kg). I_H^{max}, 100% of I_H flows for stresses above 500 MPa (10 kg). I_H is linear for the stresses in between (see Fig. 8-17). This modification of I_H shows lower overshoot and faster settling times as shown Sect. 8.4.4.

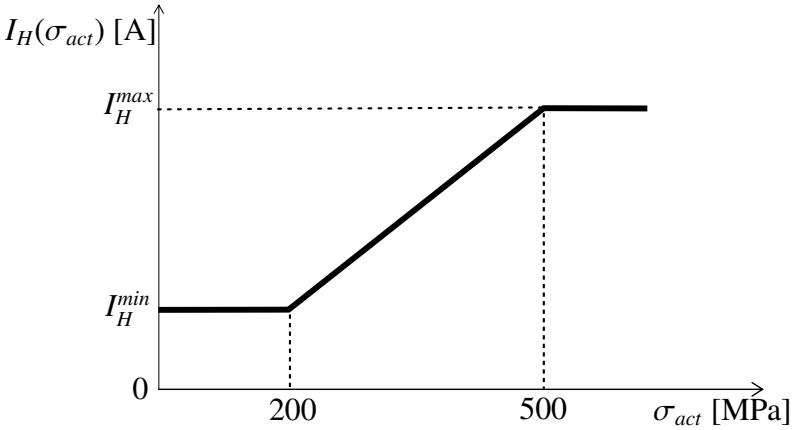

Figure 8-17: *Adaptation of I_H to stress*

8.4.4 Final EVSC control law and effect of modifications

With both modifications from Sects. 8.4.2 and 8.4.3, the final control law for the EVSC is in (8-11).

$$i_\varepsilon = \begin{cases} I_H(\sigma_{act}) & b < -\phi \\ I_L & b > 0 \\ \frac{I_H(\sigma_{act})-I_L}{-\phi} b + I_L & -\phi \leq b \leq 0 \end{cases} \tag{8-11}$$

In Fig. 8-18, the response of the SMA with a load of 4 kg is investigated with a heating step of height 1.6% strain followed by a heating step of height 1.2% strain. This desired strain sequence is particularly challenging because it consists of two subsequent heating steps of small height. As mentioned in Sect. 8.3, a small step is difficult to control because of the steepness of the hysteresis loop. Further, in Fig. 8-18(a), the transition between the strains is a ramp with a duration of 1s.

The response using VSC controller according to [EA02] is shown by the purple curve in both figures. It has fast rising and settling times, however it is plagued with overshoots due to the challenges associated with small steps. The system response also displays considerable steady state error[8] due to its symmetrical boundary layer.

To combat these problems, two modifications were made: the first was the use of an asymmetric boundary layer as described in Sect. 8.4.2 and the second was the use of adaptive control current as described in Sect. 8.4.3. The green and orange curves in both Fig. 8-18(a) and (b) show the effect of the modifications, respectively. The combination of both modifications are successful in eliminating the overshoots and reducing the steady state error, however, at the cost of considerable reduction in the rising time (see orange curves in Fig. 8-18).

The extended VSC controller (EVSC) according to the control architecture in Fig. 8-12 produces a response as shown by the blue curve in both figures. The EVSC is a model-based large signal temperature controller and a small signal controller consisting of a VSC with an asymmetric boundary layer and adaptive control current (cf. (8-11)). The EVSC shows the best performance of all the aforementioned controllers as shown in Fig. 8-18. The response has no overshoot, low steady state error and a good compromise between fast rising and settling times. Despite the challenges presented by a desired strain profile consisting of two subsequent small heating steps, the EVSC is able to control the SMA precisely.

[8] In [EA02], the steady state error issues with this controller are confirmed.

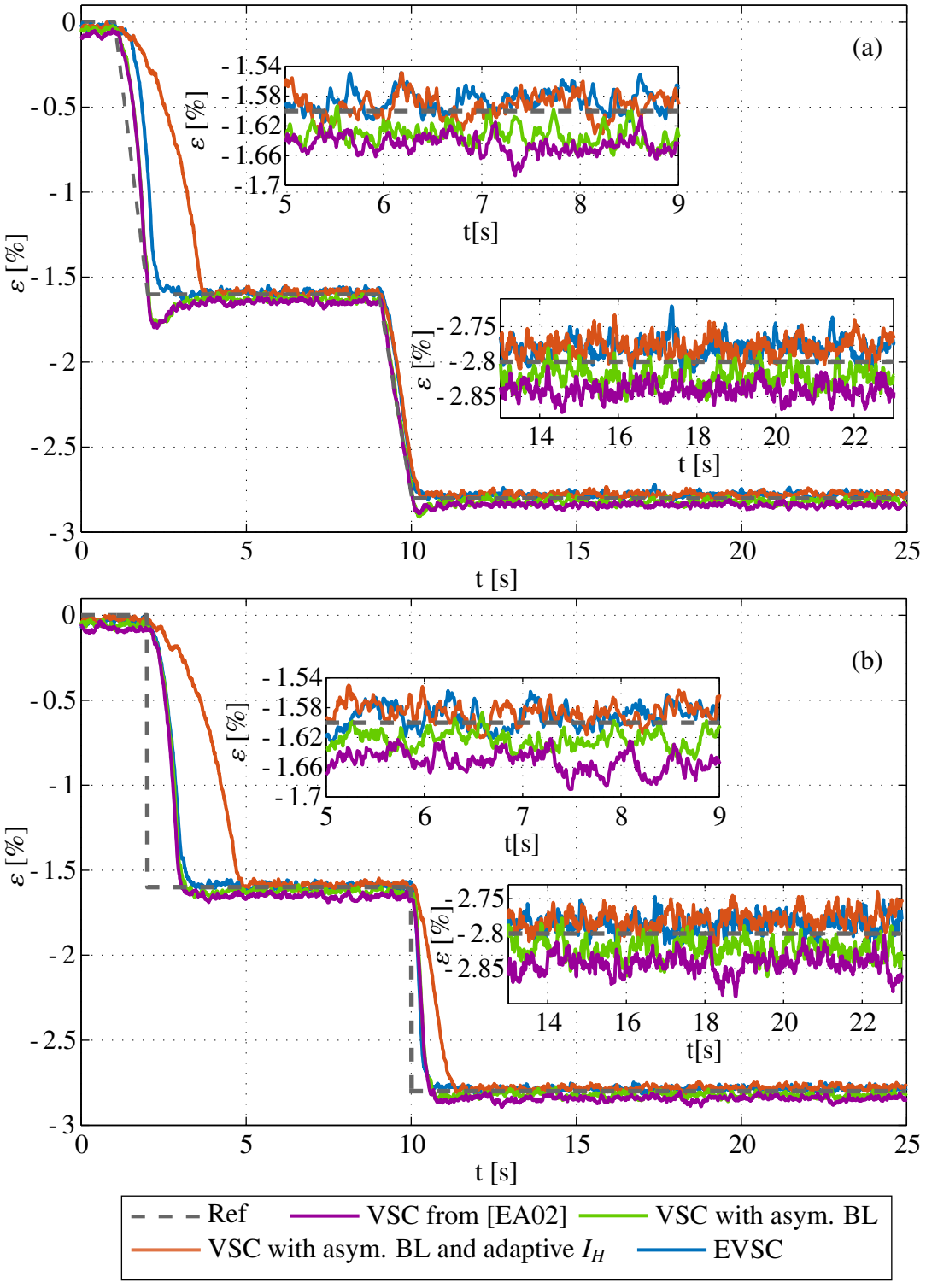

Figure 8-18: *Tracking response with VSC and proposed EVSC controller (large signal model-based and small signal controllers) for two small steps with (a) ramp transition (b) step transition*

8.5 Step Response with Constant Masses with EPWM and EVSC

This section presents multiple results for precision position control using the EPWM and EVSC controllers. The desired strain is a sequence of 6 steps of different heights, as shown in Fig. 8-19. Steps ❶, ❹ and ❺ are heating steps and steps ❷, ❸ and ❻ are cooling steps. These steps were selected to ensure that the SMA actuator performance is investigated at various positions on the hysteresis loop. Further, the desired strain sequence causes the SMA to run in both major and minor loops of the hysteresis.

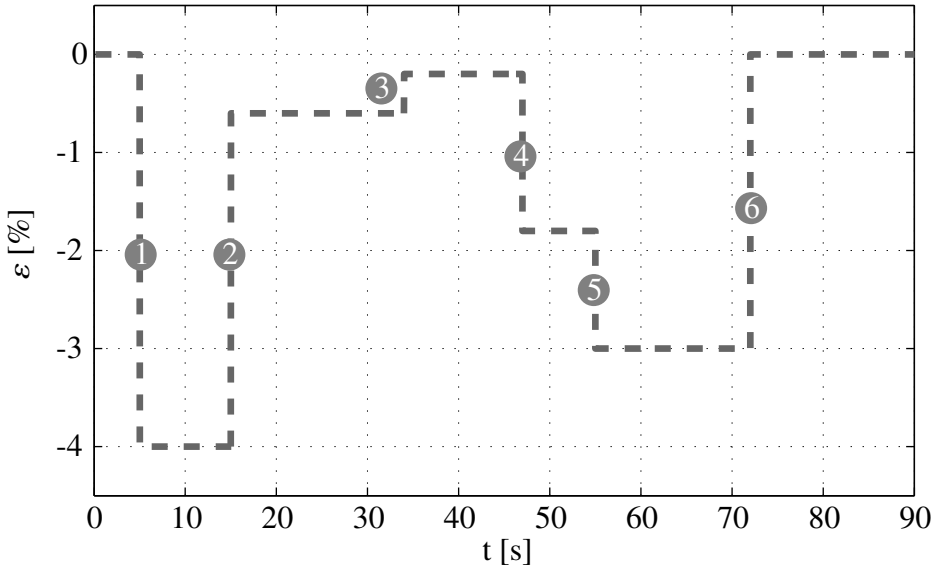

Figure 8-19: *Desired Strain*

The experiment was carried out on an SMA wire loaded with constant masses from 2 kg to 10 kg, in 1 kg increments (excluding 6 kg). The control parameters for the EPWM and EVSC controllers are in Tab. 8-5 and Tab. 8-6, respectively. The results are shown in Fig. 8-20 for the EPWM controller and in Fig. 8-21 for the EVSC controller, where the black squares show when the large signal controller is selected and the black circles show when the small signal controller is selected. A detailed analysis of the results considering rising and settling times as well as steady state error distribution for all the steps are presented simultaneously for both controllers in the following sections.

Table 8-5: *Control Parameters for EPWM controller*

K_T^P	K_T^{P2}	K_T^{P3}	K_ε^P	K_ε^D	K_ε^{P2}	K_ε^{P3}	δ_T	δ_ε
0.04	1e-4	1e-4	160	140	2e4	2e4	1°C	0.3%

Table 8-6: *Control Parameters for EVSC controller*

K_T^P	K_T^{P2}	K_T^{P3}	ϕ	λ	I_L	I_H^{min}	I_H^{max}	δ_T	δ_ε
0.1	4e-3	4e-3	6e-3	10	0.05 A	1.9 A	3 A	1°C	0.5%

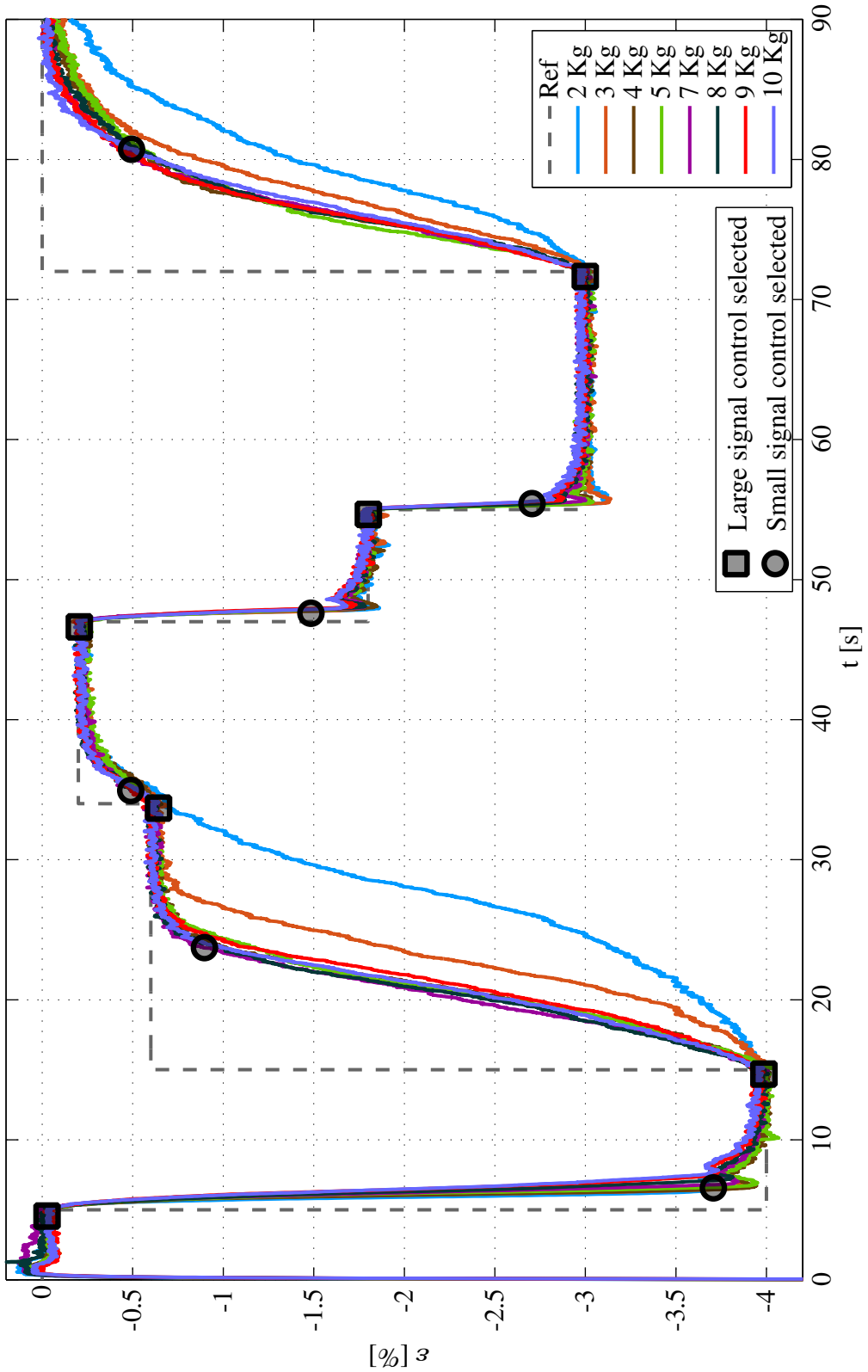

Figure 8-20: *Actuator response with EPWM controller different constant masses and several steps*

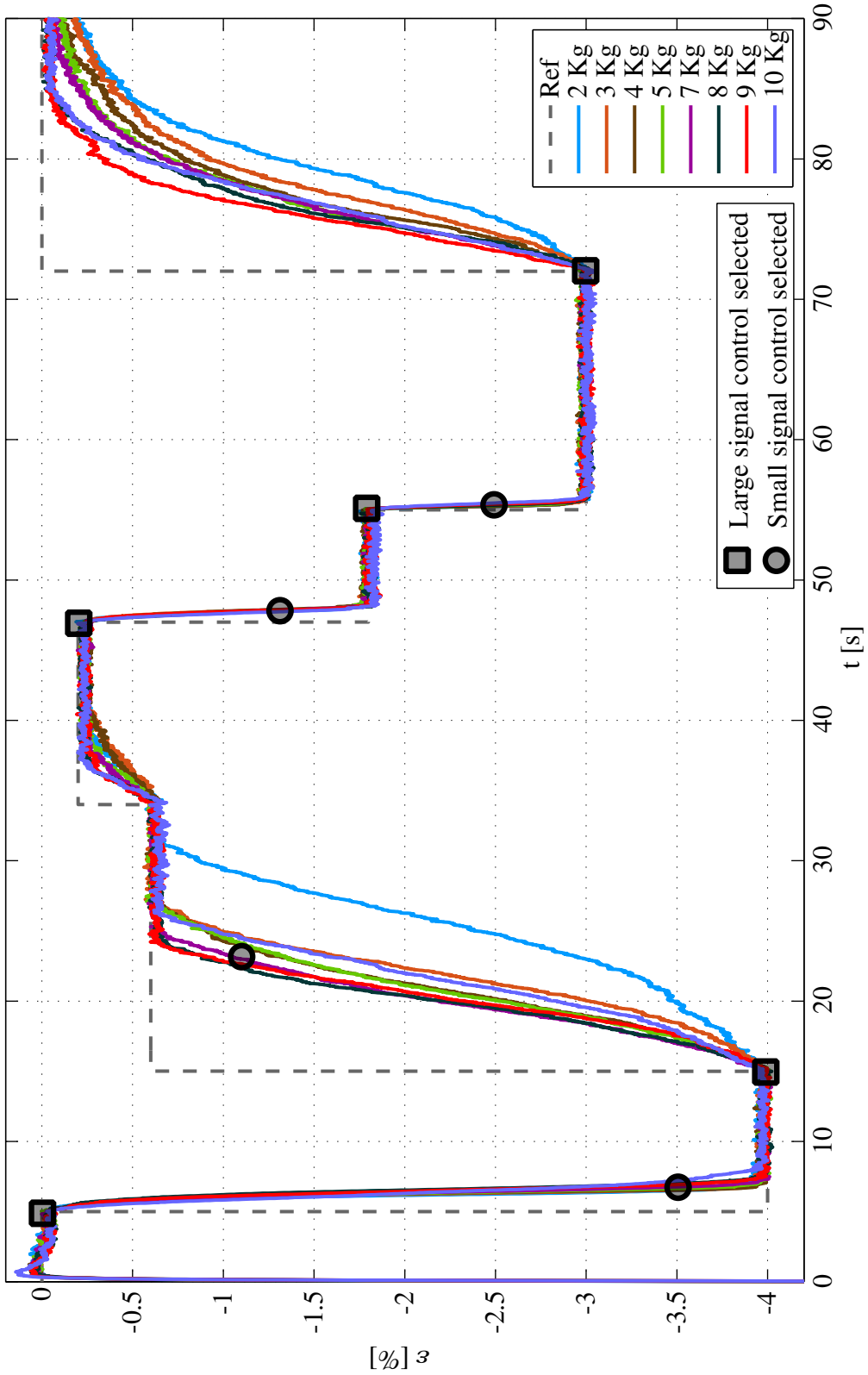

Figure 8-21: *Actuator response with EVSC controller for different constant masses and several steps*

8.5.1 Step response at first step (heating)

At the start of the experiment, the first large step is a heating step at 5s that expects a strain of -4%. As the temperature required is far from the actual temperature, the large signal controller is valid here until either δ_T or δ_ε is reached. This occurs on average 2s (EPWM) and 1.8s (EVSC) after the step (considering all masses). After this, the small signal controller takes over. The black dashed line in Fig. 8-22(a) and 8-22(b) shows the strain at 90% of the step height (ε_R). The rising time t_r to reach this strain is shown in Fig. 8-23 for all masses. t_r varies between 1.3s and 2.5s (EPWM) and 1.5s and 2.3s (EVSC), with the fastest times for the 2-kg mass and the slowest for the 10-kg mass. This is expected since higher masses require more energy, and therefore time, for the phase transformation from martensite to austenite.

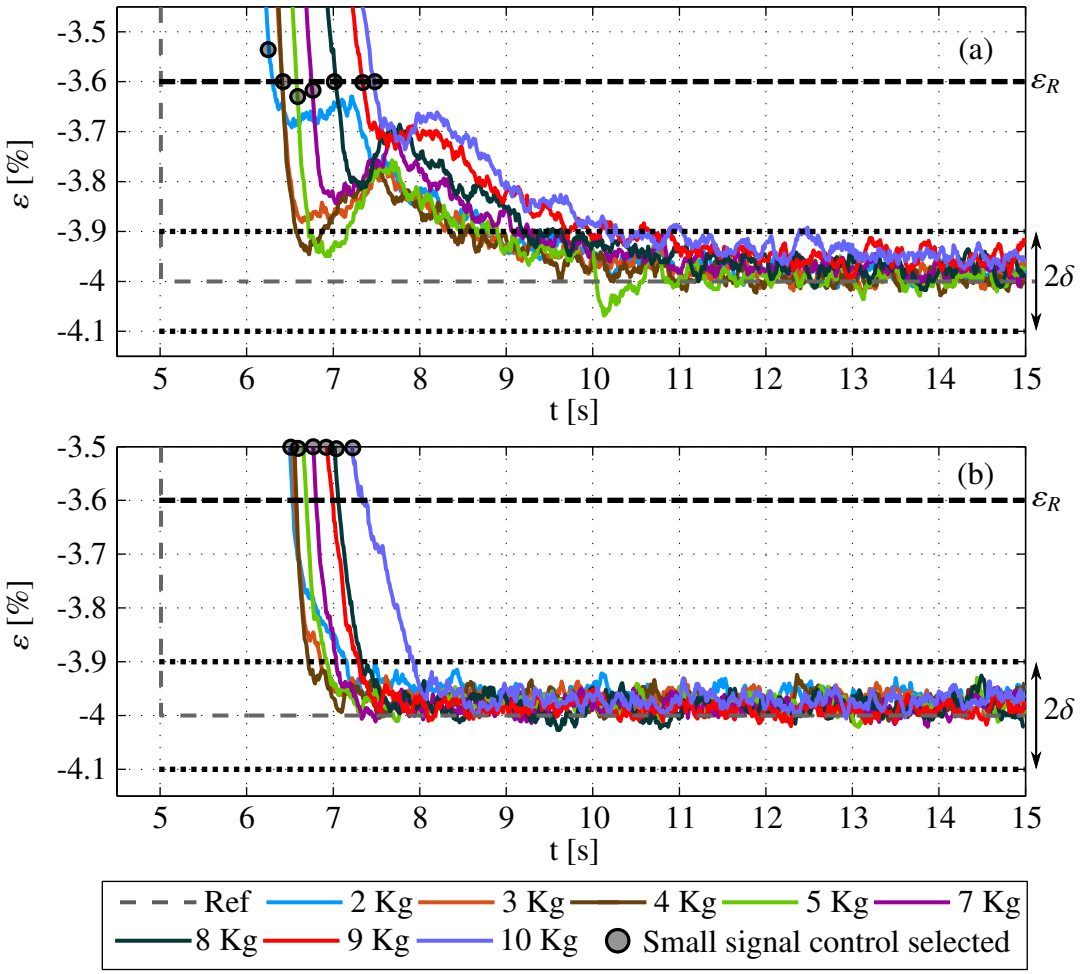

Figure 8-22: *Actuator response with EPWM (a) and EVSC (b) at first step (heating)*

The small 'peaks' in the strain response between 6.2 and 7.5 sec for the EPWM controller as shown in Fig. 8-22(a) is caused by the switch from the large to small signal controllers. Conversely, the EVSC controller shows a smooth transition from the large to small signal controllers due to the overlapping of the boundary layer and δ_ε and the inclusion of a sliding surface. The settling time t_s within a $\pm\delta$ error band of 0.1% (as shown by the black

dotted lines in Figs. 8-22(a) and (b) varies between 3.6 and 7.5s (EPWM) and between 1.7 and 2.9s (EVSC), depending on the mass as shown in Fig.8-23. (Note that in Fig.8-23 the heights of the bars show the rising and settling times as shown exemplary for the 2-kg mass as t_r = 1.3s and t_s = 3.9s.). The average values for the rising time t_r^{avg} and settling time t_s^{avg} for all masses is in Tab. 8-7. While the rising time between the two controller is comparable, the EVSC controller shows considerably faster settling times due to the smooth transition between the controllers.
The steady state error distribution of the system is in Fig. 8-24 for all masses. The EPWM controller shows a worst case steady state error band ($\Delta\varepsilon_{ss}$) between -0.11 and 0.036%. Considering that the wire length is 10.0 cm, this represents a worst case steady state error band between -110 and 36 μm. For the EVSC controller, $\Delta\varepsilon_{ss}$ is between 0.02 and -0.08% (see Fig. 8-24). For a wire length of 9.85 cm, this represents a worst case steady state error band between 23 and -77 μm. The average steady state error e_{ss}^{avg} and steady state RMSE e_{ss}^{RMS} are in Tab. 8-7.

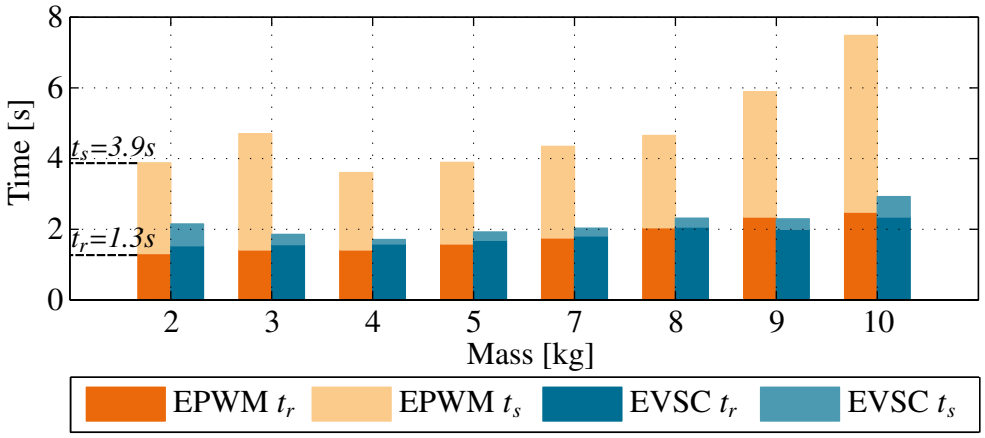

Figure 8-23: *Rising and settling time with EPWM and EVSC at first step (heating)*

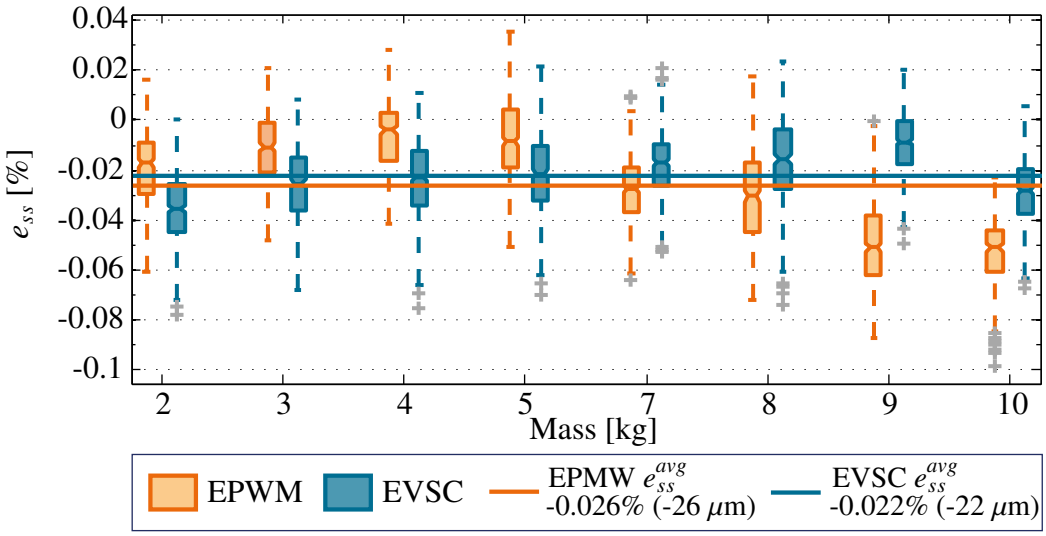

Figure 8-24: *Steady state error distribution with EPWM and EVSC at first step (heating)*

Table 8-7: *Response for SMA actuator with EPWM and EVSC at first step*

Controller	Step: H or C	t_r^{avg}	t_s^{avg}	e_{ss}^{avg}	e_{ss}^{RMS}
EPWM	Step 1: H	1.8s	4.8s	-0.026% (-26μm)	0.031% (31μm)
EVSC	Step 1: H	1.8s	2.1s	-0.022% (-22μm)	0.027% (27μm)

Note that both controllers have negative e_{ss}^{avg}, meaning that they tend to underheat, rather than overheat the wire. This is more advantageous than having positive e_{ss}^{avg} because the cooling response is slow and overheating would reduce the bandwidth even further.

8.5.2 Step response at second and third steps (cooling)

The large scale controller is selected again at 15s where a large cooling step is expected. The results are in Fig. 8-25(a) for EPWM and (b) for EVSC.

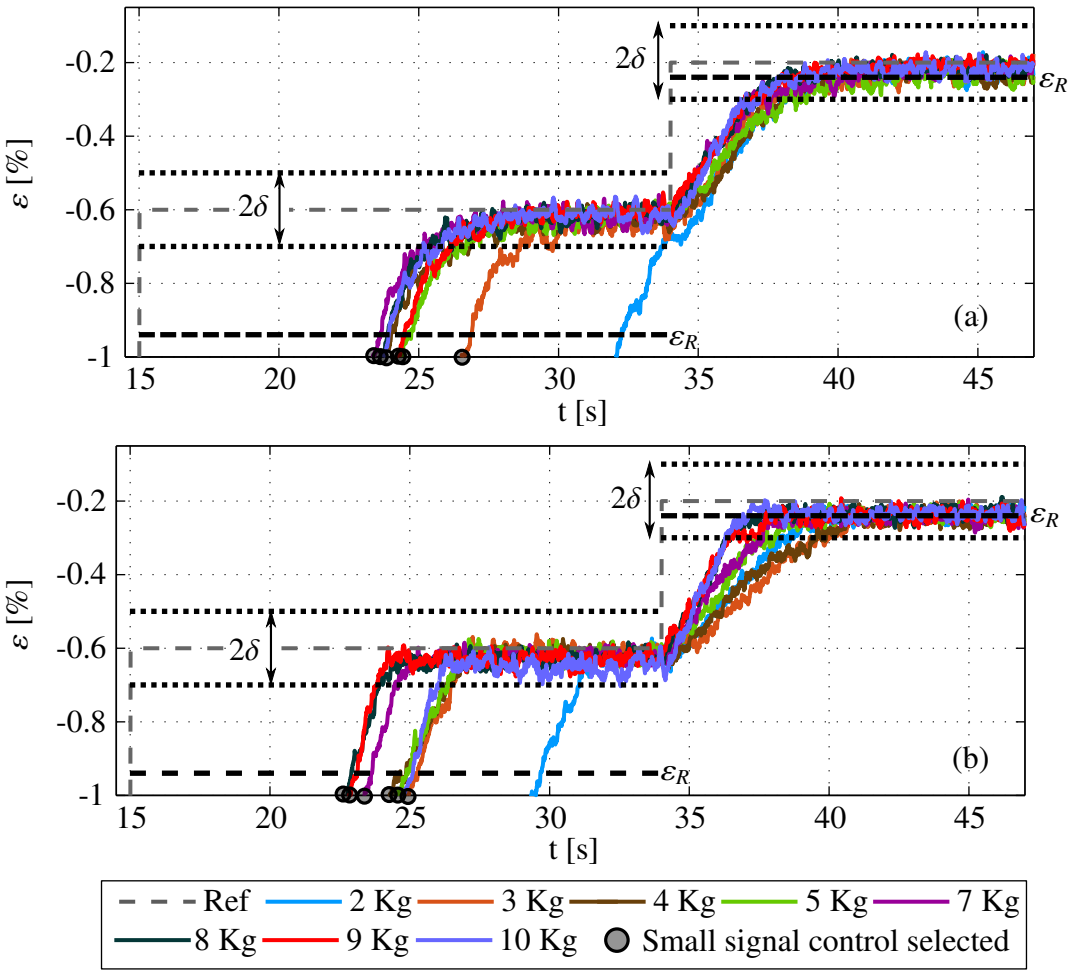

Figure 8-25: *Actuator response with EPWM (a) and EVSC (b) controller at second, third steps (cooling)*

The wire cools by natural convection (no control here) and, as expected, the higher masses cool faster than the lower masses because the M_s and M_f transformation temperatures are higher (cf. Chap. 6). The rising time to 90% of the step height (dashed line in Figs. 8-25(a) and (b)) and the settling time within the $\pm\delta$ error band of 0.1% is shown in Fig.8-26. Note that the 2 kg mass has the worst rising time due to its low M_s and M_f temperatures and is hardly able to reach steady state. The small signal controller takes over when the strain is close to the desired strain within δ_ε. The steady state error distribution is in Fig.8-27 with average values for both controllers in Tab. 8-8. The performance of both controllers is comparable. This is expected since little control is possible due to lack of an active cooling mechanism.

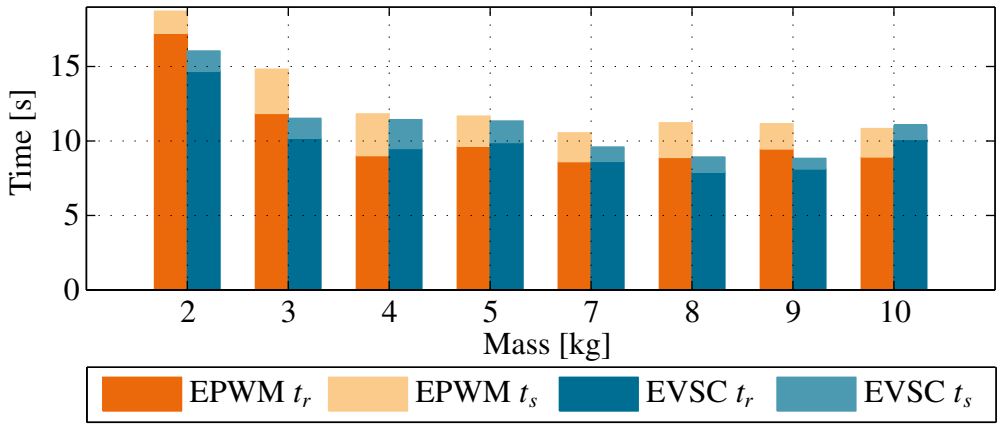

Figure 8-26: *Rising and settling time with EPWM and EVSC at second step (cooling)*

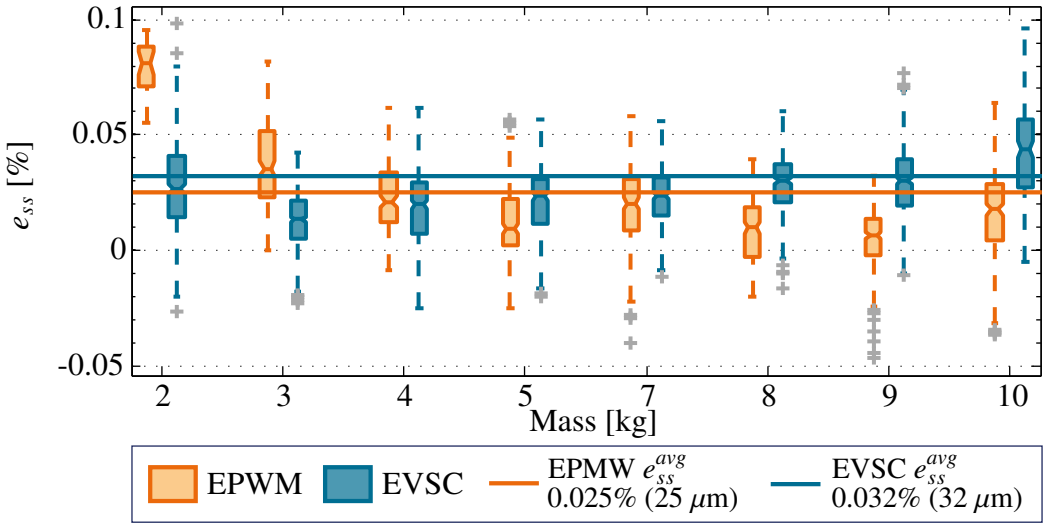

Figure 8-27: *Steady state error distribution with EPWM and EVSC at second step*

With the EPWM controller, the large signal controller is selected again at 34s in preparation for the next cooling step, however, since the step height is only 0.4%, the small signal controller takes over after about 1s. For EVSC, the small signal controller remains valid for the cooling step at 34s because the strain difference between the two steps is smaller than δ_ε. Due to the low step height, the rising time and settling times as shown in Fig. 8-28, with

average values in Tab. 8-8 are lower than for the larger cooling step (step ❷). Note that for this step height, the settling time is lower than the rising time because the rising strain is higher than the settling strain as shown in Fig. 8-25(a) and (b). The steady state error distribution is shown in Fig. 8-29, with average values in Tab. 8-8. While EPWM shows similar performance to the previous cooling step, the EVSC controller shows considerable more steady state error for this small cooling step. However, e_{ss}^{avg} is still low and therefore acceptable for tracking.

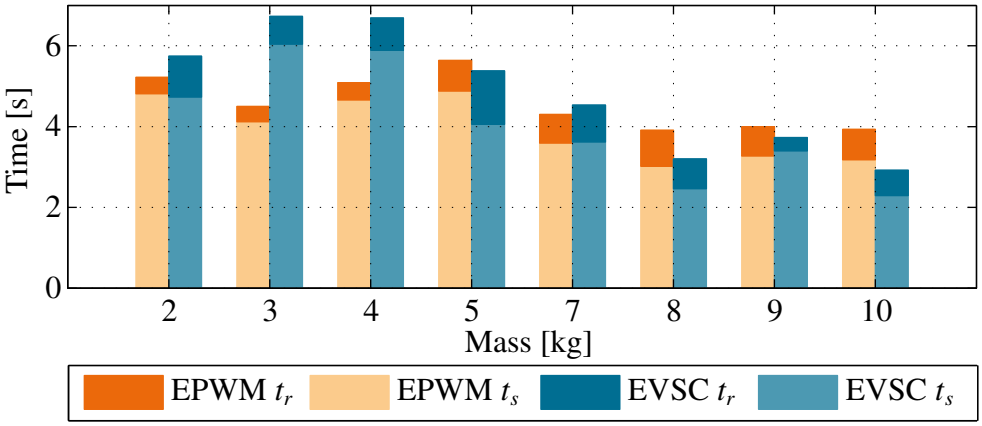

Figure 8-28: *Rising and settling time with EPWM and EVSC at third step (cooling)*

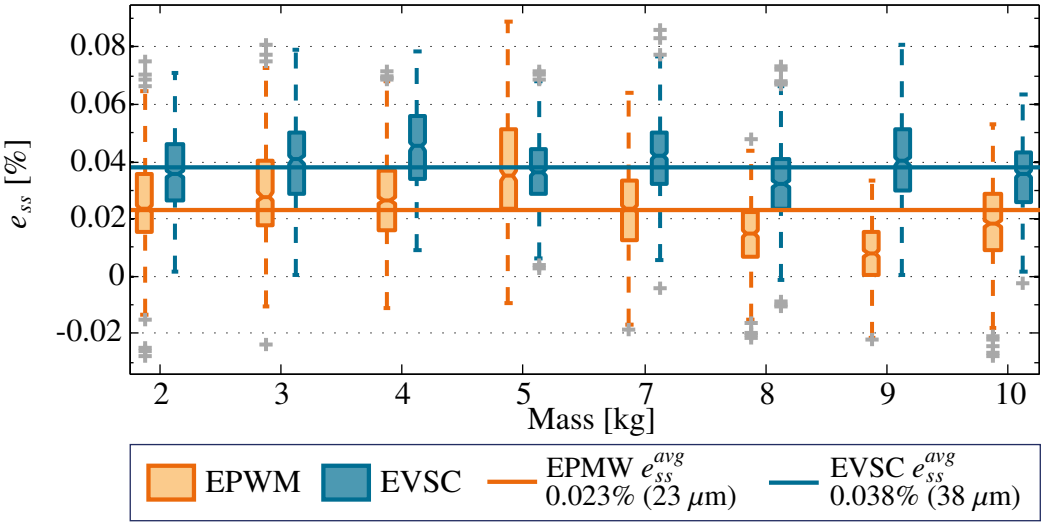

Figure 8-29: *Steady state error distribution with EPWM and EVSC at third step*

Table 8-8: *Response for SMA actuator with EPWM and EVSC at second and third step*

Controller	Step: H or C	t_r^{avg}	t_s^{avg}	e_{ss}^{avg}	e_{ss}^{RMS}
EPWM	Step 2: C	10.5s	12.6s	0.025% (25μm)	0.032% (32μm)
EVSC	Step 2: C	9.9s	11.9s	0.026% (26μm)	0.03% (30μm)
EPWM	Step 3: C	4.6s	3.9s	0.023% (23μm)	0.028% (28μm)
EVSC	Step 3: C	4.9s	4.1s	0.038% (38μm)	0.04% (40μm)

8.5.3 Step response at fourth step (heating)

The next (fourth) step is a small heating step at 47s and the large signal controller is valid from the step transition until the error is within δ_ε, after which the small signal controller is valid. The system response is shown in Fig. 8-30(a) for EPWM and (b) for EVSC. The rising time for both controllers is comparable (see Fig. 8-31 and Tab. 8-9).
With the EPWM controller, the 2-kg and 4-kg masses show overshoots with a peak error of 0.06% (60 μm) and 0.05% (50 μm), respectively, as shown in Fig. 8-30(a). Recall that overshoots are critical in SMAs due to the slow cooling response and are not desirable. The EVSC controller, on the other hand, shows no overshoots. This is reflected in the higher settling times for the EPWM controller (between 2 and 7.6 s) as opposed to the EVSC controller (between 1 and 1.2s) as shown in Fig. 8-31. The performance of the EVSC controller is exceptional, considering that this step is a small step located on the steep portions of the hysteresis loop.
The steady state error distribution is shown in Fig. 8-32, with average values in Tab. 8-9. Even though both controllers show excellent steady state tracking, the EVSC controller shows steady state errors as low as 5μm[9]

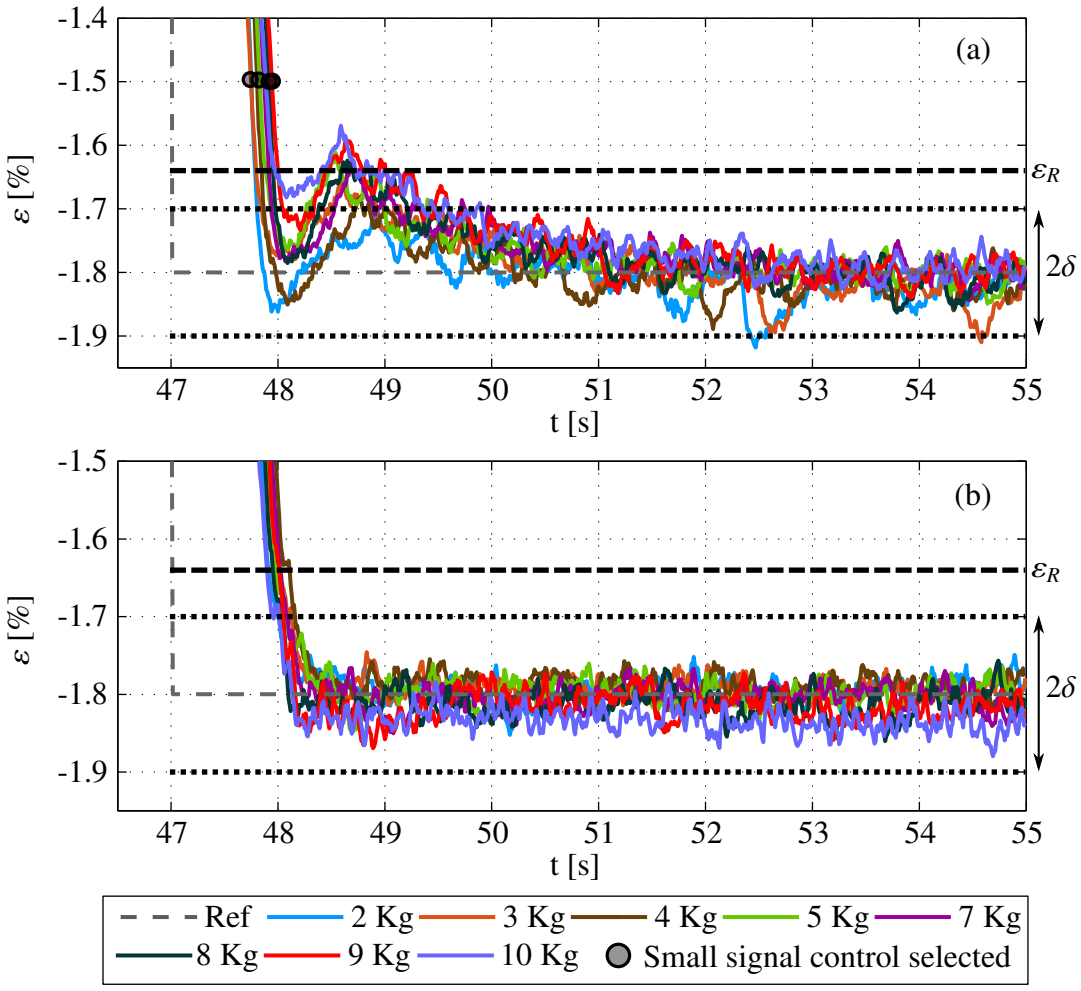

Figure 8-30: *Actuator response with EPWM (a) and EVSC (b) at fourth step (heating)*

[9]Note that although the EVSC showed poorer steady state error for small cooling steps, it shows excellent performance for small heating steps.

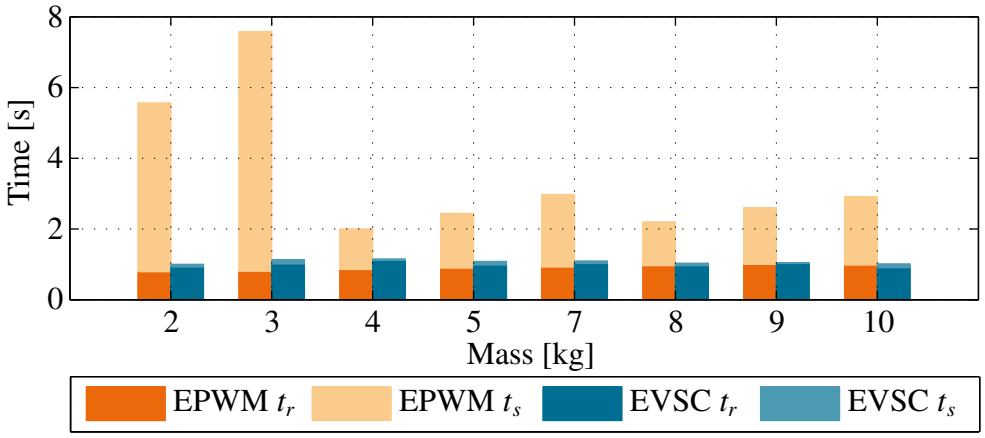

Figure 8-31: *Rising and settling time with EPWM and EVSC at fourth step (heating)*

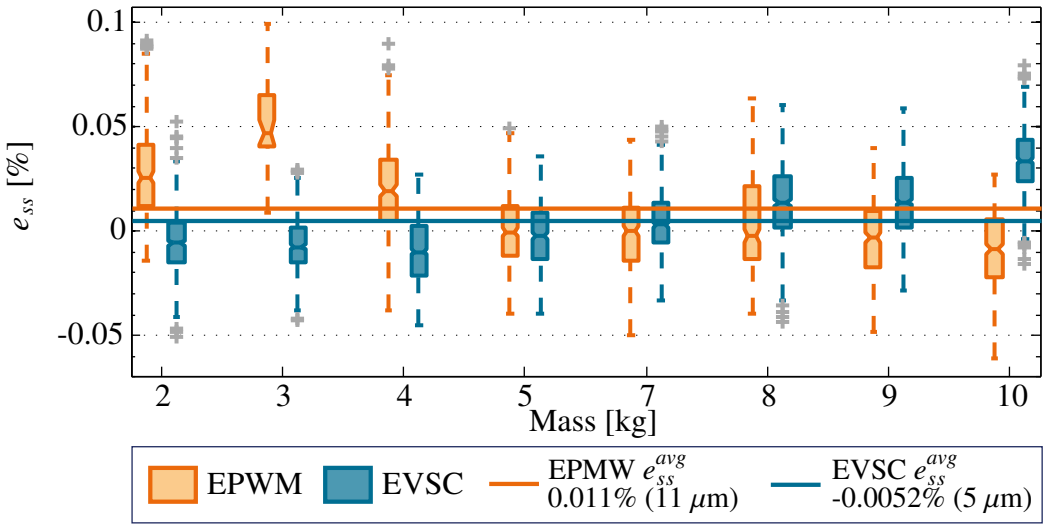

Figure 8-32: *Steady state error distribution with EPWM and EVSC at fourth step*

8.5.4 Step response at fifth step (heating)

The final heating step at 55s is again a small step, and similar to all other steps, there is an exchange between the large and small signal controllers at the step transitions and when the strain error is within δ_ε. The system response with EPWM and EVSC is in Fig. 8-33. This step also shows fast rising times for all masses as shown in Fig. 8-34, with average values in Tab. 8-9. EPWM again produces overshoots for all masses between 2 and 7 kg (maximum 0.13% (130 μm) at 2 and 3-kg masses), while EVSC shows no overshoots. Correspondingly, the settling time varies between 0.37 and 2.45s (EPWM) and between 0.44 and 0.73s (EVSC). This step is challenging as it is a small heating step directly following the previous small heating step and overshoots are expected. The performance of the EVSC controller, which shows no overshoots even for this step, is exceptional.
The steady state error distribution in Fig. 8-35, with the average values in Tab. 8-9 shows excellent steady state tracking for both controllers. Despite the overshoots and larger settling times with EPWM, the steady state error stabilises for this step.

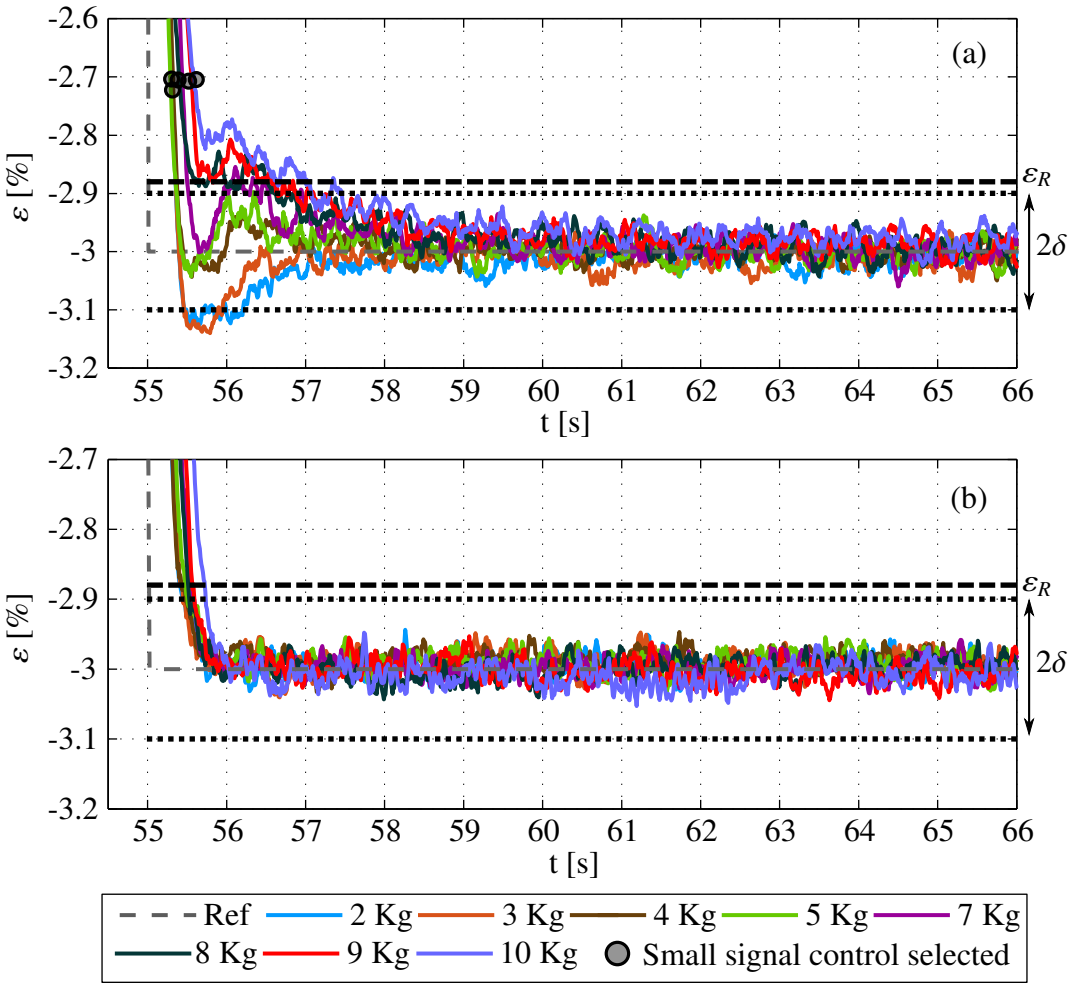

Figure 8-33: *Actuator response with EPWM (a) and EVSC (b) at fifth step (heating)*

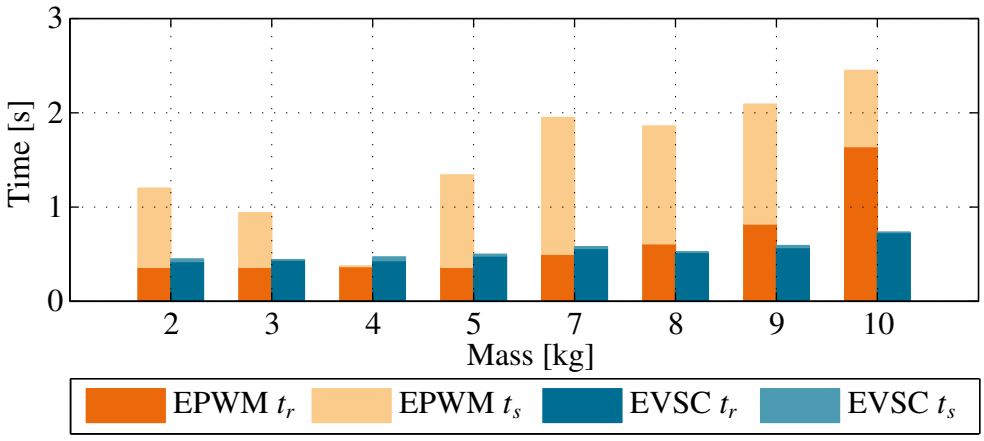

Figure 8-34: *Rising and settling time with EPWM and EVSC at fifth step (heating)*

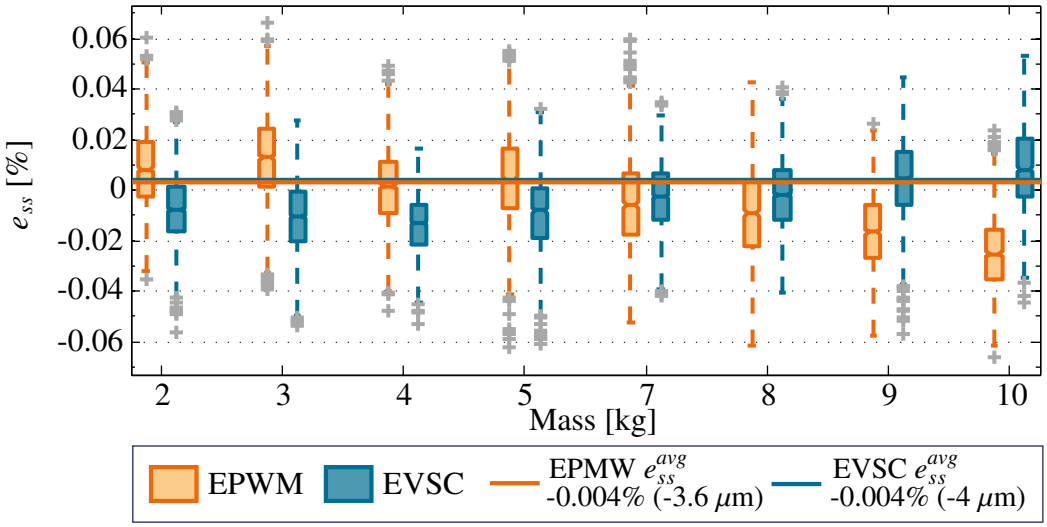

Figure 8-35: *Steady state error distribution with EPWM and EVSC at fifth step*

Table 8-9: *Response for SMA actuator with EPWM and EVSC at fourth and fifth step*

Controller	Step: H or C	t_r^{avg}	t_s^{avg}	e_{ss}^{avg}	e_{ss}^{RMS}
EPWM	Step 4: H	0.9s	3.5s	0.011% 11μm)	0.028% (28μm)
EVSC	Step 4: H	1.0s	1.1s	0.0052% (5μm)	0.02% (19μm)
EPWM	Step 5: H	0.6s	1.5s	-0.0036% (-3.6μm)	0.021% (21μm)
EVSC	Step 5: H	0.5s	0.5s	-0.0041% (-4μm)	0.02% (16μm)

The last step is a cooling step back to 0% strain and is similar to the cooling step at 15s. On average, the EVSC controller performs better than the EPWM controller. The only drawback to the EVSC was observed when the desired strain consists of small cooling steps as was the case for step ❸ (see Fig. 8-19). Here, the EVSC shows higher steady state error than the EPWM controller. However, the error is below 0.04% (40μm) and therefore acceptable.

8.6 Sinusoidal Response with Constant Masses with EPWM and EVSC Controllers

In this section, the desired strain is a sinusoidal signal with a frequency of 0.02 Hz and an amplitude of 2% (peak-to-peak strain of 4%). The wire is loaded with various constant masses from 2 to 10 kg (excluding 6 kg). The results with the corresponding tracking errors are shown in Fig. 8-36 for EPWM and in Fig. 8-37 for EVSC. The minor peaks at the beginning of the experiment arise due to the fact that the maximum of the desired sinusoidal strain is set slightly lower than the strain at room temperature. This is to ensure that the wire is physically able to reach the maximum desired strain. The tracking performance is subsequently discussed simultaneously for both controllers.

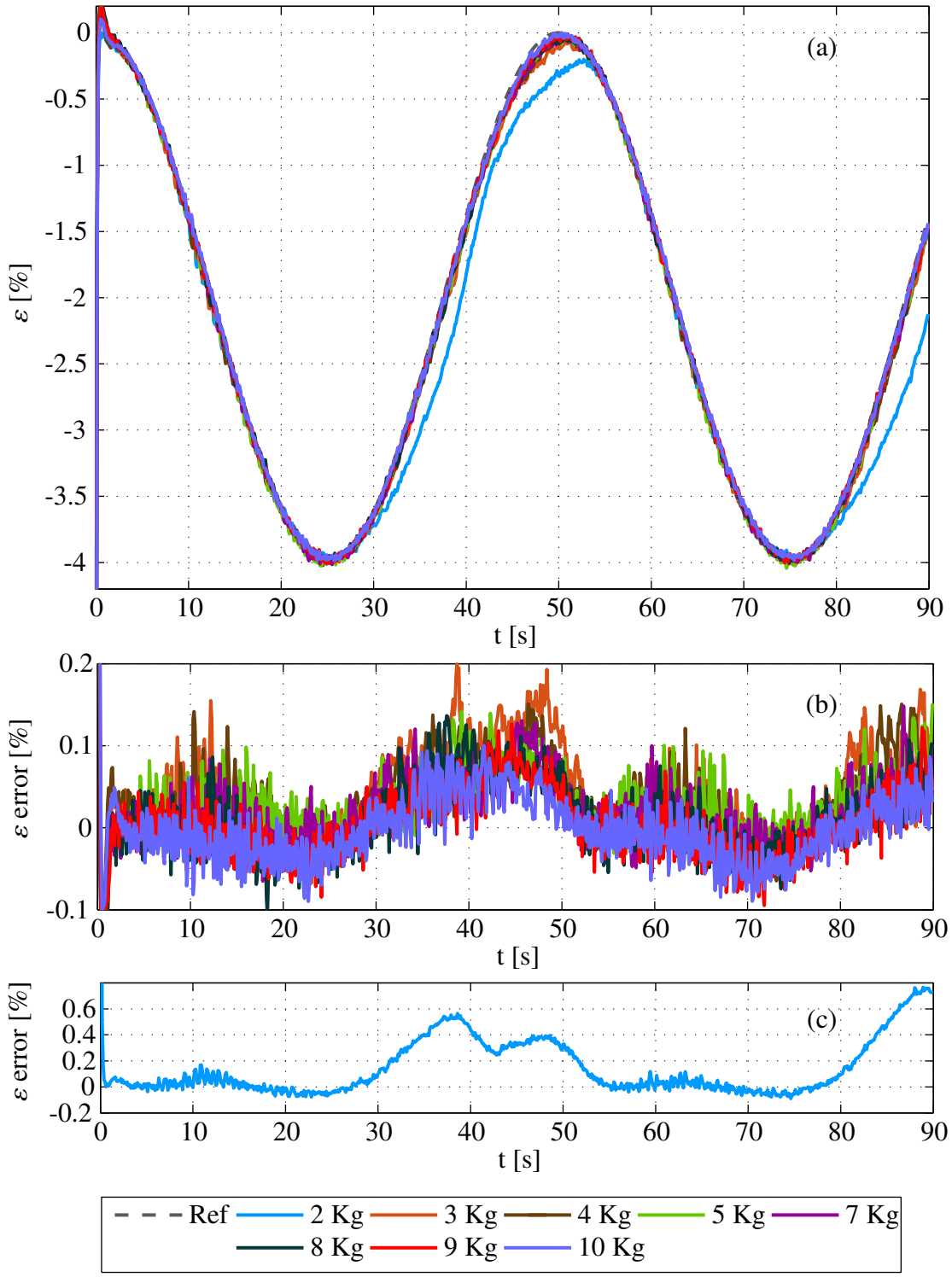

Figure 8-36: *Sinusoidal response with different constant masses with EPWM controller*

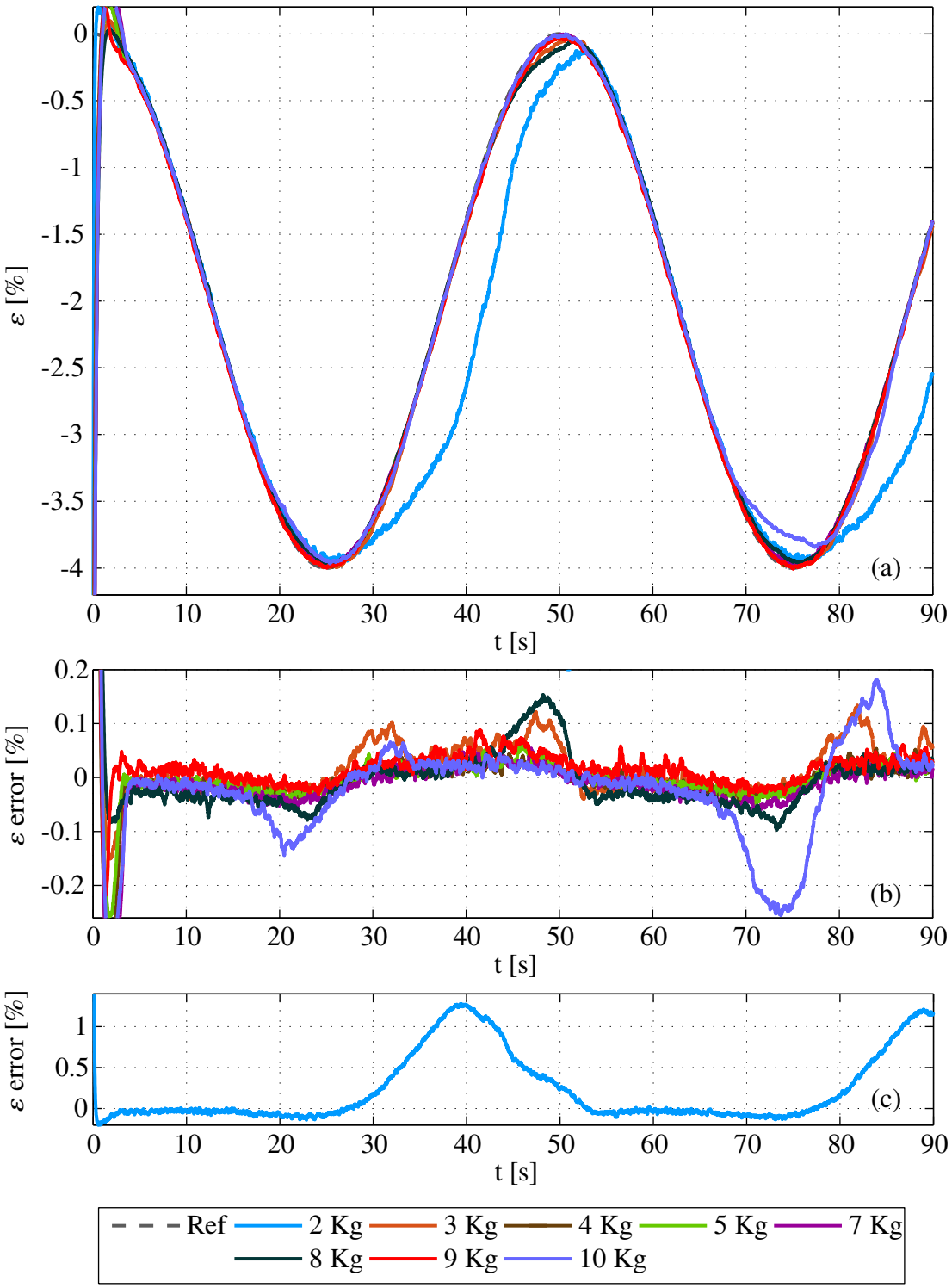

Figure 8-37: *Sinusoidal response with different constant masses with EVSC controller*

In the segments from 0 to 25s and 50 to 75s, the desired strain decreases from 0% to -4%, and the SMA wire needs to be heated to track the sinusoid. The tracking performance using both controllers is shown for a portion of the first heating segment and the first minimum in Fig 8-38(a) using the EPWM controller and in (b) for the EVSC controller. Similar performance is observed for the heating portion from 50 to 75s (not shown). The error distribution for both heating phases at each mass with EPWM and EVSC is shown in Fig. 8-39[10].

From both figures, it can be deduced, that the SMA is able to follow the desired sinusoidal trajectory including the minimum for all loads exceptionally. The average tracking error e_{ε}^{avg} when using EPWM is -0.004% (3.6 μm with a wire length of 9.9 cm). The average with EVSC is about 10 times larger at -0.033% (36 μm with a wire length of 10.8 cm). The error in the EVSC controller is particularly observable when tracking the minimum (see Fig. 8-38(b)). The worst performance is shown by the 10-kg load (cf. Fig. 8-37 between 70 and 80s), with a high peak error of -0.25% (270 μm). These errors arise due to the fact that the temperatures required to track the minimum at a load of 10 kg are very high and close to current limit set by the current supply. While the EPWM on average tracks the sinusoid better than the EVSC, it oscillates around the desired strain (see Fig. 8-38(a)), thereby causing larger dispersion in the data. Data dispersion can be represented with the interquartile range (IQR), which in turn is the height of individual bars in a box plot [UC96]. Therefore, as the height of the bars for EPWM in Fig. 8-39 are, with the exception of 10 kg, larger than for EVSC, this shows that the EPWM controller response is more oscillatory.

The tracking performance for the cooling portion from 25 to 50s and 50 to 90s is not as good as for the heating portion (cf. Figs. 8-36 and 8-37). This is expected since cooling occurs through natural convection which is sluggish in comparison to heating. The 2-kg mass shows the poorest performance in both cooling phases with a peak error of 0.6%(594 μm) for EPWM and 1.26%(1.4 mm) for EVSC (see Figs. 8-36(c) and 8-37(c)). These errors arises due to the fact that the cooling transformation temperatures at lower masses are lower and natural convection is insufficient to cool the wire fast enough. This is most noticeable as the maximum is approached as shown in Fig. 8-40(a) for EPWM and (b) for EVSC, where it is observed that all masses have tracking difficulties. The 10-kg mass shows the best performance, attributed to the higher cooling transformation temperatures at higher stresses.

The error distribution with both controller is in Fig. 8-41 for the masses 3 to 10 kg[11]. Here the EPWM controller has an average error of 0.045% (45 μm) and the EVSC of 0.026% (28 μm). Comparing these values with the heating segments shows that while the EVSC controller performance is comparable during heating and cooling, the EPWM controller has much poorer performance during cooling. The high IQR in the data for EPWM shows that, similar, to the heating case, the EPWM controller oscillates around the desired strain.

[10] In investigating the tracking performance, the first segment is considered from 5 to 25s in order to avoid considering the minor peak at the beginning of the experiment. Similarly, the second segment is considered from 55 to 75s to avoid considering the remnants of the prior cooling portion.

[11] The error for 2 kg is omitted here because its error is much larger than the other masses and therefore dwarfs their values if included in the box plot.

Tab. 8-10 shows the RMS errors for each mass for both EPWM and EVSC controllers. The EVSC controller, on average, shows better tracking performance for all masses, with the exception of at 2 kg and 10 kg.

Note that the strain errors of all experiments, excluding the 2-kg mass, are below the threshold $\delta_\varepsilon = 0.3\%$ (EPWM) and $\delta_\varepsilon = 0.5\%$ (EVSC). Therefore, only the small signal controller is selected for tracking the sinusoid. For the 2-kg mass, the error is higher than δ_ε only in the cooling phases, where a switch to the large signal controller has no effect on the system response due to lack of an active cooling mechanism.

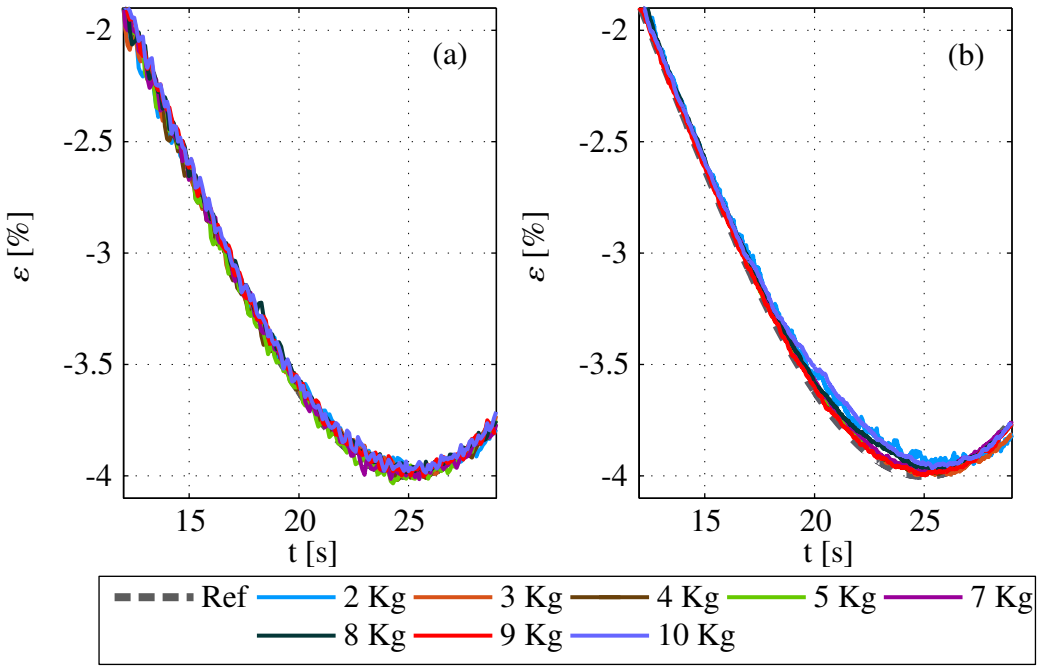

Figure 8-38: *Tracking of sinusoidal strain (a) EPWM and (b) EVSC during heating*

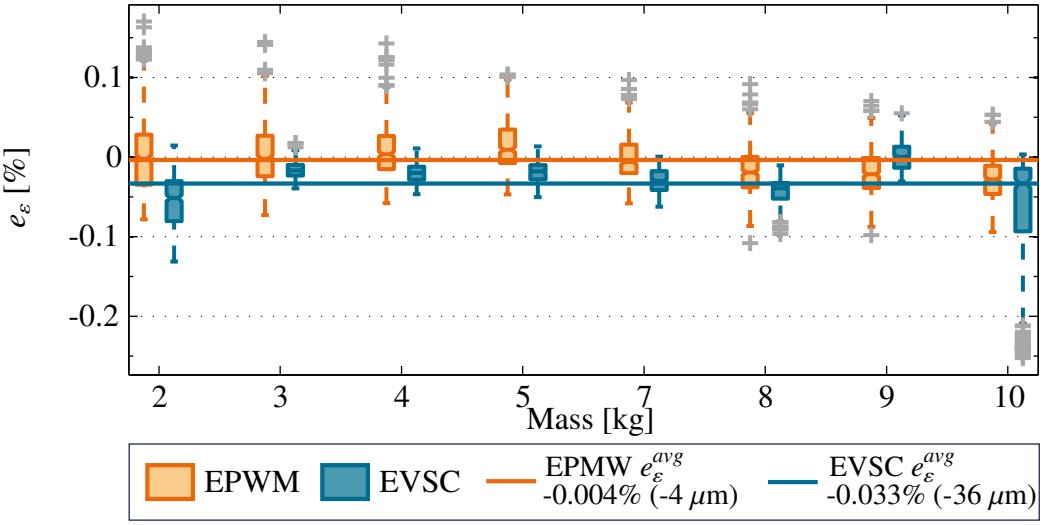

Figure 8-39: *Tracking error with (a) EPWM and (b) EVSC during heating*

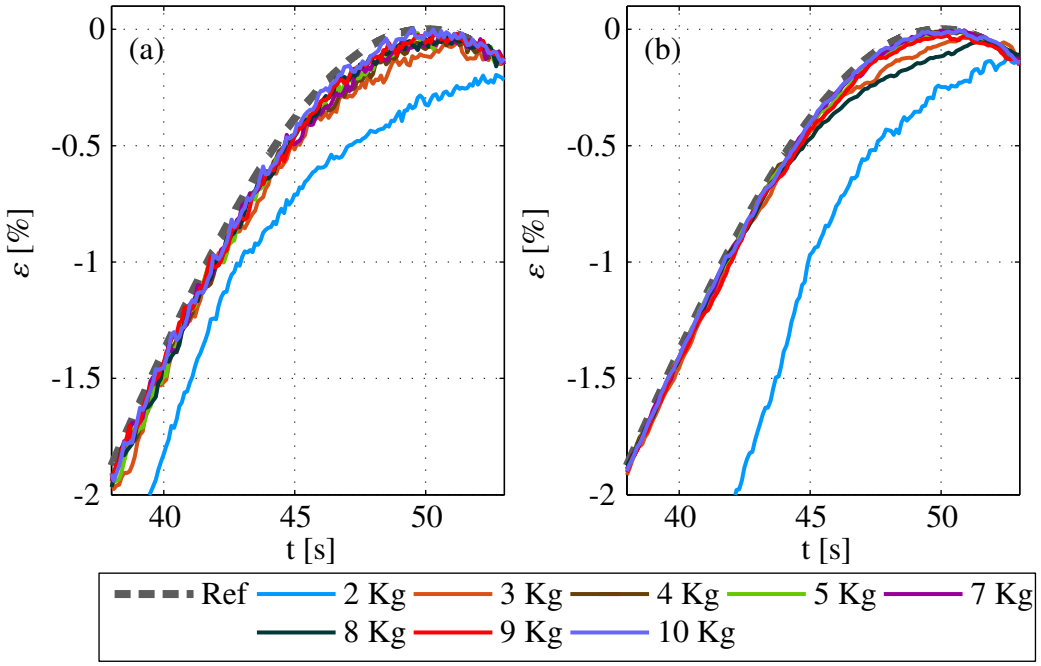

Figure 8-40: *Tracking of sinusoidal strain (a) EPWM and (b) EVSC during cooling*

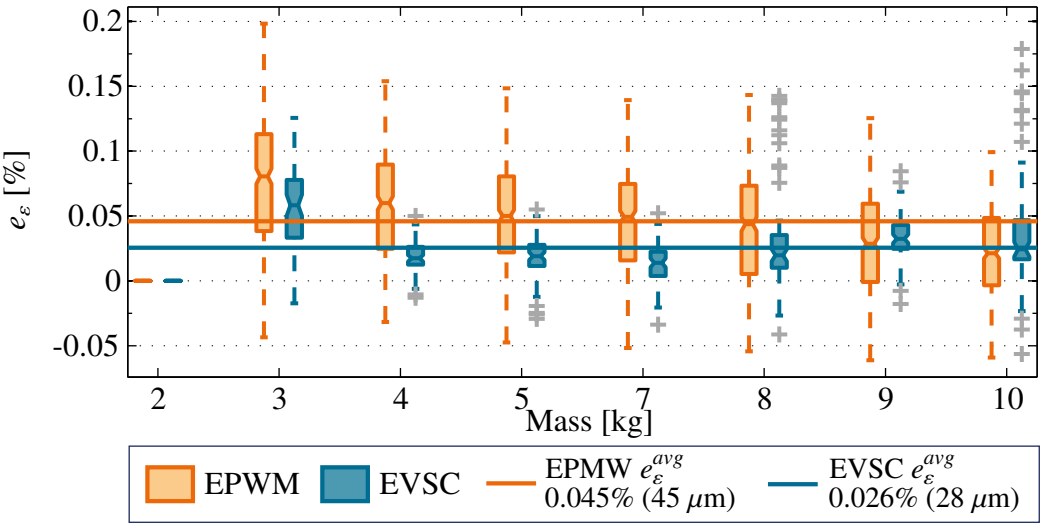

Figure 8-41: *Tracking error with (a) EPWM and (b) EVSC during cooling*

Table 8-10: *RMS errors for sinusoidal desired strain with EPWM and EVSC controllers*

	Mass(kg)	2	3	4	5	7	8	9	10
EPWM	RMSE(%)	0.25	0.068	0.056	0.049	0.045	0.045	0.04	0.038
	RMSE(μm)	251	67	55	49	45	45	40	38
EVSC	RMSE(%)	0.49	0.045	0.021	0.022	0.027	0.048	0.028	0.08
	RMSE(μm)	526	49	23	23	29	52	30	86

8.7 Bandwidth

In this section, the SMA response to various desired sinusoidal strain signals as shown in Fig. 8-37 are investigated. Since the EVSC controller showed better performance for sinusoidal tracking in the previous section, it is selected for the bandwidth investigations in this section. The wire is loaded with various constant masses from 2 to 7 kg. The results for tracking a sinusoid with an amplitude of 2% (peak-to-peak strain of 4%) and frequencies 0.02 Hz, 0.025 Hz and 0.033 Hz are shown in Fig. 8-42(a)-(c). The corresponding tracking errors are shown in Fig. 8-42(d)-(f) and the RMS errors are in Tab. 8-11.

The results show that at a frequency of 0.02 Hz, the SMA is able to follow the desired sinusoidal trajectory for loads from 4 to 9 kg, with 3 kg showing the poorest performance. At 0.025 Hz, the SMA with a 4 kg load shows a peak error of 0.22% (238 μm) in both cooling phases. Further, at 7 kg an error of about 0.2% (216 μm) is observed at the second minimum. At a frequency of 0.033 Hz, the SMA with loads from 3-7 kg follows the desired trajectory, with 7 kg showing the poorest performance in the cooling phases. At loads as high as 7 kg, the SMA experiences high deformation strains at room temperature. Although the cooling transformation temperatures are high, the amount of energy that needs to be removed to recover this strain rises. Since the desired strain frequency is also high, natural convection proves to be insufficient to cool the wire. The mean RMSE over all loads is 0.12%(130 μm) as shown in Tab. 8-11. However, without including the 7 kg mass, the RMSE drops to 0.05%(54 μm).

When the amplitude of the reference signal is reduced from 2% to 1% (Fig. 8-43(a)), then the SMA is able to track the sinusoid with a frequency of 0.05 Hz with loads from 4-7 kg. When the amplitude is further reduced to 0.5%, then good tracking is shown at a frequency of 0.1 Hz (Fig. 8-43(b)) and reasonable tracking is shown at frequencies of 0.15 Hz (Fig. 8-43(c)). 0.15 Hz at 1% amplitude is the tracking limit without active cooling. Note that the maximum of the desired strain is set much lower that the strain in the SMA wire at room temperature. Therefore, for the first few seconds of the experiments shown in Fig. 8-43, the SMA wire has to be heated considerably in order to reach the desired strain. The RMS errors for the different loads and frequencies, shown in Tab. 8-11, are calculated a few seconds after the start of the experiment when the wire has reached the desired strain in order to omit this starting phase.

All experiments are controlled by the small signal controller since their errors are below δ_ε. The only exception to this is in the 0.033 Hz, 7 kg experiment. However, since these errors occur in the cooling phase where no control is possible due to lack of an active cooling mechanism, the switch to the large signal controller has no effect on the system response.

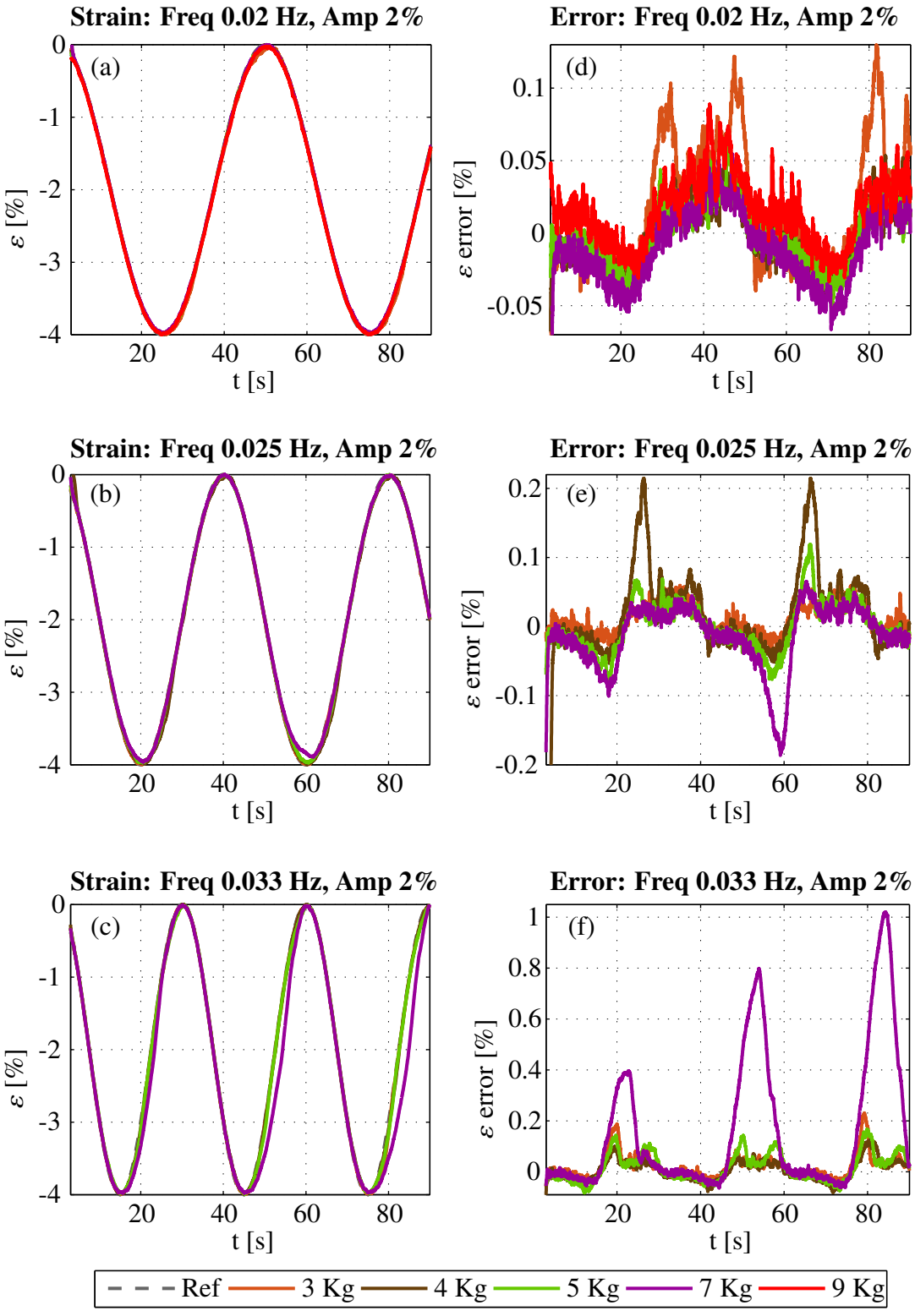

Figure 8-42: *Actuator response with different constant masses and frequencies from 0.02 to 0.033 Hz with EVSC controller*

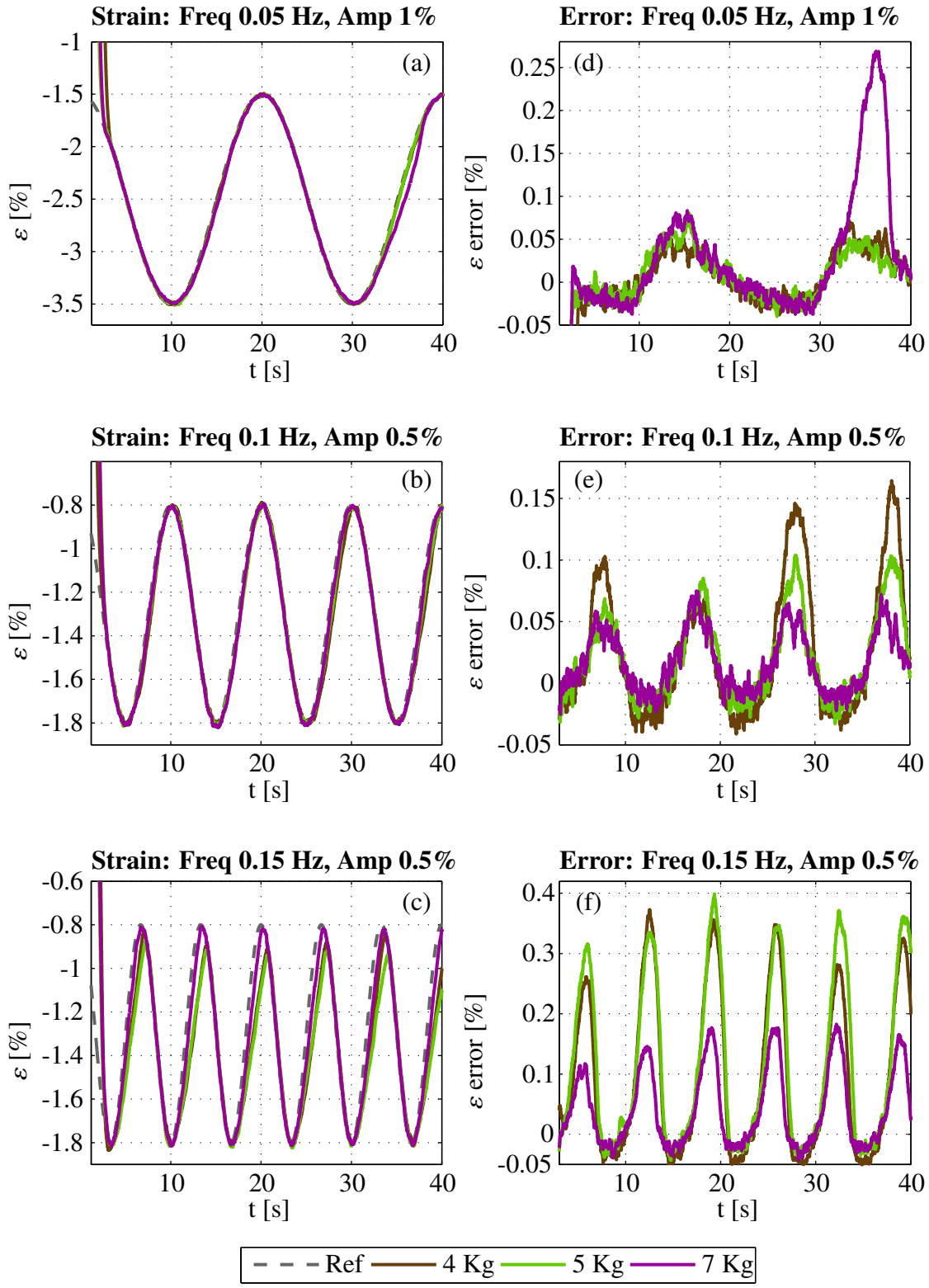

Figure 8-43: *Actuator response with different constant masses and frequencies from 0.05 to 0.15 Hz with EVSC controller*

Table 8-11: *RMS errors for sinusoid signal with EVSC controller*

Freq:	0.02 Hz	0.025 Hz	0.033 Hz	0.05 Hz	0.1 Hz	0.15 Hz
Amp:	2%	2%	2%	1%	0.5%	0.5%
3 kg	0.045%	0.024%	0.052%	-	-	-
	49 μm	26 μm	56 μm	-	-	-
4 kg	0.021%	0.072%	0.041%	0.033%	0.063%	0.19%
	23 μm	78 μm	44 μm	35 μm	69 μm	202 μm
5 kg	0.022%	0.036%	0.058%	0.031%	0.043%	0.20%
	23 μm	39 μm	62 μm	33 μm	46 μm	215 μm
7 kg	0.029%	0.049%	0.32%	0.072%	0.030%	0.092%
	31 μm	53 μm	349 μm	78 μm	32 μm	99 μm
mean	0.029%	0.045%	0.12%	0.045%	0.045%	0.16%
	31 μm	49 μm	128 μm	49 μm	49 μm	172 μm

8.8 Disturbance Rejection and Dynamic Masses

In this section, dynamic load changes and disturbance rejection are investigated using both the EPWM and EVSC controllers. For the EPWM controller, the SMA wire is loaded with a 10 kg mass, realised with a 2, 3 and 5-kg-slotted weight. The desired strain is a sinusoidal signal with an amplitude of 1.75% and a frequency of 0.02 Hz. During the experiment, either only the 3-kg mass or both the 3 and 5-kg masses is/are removed or added to the wire. The mass change is performed abruptly in order to expose the SMA to an impulse-like load disturbance (see Fig 8-44(b)). In this manner both dynamic load change and disturbance rejection could be investigated in the same experiment.

For the EVSC controller, the SMA wire is loaded with a 9 kg mass, realised with a 2-kg and a 7-kg-slotted weight[12]. The desired strain is a sinusoidal signal with an amplitude of 2% and a frequency of 0.02 Hz as in Fig. 8-45(a). Similar to the EPWM case, during the experiment, either the 2-kg mass or the 7-kg mass were abruptly removed or added to the wire (Fig 8-45(b)) to produce disturbances and dynamic load changes.

The results are in Figs. 8-44 and 8-45, for EPWM and EVSC, respectively. As responses using both controllers are very similar, only the EPWM controller will subsequently be used to explain the response.

The EPWM controller starts tracking the sinusoid with the small signal controller valid at the start of the experiment because the strain error is low. The first disturbance is at position A (see top of Fig 8-44), generated by the abrupt removal of a 3-kg mass. The strain decreases here because lower masses at the same temperature displays less strain than higher masses. The removal of a 3-kg mass causes a large strain error. This in turn triggers a switch from the small signal to the large signal controller. The large signal controller is selected until the strain error is less than δ_ε, at which point the small signal controller is once again selected. The controller is able to recover the disturbance and continues tracking the sinusoid, albeit with a different mass than at the start of the experiment. Therefore, the

[12] Due to tracking problems with 10 kg when using the EVSC controller (cf. Fig. 8-37 and Tab. 8-10), 9 kg, which shows better tracking response is used for this experiment in order to be able to investigate disturbance rejection without considering other effects.

controller is able to deal with dynamic load changes, including situations where the load change occurs abruptly.

When the 3-kg mass is dropped onto the wire again at B, the tracking response is hardly affected. The reason for difference in response is due to the fact that at A, the SMA needs to be cooled to recover from the disturbance, while at B, the wire needs to be heated. As heating is much faster than cooling, the responses are correspondingly different.

A large mass removal of 8 kg at C, causes the wire to deviate significantly from the desired strain, but the switch of controllers from small to large and back to small signal succeeds in overcoming the disturbance and tracking the desired signal. The response of the system when the 8-kg mass is dropped onto the wire again at D employs the same controller switching, with a much faster recovery than at C. This switch of controllers, depending on the magnitude of the disturbance and therefore strain error, is observed for the rest of the load changes from E-L. Additonally, the difference in disturbance recovery, i.e. faster recovery for load increase rather than load decrease is likewise observed for the rest of the experiment.

The response using the EVSC controller is analogous to the EPWM controller as the same switch between large and small signal controllers is very successful in rejecting the disturbances. The controller is also able to deal with dynamically changing masses (see Fig 8-45).

8.9 Summary

In this chapter, the results of precision position control of SMA actuators is presented.

The controller architecture used consists of the combination of large and small signal controllers. The large signal controller, responsible for course positioning, is an P-P^2P^3 temperature controller that gets its desired temperature value online from the inverse constitutive and phase kinetics SMA models from Chap. 7.
The small signal controller, responsible for fine positioning, uses two different types of controllers alternatively: an PD-P^2P^3 controller whose control signals are modulated with Pulse Width Modulation (PWM) and a variable structure controller (VSC). The VSC uses an asymmetrical boundary layer to prevent over-heating of the wire, therefore reducing the steady state error and its control signals adapt to the dynamic load on the wire, therefore reducing overshoots.
Both controllers are used for positioning of an SMA wire at various loads. The results show exceptional and precise tracking performance for steps of various heights. Sinusoidal tracking is also precise, however, a frequency of 0.15 Hz at 1% strain amplitude is shown as the tracking limit without active cooling. The robustness of the controller is shown by accurate sinusoidal tracking with dynamical loads and exceptional disturbance rejection with disturbances as high as 8 kg. Large disturbances are effectively rejected by using a switch between the large and small signal controllers.
The EVSC controller on average shows better performance as the EPWM controller for both step and sinusoidal desired strains. As the control law and models used are simple, easy to implement and run in real time, the next chapter presents the implementation of the controller on an embedded processor for an industrial clamping application.

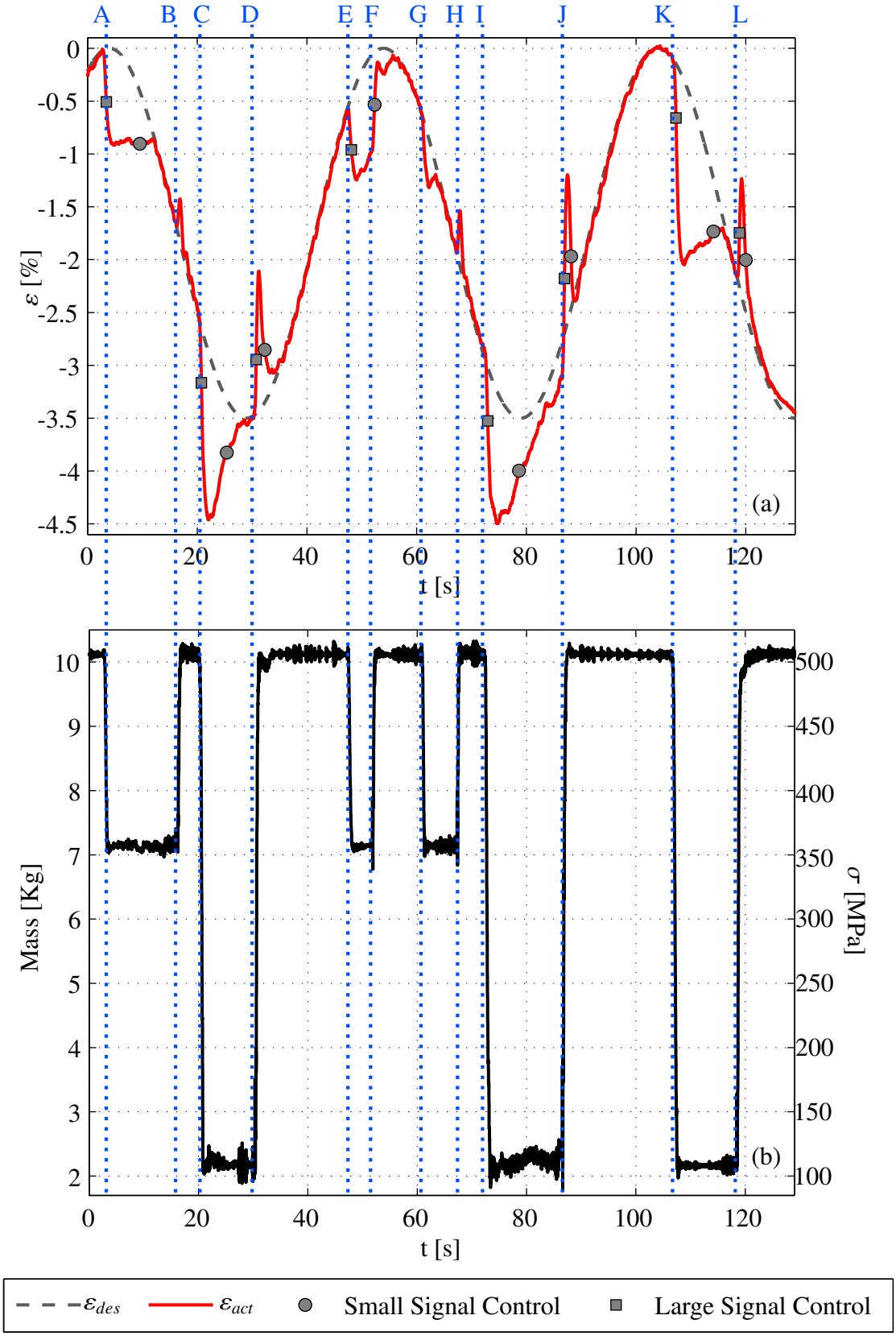

Figure 8-44: *Actuator response with disturbances and dynamic loads (EPWM controller)*

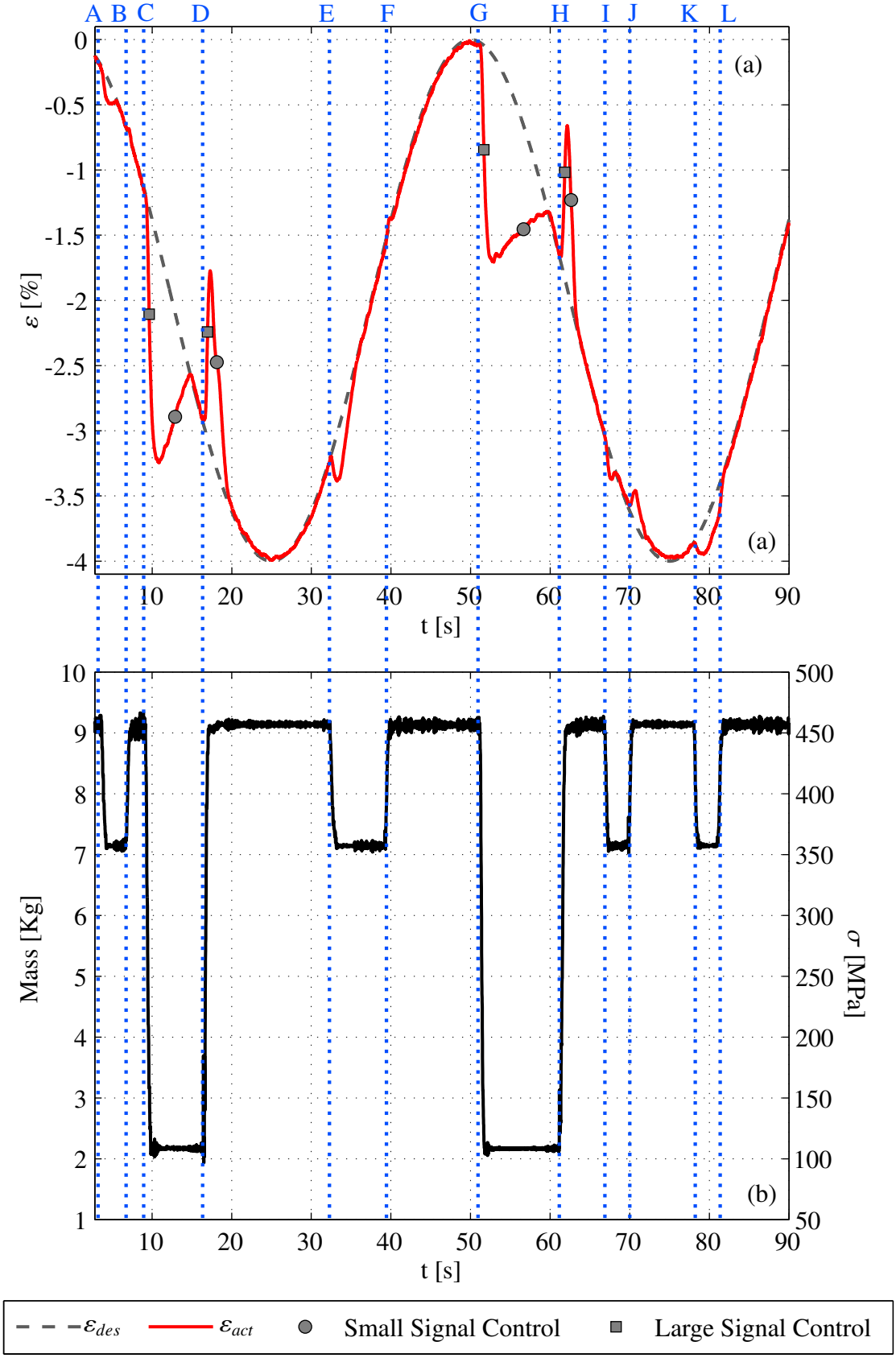

Figure 8-45: *Actuator response with disturbances and dynamic loads (EVSC controller)*

9 Embedded Force and Position Control for an Industrial Clamping Application

Clamping is an integral component of several industrial processes. For example, in milling and drilling industries, clamping vices are required for work piece holding; in pick and place applications, clamps are required to transport material from one point to another etc. The clamping process usually employs vices as shown in Fig. 9-1, which are controlled using hydraulic, pneumatic or mechanical methods. When clamping delicate objects, e.g. thin-walled glass, the clamping force is an important factor that needs to be considered. On the one hand, the object has to be clamped with a force that is large enough to allow for accurate processing. On the other hand, the clamping force should not be too high to prevent damaging the object. A balance between these conflicting constraints has to be found. A force controlled clamp can assist in achieving this balance, however, the clamps usually do not have any force control because of larger installation space, complexity and higher costs.

In this chapter, a force controlled clamping vice with shape memory alloy wires is presented. Due to the fact that SMAs have a high energy density, the transition from a manual to an automatic clamping process requires no extra installation space. In order to make the SMA-based clamping vice viable for industrial applications, the control algorithms are implemented on an embedded processor and all the components are selected from a low price range.

Further, according to current trends in industrial digitalisation according to cyber-physical-systems (CPS) and Industry 4.0 [MKB+16] [LBK15], an android-based mobile platform is used to set the desired clamping force, to monitor the clamping process and to display relevant process data. The communication between the mobile platform and the clamping vice is realised via an industrial wireless communication protocol. Due to the use of a mobile platform, the process data can also easily be loaded onto a cloud service to be viewed and analysed remotely.

(a) (b)

Figure 9-1: *Industrial clamping vices (a) mechanical (manual), (b) pneumatic [Sch16]*

9.1 SMA-based Clamping Vice

The clamping vice, shown in Fig. 9-2(a), consists of guide rails on which a movable stage is mounted. An SMA wire, with an $A_s > 95°C$ is attached between the stage and one end of the vice. Restoring springs wrapped around the guide rail are also attached between the stage and the end of the vice, such that they are parallel to the SMA wire[1]. In this chapter, the objects to be clamped are restricted to round, thin-walled test tubes, where force control during clamping is necessary to avoid damaging the test tube. To this end, a pair of jaws is mounted on the vice, where one of the jaws is v-shaped in order to facilitate clamping. In Fig. 9-2(b), the clamping vice is shown with the test tube positioned on the v-shaped side of the jaws. The SMA is at room temperature ($T < M_f$ i.e. cold) and the clamping vice is in its initial state. When the wire is heated by passing a current through it, it contracts and in doing so, pulls the stage and thereafter clamps the test tube as shown in Fig. 9-2(c). When the wire cools, the restoring springs re-elongate to their initial length, push the jaws apart and re-elongate the wire to its initial length. The clamp is therefore restored to its initial state in Fig. 9-2(b). The clamping force is hence proportional to the length of the wire. As the length of the wire is controlled through the wire temperature and therefore through the current passing through the wire, the clamping force can be regulated with the wire current. When pressure sensors are employed, the clamping force can further be controlled in closed-loop without extra installation space or complexity. The system and control architecture to this end are shown in the next section.

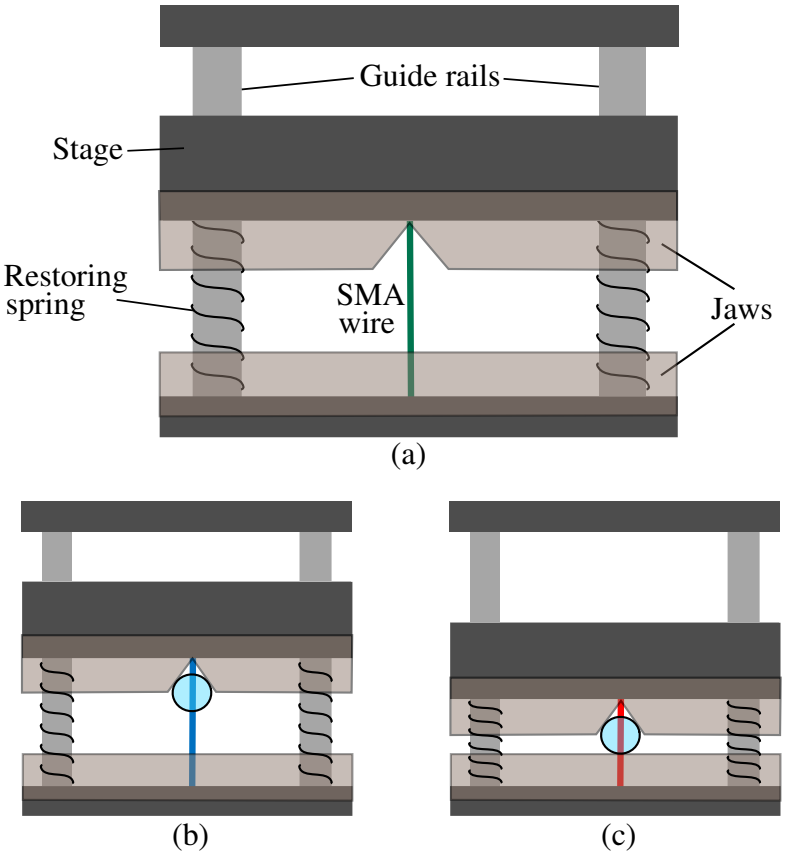

Figure 9-2: *(a) SMA-based clamping vice (b) initial state (c) clamping a test tube*

[1] Attaching the restoring springs to the other side of the stage as the SMA wire has the same effect.

9.2 System Architecture

The system architecture, shown in Fig. 9-3, consists of the clamping vice in Fig. 9-2, with the same 0.5mm SMA wire used in the experiments in the previous chapters, enhanced with the following components (data sheets of all components are in Appendix A2.12 to A2-18):

Controller The controller unit for the clamping vice is a *STM32 ARM® Cortex™-M4* microcontroller, mounted on the *Mikromedia 7 for STM32F4* from MicroElektronika (see A2-18). It has an integrated touch display which is useful for debugging and displaying measurement data.

Android mobile plattform An android tablet is used to set the desired force for clamping the test tube and to monitor the clamping process. The data communication occurs through the Serial Peripheral Interface (SPI) of the microcontroller via Bluetooth®.

Force measurement The clamping force is measured with a force sensing register (FSR). FSRs are robust polymer thick film devices that exhibit a decrease in resistance with an increase in force applied to the sensor surface (see A2.16). With a thickness of 0.46 mm, the sensors are thin enough to be used in this application. The force sensitivity range is from 0.2 to 20N. However, the sensors are low cost (under 5 Euros) and are therefore not accurate [Ada16]. The calibration of the sensor was carried out with standard weights from 10g to 2kg in 10g steps.

Temperature measurement The temperature of the wire is measured with the same thermocouple as used in the phase kinetics experiments in Chap. 6 and in the control experiments in Chap. 8. The signals from the thermocouple are likewise sent to a converter *MAS Thermo-K* with galvanic isolation before being routed to the microcontroller (see A2.12 and A2.13).

Current source The current in the wire is regulated using a constant controlled current source from MyTinySun® [MyT16] (see A2.14) that outputs an analog current upto 3A when triggered, just as in the phase kinetics experiments in Chap. 6 and in the control experiments in Chap. 8.

Current measurement The current in the wire is measured with a current shunt monitor from Texas Instruments (see A2.17). This is necessary to ensure that the wire does not overheat.

The desired force is set on the android tablet and sent via Bluetooth® to the SPI interface of the microcontroller. The three sensors (force, temperature and current) transmit their data via analog inputs into the microcontroller. Based on the desired force and the sensor data, the control strategy, which is implemented on the microcontroller computes the required current to clamp the test tube as desired. The microcontroller then sends an analog output signal to the current source to bring the required current to the wire[2]. The process data, collected from the sensors, is sent to the android tablet for display and monitoring. Note that a distance sensor is not used in the set-up.

[2]Note that although a current sensor is used in the set-up, no feedback current control loop is implemented. This is due to the fact that a temperature controller is more effective in controlling the SMA.

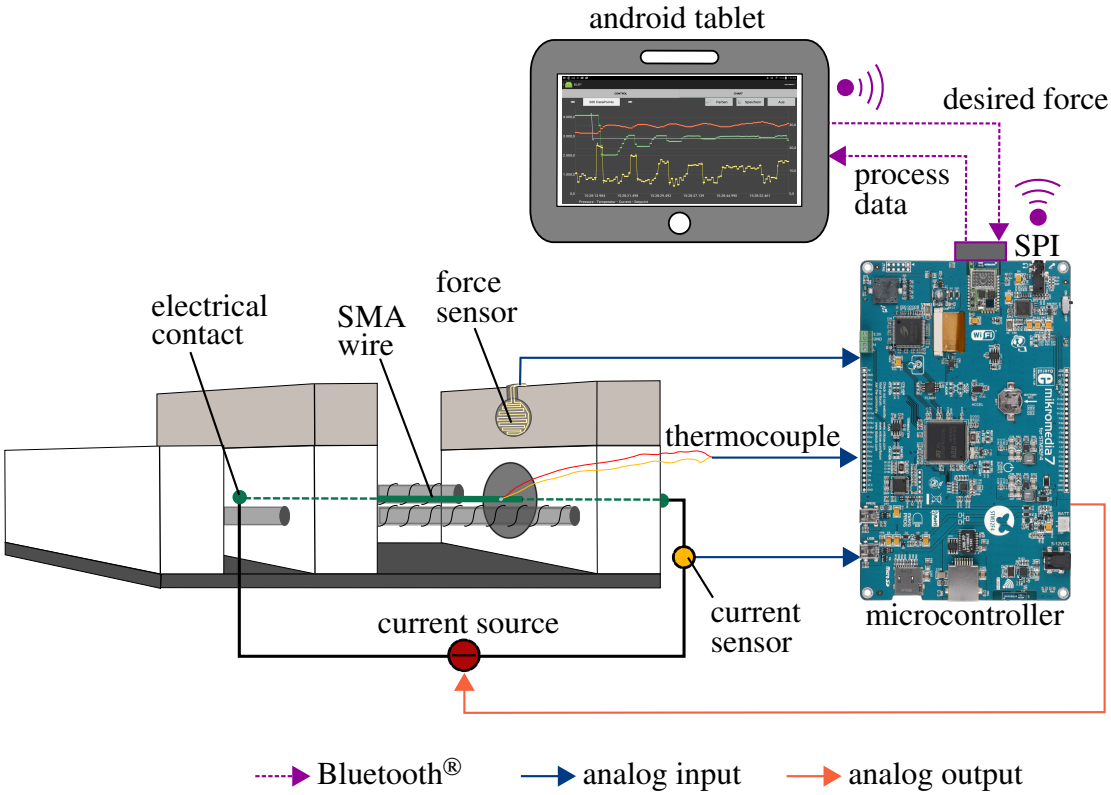

Figure 9-3: *SMA-based clamping vice system architecture*

9.3 Mechanics

Fig. 9-4 shows a schematic diagram of the jaws, with a test tube, in the initial state of the clamping vice (see Fig. 9-2(b)). Due to the system architecture, the force sensor can only output force measurements when the test tube (that should be clamped) is touching the sensor i.e. when the SMA wire is Δx_{min} shorter as in its initial cold state. Δx_{min} and the corresponding strain $\Delta\varepsilon_{min}$ are calculated with (9-4) and (9-5), respectively. The jaw dimensions W, H, B, the diameter of the test tube D and the length of the SMA wire $l_{S\,MA}$ are known. x and h in (9-2) and (9-3), respectively are calculated with y from (9-1).

$$y = D\sin\left(\frac{\pi}{2} - \operatorname{atan}\left(\frac{B/2}{H}\right)\right) \tag{9-1}$$

$$x = \frac{D}{2} - \frac{1}{2}\sqrt{D^2 - y^2} \tag{9-2}$$

$$h = \frac{Hy}{B} \tag{9-3}$$

$$\Delta x_{min} = W - D - (h - x) \tag{9-4}$$

$$\Delta\varepsilon_{min} = \frac{\Delta x_{min}}{l_{S\,MA}} \tag{9-5}$$

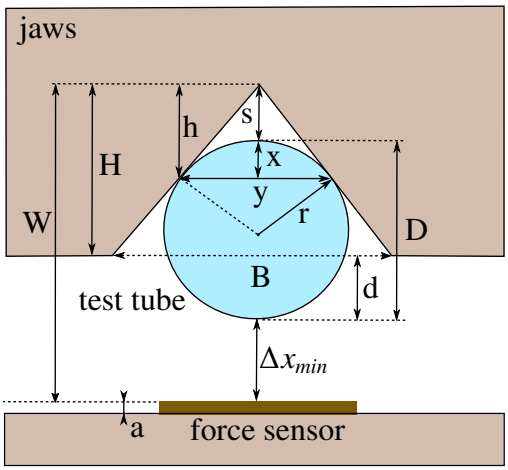

Figure 9-4: *Initial state of clamping vice with test tube showing all dimensions*

Due to the architecture of the clamping vice, the forces in the springs and the force in the SMA are equal and opposite as shown mathematically in (9-6), where k_s [N/m] is the spring constant. Friction in the system is neglected. Converting the forces to stresses and Δx to $\Delta\varepsilon$ gives (9-7) , where l_{SMA} and A_{SMA} are the length and cross sectional area of the SMA wire. The spring constant is then K_s [Pa/-].

The length of the wire and the restoring springs are measured before they are installed into the clamping vice. ⓪ in Fig. 9-5 is the total strain in the system, which can be set by varying the length between the jaws (and therefore the SMA wire length). After installing the wire and spring in the vice, equilibrium is reached at ① in Fig. 9-5, which is determined by measuring the spring and/or wire lengths after installation in the vice to give $(\varepsilon_{m0}, \sigma_{m0})$. The stress in the SMA and the springs is given by (9-8), where $\Delta\varepsilon_{s0}$ is the strain in the spring after installation.

$$F_{SMA}(T) = F_s \quad = k_s \Delta x \tag{9-6}$$

$$\sigma_{SMA}(T) = \sigma_s \quad = k_s \frac{l_{SMA}}{A_{SMA}} \Delta\varepsilon = K_s \Delta\varepsilon \tag{9-7}$$

$$\sigma_{SMA}(T < M_f) = \sigma_{m0} = K_s \Delta\varepsilon_{s0} \tag{9-8}$$

As the temperature in the wire is increased, it contracts and in doing so has to overcome the spring forces. Therefore its stress-strain characteristic is constrained to the line ①→④, which has a slope of K_s.

When the SMA is heated to a temperature T_{min} such that it contracts by a strain $\Delta\varepsilon_{min}$ (cf. (9-5)), it pulls the guide and v-shaped portion of the jaws such that the force sensor touches the test tube. The stresses in the system are given by (9-9), which is equivalent to (9-10). On the stress-strain diagram in Fig. 9-5, this is at ②, with coordinates $(\varepsilon_{min}, \sigma_{min})$, according to (9-11) and (9-10).

$$\sigma_{SMA}(T_{min}) = \sigma_{min} = K_s(\Delta\varepsilon_{s0} + \Delta\varepsilon_{min}) \tag{9-9}$$

$$\sigma_{min} = \sigma_{m0} + K_s \Delta\varepsilon_{min} = \sigma_{m0} + \sigma_{\Delta s} \tag{9-10}$$

$$\varepsilon_{min} = \varepsilon_{m0} - \Delta\varepsilon_{min} \tag{9-11}$$

When the temperature of the SMA wire is increased further, the presence of the test tube prevents the wire from contracting further. The result of this is that the force impinged on the test tube increases with increasing temperature. In this manner, the desired force F_{des} and therefore the desired stress $\sigma_{des} = F_{des}/A_{SMA}$ can be applied to clamp the test tube. This is shown by 3, where $\sigma_{SMA}(T) = \sigma_T$ is the total stress in the system given by (9-12) and (9-13).

$$\sigma_{SMA}(T) = K_s(\Delta\varepsilon_{s0} + \Delta\varepsilon_{min}) + \sigma_{des} \tag{9-12}$$

$$\sigma_T = \sigma_{m0} + \sigma_{\Delta s} + \sigma_{des} \tag{9-13}$$

Note that the maximum force (stress), σ_{des}^{max} that can be impinged onto the test tube is constrained by the maximum stress that can be applied when the wire is fully austenite as shown in Fig. 9-5 at 5 and in (9-14). This (correctly) implies that when the test tube has a large diameter, $\Delta\varepsilon_{min}$ is low, therefore σ_{min} is low and the SMA can impinge more force on the test tube as when the diameter is small, where the contrary is the case.

$$\sigma_{des}^{max} = \sigma_{SMA}(T > A_f) - \sigma_{min} \tag{9-14}$$

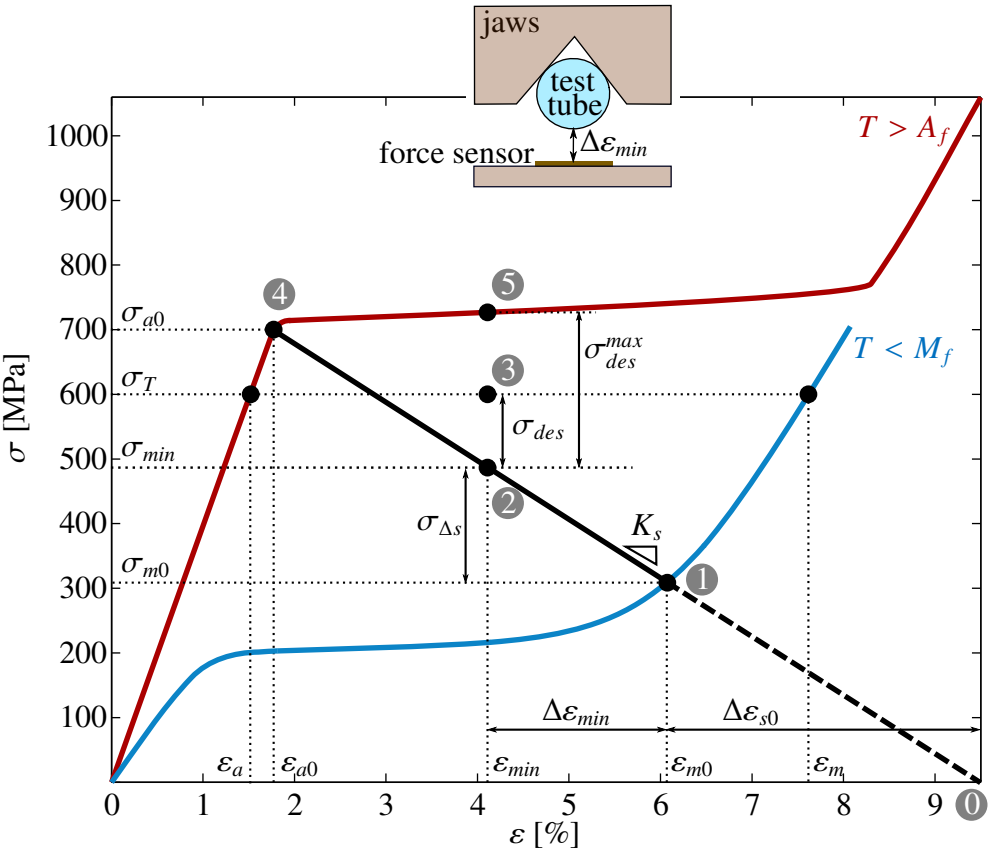

Figure 9-5: *Stress-strain diagram for SMA-based clamping vice*

9.4 Controller Architecture

The controller architecture used for the clamping vice is shown in Fig. 9-6. It is identical in structure to the control architecture for position control from Chap. 8 in that the controllers are separated into large and small signal controllers. However, while the large signal controller, as before, is responsible for coarse positioning, the small signal controller is responsible for force control.

Recall that at the initial state, the temperature of the SMA wire is low and the test tube is $\Delta\varepsilon_{min}$ away from touching the force sensor. Force measurement is therefore non-existent at the beginning of the clamping process. Based on the mechanics of the system and the desired clamping force, the large signal controller calculates a desired temperature T_{cal} in order to drive the system to the desired state $(\varepsilon_{min}, \sigma_T)$ at ③ in Fig. 9-5. In doing so, the test tube is eventually brought into contact with the force sensor at ② and meaningful force measurements can be collected between ② and ③. When either the force error e_F is within a threshold δ_F or the temperature error e_T is within a threshold δ_T, the controller switches from the large signal temperature/position controller to the small signal force controller.

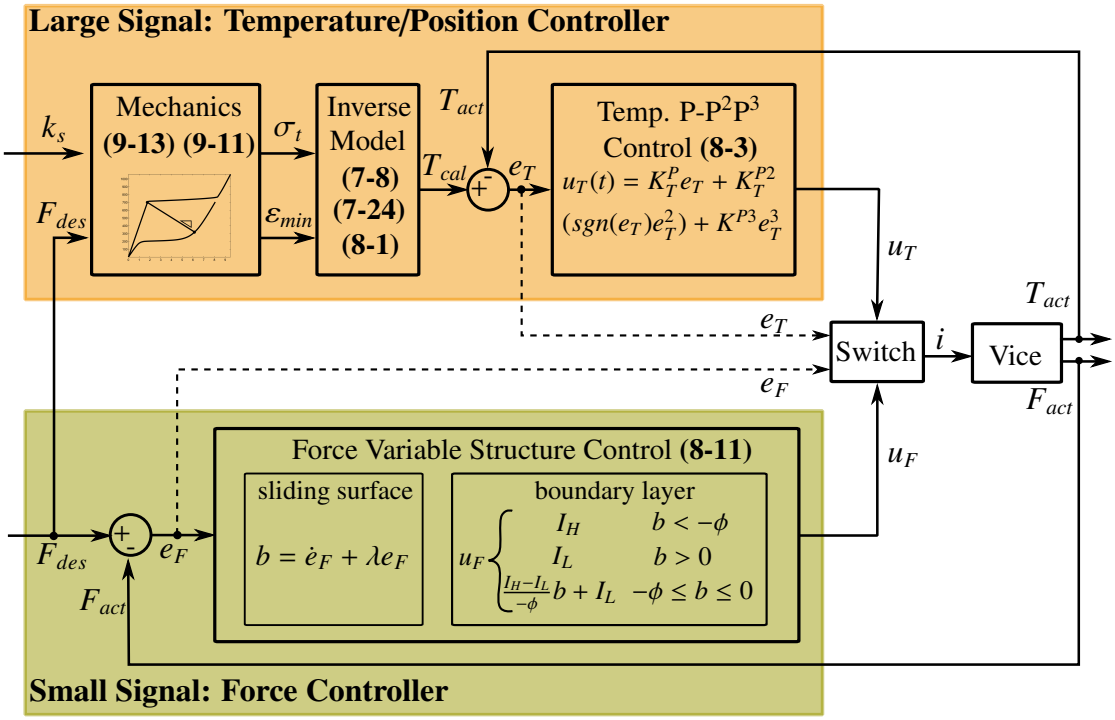

Figure 9-6: *SMA-based clamping vice control architecture*

T_{cal}, the temperature required to reach the desired state $(\varepsilon_{min}, \sigma_T)$, as computed from the mechanics in Sect. 9.3, is calculated using the inverse model in Chap. 7. The value of the required martensite fraction ξ_{des} is found by normalising ε_{min} using the maximum and minimum strains at σ_T as the normalisation constants. These strains are ε_m and ε_a as shown in Fig. 9-5. They are calculated by the constitutive inverse model (7-8) with $\sigma = \sigma_T$ and ξ_{des} is calculated with (8-1) for $\varepsilon_{des} = \varepsilon_{min}$. The desired temperature T_{cal} is then calculated using the phase kinetics inverse model in (7-24) (cf. Fig. 8-3).

Note that the phase kinetics model can be used for both the temperature/position controlled portion from ❶ to ❷ as well as the force controlled portion from ❷ to ❸ seamlessly without *a priori* knowledge of the actuator travel. This is due to the fact that ε_m and ε_a change dynamically with the load (c.f. Fig. 6-6).

Given the desired temperature, the large signal controller is identical to that in Chap. 8 i.e. a P-P^{2}P^3 temperature controller with the actual temperature T_{act} measured with the thermocouple.

The small signal controller is the same variable structure controller as in (8-11) i.e. with an asymmetric boundary layer and adaptive current based on the wire stress. Instead of the desired strain, however, the desired force is the input to the controller and the feedback signal is the force measured by the force sensor.

As both the large and small signal controllers, including the models involved, are computationally efficient, the controller is successfully implemented on the microcontroller, which is able to perform all required calculations with a sampling rate of 3 ms.

9.5 SMA-based Clamping Vice Performance

Using the control parameters in Tab. 9-1, the controller results are presented in this section for a series of steps (Sect. 9.5.1), various sinusoids (Sect. 9.5.2) and showing disturbance rejection (Sect. 9.5.3).

Table 9-1: *Control Parameters for EVSC position force controller*

K_T^P	K_T^{P2}	K_T^{P3}	ϕ	λ	I_L	I_H^{min}	I_H^{max}	δ_T	δ_F
10	10	10	0.2N	100	0.1A	1.5 A	3 A	2^oC	0.3N

9.5.1 Step response

The desired force set from the android tablet is a series of steps of different height, as shown by the orange dashed line in Fig. 9-7 that call for either heating or cooling of the wire. The response of the clamping vice is shown with the green solid line and shows good tracking, even with a low cost force sensor. Note that the delay at the first step occurs because the force sensor first shows measurements when the SMA wire has contracted by a strain of $\Delta\varepsilon_{min}\%$. The large signal controller is valid at this time until the force threshold $\delta_F = 0.2N$ is reached, after which the small signal controller is selected. This switch between the controllers occurs at every step, except where the step height is less than δ_F. This occurs at approximately $t = 22$s. The average rising time t_r^{avg}, average settling time t_s^{avg}, average steady state error $|e_{ss}^{avg}|$ and steady state RMSE e_{ss}^{RMS} is in Tab. 9-2.

Table 9-2: *Step response for SMA-based clamping vice*

Step: H or C	t_r^{avg}	t_s^{avg}	e_{ss}^{RMS}	e_{ss}^{avg}
Step 1: H	4.0s	4.0s	0.045N	0.031N
Step 2: C	3.8s	4.6s	0.069N	0.056N
Step 3: H	0.2s	0.4s	0.059N	0.049N
Step 4: H	0.2s	0.8s	0.051N	0.039N
Step 5: C	1.45s	1.5s	0.048N	0.041N
Step 6: H	0.2s	1.0s	0.042N	0.030N

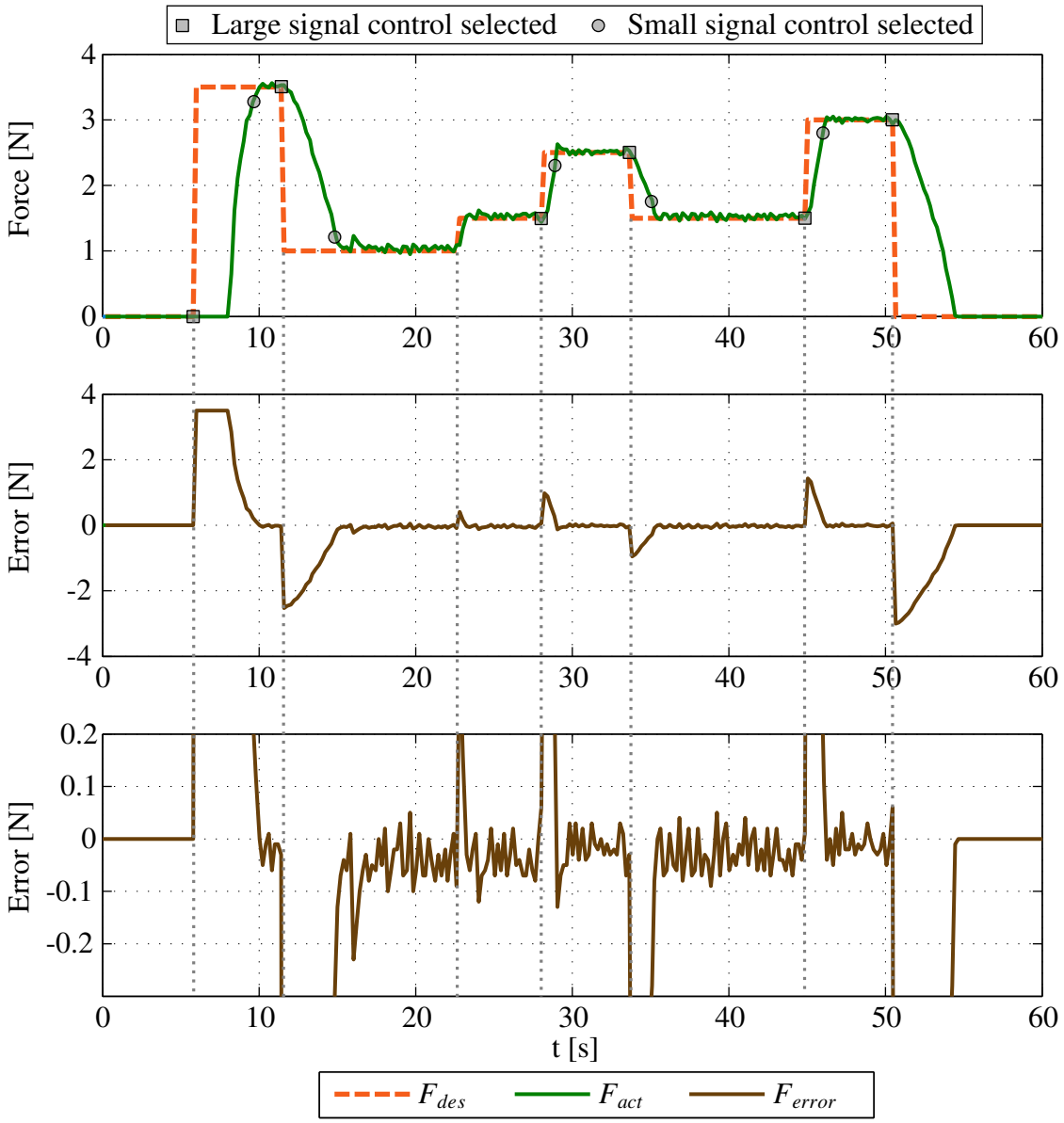

Figure 9-7: *SMA-based clamping vice response to various steps*

9.5.2 Sinusoidal response

Force tracking for the clamping vice is then investigated with a sinusoidal desired force with a peak-to-peak force of about 3N (0.75N to 3.75N) and a frequency of 1/60 Hz. The response, shown in Fig. 9-8 shows reasonable tracking with an RMSE of 0.09N (NRMSE 2.5%). Note that, similar to the step response, there is a delay at the start of the experiment until the force sensor reads measurements. The large signal controller is selected only in this initial phase until e_F falls below $\delta_F = 0.2N$. After this, the small signal controller is selected for the rest of the experiment, as the error remains within δ_F. The maximum error after the small signal controller is selected is 0.25N.
In order to investigate the bandwidth of the clamping vice, a sinusoidal desired strain with the same amplitude as before but with 4 different frequencies: 1/30, 1/20, 1/12 and 1/6 Hz is used. The results are shown in Fig. 9-9.

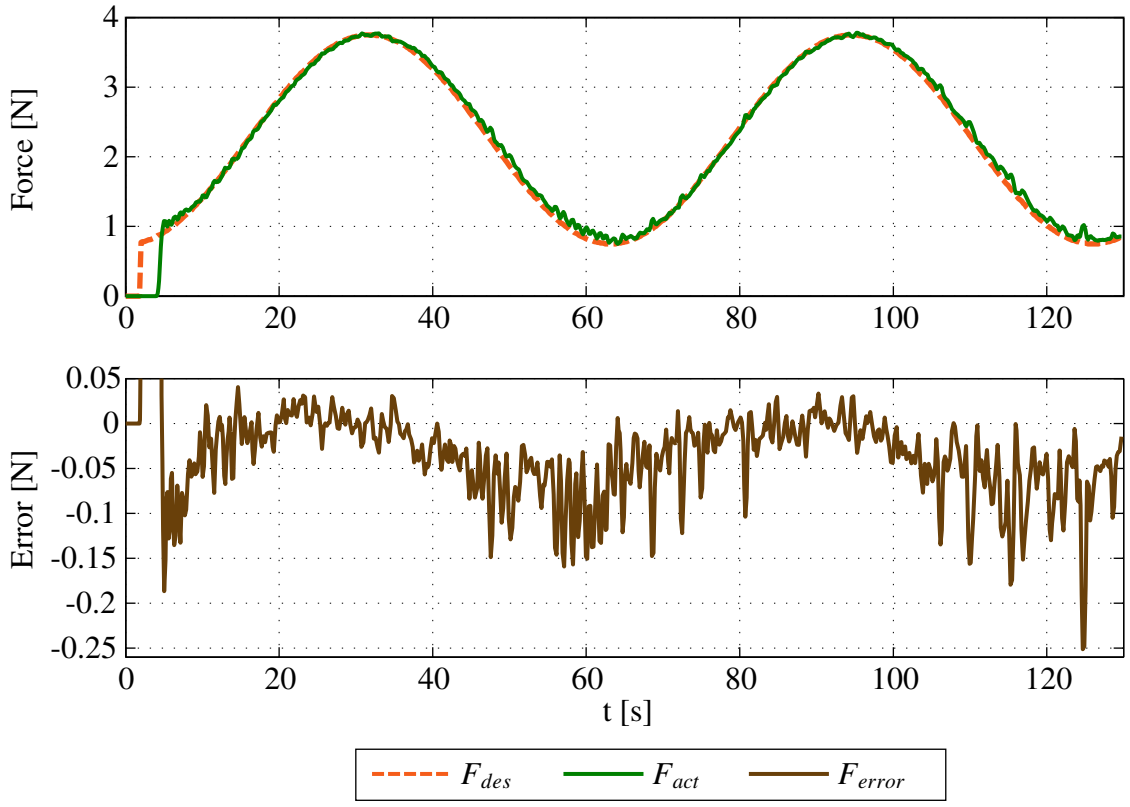

Figure 9-8: *SMA-based clamping vice response to sinusoid*

Frequencies 1/30 and 1/20 Hz show reasonable tracking with RMSE of 0.12N and 0.15N (NRMSE 3.2% and 3.9%). However, with 1/12 Hz, the cooling phases (decreasing force) start to show tracking errors (RMSE 0.27N, NRMSE 8.6%). A frequency of 1/6 Hz is too fast for the SMA to track, again, due to the slow cooling response. This shows that SMA-based clamping vice cannot be used in applications where large frequencies are required e.g. when the clamps are additionally used as active vibration dampers, where frequencies are larger than 50 Hz are required.

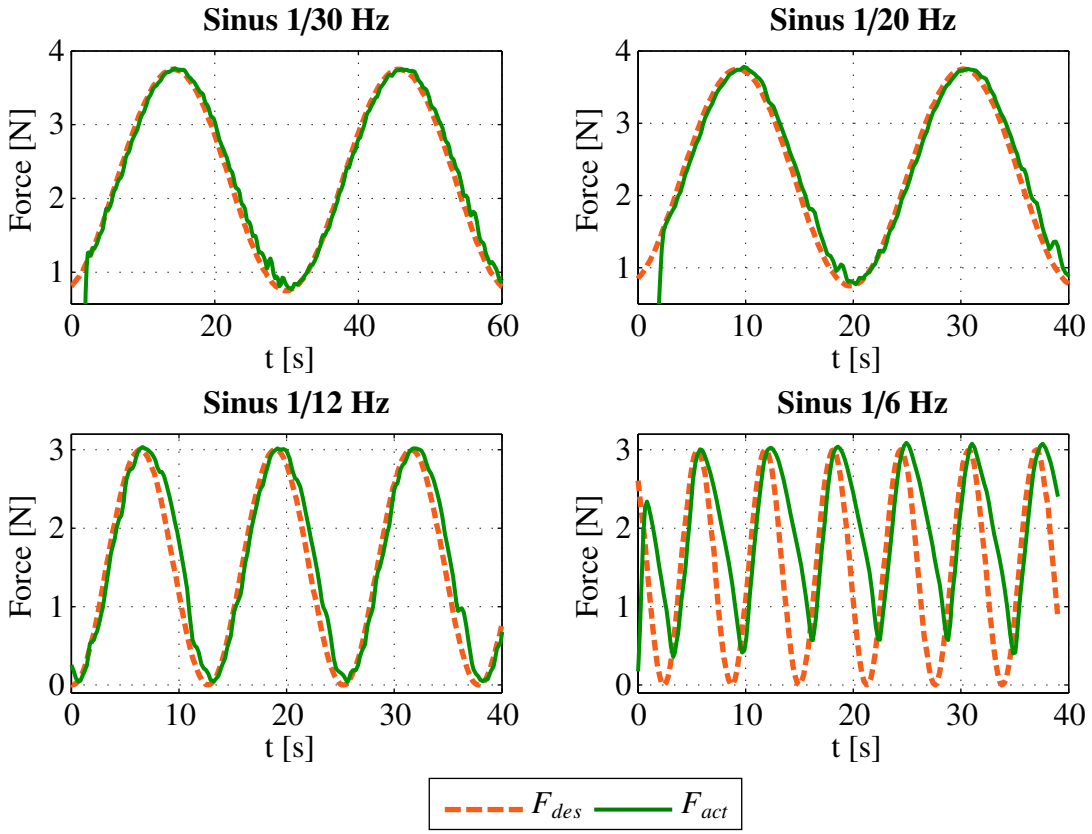

Figure 9-9: *SMA-based clamping vice response to sinusoid at various frequencies*

9.5.3 Disturbance rejection

In order to investigate disturbance rejection, a sinusoidal signal with a frequency of 1/30 Hz and peak-to-peak amplitude of 3N is used as the desired strain. During the experiment, both the front and back of the test tube are struck with a metal bar at random times and with random force. The results, shown for 2 experiments in Fig. 9-10, display good disturbance rejection. When the disturbance is small i.e. the force error is less than δ_F, the small signal controller is sufficient to reject the disturbance. However, for larger disturbances, the controller switches from small signal to large signal, which drives the actual force towards the desired force and the small signal controller then takes over when the force error is once again less than δ_F. This switch between the large and small signal controllers, also observed for disturbances during position control in Sect. 8.8, is successful in rejecting disturbances as high as 1.3N (43%). The worst performance is observed when the following conditions are met: Firstly, when disturbance occurs shortly before the maxima i.e. at the transition from heating to cooling. Secondly, when the test tube is hit away from the force sensor, causing a force decrease to be measured (plot (a)) as opposed to towards the force sensor (plot (b)). This occurs since a force decrease at the maxima causes the controller to cool, which is slow due to lack of an active cooling mechanism.

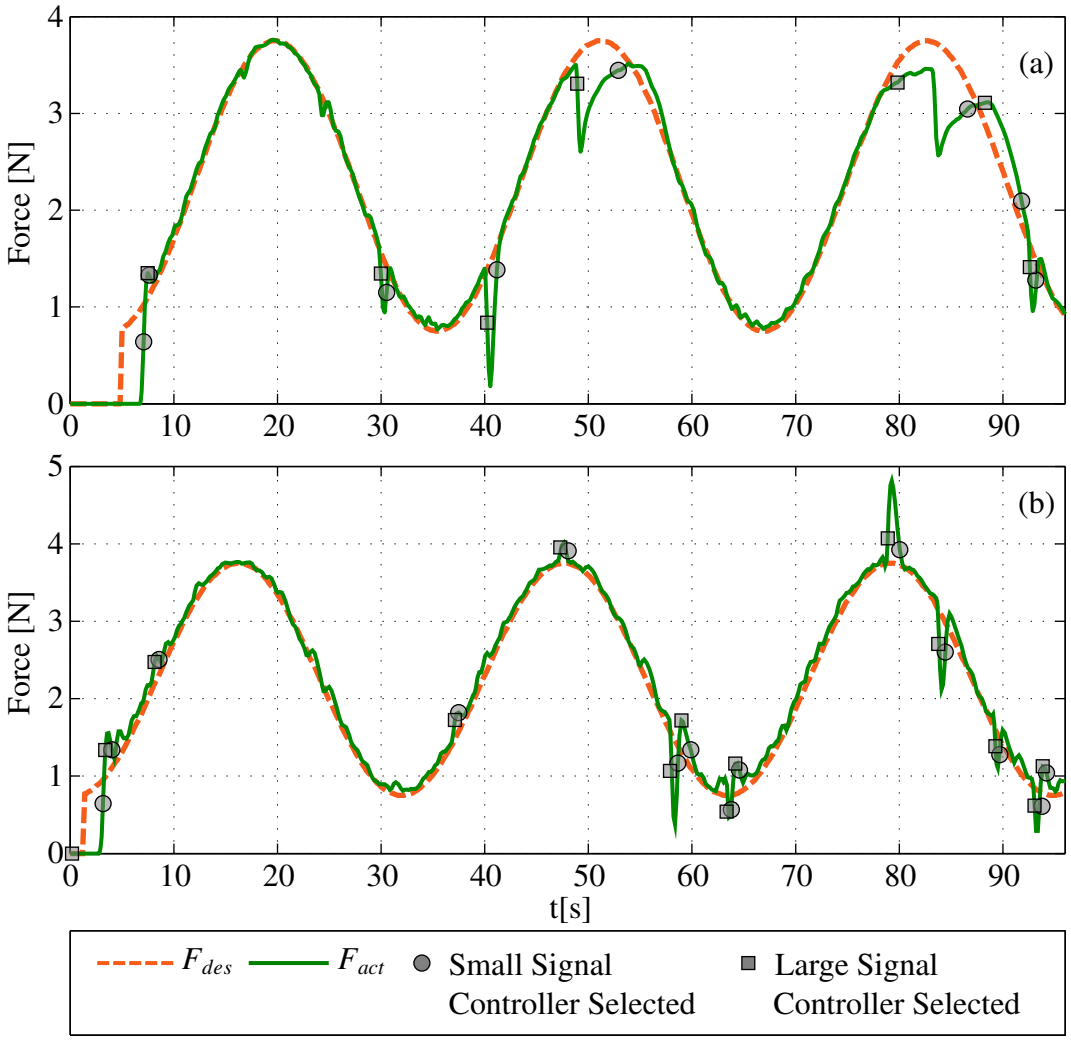

Figure 9-10: *SMA-based clamping vice response to disturbance*

9.6 Summary

This chapter presents an SMA-based clamping vice inspired by clamping applications in the industry. The vice consists of an SMA wire that moves a pair of jaws relative to one another in order to clamp an object. In order to allow for force controlled clamping, a force sensor is attached to one of the jaws. A thin-walled test tube is used as the specimen to be clamped.

The control unit is an ARM®-processor based microcontroller, on which the controller algorithms are implemented. The desired clamping force is set on an android-based tablet and sent to the mircocontroller via Bluetooth®. Sensor data is transmitted to the microcontroller via analog inputs. Based on the desired force and the sensor data, the controller computes the the current required to clamp the test tube and sends it to a current source though an analog output channel. The process data is collected, displayed and monitored by the android tablet.

The controller consists of a large signal temperature/position controller responsible for coarse positioning of the jaws such that the desired clamping force could be impinged on the test tube. The desired temperature is calculated online by considering the jaw

and test tube dimensions, the mechanics of the vice and the inverse constitutive and phase kinetics models (as previously for the position controller). A small signal force controller is used for finer force control. It consists of a variable structure controller with an asymmetrical boundary layer and adaptive current. It is valid when both jaws are touching the test tube and when the force is within a pre-defined threshold. The controller, including all models required, is simple and computationally efficient enough to run on the microcontroller with a sampling time of 3 ms. The control results using steps and sinusoids of various frequencies show reasonable tracking considering that low cost sensors are used. The maximum bandwidth considering a peak-to-peak force amplitude of 3N is 1/12 Hz. Disturbance rejection of the clamping vice is successfully achieved by the synergy between the large and small signal controllers, showing that the proposed controller is both robust and precise.

In comparison to force controlled clamping vices in the industry, the SMA-based vice requires much lower installation space and lower complexity. In fact, the SMA-based clamp requires minimal increase of the installation space of a manual vice, while simultaneously increasing the functionality and intelligence of the manual vice.

10 Conclusions and Future Work

The specific goals of this thesis, as outlined in Sect. 1.2, were the

- development of **computationally efficient models** to accurately predict macroscopic SMA behaviour, relevant to their use as actuators.
- Use of these models to **design non-linear controllers**,
- that allow for **precise and robust control** of the SMA,
- while being **computationally efficient** enough to run on **embedded** processors,
- thereby **miniaturising** both the actuator and the controller and thus make them more **attractive** for **industrial applications**.

Computationally efficient models to predict macroscopic SMA behaviour are developed on basis of macroscopically observable phenomena relevant to the use of SMAs as actuators. Two sets of novel models are developed in this thesis: a constitutive (stress-strain) model at various temperatures and a phase kinetic (strain-temperature) model that predicts the phase changes in SMAs when exposed to dynamically changing temperatures and stresses. The models are based on analytical equations that are continuous and differentiable, with parameters that are few, physical and easy to identify. The parameter identification process has to be carried out only once for the same batch of wires using the data from simple experiments and/or the SMA data sheets. The model's simplicity guarantees computational efficiency without compromising accuracy in predicting observed behaviour, as was verified with various experiments, including wires different than those used to extract the model parameters.

In order to use the developed models to **design non-linear controllers**, it is necessary to invert the models so that they can be used online within a control loop. As both models are not analytically invertible, the inverse is calculated by analytical equations that approximate both the constitutive and phase kinetic forward models. The forward and inverse models were shown to have sufficient correlation with one another. As they are analytical, the inverse models are also computationally efficient and can be used online in a control loop.

Precise and robust control of the SMAs is achieved by using a controller architecture that consists of the combination of large and small signal controllers. The large signal controller, responsible for course positioning, is a P-P^2P^3 temperature controller that gets its desired temperature value online from the inverse constitutive and phase kinetics SMA model developed previously. The small signal controller, responsible for fine positioning, uses two different types of controllers: when the control signals are modulated with Pulse Width Modulation (PWM), the small signal strain controller is also a PD-P^2P^3 controller. When the control signals are directly sent to the wire, the small signal controller is a variable structure controller (VSC) that uses an asymmetrical boundary layer to prevent over-heating of the wire and whose control signals adapt to the dynamic load on the wire to avoid overshoots. Investigation of the controller performance shows robust and precise position tracking control for various constant loads with steps of various heights and for

sinusoids of various frequencies. The maximum bandwidth without active cooling is shown to be 0.15 Hz at 1% strain amplitude. The robustness of the controller is shown with precise sinusoidal tracking when the wire is exposed to dynamical loads and exceptional disturbance rejection with disturbances as high as 8 kg.

As the control law and models used are simple, easy to implement, they are **computationally efficient** enough to run on **embedded** processors. This was shown on a prototypical **industrial SMA-based clamping vice** to clamp a thin-walled test tube. The vice consists of an SMA wire that moves a pair of jaws relative to one another in order to clamp an object. In order to allow for force controlled clamping, a low cost force sensor is attached to one of the jaws. In staying with the trends of Industry 4.0 and Cyber-Physical-Systems, the desired force is set with an android-based tablet, which also collects, monitors and displays the process data. The control unit is an ARM®-processor based microcontroller.

The controller consists of the same large signal temperature/position controller used previously and is responsible for coarse positioning of the jaws such that the desired clamping force could be impinged on the test tube. A small signal force controller, that is valid when both jaws are touching the test tube and when the force is within a pre-defined threshold is used for finer force control. It consists of the same variable structure controller with an asymmetrical boundary layer and adaptive current used previously.

Note that the same control architecture consisting of large and small signal controllers is used for both **precise and robust position and force control** of SMA actuators. The controller, including all models required, are simple and computationally efficient enough to run on the microcontroller with a **sampling time of 3 ms**. The controller performance, investigated using desired force steps and sinusoids of various frequencies, show reasonable tracking considering that low cost sensors are used. The maximum bandwidth considering a peak-to-peak force amplitude of 3N is 1/12 Hz. The robustness of the clamping vice against disturbances is also shown to be good.

In the prototypical industrial SMA-based clamping vice, force controlled clamping is demonstrated with very little additional volume or mass when compared with a passive clamp. In comparison to a force controlled clamp, the SMA-based vice is much smaller, less complex and more economical. The successful implementation and validation of an SMA-actuator in an industrial application with embedded processors shows that both the actuator and the controller can be **miniaturised**, making them more **attractive** for **industrial applications**.

While the control algorithms and prototypical application use only one SMA wire, multi-dimensional applications e.g. in a multi-link robot, for pitch and yaw movements of an automobile headlamp, in pick-and-place grippers etc. can also be realised by using multiple controllers. In order to achieve this, future work dealing with the design of multi-variable and multi-dimensional control algorithms is necessary.

The fast-growing research area of soft robotics can also benefit from SMA actuators to change the stiffness of soft, malleable materials like silicone or other polymers by embedding SMA wire(s) into the host material. In this manner, shape control of the host material can be achieved, which can be used in a variety of applications e.g. movement of soft robotic fingers, locomotion in soft worms, shape changing lenses etc.

Although this thesis sets the basis for an SMA actuator for use in the industry, further development is necessary to make an off-the-shelf, commercially viable product, including market research about potential applications.

To this end future work should include the development of observers (virtual sensors) to either replace existing sensors and thereby save space and reduce costs and/or to monitor states that are not measured. Further, investigation of the actuator's limitation regarding fatigue (life cycle), maximum load, maximum stroke, maximum temperature (current) etc. is necessary.

In order to optimise SMA actuator behaviour for industrial applications, it is necessary to work directly with material scientists and engineers for improvement of stability, reproducibility and reliability of the SMA. For example, better fatigue characteristics to increase actuator life, larger recoverable strain to increase actuator stroke, smaller hysteresis width to increase system bandwidth etc. can be improved in SMAs. This synergy is also useful in order to investigate the use of other materials such as high temperature SMAs (HT-SMAs) in application.

Through Industry 4.0 and CPS, current trends in the industry are digitalisation, networking between machines, sensors, actuators etc. This means that the SMA-actuator, when in an industrial context, cannot be stand-alone but has to be an active component with interfaces implemented that will allow bi-directional communication with other components and systems.

With such interfaces implemented, the SMA actuator could receive commands and send process data to a cloud based system, which opens up a plethora of future developments. Such developments include the use of process data collected to refine the existing models or to develop new models. Machine learning techniques can also be utilized for condition monitoring systems that analyse process data for quality assurance, predictive maintenance etc. For example, as the SMA actuator fatigues over time and usage, the models present in the controllers can be updated with new parameters from a learning algorithm in the cloud.

Shape memory alloys are promising materials in their use as actuators. The past couple of years have seen a growth in the number of SMA-based devices in industrial applications and in consumer products. Although, most current industrial applications use the SMA as a switch, this thesis presents the foundation, including an industrial prototype, to assist in the transition to position and force controlled applications, thereby fully exploiting the capabilities of this fascinating material.

Bibliography

[ABF00] Amalraj, J. J. ; Bhattacharyya, A. ; Faulkner, M. G.: Finite-Element Modeling Of Phase Transformation In Shape Memory Alloy Wires With Variable Material Properties. In: *Smart materials and structures* 9 (2000), Nr. 5, S. 622

[ABSU14] Auricchio, F. ; Bonetti, E. ; Scalet, G. ; Ubertini, F.: Theoretical And Numerical Modeling Of Shape Memory Alloys Accounting For Multiple Phase Transformations And Martensite Reorientation. In: *International Journal of Plasticity* 59 (2014), S. 30–54

[Ach89] Achenbach, M.: A Model for an Alloy with Shape Memory. In: *International Journal of Plasticity* 5 (1989), Nr. 4, S. 371–395

[ACR98] Airoldi, G. ; Corsi, A. ; Riva, G.: Step-Wise Martensite To Austenite Reversible Transformation Stimulated By Temperature Or Stress: A comparison in NiTi alloys. In: *Materials Science and Engineering: A* 241 (1998), Nr. 1-2, S. 233–240

[AD14] Ayvali, E. ; Desai, J. P.: Pulse width modulation-based temperature Pulse Width Modulation-Based Temperature Tracking For Feedback Control Of A Shape Memory Alloy Actuator. In: *Journal of Intelligent Material Systems and Structures* 25 (2014), Nr. 6, S. 720–730

[Ada16] Adafruit Learning System: *Force Sensitive Resistor (FSR)*. `https://learn.adafruit.com/force-sensitive-resistor-fsr/overview`. Version: 27/09/2016

[AEGA06] Asua, E. ; Etxebarria, V. ; García-Arribas, A.: Micropositioning Control using Shape Memory Alloys. In: *Proceedings of the 2006 IEEE International Conference on Control Applications* (2006), S. 3229–3234

[AEGA08] Asua, E. ; Etxebarria, V. ; García-Arribas, A.: Neural Network-Based Micropositioning Control Of Smart Shape Memory Alloy Actuators. In: *Engineering Applications of Artificial Intelligence* 21 (2008), Nr. 5, S. 796–804

[AK06] Ahn, K. K. ; Kha, N. B.: Improvement Of The Performance Of Hysteresis Compensation In SMA Actuators By Using Inverse Preisach Model In Closed - Loop Control System. In: *Journal of Mechanical Science and Technology* 20 (2006), Nr. 5, S. 634–642

[AO16] Alaneme, K. ; Okotete, E. A.: Reconciling viability and cost-effective shape memory alloy options – A review of copper and iron based shape memory metallic systems. In: *Engineering Science and Technology, an International Journal* 19 (2016), Nr. 3, S. 1582–1592

[Ash06] Ashrafiuon, H.: Position Control of a Three-link Shape Memory Alloy Actuated Robot. In: *Journal of Intelligent Material Systems and Structures* 17 (2006), Nr. 5, S. 381–392

[Bau16] Baumer Elektric AG: *OADM 12U7460/S35A*. http://www.baumer.com. Version: 13/10/2016

[BH96] Brinson, C. L. ; Huang, M. S.: Simplifications and Comparisons of Shape Memory Alloy Constitutive Models. In: *Journal of Intelligent Material Systems and Structures* 7 (1996), Nr. 1, S. 108–114

[BL93] Brinson, C. L. ; Lammering, R.: Finite element analysis of the behavior of shape memory alloys and their applications. In: *International Journal of Solids and Structures* 30 (1993), Nr. 23, S. 3261–3280

[BL96] Boyd, J. G. ; Lagoudas, D. C.: A Thermodynamical Constitutive Model For Shape Memory Materials. Part I. The Monolithic Shape Memory Alloy. In: *International Journal of Plasticity* 12 (1996), Nr. 6, S. 805–842

[Bri93] Brinson, C. L.: One-Dimensional Constitutive Behavior of Shape Memory Alloys: Thermomechanical Derivation with Non-Constant Material Functions and Redefined Martensite Internal Variable. In: *Journal of Intelligent Material Systems and Structures* 4 (1993), Nr. 2, S. 229–242

[Bro16] Broy, M.: *Cyber-Physical Systems*. Berlin, Heidelberg : Springer Berlin Heidelberg, 02.11.2016 http://www.acatech.de/fileadmin/user_upload/Baumstruktur_nach_Website/Acatech/root/de/Publikationen/acatech_diskutiert/acatech_diskutiert_CPS_einseitig_oI.pdf

[BS96] Brokate, M. ; Sprekels, J.: *Applied Mathematical Sciences*. Bd. 121: *Hysteresis and Phase Transitions*. Springer, 1996

[CHKC01] Choi, S. ; Han, Y. M. ; Kim, J. H. ; Cheong, C. C.: Force tracking control of a flexible gripper featuring shape memory alloy actuators. In: *Mechatronics* 11 (2001), Nr. 6, S. 677–690

[CSI09] Churchill, C. B. ; Shaw, J. A. ; Iadicola, M. A.: Tips And Tricks For Characterizing Shape Memory Alloy Wire: Part 2-Fundamental Isothermal Responses. In: *Experimental Techniques* 33 (2009), Nr. 1, S. 51–62

[CWL+14] Cladera, A. ; Weber, B. ; Leinenbach, C. ; Czaderski, C. ; Shahverdi, M. ; Motavalli, M.: Iron-based shape memory alloys for civil engineering structures: An overview. In: *Construction and Building Materials* 63 (2014), S. 281–293

[Da 07] Da Silva, E.: Beam shape feedback control by means of a shape memory actuator. In: *Materials & Design* 28 (2007), Nr. 5, S. 1592–1596

[DG05] Dutta, S. M. ; Ghorbel, F. H.: Differential Hysteresis Modeling of a Shape Memory Alloy Wire Actuator. In: *IEEE/ASME Transactions on Mechatronics* 10 (2005), Nr. 2, S. 189–197

[DMS90] Duerig, T. W. ; Melton, K. N. ; Stöckel, D.: *Engineering Aspects of Shape Memory Alloys*. Elsevier Science, 1990

[Duh00] Duhem, P.M.M.: *Die dauernden Änderung und die Thermodynamik*. W. Engelmann, 1900

[EA02] Elahinia, M. H. ; Ashrafiuon, H.: Nonlinear Control of a Shape Memory Alloy Actuated Manipulator. In: *Journal of Vibration and Acoustics* 124 (2002), Nr. 4, S. 566–575

[EA05a] Elahinia, M. H. ; Ahmadian, M.: An enhanced SMA phenomenological model: I. The shortcomings of the existing models. In: *Smart Materials and Structures* 14 (2005), Nr. 6, S. 1297–1308

[EA05b] Elahinia, M. H. ; Ahmadian, M.: An enhanced SMA phenomenological model: II. The experimental study. In: *Smart Materials and Structures* 14 (2005), Nr. 6, S. 1309–1319

[EAAT05] Elahinia, M. H. ; Ashrafiuon, H. ; Ahmadian, M. ; Tan, H.: A Temperature-based Controller for a Shape Memory Alloy Actuator. In: *Journal of Vibration and Acoustics* 127 (2005), Nr. 3, S. 285–291

[EE08] Esfahani, E. T. ; Elahinia, M. H.: Developing an Adaptive Controller for a Shape Memory Alloy Walking Assistive Device. In: *Journal of Vibration and Control* (2008)

[ES 16] ES Electronic Sensor GmbH: *Drahtthermoelemente, isoliert*. `http://www.electronic-sensor.de/de/`. Version: 31/10/2016

[FCS12] Furst, S. ; Crews, J. H. ; Seelecke, S.: Numerical and experimental analysis of inhomogeneities in SMA wires induced by thermal boundary conditions. In: *Continuum Mechanics and Thermodynamics* 24 (2012), Nr. 4-6, S. 485–504

[FGD+10] Frenzel, J. ; George, E. P. ; Dlouhy, A. ; Somsen, Ch. ; Wagner, M.F.-X. ; Eggeler, G.: Influence of Ni on martensitic phase transformations in NiTi shape memory alloys. In: *Acta Materialia* 58 (2010), Nr. 9, S. 3444–3458

[FKL+13] Föllinger, O. ; Konigorski, U. ; Lohmann, B. ; Roppenecker, G. ; Trächtler, A.: *Regelungstechnik: Einführung in die Methoden und ihre Anwendung*. 11. VDE-Verlag, 2013

[Flu16] Fluke: *Fluke 52 II Dual Input Digital Thermometer*. `http://en-us.fluke.com/products/thermometers/fluke-52-ii-thermometer.html`. Version: 31/10/2016

[FS12] Furst, S. ; Seelecke, S.: Modeling and experimental characterization of the stress, strain, and resistance of shape memory alloy actuator wires with controlled power input. In: *Journal of Intelligent Material Systems and Structures* 23 (2012), Nr. 11, S. 1233–1247

[GH97] Grant, D. ; Hayward, V.: Variable structure control of shape memory alloy actuators. In: *IEEE Control Systems Magazine* 17 (1997), Nr. 3, S. 80–88

[GH00] Grant, D. ; Hayward, V.: Constrained force control of shape memory alloy actuators. In: *International Conference on Robotics and Automation* 2 (2000), S. 1314–1320 vol.2

[GHB00] Gao, X. ; Huang, M. ; Brinson, C. L.: A multivariant micromechanical model for SMAs Part 1. Crystallographic issues for single crystal model. In: *International Journal of Plasticity* 16 (2000), Nr. 10-11, S. 1345–1369

[GL97] Goo, B. ; Lexcellent, C.: Micromechanics-based modeling of 2–way memory effect of a single crystal SMA. In: *Acta Materialia* 45 (1997)

[GSA+01] Gall, K. ; Sehitoglu, H. ; Anderson, R. ; Karaman, I. ; Chumlyakov, Y. ; Kireeva, I.: On the mechanical behavior of single crystal NiTi shape memory

alloys and related polycrystalline phenomenon. In: *Materials Science and Engineering: A* 317 (2001), Nr. 1-2, S. 85–92

[GSW10] Grossmann, C. ; Schaefer, A. ; Wagner, M. F.-X.: A finite element study on localized deformation and functional fatigue in pseudoelastic NiTi strips. In: *Materials Science and Engineering: A* 527 (2010), Nr. 4-5, S. 1172–1178

[Hei04] Heintze, Olaf a.: A computationally efficient free energy model for shape memory alloys-experiments and theory. (2004)

[HFA97] Huber, J. E. ; Fleck, N. A. ; Ashby N. A.: The Selection of Mechanical Actuators Based on Performance Indices. In: *Proceedings: Mathematical, Physical and Engineering Sciences* 453 (1997), Nr. 1965, S. 2185–2205

[HGB00] Huang, M. ; Gao, X. ; Brinson, C. L.: A multivariant micromechanical model for SMAs Part 2. Polycrystal model. In: *International Journal of Plasticity* 16 (2000), Nr. 10-11, S. 1371–1390

[Hor91] Hornbogen, E.: *Advanced Structural and Functional Materials: Shape Memory Alloys*. Springer Berlin Heidelberg, 1991

[Hot16] Hottinger Baldwin Messtechnik GmbH: *Hochpräziser S-Type Kraftsensor 3364 s2m*. `https://www.hbm.com/de/`. Version: 13/10/2016

[Hum01] Humbeeck van, J.: Shape Memory Alloys: A Material and a Technology. In: *Advanced Engineering Materials* 3 (2001), Nr. 11, S. 837–850

[IE16] Industrie-Elektronik, ATR: *Schaltanlagen, Schaltanlagenbau und Steuerungsanlagen.* `http://www.atrie.de/de/`. Version: 13/10/2016

[iFi16] iFixit: *Microsoft Surface Book Teardown*. `https://de.ifixit.com/Teardown/Microsoft+Surface+Book+Teardown/51972`. Version: 27/09/2016

[Int16] Interlink Electronics: *FSR 400*. `http://www.interlinkelectronics.com/FSR402.php`. Version: 27/09/2016

[IP94] Ivshin, Y. ; Pence, T. J.: A Thermomechanical Model for a One Variant Shape Memory Material. In: *Journal of Intelligent Material Systems and Structures* 5 (1994), Nr. 4, S. 455–473

[ITH91] Ikuta, K. ; Tsukamoto, M. ; Hirose, S.: Mathematical Model and Experimental Verification of Shape Memory Alloy for Designing Micro Actuator. In: *Micro Electro Mechanical Systems, 1991, MEMS '91, Proceedings. An Investigation of Micro Structures, Sensors, Actuators, Machines and Robots. IEEE* (1991), S. 103–108

[Jen98] Jendritza, D. J.: *Technischer Einsatz neuer Aktoren: Grundlagen, Werkstoffe, Designregeln und Anwendungsbeispiele*. Bd. Bd. 484 : Elektronik. 2., verb. Aufl. Renningen-Malmsheim : Expert-Verl., 1998

[JPNO08] Jayender, J. ; Patel, R. V. ; Nikumb, S. ; Ostojic, M.: Modeling and Control of Shape Memory Alloy Actuators. In: *IEEE Transactions on Control Systems Technology* 16 (2008), Nr. 2, S. 279–287

[Kan11] Kannan, S.: *Modeling and control of Shape Memory Alloy Actuator*. Paris, École Nationale Supérieure d'Arts et Métiers, Doctors Thesis, December 2011

[KLH06] Kumagai, A. ; Liu, T.-I. ; Hozian, P.: Control of Shape Memory Alloy Actuators with a Neuro-fuzzy Feedforward Model Element. In: *Journal of Intelligent Manufacturing* 17 (2006), Nr. 1, S. 45–56

[KNK+12] Krooss, P. ; Niendorf, T. ; Karaman, I. ; Chumlyakov, Y. ; Maier, H. J.: Cyclic Deformation Behavior Of Aged FeNiCoAlTa Single Crystals. In: *Functional Materials Letters* 05 (2012), Nr. 04, S. 1250045

[KV11] Kirkpatrick, Kj ; Valasek, J.: Active Length Control of Shape Memory Alloy Wires Using Reinforcement Learning. In: *Journal of Intelligent Material Systems and Structures* (2011)

[Lag08] Lagoudas, D. C.: *Shape Memory Alloys: Modeling and Engineering Applications*. Springer-Verlag US, 2008

[LAU16] LAUDA Dr. R. Wobser GmbH & Co. KG: *LAUDA Proline Edition X RP 845 C*. http://www.lauda.de/shop/en/rp-845-c-7984/. Version: 31/10/2016

[LBK15] Lee, J. ; Bagheri, B. ; Kao, H.-A.: A Cyber-Physical Systems architecture for Industry 4.0-based manufacturing systems. In: *Manufacturing Letters* 3 (2015), S. 18–23

[LHY09] Liu, S.-H. ; Huang, T.-S. ; Yen, J.-Y.: Tracking Control of Shape-Memory-Alloy Actuators Based on Self-Sensing Feedback and Inverse Hysteresis Compensation. In: *Sensors* 10 (2009), Nr. 1, S. 112–127

[Mea16] Measurement Computing Corporation: *PCI Data Acquisition Card PCI-DAS6014*. http://www.mccdaq.com/pci-data-acquisition/. Version: 13/10/2016

[Mic16] Microsoft: *Microsoft Surface-Laptops*. https://www.microsoft.com/surface/de-de/devices/surface-book. Version: 27/09/2016

[Mik16] MikroElektonika: *mikromedia 7 for STM32F4*. http://www.mikroe.com/mikromedia/7/stm32f4/. Version: 27/09/2016

[MKB+16] Monostori, L. ; Kádár, B. ; Bauernhansl, T. ; Kondoh, S. ; Kumara, S. ; Reinhart, G. ; Sauer, O. ; Schuh, G. ; Sihn, W. ; Ueda, K.: Cyber-physical systems in manufacturing. In: *CIRP Annals - Manufacturing Technology* 65 (2016), Nr. 2, S. 621–641

[MKH01] Majima, S. ; Kodama, K. ; Hasegawa, T.: Modeling of Shape Memory Alloy Actuator and Tracking Control System with the Model. In: *IEEE Transactions Control Systems Technology* 9 (2001), Nr. 1, S. 54–59

[MS03] Ma, N. ; Song, G.: Control of shape memory alloy actuator using pulse width modulation. In: *Smart Materials and Structures* 12 (2003), Nr. 5, S. 712–719

[MSL04] Ma, N. ; Song, G. ; Lee, H-J: Position control of shape memory alloy actuators with internal electrical resistance feedback using neural networks. In: *Smart Materials and Structures* 13 (2004), Nr. 4, S. 777

[MT09] Moallem, M. ; Tabrizi, V. A.: Tracking Control of an Antagonistic Shape Memory Alloy Actuator Pair. In: *Control Systems Technology, IEEE Transactions on* 17 (2009), Nr. 1, S. 184–190

[MTS16] MTS Systems Corporation: *MTS 858 Table Top Systems*. http://www.mts.com/de/index.htm. Version: 30/10/2016

[MW98] Madill, D. R. ; Wang, D. W. L.: Modelling and L2-Stability of a Shape Memory Alloy Position Control System. In: *IEEE Trans. Control Systems Technology* 6 (1998), Nr. 4, S. 473–481

[MyT16] MyTinySun: *3A Buck Constant Current Power Supply with Controller*. http://jtl.mytinysun.com/. Version: 27/09/2016

[NRD12] Nakshatharan, S. S. ; Ruth, D. Josephine S. ; Dhanalakshmi, K.: Design based Active Vibration Control of a flexible structure using shape memory alloy wire actuators. (2012), S. 476–480

[OR05] Otsuka, K. ; Ren, X.: Physical metallurgy of Ti–Ni-based shape memory alloys. In: *Progress in Materials Science* 50 (2005), Nr. 5, S. 511–678

[Pai07] Pai, A.: *A phenomenological model of SMAs including time varying stress*. Masters thesis, University of Waterloo, 2007

[PB92] Pacejka, H. B. ; Bakker, E.: The Magic Formula Tyre Model. In: *Vehicle System Dynamics* 21 (1992), Nr. sup001, S. 1–18

[PG06] Pai, A. ; Gorbet, R. B.: Extenstion of Madill's SMA Model to Include Time-Varying Stress. In: *International Conference on Smart Materials and Structures, Toronto, Canada, 12 - 13 October 2006* (2006), S. 60–70

[PG07] Pai, A. ; Gorbet, R. B.: Memory alloy actuator. In: *Advanced intelligent mechatronics, 2007 IEEE/ASME international conference on* (2007)

[PNK+15] Pai, A. ; Niendorf, T. ; Krooss, P. ; Koke, I. ; Traechtler, A. ; Schaper, M.: Modelling The Constitutive Behaviour Of Martensite And Austenite In Shape Memory Alloys Using Closed-Form Analytical Continuous Equations. In: *7th ECCOMAS Thematic Conference on Smart Structures and Material SMART 2015* 2015 (2015)

[Pre35] Preisach, F.: Ueber die magnetische Nachwirkung. In: *Zeitschrift fuer Physik* 94 (1935), S. 277–302

[RKA08] Rahman, S. M. ; Kwan Ahn, K. ; Anh, P. H.: A comparative study of position control of a SMA actuated manipulator. In: *Communications and Electronics, 2008. ICCE 2008. Second International Conference on* (2008), S. 29–32

[RL97] Rogers, C. A. ; Liang, C.: One-dimensional thermomechanical constitutive relations for shape memory materials. In: *Journal of Intelligent Material Systems and Structures* 8 (1997), Nr. 4, S. 285–302

[RLS07] Ren, W. ; Li, H. ; Song, G.: Phenomenological modeling of the cyclic behavior of superelastic shape memory alloys. In: *Smart materials and structures* 16 (2007), Nr. 4, S. 1083

[RNTJ13] Riccardi, L. ; Naso, D. ; Turchiano, B. ; Janocha, H.: Adaptive Control of Positioning Systems With Hysteresis Based on Magnetic Shape Memory Alloys. In: *Control Systems Technology, IEEE Transactions on* 21 (2013), Nr. 6, S. 2011–2023

[RS 16] RS Components Ltd.: *RS Pro K Type Thermocouple*. http://uk.rs-online.com/web/p/thermocouples/3971589/. Version: 13/10/2016

[RT09] Romano, R. ; Tannuri, E. A.: Modeling, control and experimental validation of a novel actuator based on shape memory alloys. In: *Mechatronics* 19 (2009), Nr. 7, S. 1169–1177

[Rv94] Reynaerts, D. ; van Brussel, H.: Shape memory alloy based electrical actuation for robotic applications. In: *Proceedings of the First International Conference on Shape Memory and Superelastic Technologies* (1994), S. 271–276

[Saea] Saes Getters: *Shape Memory Alloys*. https://www.saesgetters.com/products-functions/products/shape-memory-alloys/shape-memory-alloys-nitinol-components/SaesSmartMaterials.pdf

[Saeb] Saes Getters: *SmartFlex Wire*. https://www.saesgetters.com/products-functions/products/shape-memory-alloys/shape-memory-alloys-nitinol-components/SmartFlexWire.pdf

[Sae16] Saes Group: Smartflex Broschure 2014. (28.10.2016). https://www.saesgetters.com/sites/default/files/Brochure%20SmartFlex.pdf

[SAS05] Shameli, E. ; Alasty, A. ; Salaarieh, H.: Stability analysis and nonlinear control of a miniature shape memory alloy actuator for precise applications. In: *Mechatronics* 15 (2005), Nr. 4, S. 471–486

[SCB03a] Song, G. ; Chaudhury, V. ; Batur, C.: A Neural Network Inverse Model for a Shape Memory Alloy Wire Actuator. In: *Journal of Intelligent Material Systems and Structures* 14 (2003), Nr. 6, S. 371–377

[SCB03b] Song, G. ; Chaudhury, V. ; Batur, C.: Precision tracking control of shape memory alloy actuators using neural networks and sliding-mode based robust controller. In: *Smart Materials and Structures* 12 (2003), S. 223–231

[Sch16] Schunk: *Superior Clamping and Gripping*. https://de.schunk.com/de_de/startseite/#/. Version: 27/09/2016

[SDUS12] Senthilkumar, P. ; Dayananda, G. N. ; Umapathy, M. ; Shankar, V.: Experimental evaluation of a shape memory alloy wire actuator with a modulated adaptive controller for position control. In: *Smart Materials and Structures* 21 (2012), Nr. 1, S. 15015

[See02] Seelecke, S.: Modeling the dynamic behavior of shape memory alloys. In: *International Journal of Non-Linear Mechanics* 37 (2002), Nr. 8, S. 1363–1374

[Sha95] Shaw, J.: Thermomechanical aspects of NiTi. In: *Journal of the Mechanics and Physics of Solids* 43 (1995), Nr. 8, S. 1243–1281

[Sha02] Shaw, J.: A thermomechanical model for a 1-D shape memory alloy wire with propagating instabilities. In: *International Journal of Solids and Structures* 39 (2002), Nr. 5, S. 1275–1305

[SHC+09] Sohn, J. W. ; Han, Y. M. ; Choi, Seung-Bok ; Lee, Y. S. ; Han, M. S.: Vibration and Position Tracking Control of a Flexible Beam Using SMA Wire Actuators. In: *Journal of Vibration and Control* 15 (2009), Nr. 2, S. 263–281

[SM04] Seelecke, S. ; Müller, I.: Shape memory alloy actuators in smart structures: Modeling and simulation. In: *Applied Mechanics Reviews* 57 (2004), Nr. 1, S. 23

[Smi05] Smith, R. C.: *Frontiers in applied mathematics*. Bd. 32: *Smart material systems: Model development*. Society for Industrial and Applied Mathematics, 2005

[SZ12] Sayyaadi, H. ; Zakerzadeh, M. R.: Position control of shape memory alloy actuator based on the generalized Prandtl–Ishlinskii inverse model. In: *Mechatronics* 22 (2012), Nr. 7, S. 945–957

[TA12] Tai, N. T. ; Ahn, K. K.: A hysteresis functional link artificial neural network for identification and model predictive control of SMA actuator. In: *Journal of Process Control* 22 (2012), Nr. 4, S. 766–777

[Tex16] Texas Instruments: *INA139 Current Sense Amplifiers Analog Output*. `http://www.ti.com/product/INA139`. Version: 27/09/2016

[TF08] Teh, Y. H. ; Featherstone, R.: An Architecture for Fast and Accurate Control of Shape Memory Alloy Actuators. In: *The International Journal of Robotics Research* 27 (2008), Nr. 5, S. 595–611

[TKS86] Tanaka, K. ; Kobayashi, S. ; Sato, Y.: Thermomechanics of transformation pseudoelasticity and shape memory effect in alloys. In: *International Journal of Plasticity* 2 (1986), Nr. 1, S. 59–72

[UC96] Upton, J. G. ; Cook, I.: *Understanding statistics*. Oxford : Oxford University Press, 1996

[VF13] Vermesan, O. ; Friess, P.: *Internet of things: Converging technologies for smart environments and integrated ecosystems*. Aalborg, Denmark : River Publishers, 2013

[VL98] Vivet, A. ; Lexcellent, C.: Micromechanical modelling for tension–compression pseudoelastic behavior of AuCd single crystals. In: *The European Physical Journal Applied Physics* 4 (1998), Nr. 2, S. 125–132

[Voj89] Vojta, G.: M. A. Krasnosel'skil, A. V. Pokrovskii. Systems with Hysteresis. Springer–Verlag 1989. In: *Crystal Research and Technology* 24 (1989), Nr. 8, S. K142–K142

[VP12] Velázquez, R. ; Pissaloux, E. E.: Modelling And Temperature Control Of Shape Memory Alloys With Fast Electrical Heating. In: *International Journal of Mechanics and Control* 13 (2012), Nr. 2

[Wei16] Weidmüller Interface GmbH & Co. KG: *MAS Thermo-K 0 Amplifier*. `http://catalog.weidmueller.com/`. Version: 13/10/2016

[WLK99] Webb, G. ; Lagoudas, D. ; Kurdila, A.: Adaptive Hysteresis Compensation for SMA Actuators with Stress-Induced Variations in Hysteresis. In: *Journal of Intelligent Material Systems and Structures* 10 (1999), Nr. 11, S. 845–854

[WSE10] Williams, E. A. ; Shaw, G. ; Elahinia, M. H.: Control of an automotive shape memory alloy mirror actuator. In: *Mechatronics* 20 (2010), Nr. 5, S. 527–534

[WSL+12] Wang, T.-M. ; Shi, Z.-Y. ; Liu, D. ; Ma, C. ; Zhang, Z.-H.: An Accurately Controlled Antagonistic Shape Memory Alloy Actuator with Self-Sensing. In: *Sensors* 12 (2012), Nr. 6, S. 7682–7700

[YRHL06] Yang, S.-M. ; Roh, J.-H. ; Han, J.-H. ; Lee, I.: Experimental Studies on Active Shape Control of Composite Structures using SMA Actuators. In: *Journal of Intelligent Material Systems and Structures* 17 (2006), Nr. 8-9, S. 767–777

[ZS13] Zakerzadeh, M. R. ; Sayyaadi, H.: Precise position control of shape memory alloy actuator using inverse hysteresis model and model reference adaptive control system. In: *Mechatronics* 23 (2013), Nr. 8, S. 1150–1162

Appendix

Table of Contents

A1 Detailed Derivations

A1.1 Calculation of s-shaped curve

The s-shaped curve forms the base of the stress-strain SMA model, as presented in Sect. 4.1. The derivation of (4-5) is shown below:

From (4-1):

$$\frac{\partial\sigma}{\partial\varepsilon} = \frac{(E_1 - E_2)}{1 + e^{k_1(\varepsilon-\varepsilon_1)}} + E_2 + \frac{(E_3 - E_2)}{1 + e^{-k_2(\varepsilon-\varepsilon_2)}}$$

$$\int \frac{\partial\sigma}{\partial\varepsilon}d\varepsilon = \int \frac{(E_1 - E_2)}{1 + e^{k_1(\varepsilon-\varepsilon_1)}}d\varepsilon + \int E_2 d\varepsilon + \int \frac{(E_3 - E_2)}{1 + e^{-k_2(\varepsilon-\varepsilon_2)}}d\varepsilon \tag{A1-1}$$

Consider the following integral

$$\int \frac{1}{1 + e^{a(x-b)}}dx = \int \frac{1 + e^{a(x-b)} - e^{a(x-b)}}{1 + e^{a(x-b)}}$$

$$= \int 1dx - \int \frac{e^{a(x-b)}}{1 + e^{a(x-b)}}dx$$

$$= x - \frac{1}{a}\ln(1 + e^{a(x-b)}) + C \tag{A1-2}$$

Using (A1-2) to solve the integrals in (A1-1) gives:

$$\sigma = (E_1 - E_2)\left[\varepsilon - \frac{1}{k_1}\ln\left(1 + e^{k_1(\varepsilon-\varepsilon_1)}\right)\right] + E_2\varepsilon +$$

$$(E_3 - E_2)\left[\varepsilon + \frac{1}{k_2}\ln\left(1 + e^{-k_2(\varepsilon-\varepsilon_2)}\right)\right] + C \tag{A1-3}$$

Considering that $(\varepsilon_p, \sigma_p)$ is any point on the curve, then C can be calculated by setting $\varepsilon = \varepsilon_p$ and $\sigma = \sigma_p$ in (A1-3) and solving for C to give (A1-4):

$$C = \sigma_p - (E_1 - E_2)\left[\varepsilon_p - \frac{1}{k_1}\ln\left(1 + e^{k_1(\varepsilon_p-\varepsilon_1)}\right)\right] -$$

$$E_2\varepsilon_p - (E_3 - E_2)\left[\varepsilon_p + \frac{1}{k_2}\ln\left(1 + e^{-k_2(\varepsilon_p-\varepsilon_2)}\right)\right] \tag{A1-4}$$

Substituting C from (A1-4) back into (A1-3) and rearranging gives σ as defined by (4-5):

$$\sigma = \overbrace{(E_1 - E_2)\left[\varepsilon - \varepsilon_p + \frac{1}{k_1}\ln\left(\frac{1 + e^{k_1(\varepsilon_p - \varepsilon_1)}}{1 + e^{k_1(\varepsilon - \varepsilon_1)}}\right)\right]}^{\sigma_1} + \overbrace{E_2(\varepsilon - \varepsilon_p) + \sigma_p}^{\sigma_2} + \underbrace{(E_3 - E_2)\left[\varepsilon - \varepsilon_p - \frac{1}{k_2}\ln\left(\frac{1 + e^{-k_2(\varepsilon_p - \varepsilon_2)}}{1 + e^{-k_2(\varepsilon - \varepsilon_2)}}\right)\right]}_{\sigma_3}$$

A1.2 Calculation of k_1 and k_2 during parameter identification

The parameter identification process in Section 4.3 includes the calculation of k_1 and k_2 in (4-13) and (4-14). The derivation of these equations is presented below.

Consider the base equation at $(\sigma_p, \varepsilon_p) = (\sigma^1_{ab}, \varepsilon^1_{ab})$ and $(\sigma, \varepsilon) = (\sigma_{\varepsilon_1}, \varepsilon_1)$:

$$\sigma_{\varepsilon_1} = \overbrace{(E_1 - E_2)\left[\varepsilon_1 - \varepsilon^1_{ab} + \frac{1}{k_1}\ln\left(\frac{1 + e^{k_1(\varepsilon^1_{ab} - \varepsilon_1)}}{1 + e^{k_1(\varepsilon_1 - \varepsilon_1)}}\right)\right]}^{\sigma_1} + \overbrace{E_2(\varepsilon_1 - \varepsilon^1_{ab}) + \sigma^1_{ab}}^{\sigma_2} + \underbrace{(E_3 - E_2)\left[\varepsilon_1 - \varepsilon^1_{ab} - \frac{1}{k_2}\ln\left(\frac{1 + e^{-k_2(\varepsilon^1_{ab} - \varepsilon_2)}}{1 + e^{-k_2(\varepsilon_1 - \varepsilon_2)}}\right)\right]}_{\sigma_3} \tag{A1-5}$$

As $\varepsilon^1_{ab} < \varepsilon_2$ and $\varepsilon_1 < \varepsilon_2$, then $\frac{1}{k_2}\ln\left(\frac{1+e^{-k_2(\varepsilon^1_{ab} - \varepsilon_2)}}{1+e^{-k_2(\varepsilon_1 - \varepsilon_2)}}\right) \approx \frac{1}{k_2}\ln\left(\frac{e^{-k_2(\varepsilon^1_{ab} - \varepsilon_2)}}{e^{-k_2(\varepsilon_1 - \varepsilon_2)}}\right) \approx \varepsilon_1 - \varepsilon^1_{ab}$. Therefore, $\sigma_3 \approx 0$.

Further, in σ_1, $\left(1 + e^{k_1(\varepsilon^1_{ab} - \varepsilon_1)}\right) \approx 1$ since $\varepsilon_{ab} < \varepsilon_1$. (A1-5) then simplifies to:

$$\sigma_{\varepsilon_1} = (E_1 - E_2)\left[\varepsilon_1 - \varepsilon^1_{ab} + \frac{1}{k_1}\ln\left(\frac{1}{2}\right)\right] + E_2(\varepsilon_1 - \varepsilon^1_{ab}) + \sigma^1_{ab} \tag{A1-6}$$

Solving (A1-6) for k_1 gives (A1-7)

$$k_1 = -\ln(2)\left(\frac{E_1 - E_2}{\sigma_{\varepsilon_1} - \sigma^1_{ab} - E_1(\varepsilon_1 - \varepsilon^1_{ab})}\right) \tag{A1-7}$$

Similarly, to calculate k_2, Consider the base equation at $(\sigma_p, \varepsilon_p) = (\sigma^2_{ef}, \varepsilon^2_{ef})$ and $(\sigma, \varepsilon) = (\sigma_{\varepsilon_2}, \varepsilon_2)$:

$$\sigma_{\varepsilon_2} = \overbrace{(E_1 - E_2)\left[\varepsilon_1 - \varepsilon^2_{ef} + \frac{1}{k_1}\ln\left(\frac{1 + e^{k_1(\varepsilon^2_{ef} - \varepsilon_1)}}{1 + e^{k_1(\varepsilon_2 - \varepsilon_1)}}\right)\right]}^{\sigma_1} + \overbrace{E_2(\varepsilon_2 - \varepsilon^2_{ef}) + \sigma^2_{ef}}^{\sigma_2} + \underbrace{(E_3 - E_2)\left[\varepsilon_2 - \varepsilon^2_{ef} - \frac{1}{k_2}\ln\left(\frac{1 + e^{-k_2(\varepsilon^2_{ef} - \varepsilon_2)}}{1 + e^{-k_2(\varepsilon_2 - \varepsilon_2)}}\right)\right]}_{\sigma_3}$$

Here, $\sigma_1 \approx 0$ since $\varepsilon_{ef} > \varepsilon_1$ and $\varepsilon_2 > \varepsilon_1$, therefore $\frac{1}{k_1} \ln\left(\frac{1+e^{k_1(\varepsilon^1_{ab}-\varepsilon_1)}}{1+e^{k_1(\varepsilon_2-\varepsilon_1)}}\right) \approx \varepsilon^2_{ef} - \varepsilon_2$ and in σ_3, $\left(1 + e^{-k_2(\varepsilon^2_{ef}-\varepsilon_2)}\right) \approx 1$ since $\varepsilon^2_{ef} > \varepsilon_2$. Then k_2 is calculated in (A1-8) below:

$$k_2 = \ln(2)\left(\frac{E_3 - E_2}{\sigma_{\varepsilon_2} - \sigma^2_{ef} - E_3(\varepsilon_2 - \varepsilon^2_{ef})}\right) \tag{A1-8}$$

A1.3 Calculation of k_2 for austenite unloading

For austenite unloading, presented in Sect. 4.5.1, the stress-strain curves follow a parabolic locus. This affects the value of k_2. Consider $(\frac{\partial\sigma}{\partial\varepsilon})$ from (4-1), shown again for ease of reading in (A1-9). Computing $\frac{\partial^2\sigma}{\partial\varepsilon^2}$, evaluated at ε_2 gives (A1-10). Recall from Fig. 4-2, that the parabolic locus causes a slope in the $(\frac{\partial\sigma}{\partial\varepsilon})$ curve. For a smooth transition between the parabola and the rest of the curve, (A1-10) is set to the parabolic constant q, as shown in Fig. A1-1 and in (A1-11). The value of k_2 is then calculated with (A1-12) (cf. (4-26)).

$$\frac{\partial\sigma}{\partial\varepsilon} = \frac{(E_1 - E_2)}{1 + e^{k_1(\varepsilon-\varepsilon_1)}} + \frac{(E_3 - E_2)}{1 + e^{-k_2(\varepsilon-\varepsilon_2)}} + E_2 \tag{A1-9}$$

$$\frac{\partial^2\sigma}{\partial\varepsilon^2} = \frac{k_2(E_3 - E_2)e^{-k_2(\varepsilon_2-\varepsilon_2)}}{(1 + e^{-k_2(\varepsilon_2-\varepsilon_2)})^2} \tag{A1-10}$$

$$q = \frac{k_2(E_3 - E_2)}{4} \tag{A1-11}$$

$$k_2 = \frac{4q}{E_3 - E_2} \tag{A1-12}$$

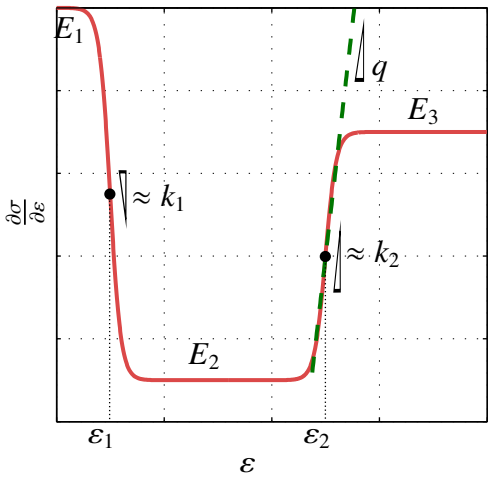

Figure A1-1: *Partial derivative of stress strain curve (red) with parabolic locus (green)*

A1.4 Calculation of q for austenite unloading

The unloading behaviour of austenite and martensite both include the presence of a parabolic locus after the second knee, as shown in Sects. 4.5.1 and 4.6.1. The calculation of the parabolic constant q is presented below.

The entire s-curve equation for reloading is given below (the * have been omitted for simplicity):

$$
\begin{aligned}
\sigma_1 &= (E_1 - E_2)\left[\varepsilon - \varepsilon_p + \frac{1}{k_1}\ln\left(\frac{1+e^{k_1(\varepsilon_p-\varepsilon_1)}}{1+e^{k_1(\varepsilon-\varepsilon_1)}}\right)\right] \\
\sigma_2 &= E_2(\varepsilon - \varepsilon_p) + \sigma_p \\
\sigma_3 &= (E_3 - E_2)\left[\varepsilon - \varepsilon_p - \frac{1}{k_2}\ln\left(\frac{1+e^{-k_2(\varepsilon_p-\varepsilon_2)}}{1+e^{-k_2(\varepsilon-\varepsilon_2)}}\right)\right] \\
\sigma_q &= q(\varepsilon - \varepsilon_2)\left[\varepsilon - \varepsilon_2 + \frac{1}{k_2}\ln\left(1+e^{-k_2(\varepsilon-\varepsilon_2)}\right)\right] \\
&\quad - q(\varepsilon_p - \varepsilon_2)\left[\varepsilon_p - \varepsilon_2 + \frac{1}{k_2}\ln\left(1+e^{-k_2(\varepsilon_p-\varepsilon_2)}\right)\right] \\
\sigma &= \sigma_1 + \sigma_2 + \sigma_3 + \sigma_q
\end{aligned}
\tag{A1-13}
$$

As shown in Fig. A1-2, consider that in addition to the unloading point $(\varepsilon_p, \sigma_p)$, the coordinates of the second unloading knee $(\varepsilon_2, \sigma_{\varepsilon 2})$ are known from (4-23) and (4-24). Further the value of k_2 is taken from (4-26) to ensure a smooth transition from the parabola to the rest of the curve.

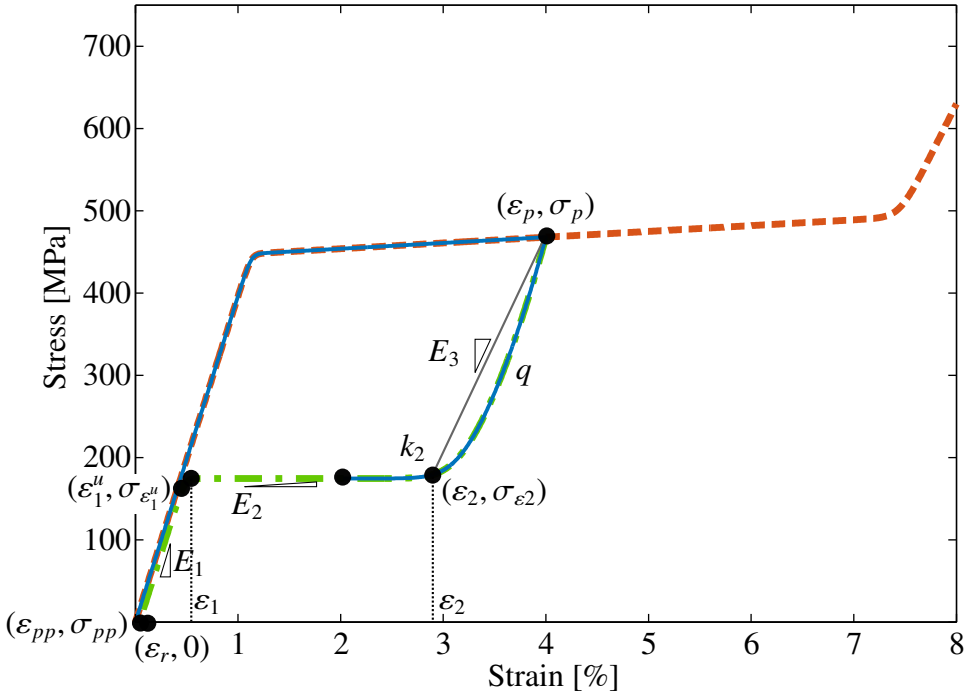

Figure A1-2: *Parameter update for unloading in austenite*

Setting $\varepsilon = \varepsilon_2$ in (A1-13), $\sigma_1 \approx 0$ since $\varepsilon_p > \varepsilon_1$ and $\varepsilon_2 > \varepsilon_1$, therefore $\frac{1}{k_1} \ln\left(\frac{1+e^{k_1(\varepsilon_p-\varepsilon_1)}}{1+e^{k_1(\varepsilon_2-\varepsilon_1)}}\right) \approx \varepsilon_p - \varepsilon_2$ and in σ_3, $\left(1 + e^{-k_2(\varepsilon_p-\varepsilon_2)}\right) \approx 1$ since $\varepsilon_p > \varepsilon_2$. Further, since ε_2 is always smaller than ε_p, $\frac{1}{k_2} \ln\left(1 + e^{-k_2(\varepsilon_p-\varepsilon_2)}\right)$ in σ_q is approximately 0. σ simplifies according to (A1-14) and (A1-15):

$$\sigma_1 \approx 0$$

$$\sigma_2 = E_2(\varepsilon_2 - \varepsilon_p) + \sigma_p$$

$$\sigma_3 = (E_3 - E_2)\left[(\varepsilon_2 - \varepsilon_p) + \frac{\overbrace{E_3 - E_2}^{k_2 \text{ from (A1-12)}}}{4q} \ln(2)\right]$$

$$\sigma_q \approx -q(\varepsilon_p - \varepsilon_2)^2$$

$$\sigma_{\varepsilon 2} = \sigma_1 + \sigma_2 + \sigma_3 + \sigma_q \tag{A1-14}$$

$$\sigma_{\varepsilon 2} = \underbrace{E_3(\varepsilon_2 - \varepsilon_p) + \sigma_p}_{\sigma_c} + \frac{(E_3 - E_2)^2}{4q} \ln(2) - q(\varepsilon_p - \varepsilon_2)^2 \tag{A1-15}$$

However, recall from (4-24) that $\sigma_{\varepsilon_2} = E_3(\varepsilon_2 - \varepsilon_p) + \sigma_p = \sigma_c$, therefore q is given by (A1-16) (c.f (4-25)).

$$q^2(\varepsilon_p - \varepsilon_2)^2 = \frac{(E_3 - E_2)^2 \ln(2)}{4}$$

$$q = \frac{(E_3 - E_2)\sqrt{\ln(2)}}{2(\varepsilon_p - \varepsilon_2)} \tag{A1-16}$$

A1.5 Calculation of q for martensite reloading

The reloading behaviour of martensite also includes the presence of a parabolic locus before the first knee, as shown in Sects. 2.3 and 4.6.2. The calculation of the parabolic constant q is presented below.

The entire s-curve equation for reloading is given below (the * have been omitted for simplicity):

$$
\begin{aligned}
\sigma_1 &= (E_1 - E_2)\left[\varepsilon - \varepsilon_p + \frac{1}{k_1}\ln\left(\frac{1+e^{k_1(\varepsilon_p-\varepsilon_1)}}{1+e^{k_1(\varepsilon-\varepsilon_1)}}\right)\right] \\
\sigma_2 &= E_2(\varepsilon - \varepsilon_p) + \sigma_p \\
\sigma_3 &= (E_3 - E_2)\left[\varepsilon - \varepsilon_p - \frac{1}{k_2}\ln\left(\frac{1+e^{-k_2(\varepsilon_p-\varepsilon_2)}}{1+e^{-k_2(\varepsilon-\varepsilon_2)}}\right)\right] \\
\sigma_q &= q(\varepsilon - \varepsilon_1)\left[\varepsilon - \varepsilon_1 - \frac{1}{k_1}\ln\left(1+e^{k_1(\varepsilon-\varepsilon_1)}\right)\right] \\
&\quad - q(\varepsilon_p - \varepsilon_1)\left[\varepsilon_p - \varepsilon_1 - \frac{1}{k_1}\ln\left(1+e^{k_1(\varepsilon_p-\varepsilon_1)}\right)\right] \\
\sigma &= \sigma_1 + \sigma_2 + \sigma_3 + \sigma_q
\end{aligned}
\tag{A1-17}
$$

Consider that in addition to the reloading point $(\varepsilon_p, \sigma_p)$, the coordinates of the first reloading knee $(\varepsilon_1, \sigma_{\varepsilon 1}) = (\varepsilon_{pp}, \sigma_{pp})$ are known, as shown in Fig. A1-3.

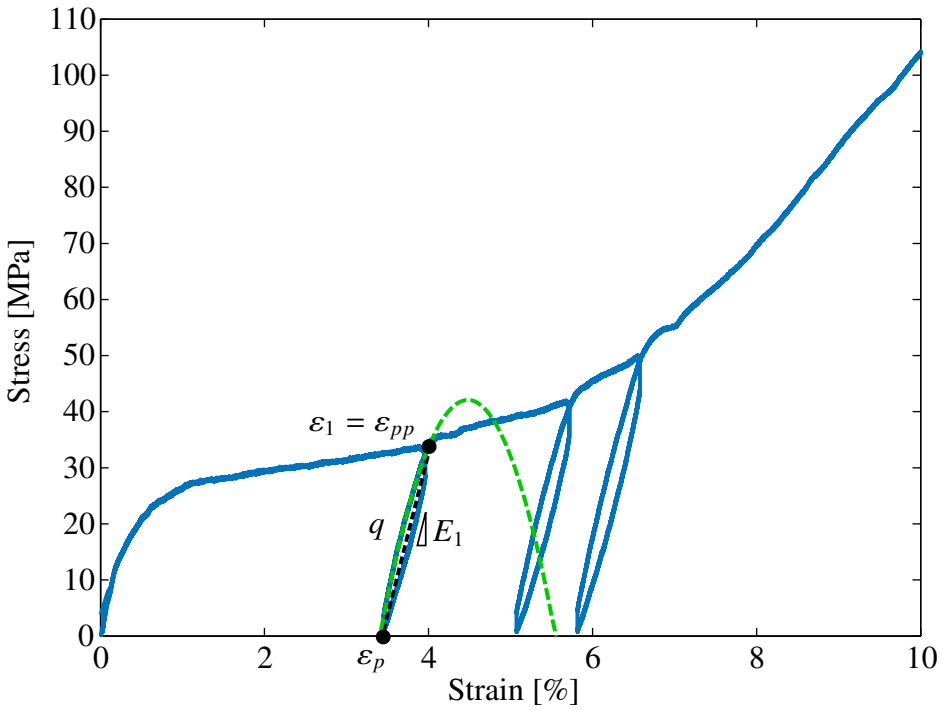

Figure A1-3: *Modelling martensite reloading*

Eq. (A1-17) can be written as in (A1-18) (cf. (4-33)), where $\sigma_1, \sigma_2, \sigma_3$ are evaluated at $\varepsilon = \varepsilon_1$: (Note that since ε_1 is always larger than ε_p, $\frac{1}{k_1}\ln\left(1+e^{k_1(\varepsilon_p-\varepsilon_1)}\right)$ in σ_q is approximately 0.)

$$
\begin{aligned}
\sigma_{pp} &= \sigma_1 + \sigma_2 + \sigma_3 - q(\varepsilon_p - \varepsilon_1)^2 \\
q &= \frac{\sigma_1 + \sigma_2 + \sigma_3 - \sigma_{pp}}{(\varepsilon_p - \varepsilon_1)^2}
\end{aligned}
\tag{A1-18}
$$

A1.6 Calculation of switching parameters: heating to cooling

Recall that in the phase kinetics model in Chap. 6, when the temperature switches from heating to cooling before the SMA is fully austenite, minor loops start to form (see Fig. 6-3). In order to mathematically describe these minor loops, switching conditions are defined in (6-7), reprinted here for clarity:

$$\text{Continuity} \quad : \quad \xi_T^C(T_{sw}, \sigma_{sw}) \;=\; \xi_T^H(T_{sw}, \sigma_{sw})$$

$$\text{Common Origin} \quad : \quad \xi_T^C(T_m, \sigma_{sw})\Big|_{\substack{\alpha_T^{aC} = \alpha_T^{aC}(T_{sw}) \\ \gamma = \gamma(T_{sw})}} \;=\; \xi_T^{H,C}(T_m, \sigma)\Big|_{\substack{\alpha_T^{a} = \alpha_T^{a}(T_m) = 1 \\ \gamma = \gamma(T_m) = 0}}$$

$$\text{Common Limit} \quad : \quad \lim_{T\to\infty} \xi_T^H(T, \sigma_{sw})\Big|_{\substack{\alpha_T^{aH} = \alpha_T^{aH}(T_{sw}) \\ \gamma = \gamma(T_{sw})}} \;=\; \lim_{T\to\infty} \xi_T^{H,C}(T, \sigma)\Big|_{\substack{\alpha_T^{a} = \alpha_T^{a}(T_m) = 1 \\ \gamma = \gamma(T_m) = 0}}$$

Using T_{sw}^- and T_{sw}^+ to specify instants before and after switching, and σ_{sw}^- and σ_{sw}^+ to specify the stress at instants before and after switching, ξ_T is calculated with the following:

$$\text{Before Switching: } \xi_T^H(T_{sw}^-, \sigma_{sw}^-) \;=\; \frac{\alpha_T^{aH}(T_{sw}^-)(1 + e^{k^H(T_m - \beta^H(\sigma_{sw}^-))})}{1 + e^{k^H(T_{sw}^- - \beta^H(\sigma_{sw}^-))}} + \gamma_T^H(T_{sw}^-)$$

$$\text{After Switching: } \xi_T^C(T_{sw}^+, \sigma_{sw}^+) \;=\; \frac{\alpha_T^{aC}(T_{sw}^+)(1 + e^{k^C(T_m - \beta^C(\sigma_{sw}^+))})}{1 + e^{k^C(T_{sw}^+ - \beta^C(\sigma_{sw}^+))}} + \gamma_T^C(T_{sw}^+)$$

The parameters $\alpha_T^{aC}(T_{sw}^+)$ and $\gamma_T^C(T_{sw}^+)$ are the unknowns.
From the common origin condition:

$$\begin{aligned}
\xi_T^C(T_m, \sigma_{sw}^+) \;&=\; \xi_T^H(T_m, \sigma_{sw}^-) \\
\frac{\alpha_T^{aC}(T_{sw}^+)(1 + e^{k^C(T_m - \beta^C(\sigma_{sw}^+))})}{1 + e^{k^C(T_m - \beta^C(\sigma_{sw}^+))}} + \gamma_T^C(T_{sw}^+) \;&=\; \frac{\alpha_T^{aH}(T_m)(1 + e^{k^H(T_m - \beta^H(\sigma_{sw}^-))})}{1 + e^{k^H(T_m - \beta^H(\sigma_{sw}^-))}} + \gamma_T^H(T_m) \\
\alpha_T^{aC}(T_{sw}^+) + \gamma_T^C(T_{sw}^+) \;&=\; \alpha_T^{aH}(T_m) + \gamma_T^H(T_m) \;=\; 1 + 0 \\
\gamma_T^C(T_{sw}^+) \;&=\; 1 - \alpha_T^{aC}(T_{sw}^+)
\end{aligned} \tag{A1-19}$$

From the continuity condition:

$$\begin{aligned}
\xi_T^C(T_{sw}^+, \sigma_{sw}^+) \;&=\; \xi_T^H(T_{sw}^-, \sigma_{sw}^-) \\
\frac{\alpha_T^{aC}(T_{sw}^+)(1 + e^{k^C(T_m - \beta^C(\sigma_{sw}^+))})}{1 + e^{k^C(T_{sw}^+ - \beta^C(\sigma_{sw}^+))}} + \gamma_T^C(T_{sw}^+) \;&=\; \xi_T^H(T_{sw}^-, \sigma_{sw}^-) \\
\gamma_T^C(T_{sw}^+) \;&=\; \xi_T^H(T_{sw}^-, \sigma_{sw}^-) - \frac{\alpha_T^{aC}(T_{sw}^+)(1 + e^{k^C(T_m - \beta^C(\sigma_{sw}^+))})}{1 + e^{k^C(T_{sw}^+ - \beta^C(\sigma_{sw}^+))}}
\end{aligned} \tag{A1-20}$$

Equating (A1-19) and (A1-20) and solving for α_T^{aC}:

$$\begin{aligned}
\xi_T^H(T_{sw}^-, \sigma_{sw}^-) - \frac{\alpha_T^{aC}(T_{sw}^+)(1 + e^{k^C(T_m - \beta^C(\sigma_{sw}^+))})}{1 + e^{k^C(T_{sw}^+ - \beta^C(\sigma_{sw}^+))}} &= 1 - \alpha_T^{aC}(T_{sw}^+) \\
\frac{\alpha_T^{aC}(T_{sw}^+)(1 + e^{k^C(T_m - \beta^C(\sigma_{sw}^+))})}{1 + e^{k^C(T_{sw}^+ - \beta^C(\sigma_{sw}^+))}} - \alpha_T^{aC}(T_{sw}^+) &= \xi_T^H(T_{sw}^-, \sigma_{sw}^-) - 1 \\
\alpha_T^{aC}(T_{sw}^+)[(1 + e^{k^C(T_m - \beta^C(\sigma_{sw}^+))}) - (1 + e^{k^C(T_{sw}^+ - \beta^C(\sigma_{sw}^+))})] &= (\xi_T^H(T_{sw}^-, \sigma_{sw}^-) - 1)(1 + e^{k^C(T_{sw}^+ - \beta^C(\sigma_{sw}^+))}) \\
\alpha_T^{aC}(T_{sw}^+)(e^{k^C(T_m - \beta^C(\sigma_{sw}^+))} - e^{k^C(T_{sw}^+ - \beta^C(\sigma_{sw}^+))}) &= (\xi_T^H(T_{sw}^-, \sigma_{sw}^-) - 1)(1 + e^{k^C(T_{sw}^+ - \beta^C(\sigma_{sw}^+))}) \\
\alpha_T^{aC}(T_{sw}^+) &= (\xi_T^H(T_{sw}^-, \sigma_{sw}^-) - 1)\left[\frac{1 + e^{k^C(T_{sw}^+ - \beta^C(\sigma_{sw}^+))}}{e^{k^C(T_m - \beta^C(\sigma_{sw}^+))} - e^{k^C(T_{sw}^+ - \beta^C(\sigma_{sw}^+))}}\right]
\end{aligned}$$

Finally, the equations for the switch from heating to cooling is with the following (cf. (6-10)):

$$\begin{aligned}
\alpha_T^{aC}(T_{sw}^+) &= (\xi_T^H(T_{sw}^-, \sigma_{sw}^-) - 1)\left[\frac{1 + e^{k^C(T_{sw}^+ - \beta^C(\sigma_{sw}^+))}}{e^{k^C(T_m - \beta^C(\sigma_{sw}^+))} - e^{k^C(T_{sw}^+ - \beta^C(\sigma_{sw}^+))}}\right] \\
\alpha_T^{C}(T_{sw}^+) &= \alpha_T^{aC}(T_{sw}^+)(1 + e^{k^C(T_m - \beta^C(\sigma_{sw}^+))}) \\
\gamma_T^{C}(T_{sw}^+) &= 1 - \alpha_T^{aC}(T_{sw}^+)
\end{aligned}$$

A1.7 Calculation of switching parameters: cooling to heating

Using a similiar nomenclature as from the switch from heating to cooling, ξ_T is calculated with the following:

$$\text{Before Switching: } \xi_T^C(T_{sw}^-, \sigma_{sw}^-) = \frac{\alpha_T^{aC}(T_{sw}^-)(1 + e^{k^C(T_m - \beta^C(\sigma_{sw}^-))})}{1 + e^{k^C(T_{sw}^- - \beta^C(\sigma_{sw}^-))}} + \gamma_T^C(T_{sw}^-)$$

$$\text{After Switching: } \xi_T^H(T_{sw}^+, \sigma_{sw}^+) = \frac{\alpha_T^{aH}(T_{sw}^+)(1 + e^{k^H(T_m - \beta^H(\sigma_{sw}^+))})}{1 + e^{k^H(T_{sw}^+ - \beta^H(\sigma_{sw}^+))}} + \gamma_T^H(T_{sw}^+)$$

The parameters $\alpha_T^{aH}(T_{sw}^+)$ and $\gamma_T^H(T_{sw}^+)$ are the unknowns.

From the common limit condition:

$$\gamma_T^H(T_{sw}^+) = \gamma_T^C(T \to \infty) = 0$$

From the continuity condition:

$$\xi_T^H(T_{sw}^+, \sigma_{sw}^+) = \xi_T^C(T_{sw}^-, \sigma_{sw}^-)$$

$$\frac{\alpha_T^{aH}(T_{sw}^+)(1 + e^{k^H(T_m - \beta^H(\sigma_{sw}^+))})}{1 + e^{k^H(T_{sw}^+ - \beta^H(\sigma_{sw}^+))}} + \gamma_T^H(T_{sw}^+) = \xi_T^C(T_{sw}^-, \sigma_{sw}^-)$$

$$\alpha_T^{aH}(T_{sw}^+)(1 + e^{k^H(T_m - \beta^H(\sigma_{sw}^+))}) = (\xi_T^C(T_{sw}^-, \sigma_{sw}^-) - \gamma_T^H(T_{sw}^+))(1 + e^{k^H(T_{sw}^+ - \beta^H(\sigma_{sw}^+))})$$

$$\underbrace{\alpha_T^{aH}(T_{sw}^+)(1 + e^{k^H(T_m - \beta^H(\sigma_{sw}^+))})}_{\alpha_T^H(T_{sw}^+)} = \xi_T^C(T_{sw}^-, \sigma_{sw}^-)(1 + e^{k^H(T_{sw}^+ - \beta^H(\sigma_{sw}^+))})$$

Finally, the equations for the switch from cooling to heating is with the following (cf. (6-11)):

$$\gamma_T^H(T_{sw}^+) = 0$$

$$\alpha_T^H(T_{sw}^+) = \xi_T^C(T_{sw}^-, \sigma_{sw}^-)(1 + e^{k^H(T_{sw}^+ - \beta^H(\sigma_{sw}^+))})$$

A1.8 Phase kinetics model extension

In the phase kinetics model in Chap. 6, (6-38) was used to compute the martensite fraction when the SMA is either fully martensite or fully austenite at no load, the SMA is then loaded at either $T < M_f$ or $T > A_f$, respectively, to a particular stress and then the temperature changes, thereby utilising the SMA as an actuator.
Consider, however, scenario 8 in Fig. A1-4(b), (identical to Fig. 6-7(d)). Here, the SMA at no load is heated to temperature T_θ at 4 (see Fig. A1-4(a),(b)), where $\xi_T(T_\theta) = \xi_{To} = 0.6$ and therefore $\xi = 0.6$, as given by (6-25). With the temperature held constant ($|\frac{dT}{dt}| = 0$), the SMA is loaded to a stress of 210 MPa to 6 (green curve in the Figure), where $\xi_S = \xi_{So} = 0.7$ and $\xi = \xi_o$ is given by (6-20), as shown in (A1-21) and at position 6a in Fig. A1-5. Consider now that the stress is held constant, but the temperature is increased, therefore ξ is now calculated with (6-31), where at this load, $\xi_S(\varepsilon_m) = 1$ and $\xi_S(\varepsilon_a) = 0$. Let this value be called ξ_B, as shown in (A1-22). It lies on the magenta curve in Fig. A1-5. In order to ensure continuity in ξ, (A1-23) has to hold. To achieve this, the value of β, used in $\xi_T(T, \sigma)$ and $\xi_S(T, \sigma)$ (cf. (6-6) and (6-18), respectively) is modified according to (A1-24), where $T_{\xi o}$ is the temperature at which $\xi_B = \xi_o$, as shown in the Figure. It is calculated with (7-24) from the inverse phase kinetics model in Sect. 7.2. Using β from (A1-24) causes a shift of the magenta curve to coincide with the blue curve passing through 6a, thereby guaranteeing continuity in ξ. From 6a, the SMA can either be cooled to a strain of ε_m, where ξ=1 or heated to ε_a, where ξ=0 (see Fig. 6-7(d)) and it follows the blue curve in the Fig. A1-5. As a further example, consider that the SMA at no load is heated to a different temperature T_θ, where $\xi_T(T_\theta) = \xi_{To} = 0.57$ and then with the temperature held constant, the SMA is loaded to a stress of 210 MPa such that $\xi_S = \xi_{So} = 0.02$ rendering $\xi = \xi_o$ at 6b in Fig. A1-5. Using β from (A1-24), causes a shift to the orange curve in Fig. A1-5, and continuity is once again given. Note that at the threshold temperatures $T = T_m$ (where by definition $T_m < M_f$) and $T > A_f$, $T_\theta = T_{\xi o}$ and β in (A1-24) is identical to β in (6-3). Once the SMA reaches these temperatures, and $|\frac{dT}{dt}|$ changes direction, then β is reset to the original value in (6-3) for all future temperature changes.

$$\xi_o = \xi_T(T_\theta, 0) + \xi_S(\varepsilon(T_\theta)) - \xi_T(T_\theta, 0)\xi_S(\varepsilon(T_\theta)) = \xi_{To} + \xi_{So} - \xi_{To}\xi_{So} \tag{A1-21}$$

$$\xi_B = \frac{\xi_T(T, \sigma) + \xi_S(T, \sigma)}{2} \tag{A1-22}$$

$$\xi_o = \xi_B \tag{A1-23}$$

$$\beta(\sigma) = \beta_o^{H,C} + c_m\sigma + T_\theta - T_{\xi o} \tag{A1-24}$$

The total martensite fraction is therefore computed by (6-38) using β in (6-3), except when $0 < \xi_{To} < 1$ and $0 < \xi_{So} < 1$ before the first temperature change i.e. the SMA is a mixture of phases before temperature increase with the presence of a load. Here, ξ is computed with by using β in (A1-24), until the SMA is a single phase, after which β in (6-3) is once again used. This distinction is not mathematically necessary, but is used in order to retain computational efficiency (since it is not necessary to compute $T_{\xi o}$ at the threshold temperatures where $\xi_o = 1$ or $\xi_o = 0$). Note that these scenarios, where $0 < \xi_{To} < 1$ and $0 < \xi_{So} < 1$ before the first temperature change at a load, rarely arise when the SMA is used as an actuator, since the SMA is typically loaded when fully martensitic ($\xi_{To} = 1$, $\xi_o = 1$).

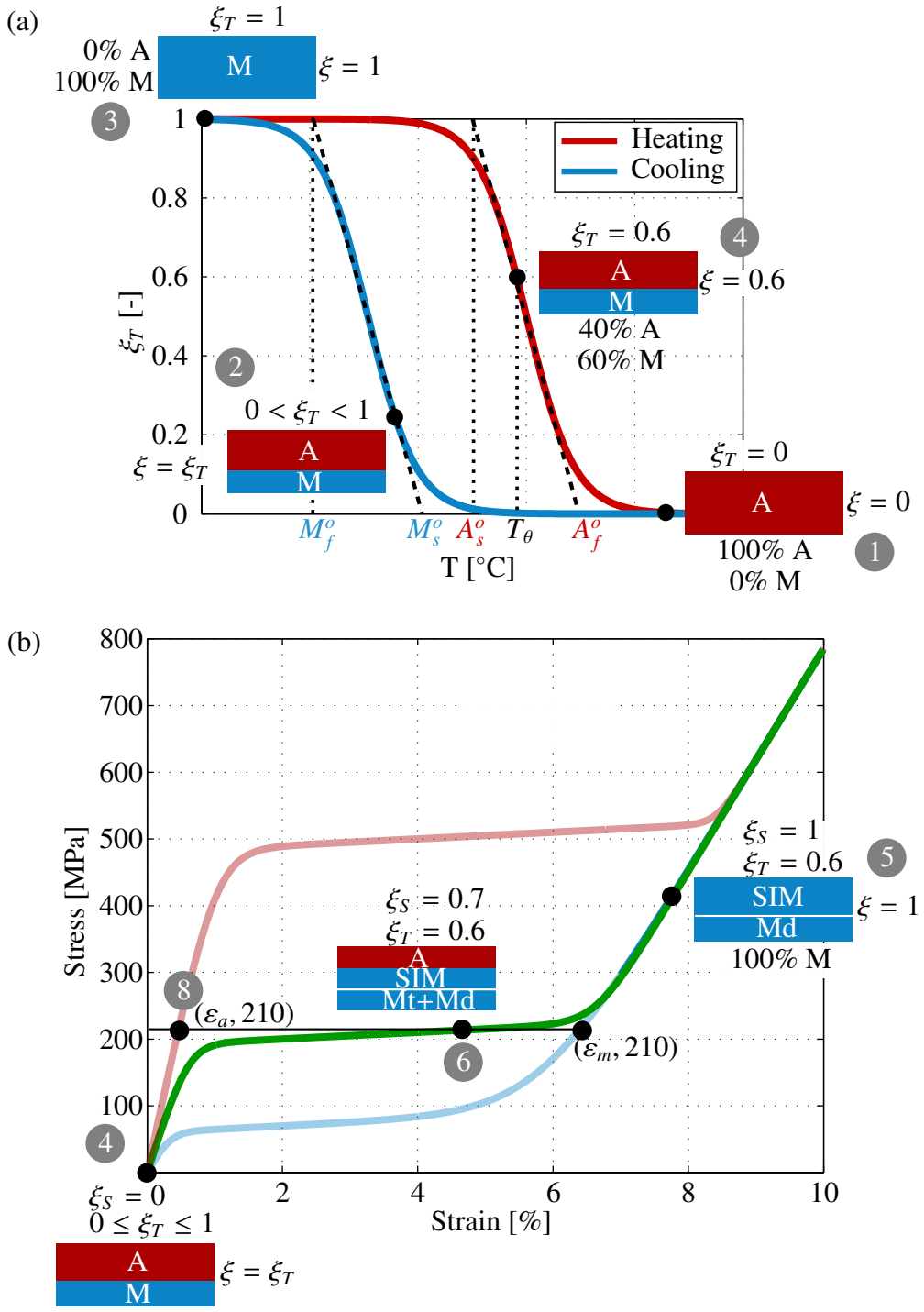

Figure A1-4: *Total martensite fraction: (a) Thermally induced martensite at no load (b) Mechanically induced martensite at* $A_s^o < T < A_f^o$ *or* $M_f^o < T < M_s^o$

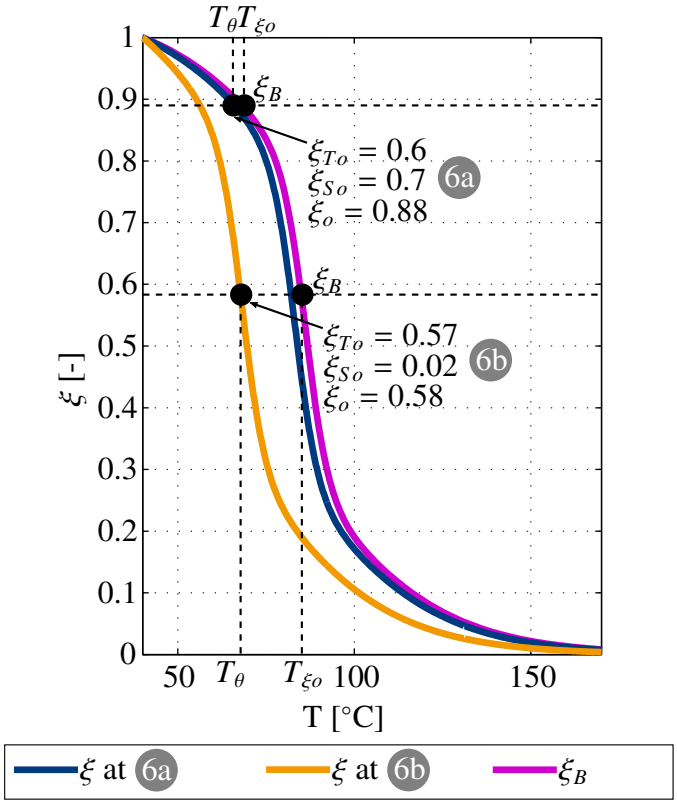

Figure A1-5: *Phase kinetic model showing continuity in ξ*

A2 Data sheets

A2.1 SMA SmartFlex Wire General Characteristics

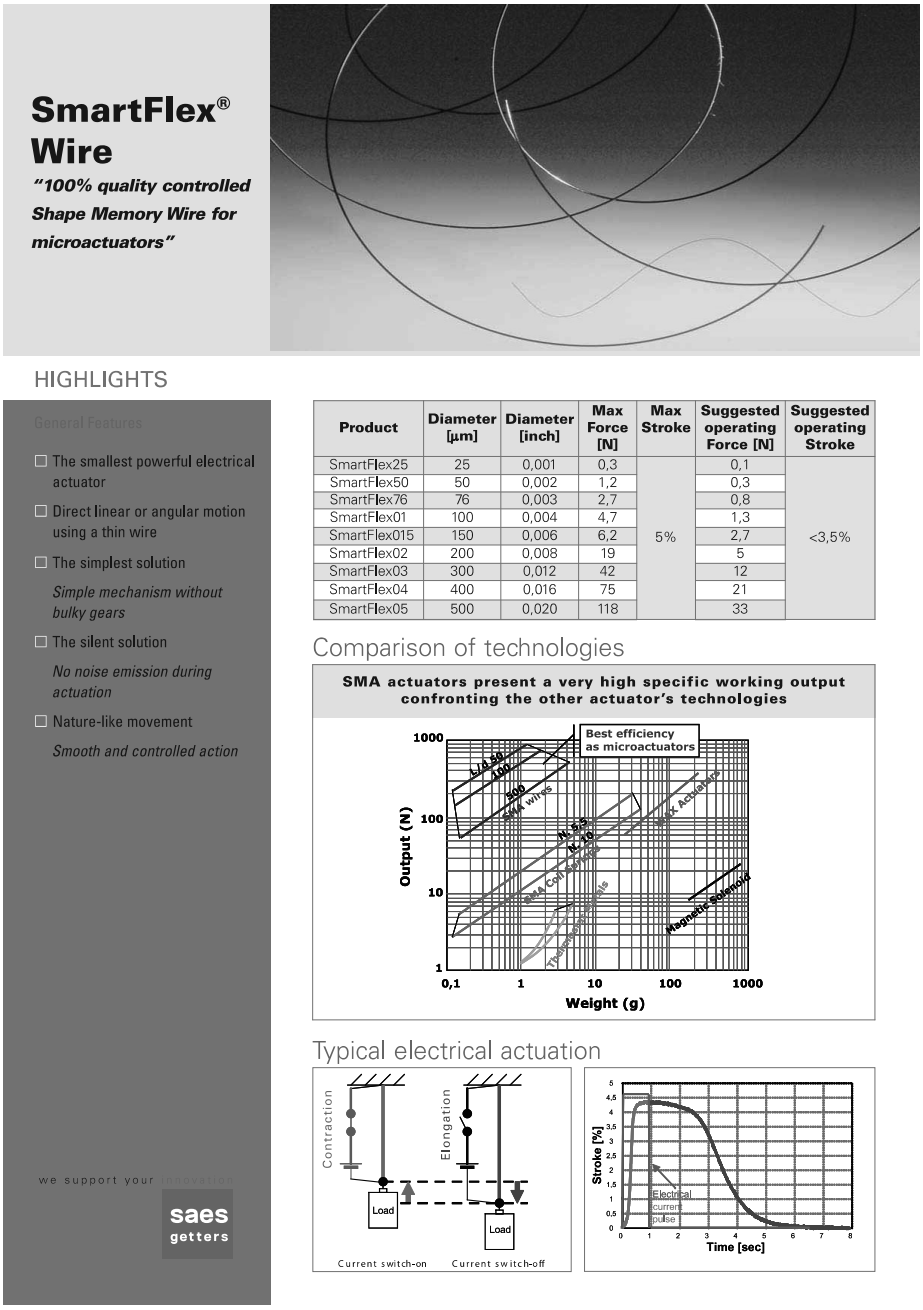

SmartFlex® Wire

"100% quality controlled Shape Memory Wire for microactuators"

HIGHLIGHTS

General Features

- ☐ The smallest powerful electrical actuator
- ☐ Direct linear or angular motion using a thin wire
- ☐ The simplest solution

  Simple mechanism without bulky gears
- ☐ The silent solution

  No noise emission during actuation
- ☐ Nature-like movement

  Smooth and controlled action

we support your innovation

saes getters

Product	Diameter [µm]	Diameter [inch]	Max Force [N]	Max Stroke	Suggested operating Force [N]	Suggested operating Stroke
SmartFlex25	25	0,001	0,3	5%	0,1	<3,5%
SmartFlex50	50	0,002	1,2		0,3	
SmartFlex76	76	0,003	2,7		0,8	
SmartFlex01	100	0,004	4,7		1,3	
SmartFlex015	150	0,006	6,2		2,7	
SmartFlex02	200	0,008	19		5	
SmartFlex03	300	0,012	42		12	
SmartFlex04	400	0,016	75		21	
SmartFlex05	500	0,020	118		33	

Comparison of technologies

Typical electrical actuation

Figure A2-1: *SMA SmartFlex wire from Saes Getters [Saeb]*

A2.2 SMA SmartFlex Wire Showing Transformation Temperatures

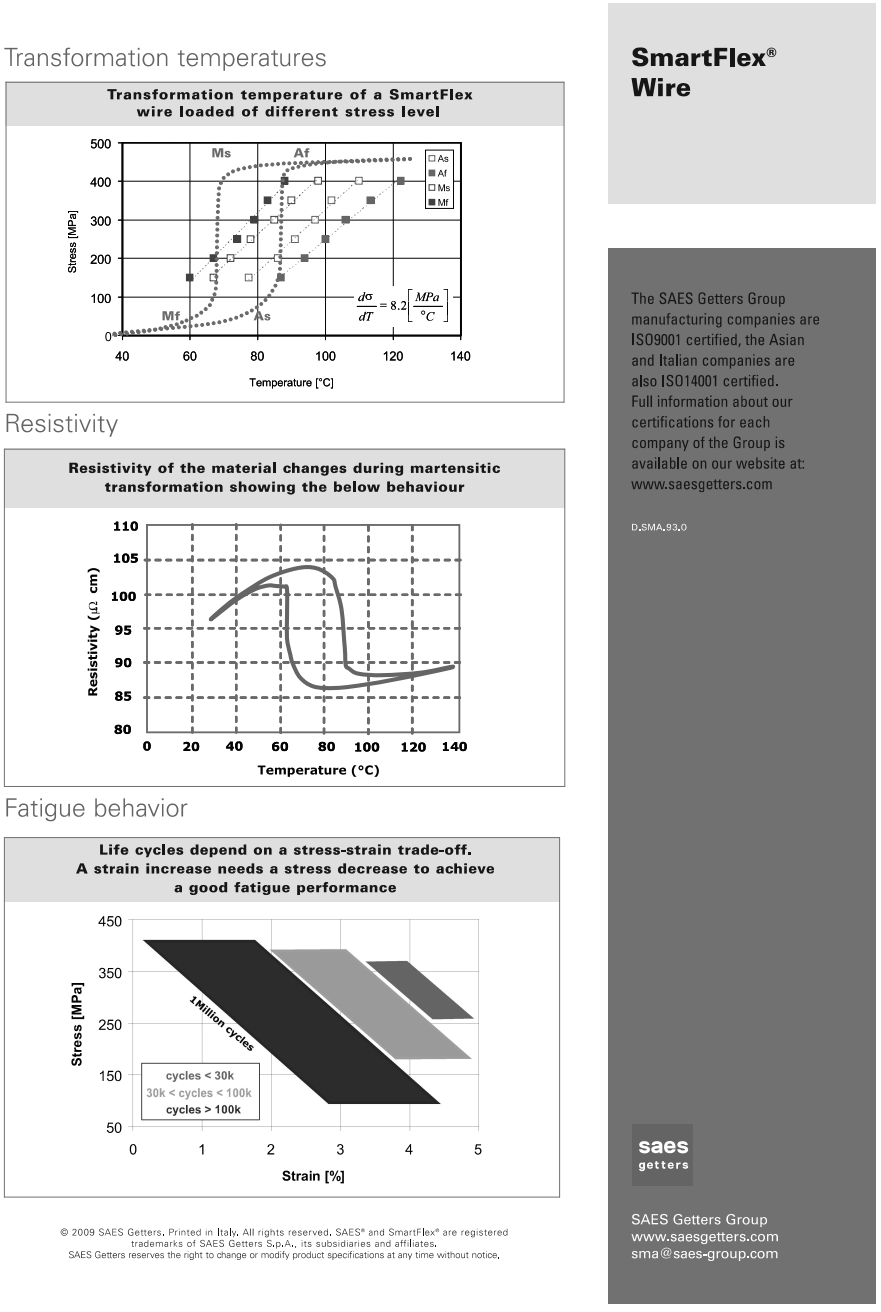

Figure A2-2: *SMA SmartFlex wire from Saes Getters showing parameter* $1/c_m = 8.2 \left[\frac{MPa}{°C}\right]$ *in the top plot [Saeb]*

A2.3 SMA SmartFlex Wire Showing Hysteresis Relationship to Stress

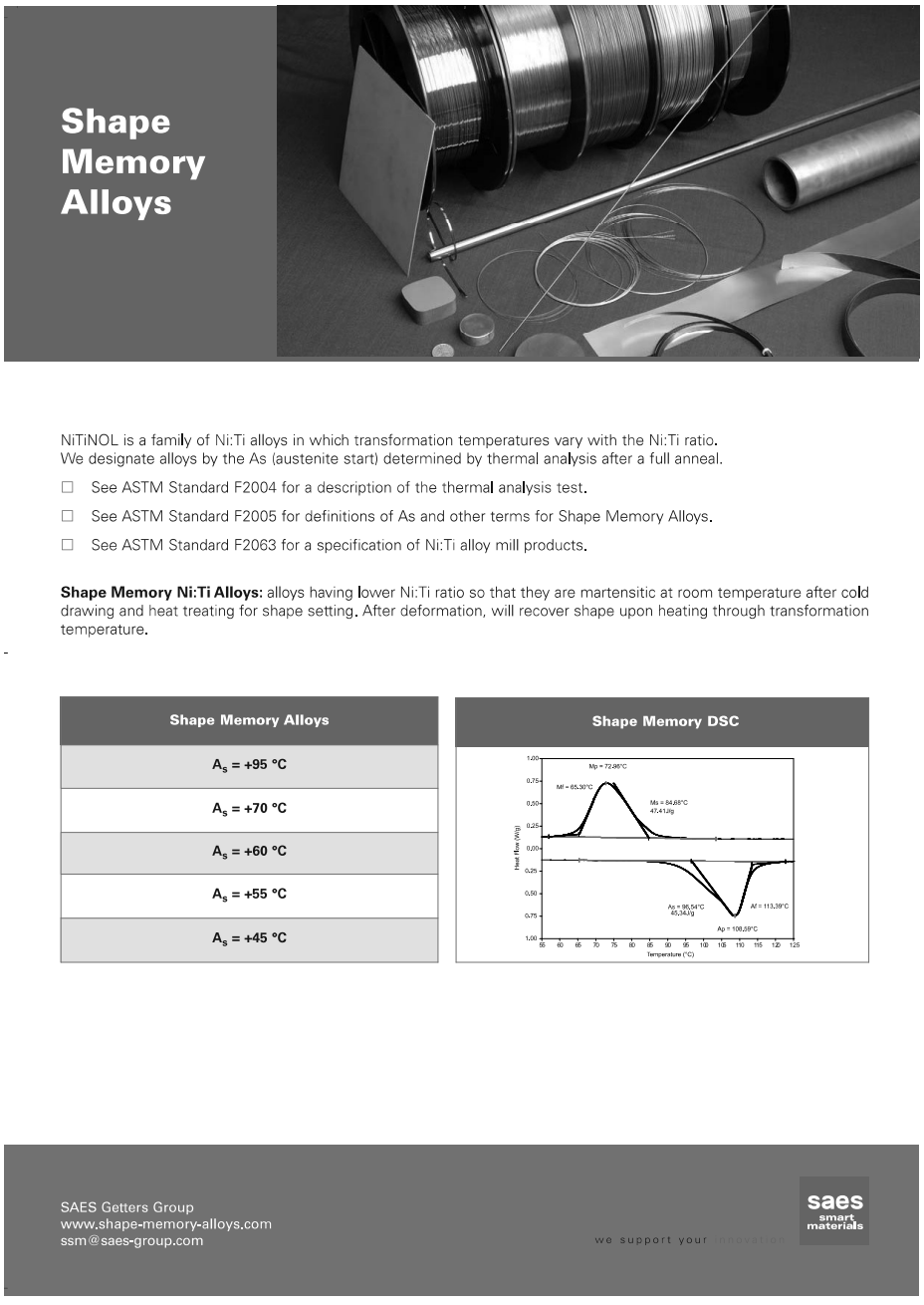

Figure A2-3: *SMA SmartFlex wire from Saes Getters showing parameters M_f, M_s, A_s, A_f in the DSC (Differential Scanning Calorimetry) curve on the right. [Saea]*

A2.4 Servo Hydraulic Tensile Tester

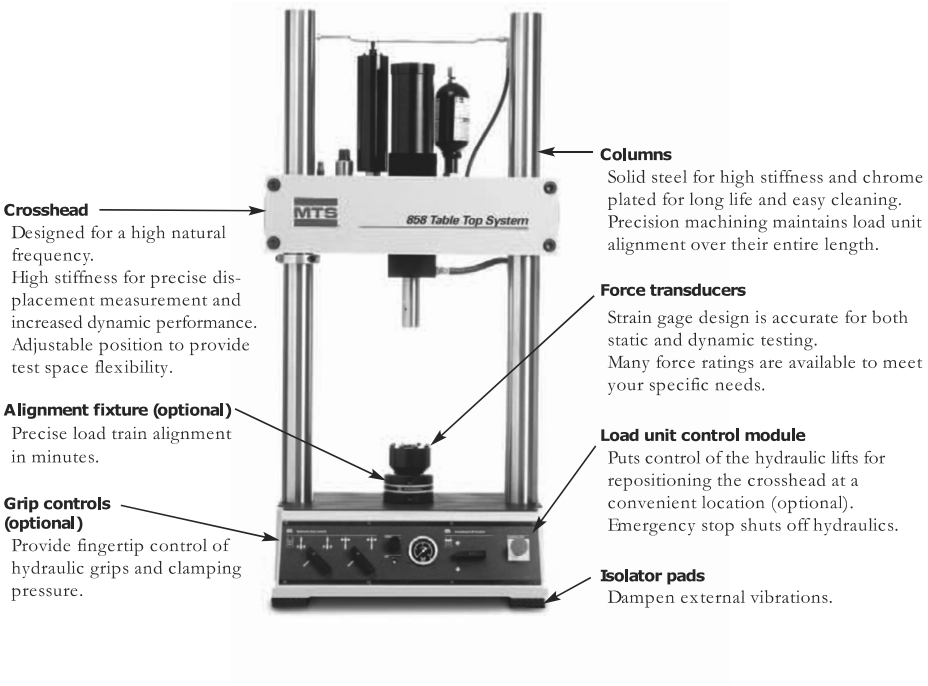

Specifications By Frame Configuration

Load unit specifications

Model	359.15 Standard	359.15 Extended	359.25 Standard	359.25 Extended
Force capacity§	15 kN (3.3 kip)	15 kN (3.3 kip)	25 kN (5.5 kip)	25 kN (5.5 kip)
Vertical test space* (A)	789 mm (31.0 in)	1289 mm (50.7 in)	789 mm (31.0 in)	1289 mm (50.7 in)
Working height (B)	278 mm (10.9 in)	278 mm (10.9 in)	278 mm (10.9 in)	278 mm (10.9 in)
Column spacing (C)	460 mm (18.1 in)	460 mm (18.1 in)	460 mm (18.1 in)	460 mm (18.1 in)
Column diameter (D)	76 mm (3.0 in)	76 mm (3.0 in)	76 mm (3.0 in)	76 mm (3.0 in)
Base width (E)	625 mm (24.6 in)	625 mm (24.6 in)	625 mm (24.6 in)	625 mm (24.6 in)
Base depth (F)	527 mm (20.8 in)	527 mm (20.8 in)	527 mm (20.8 in)	527 mm (20.8 in)
Diagonal Clearance (G)	1378 mm (54.25 in)	1879 mm (74.0 in)	1378 mm (54.25 in)	1879 mm (74.0 in)
Overall Height (H)	1687 mm (66.4 in)	2187 kN (86.1 in)	1687 mm (66.4 in)	2187 kN (86.1 in)
Stiffness†	275×10^6 N/m (1.57×10^6 lb/in) (measured)	275×10^6 N/m (1.57×10^6 lb/in) (measured)	275×10^6 N/m (1.57×10^6 lb/in) (measured)	275×10^6 N/m (1.57×10^6 lb/in) (measured)
Weight	192 kg (425 lb)	231 kg (508 lb)	192 kg (425 lb)	231 kg (508 lb)

* Test space is the maximum distance between the load cell and the actuator with the actuator fully retracted.
† Determined at each load unit's full fatigue rating with its crosshead raised 800 mm (31.5 in.) above the base plate.
§ Rated actuator force at 21 MPa (3000 psi).
Specifications are subject to change without notice. Contact MTS to verify critical specifications.

Figure A2-4: *Servo hydaulic tensile tester from MTS [MTS16]*

A2.5 Cooling Thermostat with Level Controller

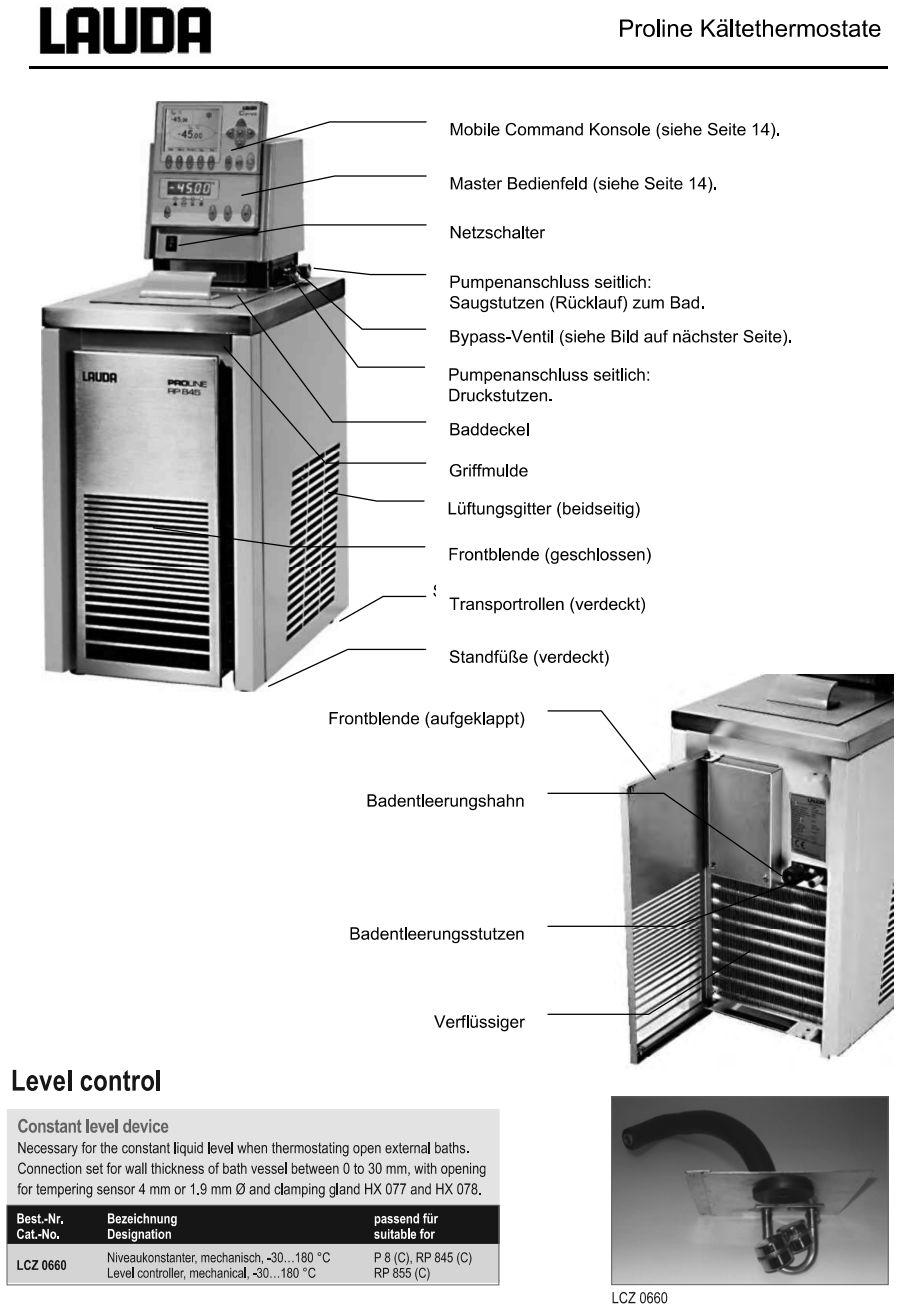

Figure A2-5: *Cooling thermostat from Lauda [LAU16]*

A2.6 Cooling Thermostat Specifications

Technical Data		LAUDA Proline Edition X RP 845 C
Working temperature min.	°C	-45
Working temperature max.	°C	200
Ambient temperature min.	°C	5
Ambient temperature max.	°C	40
Temperature stability	±K	0.01
Cooling output at 200°C measured with thermal oil	kW	1.00
Cooling output at 20°C measured with ethanol	kW	0.80
Cooling output at 0°C measured with ethanol	kW	0.70
Cooling output at -20°C measured with ethanol	kW	0.36
Cooling output at -30°C measured with ethanol	kW	0.22
Cooling output at -40°C measured with ethanol	kW	0.11
Cooling output at -45°C measured with ethanol	kW	0.05
Interface(s)		RS-232/485
Heater power	kW	3.50
Power consumption	kW	3.60
Bath volume min.	L	5.50
Bath volume max.	L	8.50
Bath opening width	mm	150
Bath opening depth	mm	150
Bath depth	mm	200
usable depth	mm	180
Dimensions (WxDxH) in mm		285x430x688
Ø nipples	mm	10
Pump pressure max.	bar	0.70
Pump suction	bar	0.40
Pump flow max. (pressure)	L/min	25
Pump flow max. (suction)	L/min	23
Pump connection thread		M16 x 1
Cat No.		LCKA1008

Figure A2-6: *Specifications of cooling thermostat from Lauda [LAU16]*

A2.7 PT100 Type K Thermocouple

Electronic Sensor ...Temperaturen messen

Tel. 07131 / 797960 -0
Fax 07131 / 79796 -29
info@electronic-sensor.de
www.electronic-sensor.de

Drahtthermoelemente, isoliert

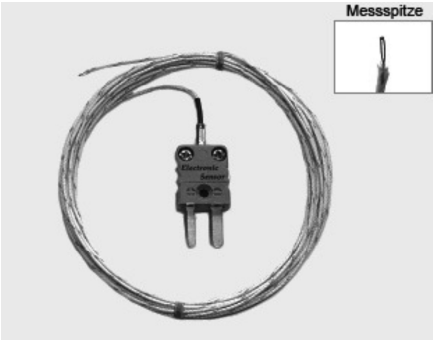

DTE 02
Draht-Thermoelement, Typ K, Klasse 1, IEC 584-3,
Adern: 2 x 0,2 mm, einzeln und gemeinsam
mit Fiberglas isoliert, grüner Kennfaden,
Messspitze < 0,5 mm,
Gesamtlänge: 3000 mm,
Durchmesser: 1,0 x 1,4 mm,
montiert mit Miniatur-Thermostecker (MFM.K)
und Zugentlastungshülse (ZEH),
Temperaturbereich von - 50 bis + 650 °C.
Bestell-Bez.:
2 K-FG14-TM/3,0m/ZEH/MFM.K

Figure A2-7: *PT100 Type K Thermocouple from Electronic Sensor [ES 16]*

A2.8 Digital Thermometer

51 & 52 Series II
Replacement Parts and Accessories

Electrical (cont.)

Measurement Accuracy, T1, T2, or T1-T2 ***(Model 52)***	J-, K-, T-, and E-type: ±[0.05 % of reading + 0.3 °C (0.5 °F)] [below -100 °C (-148 °F): add 0.15 % of reading for J-, K-, E-, and N-type; and 0.45 % of reading for T-type]
Temperature Coefficient	0.01 % of reading + 0.03 °C per °C (0.05 °F per °F) outside the specified +18 °C to 28 °C (+64 °F to +82 °F) range [below -100 °C (-148 °F): add 0.04 % of reading for J-, K-, E-, and N-type; and 0.08 % of reading for T-type]
Electromagnetic Compatibility	Susceptibility: ±2 °C (±3.6 °F) for 80 MHz to 200 MHz in 1.5 V/m field, for 200 MHz to 1000 MHz in 3 V/m field. Emmisions: Commercial Limits per EN50081-1
Maximum Differential Common Mode Voltage	1 V (Maximum voltage difference between T1 and T2)
Temperature Scale	ITS-90

Applicable Standards	NIST-175
Accuracy is specified for ambient temperatures between 18 °C (64 °F) and 28 °C (82 °F) for a period of 1 year. The above specifications do not include thermocouple error.	

Replacement Parts and Accessories

Accessory	Part Number
Holster and Flex Stand™ Assembly	1272438
AA NEDA 15A IEC LR6 batteries	376756
80PK-1 K-Type Bead Thermocouple	773135
CD-ROM	1276106
Service Manual	1276123

Figure A2-8: *Digital thermometer from Fluke [Flu16]*

A2.9 Force Sensor

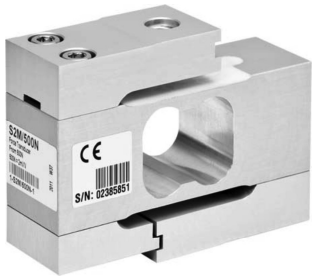

S2M

Kraftaufnehmer

Charakteristische Merkmale

- Zug-/Druckkraftaufnehmer
- Genauigkeitsklasse 0,02
- Nennkräfte: 10 N 0 1000 N
- Hohe Schutzklasse (IP67)
- Hohe Querkraftstabilität
- Sechsleiter-Schaltung

Datenblatt

Technische Daten (Angaben gemäß VDI/VDE/DKD 2638)

Typ			S2M						
Nennkraft	F_{nom}	N	10	20	50	100	200	500	1000
Genauigkeit									
Genauigkeitsklasse			0,02						
Rel. Spannweite in unveränderter Einbaulage	b_{rg}	%	0,02						
Relative Umkehrspanne	v		0,02						
Linearitätsabweichung	d_{lin}		0,02						
Relatives Kriechen über 30 min.	$d_{Cr, F+E-}$		0,02						
Biegemomenteinfluss bei 10% F_{nom} * 10 mm	d_{Mb}		0,02						
Querkrafteinfluss (Querkraft = 10% F_{nom})	d_Q		0,02						
Temperatureinfluss auf den Kennwert	TK_C	% / 10 K	0,02						
Temperatureinfluss auf das Nullsignal	TK_0		0,02						
Elektrische Kennwerte									
Nennkennwert	C_{nom}	mV/V	2						
Relative Abweichung des Nullsignals	$d_{S, 0}$	%	5						
Relative Kennwertabweichung	d_c		0,25						
Relativer Kennwertunterschied Zug/Druck	d_{ZD}		0,1						
Eingangswiderstand	R_e	Ω	u 345						
Ausgangswiderstand	R_a		350 " 50						
Isolationswiderstand	R_{is}	GΩ	u 2						
Gebrauchsbereich der Speisespannung	$B_{U, G}$	V	0,5 ... 12						
Referenzspeisespannung	U_{ref}		5						
Anschluss			Sechsleiter-Schaltung						
Temperatur									
Nenntemperaturbereich	$B_{T, nom}$	°C	−10 ... +45						
Gebrauchstemperaturbereich	$B_{T, G}$		−10 ... +70						
Lagerungstemperaturbereich	$B_{T, S}$		−10 ... +85						
Mechanische Kenngrößen									
Maximale Gebrauchskraft	F_G	%	150						
Grenzkraft	F_L		1000						
Bruchkraft	F_B		1000						
Grenzdrehmoment	M_G	Nm	4	8	25	28			
Grenzbiegemoment	$M_{b\ zul}$		6	25	34	50	71	95	125
Statische Grenzquerkraft	F_Q	% von F_{nom}	100						
Nennmessweg	s_{nom}	mm	0,27	0,21	0,18	0,15	0,13	0,12	0,13
Grundresonanzfrequenz	f_G	Hz	94,4	146	243	358	475	582	618
Relative zulässige Schwingbeanspruchung	F_{rb}	% von F_{nom}	140						
Allgemeine Angaben									
Schutzart nach DIN EN 60529			IP 67						
Messkörperwerkstoff			Aluminium						
Vergussmasse			Silikon						
Kabel			Sechsleiter-Schaltung, PUR-Isolierung, Schleppkett						
Kabellänge		m	6						
Masse (mit Kabel)	m	kg	0,5						

Änderungen vorbehalten.
Alle Angaben beschreiben unsere Produkte in allgemeiner Form. Sie stellen keine Beschaffenheits- oder Haltbarkeitsgarantie dar.

Hottinger Baldwin Messtechnik GmbH
Im Tiefen See 45 · 64293 Darmstadt · Germany
Tel. +49 6151 803-0 · Fax: +49 6151 803-9100
Email: info@hbm.com · www.hbm.com

measure and predict with confidence

HBM

B3593−1.2 de

Figure A2-9: *Force sensor from HBM [Hot16]*

A2.10 Amplifier

4.7 **VM 150 + VM 151** 4.7

www.msr-elektronik.com 6.1.2010

DMS-Verstärker / mV-Verstärker

- **Kraftmessverstärker für Vollbrücken**
- **universell einsetzbar**
- **Linearitätsfehler 0,005%**
- **Versorgung 24Vdc**

Die Verstärker wurden zum Anschluss von Dehnungsmessstreifen in Brückenschaltung (4-Leiter-Technik) entwickelt. Sie eignen sich aber auch hervorragend als mV-Verstärker. Es können einzelne oder mehrere parallel geschaltete DMS-Brücken (Gesamtwiderstand ≥120Ω) mit Sensitivitäten von 0,2...40mV/V verwendet werden. Die Brückenspeisespannung wird mittels Jumper „X6“ auf 5V oder 10V eingestellt.

Die Ausgänge von 0...10V, 0...20mA* oder 4...20mA* werden ebenfalls über Jumper eingestellt. Siehe Tabelle:

Strain Gauge Amplifier / mV Amplifier

- **force measuring amplifier for full bridges**
- **universal applicable**
- **linearity error 0.005%**
- **power supplies 24Vdc**

The amplifier was developed for the connection of foil strain gauges in a bridge circuit (four-wire technology), but they also can used as mV amplifier. 120Ω (total resistance) or greater sensors with output voltages of between 0.2...40mV/V can be used in application as strain gauge amplifier. The bridge supply voltage is set to 5V or 10V using jumper “X6”.

The output signals of 0...10V, 0...20mA* or 4...20mA* can also be preselected using a jumper. See table:

Output	Jumper X2	Jumper X3	Jumper X4
0...10V	U = on	20mA = on	20mA = on
0...20mA	I = on	20mA = on	20mA = on
4...20mA	I = on	4mA = on	20mA = off

Die Verstärkungsanpassung (45...5050) an die verschiedenen Messbrücken lässt sich mittels Jumper „X5“ auf der Leiterplatte vornehmen. Für den Abgleich von Nullpunkt- und Verstärkung stehen je zwei 20-Gang Spindeltrimmer zur Verfügung, mit denen sich der Messbereich grob und fein einstellen lässt.

Für Anzeigen steht zusätzlich ein Monitorausgang (0...10V) zur Verfügung, der mit seiner Grenzfrequenz in 2 Stufen (Jumper „X5“) einstellbar ist.

Das Gerät VM150 eignet sich für unipolare Anwendungen, wogegen der Typ VM151 auch bipolar arbeitet.

The amplifier can be coarsely adjusted to the various measuring bridges using jumper “X5” (45...5050) on the printed circuit board. For the balancing of zero point and gain, there are two 20-turn helical trimmers. These are ideal for making optimum coarse and fine adjustments to the measuring range.

The output can be monitored via an adjustable monitor output (0...10V). The cut-off frequency of the monitor output can be selected in two stages using jumper “X5”.

The unit VM150 is qualified for unipolarly and the unit VM151 is qualified for bipolarly applications.

Typübersicht:

Type summary:

Typ type	Eingang input	U-Ausgang V-output	I-Ausgang* I-output*	Hilfsenergie supply
VM 150	mV or DMS-Signal	0 ... +10V	0/4 ... 20mA	24Vdc
VM 151	mV or DMS-Signal	0 ... ±10V	---	24Vdc

* nur beim Verstärker VM150

* only at amplifier VM150

Die Verstärker sind aufrastbar auf Hutschienen TS35 und werden mit 24Vdc versorgt. Die Versorgungsspannung ist von den Signalen galvanisch getrennt.

The units can be clipped onto DIN TS35 rails and are supplied with 24Vdc. The supply voltage is electrically isolated from the signals.

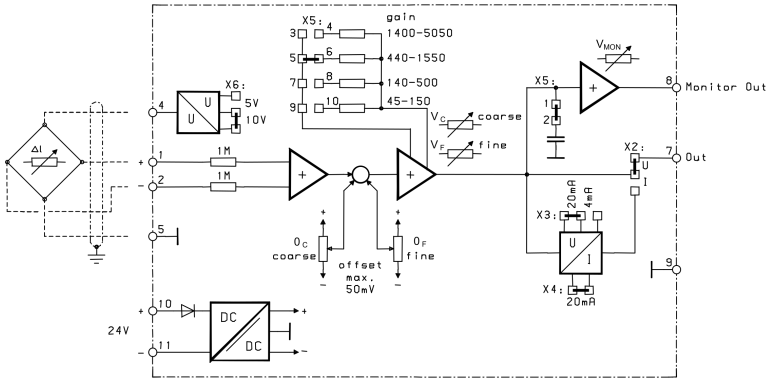

A T R Industrie-Elektronik GmbH

www.msr-elektronik.com • elektronik@atrie.de

Figure A2-10: *Amplifier from ATR [IE16]*

A2.11 Laser Distance Sensor

Baumer — Optoelektronische Sensoren

Distanz-Sensoren — **OADM 12U7460/S35A**

Masszeichnung

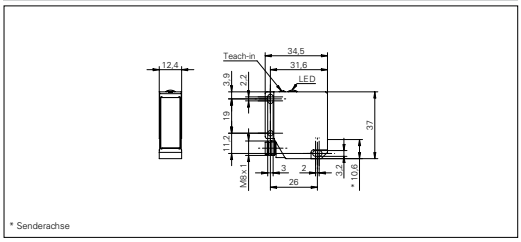

Allgemeine Daten	
Messdistanz Sd	16 ... 120 mm
Einstellung	Teach-in: Taste / Extern
Abstand Teach-In-Grenzen	> 2 mm
Betriebsanzeige	LED grün
Anzeige Alarm- / Verschmutzung	LED rot
Auflösung	0,002 ... 0,12 mm
Linearitätsabweichung	± 0,015 ... ± 0,35 mm
Lichtquelle	Laserdiode rot, gepulst
Wellenlänge	650 nm
Laserklasse	1
Strahlform	Punkt
Strahldurchmesser	0,9 ... 0,5 mm
Störimpulsunterdrückung	< 30 ms
Temperaturdrift	< 0,06 % Sde/K

Elektrische Daten	
Ansprech- / Abfallzeit	2 ... 3 ms
Betriebsspannungsbereich +Vs	12 ... 28 VDC
Stromaufnahme max. (ohne Last)	80 mA
Ausgangsschaltung	analog
Ausgangssignal	0 ... 10 VDC
Lastwiderstand	> 100 kOhm
kurzschlussfest	ja
verpolungsfest	ja, Vs zu GND

Mechanische Daten	
Breite / Durchmesser	12,4 mm
Höhe / Länge	37 mm
Tiefe	34,5 mm
Bauform	quaderförmig
Gehäusematerial	Zink-Druckguss
Frontscheibe	Glas
Anschlussart	Stecker M8 4-Pol

Foto

Anschlussbild

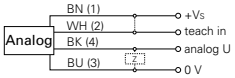

Laserwarnung

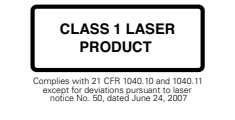

CE c UL us LISTED

OADM 12U7460/S35A — www.baumer.com — 8.1.2014

Figure A2-11: *Laser distance sensor from Baumer [Bau16]*

A2.12 Thermocouple

ENGLISH

Datasheet

ANSI Type K Fine Gauge Exposed Welded Tip Thermocouple

1-metre-long, 0.003” (0.076mm) Teflon® PFA insulated – ANSI colour code

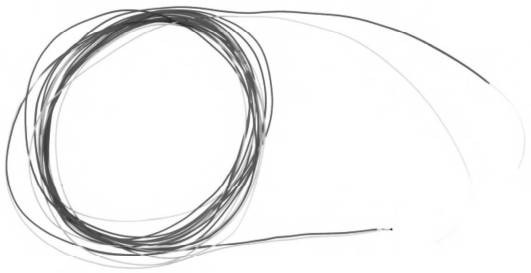

- Type K fine gauge thermocouple
- 0.003” (0.076mm) conductors
- Fast response, welded tip exposed junction
- 1-metre-long Teflon® PFA insulated wires
- ANSI colour coded (+yellow, -red)
- Temperature range –75°C to +260°C
- Ideal for test & development applications

T/C Type	Conductors	Length	+Positive tail wire	-Negative tail wire	Allied code	RS order code
‘K’	1/0.076mm	1 metre	Yellow	Red	70643872	**397-1589**

RS137/0816

Figure A2-12: *Thermocouple from RS [RS 16]*

A2.13 Thermocouple Amplifier

Datasheet

MICROSERIES
MAS Thermo-K 0...1000°C

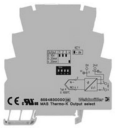

Weidmüller

Weidmüller Interface GmbH & Co. KG
Klingenbergstraße 16
D-32758 Detmold
Germany
Fon: +49 5231 14-0
Fax: +49 5231 14-2083
www.weidmueller.com

Technical data

Dimensions

Length	88 mm	Width	6.1 mm
Height	97.8 mm		

Temperatures

Operating temperature	0 °C...+55 °C	Storage temperature	-20 °C...+85 °C

Probability of failure

MTTF	437 Years

Input

Number of inputs	1	Temperature input range	0...1000 °C
Sensor	Thermocouple acc. to IEC 584, type: K		

Output

Wire break detection	Output value: > 20 mA, >10 V	cold junction compensation	Yes
load impedance voltage	≥ 10 kΩ	Number of outputs	1
load impedance current	≤ 400 Ω @ 24 V	Output voltage, note	0...10V / 0...5V
Output current	0(4)...20 mA		

General data

Accuracy	< 0.6 % of measuring range	Current-carrying capacity of cross-connect.	≤ 20 A
Galvanic isolation	2-way isolator	Input/Output	Thermocouple type: K / 0(4)...20 mA, 0...10 V, 0...5 V
Linearity	Yes	Mounting rail	TS 35
Power consumption	ca. 0.6 W	Step response time	< 0.7 s
Supply voltage	24 V DC ± 10 %	Temperature coefficient	≤ 250 ppm/K of final value
Type of connection	Screw connection		

Insulation coordination

Clearance & creepage distances	≥ 1.5 mm	EMC standards	EN 55011, EN 61000-6 /-2, EN 61326
Impulse withstand voltage	1.5 kV	Insulation voltage	500 V_{eff} / 1 s
Insulation voltage input or output/rail	500 V_{eff}	Insulation voltage input or output/supply	500 V_{eff}
Pollution severity	2	Rated voltage	100 V
Standards	DIN EN 50178, DIN EN 61000-4-2	Surge voltage category	III

Classifications

UNSPSC	30-21-18-01	eClass 5.1	27-20-02-06
eClass 6.0	27-20-02-06		

Approvals

Approvals	CE; CULUS; GOSTME25

Creation date December 9, 2011 2:15:43 PM CET

Last update 24.11.2011 / We reserve the right to make technical changes. 2

Figure A2-13: *Thermocouple Amplifier from Weidmueller [Wei16]*

A2.14 Current Driver

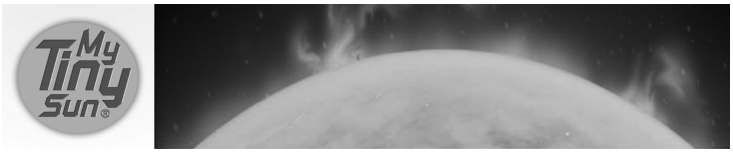

MyTinySun High Power KSQ - LED Treiber *ie406R9zdrv*

Abbildungen zeigen **ie406R9zdrv Platine** mit ie406R9con und MTS Triple Led Modul

Eigenschaften:
- LED Treiber, Abwärtswandler – Buck driver.
- 4V bis 18V Eingangsspannungsbereich.
- Bis zu 3,40A Ausgangsstrom, 3,03A nominal.
- Bis zu 95% Wirkungsgrad.
- Arbeitstemperatur -20 bis 100 Grad Celsius.
- Integrierte Temperaturreglung (interner oder externer Temperatursensor verwendbar).
- hohe Ausgangsstromstabilität über Eingangsspannungsbereich und Temperatur.
- < 30µA im Standby Betrieb.
- Ausgangsstrom analog steuerbar, stufenlos dimmen von 10-112%.
- Zusätzliche über PWM-Signal digital dimmen, <10% - 112%.
- Power 'OK' Signal.
- Treibt bis zu 4 weiße High Power LEDs in Reihe.
- Integrierte Hochfrequenzfilter für EMV-gerechte Ausführung.
- In Deutschland entwickelt und produziert.
- Durch Zusatzmodule erweiterbar, z. B. Controllerplatine ***ie406R9con***

Technische Daten / Maximalwerte:

Signal	Pins	Minimaler / Maximaler Wert:
VBATT (Eingang)	+BATT / -BATT	4V – 18V
VLED (Ausgang)	+LED / -LED	2V – (VBATT -1V)
ILED (Ausgang)	+LED / -LED	0A – 3,4A (112%)
VADJ LED (Eingang)	ADJ LED / GND	0mV – 500mV(100%) / 650mV(112%)

Lötbrücken:

3,03A / 1,84A (60%)	- Brücken um integrierten Widerstand 133kOHM zwischen ADJ und GND zu schalten - dadurch Reduzierung des Ausgangsstroms auf 1,84A (60%) - ADJ Pin kann durch externe Beschaltung wieder überschrieben werden
NTC ON BOARD	- Brücken um integrierten Temperatursensor auf der Treiberplatine und nicht den Sensor auf der LED Platine (über Anschlüsse 11 + 12) zu verwenden. - Typ ERT-J1VG103FA NTC - T_{25} = 10kOHM - B Wert = 3301 – 3400
INT TEMP. REG.	- Brücken um treiberinterne Temperaturreglung zu verwenden - Bei Brücken von NTC ON BOARD Begrenzung der Elektroniktemperatur auf etwa 80°C

Figure A2-14: *Current driver from MyTinySun [MyT16]*

A2.15 Data Aquisition Board

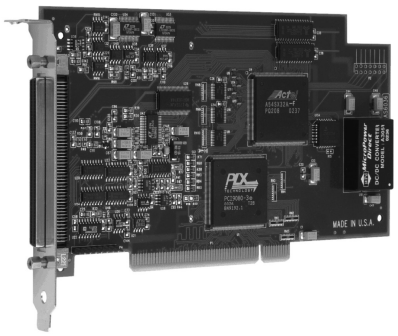

Pin out – main I/O connector

8-channel differential mode

** Not available on the PCI-DAS6013*

Signal Name	Pin	Pin	Signal Name
GND	100	50	GND
CTR2 OUT	99	49	AUXIN5 / A/D PACER GATE
CTR2 GATE	98	48	AUXIN4 / D/A START TRIGGER
CTR2 CLK	97	47	AUXIN3 / D/A UPDATE
GND	96	46	AUXIN2 / A/D STOP TRIGGER
CTR1 OUT	95	45	AUXIN1 / A/D START TRIGGER
CTR1 GATE	94	44	n/c
CTR1 CLK	93	43	AUXIN0 / A/D CONVERT
DIO7	92	42	AUXOUT2 / SCANCLK
DIO6	91	41	AUXOUT1 / A/D PACER OUT
DIO5	90	40	AUXOUT0 / D/A PACER OUT
DIO4	89	39	PC +5 V
DIO3	88	38	D/A OUT1*
DIO2	87	37	D/A GND*
DIO1	86	36	D/A OUT 0*
DIO0	85	35	AISENSE
n/c	84	34	n/c
n/c	83	33	n/c
n/c	82	32	n/c
n/c	81	31	n/c
n/c	80	30	n/c
n/c	79	29	n/c
n/c	78	28	n/c
n/c	77	27	n/c
n/c	76	26	n/c
n/c	75	25	n/c
n/c	74	24	n/c
n/c	73	23	n/c
n/c	72	22	n/c
n/c	71	21	n/c
n/c	70	20	n/c
n/c	69	19	n/c
n/c	68	18	LLGND
n/c	67	17	CH7 IN LO
n/c	66	16	CH7 IN HI
n/c	65	15	CH6 IN LO
n/c	64	14	CH6 IN HI
n/c	63	13	CH5 IN LO
n/c	62	12	CH5 IN HI
n/c	61	11	CH4 IN LO
n/c	60	10	CH4 IN HI
n/c	59	9	CH3 IN LO
n/c	58	8	CH3 IN HI
n/c	57	7	CH2 IN LO
n/c	56	6	CH2 IN HI
n/c	55	5	CH1 IN LO
n/c	54	4	CH1 IN HI
n/c	53	3	CH0 IN LO
n/c	52	2	CH0 IN HI
n/c	51	1	LLGND

PCI slot ⊥

MEASUREMENT COMPUTING™

Figure A2-15: *Data Aquisition Board from MCC [Mea16]*

A2.16 Force Resistive Sensor

FSR® 400 Series Data Sheet

Force Sensing Resistors®

® 402 Short
13mm Circle x 25mm

® 402
13mm Circle x 56mm

Device Characteristics	
Actuation Force*	~0.2N min
Force Sensitivity Range*	~0.2N – 20N
Force Resolution	Continuous (analog)
Force Repeatability Single Part	+/- 2%
Force Repeatability Part to Part	+/- 6% (Single Batch)
Non-Actuated Resistance	>10 Mohms
Hysteresis	+10% Average (RF+ - RF-)/RF+
Device Rise Time	< 3 Microseconds
Long Term Drift	
1kg load, 35 days	< 5% log10(time)
Operating Temperature Performance	
Cold: -40ºC after 1 hour	-5% average resistance change
Hot: +85ºC after 1 hour	-15% average resistance change
Hot Humid: +85ºC 95RH after 1 hour	+10% average resistance change
Storage Temperature Performance	
Cold: -25ºC after 120 hours	-10% average resistance change
Hot: +85ºC after 120 hours	-%5 average resistance change
Hot Humid: +85ºC 95RH after 240 hours	+30% average resistance change
Tap Durability	
Tested to 10 Million actuations, 1kg, 4Hz	-10% average resistance change
Standing Load Durability	
2.5kg for 24 hours	-5% average resistance change
EMI	Generates no EMI
ESD	Not ESD Sensitive
UL	All materials UL grade 94 V-1 or better
RoHS	Compliant

Specifications are derived from measurements taken at 1000 grams, and are given as (one standard deviation/mean), unless otherwise noted.
*Typical value. Force dependent on actuation interface, mechanics, and measurement electronics.

Figure A2-16: *Force Resistive Sensor from Interlink Elektronics [Int16]*

A2.17 Current Shunt Monitor

Burr-Brown Products from Texas Instruments

INA139
INA169

SBOS181D – DECEMBER 2000 – REVISED NOVEMBER 2005

High-Side Measurement CURRENT SHUNT MONITOR

FEATURES

- COMPLETE UNIPOLAR HIGH-SIDE CURRENT MEASUREMENT CIRCUIT
- WIDE SUPPLY AND COMMON-MODE RANGE
  INA139: 2.7V to 40V
- INA169: 2.7V to 60V
- INDEPENDENT SUPPLY AND INPUT COMMON-MODE VOLTAGES
- SINGLE RESISTOR GAIN SET
  LOW QUIESCENT CURRENT (60µA typ)
- SOT23-5 PACKAGE

APPLICATIONS

- CURRENT SHUNT MEASUREMENT: Automotive, Telephone, Computers
- PORTABLE AND BATTERY-BACKUP SYSTEMS
- BATTERY CHARGERS
- POWER MANAGEMENT
- CELL PHONES
- PRECISION CURRENT SOURCE

DESCRIPTION

The INA139 and INA169 are high-side, unipolar, current shunt monitors. Wide input common-mode voltage range, high-speed, low quiescent current, and tiny SOT23 packaging enable use in a variety of applications.

Input common-mode and power-supply voltages are independent and can range from 2.7V to 40V for the INA139 and 2.7V to 60V for the INA169. Quiescent current is only 60µA, which permits connecting the power supply to either side of the current measurement shunt with minimal error.

The device converts a differential input voltage to a current output. This current is converted back to a voltage with an external load resistor that sets any gain from 1 to over 100. Although designed for current shunt measurement, the circuit invites creative applications in measurement and level shifting.

Both the INA139 and INA169 are available in SOT23-5 packages and are specified for the –40°C to +85°C industrial temperature range.

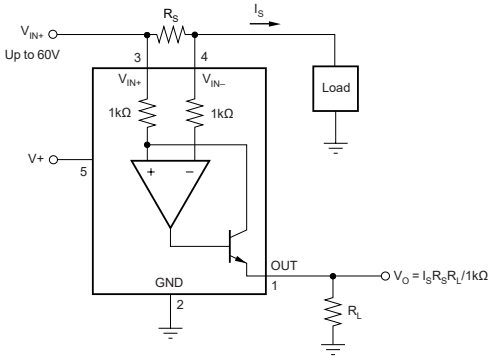

TEXAS INSTRUMENTS
www.ti.com

Figure A2-17: *Current Shunt Monitor from Texas Instruments [Tex16]*

A2.18 Microcontroller

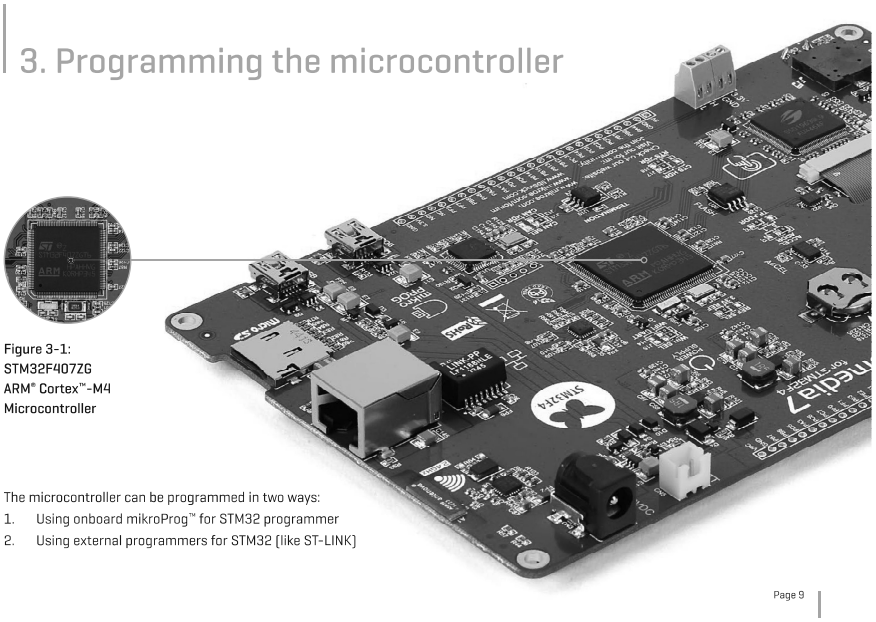

Figure A2-18: *Mircocontroller from Mikroelektronika [Mik16]*

Das Heinz Nixdorf Institut – Interdisziplinäres Forschungszentrum für Informatik und Technik

Das Heinz Nixdorf Institut ist ein Forschungszentrum der Universität Paderborn. Es entstand 1987 aus der Initiative und mit Förderung von Heinz Nixdorf. Damit wollte er Ingenieurwissenschaften und Informatik zusammenführen, um wesentliche Impulse für neue Produkte und Dienstleistungen zu erzeugen. Dies schließt auch die Wechselwirkungen mit dem gesellschaftlichen Umfeld ein.

Die Forschungsarbeit orientiert sich an dem Programm „Dynamik, Mobilität, Vernetzung: Eine neue Schule des Entwurfs der technischen Systeme von morgen“. In der Lehre engagiert sich das Heinz Nixdorf Institut in Studiengängen der Informatik, der Ingenieurwissenschaften und der Wirtschaftswissenschaften.

Heute wirken am Heinz Nixdorf Institut neun Professoren mit insgesamt 130 Mitarbeiterinnen und Mitarbeitern. Pro Jahr promovieren hier etwa 15 Nachwuchswissenschaftlerinnen und Nachwuchswissenschaftler.

Heinz Nixdorf Institute – Interdisciplinary Research Centre for Computer Science and Technology

The Heinz Nixdorf Institute is a research centre within the Paderborn University. It was founded in 1987 initiated and supported by Heinz Nixdorf. By doing so he wanted to create a symbiosis of computer science and engineering in order to provide critical impetus for new products and services. This includes interactions with the social environment.

Our research is aligned with the program “Dynamics, Mobility, Integration: Enroute to the technical systems of tomorrow.” In training and education the Heinz Nixdorf Institute is involved in many programs of study at the Paderborn University. The superior goal in education and training is to communicate competencies that are critical in tomorrows economy.

Today nine Professors and 130 researchers work at the Heinz Nixdorf Institute. Per year approximately 15 young researchers receive a doctorate.

Zuletzt erschienene Bände der Verlagsschriftenreihe des Heinz Nixdorf Instituts

Bd. 365 KLIEWE, D.: Entwurfssystematik für den präventiven Schutz Intelligenter Technischer Systeme vor Produktpiraterie**.** Dissertation, Fakultät für Maschinenbau, Universität Paderborn, Verlagsschriftenreihe des Heinz Nixdorf Instituts, Band 365, Paderborn, 2017 – ISBN 978-3-942647-84-7

Bd. 366 IWANEK, P.: Systematik zur Steigerung der Intelligenz mechatronischer Systeme im Maschinen- und Anlagenbau**.** Dissertation, Fakultät für Maschinenbau, Universität Paderborn, Verlagsschriftenreihe des Heinz Nixdorf Instituts, Band 366, Paderborn, 2017 – ISBN 978-3-942647-85-4

Bd. 367 SCHWEERS, C.: Adaptive Sigma-Punkte-Filter-Auslegung zur Zustands- und Parameterschätzung an Black-Box-Modellen**.** Dissertation, Fakultät für Maschinenbau, Universität Paderborn, Verlagsschriftenreihe des Heinz Nixdorf Instituts, Band 367, Paderborn, 2017 – ISBN 978-3-942647-86-1

Bd. 368 SCHIERBAUM, T.: Systematik zur Kostenbewertung im Systementwurf mechatronischer Systeme in der Technologie Molded Interconnect Devices (MID)**.** Dissertation, Fakultät für Maschinenbau, Universität Paderborn, Verlagsschriftenreihe des Heinz Nixdorf Instituts, Band 368, Paderborn, 2017 – ISBN 978-3-942647-87-8

Bd. 369 BODDEN, E.; DRESSLER, F.; DUMITRESCU, R.; GAUSEMEIER, J.; MEYER AUF DER HEIDE, F.; SCHEYTT, C.; TRÄCHTLER, A. (Hrsg.): Intelligente technische Systeme. Verlagsschriftenreihe des Heinz Nixdorf Instituts, Band 369, Paderborn, 2017 – ISBN 978-3-942647-88-5

Bd. 370 KÜHN, A.: Systematik zur Release-Planung intelligenter technischer Systeme**.** Dissertation, Fakultät für Maschinenbau, Universität Paderborn, Verlagsschriftenreihe des Heinz Nixdorf Instituts, Band 370, Paderborn, 2017 – ISBN 978-3-942647-89-2

Bd. 371 REINOLD, P.: Integrierte, selbstoptimierende Fahrdynamikregelung mit Einzelradaktorik**.** Dissertation, Fakultät für Maschinenbau, Universität Paderborn, Verlagsschriftenreihe des Heinz Nixdorf Instituts, Band 371, Paderborn, 2017 – ISBN 978-3-942647-90-8

Bd. 372 BÄUMER, F. S.: Indikatorbasierte Erkennung und Kompensation von ungenauen und unvollständig beschriebenen Softwareanforderungen. Dissertation, Fakultät für Wirtschaftswissenschaften, Universität Paderborn, Verlagsschriftenreihe des Heinz Nixdorf Instituts, Band 372, Paderborn, 2017 – ISBN 978-3-942647-91-5

Bd. 373 ECKELT, D.: Systematik zum innovationsorientierten Intellectual Property Management. Dissertation, Fakultät für Maschinenbau, Universität Paderborn, Verlagsschriftenreihe des Heinz Nixdorf Instituts, Band 373, Paderborn, 2017 – ISBN 978-3-942647-92-2

Bd. 374 GAUSEMEIER, J. (Hrsg.): Vorausschau und Technologieplanung. 13. Symposium für Vorausschau und Technologieplanung, Heinz Nixdorf Institut, 23. und 24. November 2017, Berlin-Brandenburgische Akademie der Wissenschaften, Berlin, Verlagsschriftenreihe des Heinz Nixdorf Instituts, Band 374, Paderborn, 2017 – ISBN 978-3-942647-93-9

Bd. 375 WESTERMANN, T.: Systematik zur Reifegradmodell-basierten Planung von Cyber-Physical Systems des Maschinen- und Anlagenbaus. Dissertation, Fakultät für Maschinenbau, Universität Paderborn, Verlagsschriftenreihe des Heinz Nixdorf Instituts, Band 375, Paderborn, 2017 – ISBN 978-3-942647-94-6

Bd. 376 JÜRGENHAKE, C.: Systematik für eine prototypenbasierte Entwicklung mechatronischer Systeme in der Technologie MID (Molded Interconnect Devices). Dissertation, Fakultät für Maschinenbau, Universität Paderborn, Verlagsschriftenreihe des Heinz Nixdorf Instituts, Band 376, Paderborn, 2017 – ISBN 978-3-942647-95-3

Bd. 377 WEBER, J.: Modellbasierte Werkstück- und Werkzeugpositionierung zur Reduzierung der Zykluszeit in NC-Programmen. Dissertation, Fakultät für Wirtschaftswissenschaften, Universität Paderborn, Verlagsschriftenreihe des Heinz Nixdorf Instituts, Band 377, Paderborn, 2018 – ISBN 978-3-942647-96-0

Bezugsadresse:
Heinz Nixdorf Institut
Universität Paderborn
Fürstenallee 11
33102 Paderborn

Zuletzt erschienene Bände der Verlagsschriftenreihe des Heinz Nixdorf Instituts

Bd. 378 OESTERSÖTEBIER, F.: Modellbasierter Entwurf intelligenter mechatronischer Systeme mithilfe semantischer Technologien. Dissertation, Fakultät für Maschinenbau, Universität Paderborn, Verlagsschriftenreihe des Heinz Nixdorf Instituts, Band 378, Paderborn, 2018 – ISBN 978-3-942647-97-7

Bd. 379 ABELDGAWAD, K.: A System-Level Design Framework for Networked Driving Simulation. Dissertation, Fakultät für Maschinenbau, Universität Paderborn, Verlagsschriftenreihe des Heinz Nixdorf Instituts, Band 379, Paderborn, 2018 – ISBN 978-3-942647-98-4

Bd. 380 JUNG, D.: Local Strategies for Swarm Formations on a Grid. Dissertation, Fakultät für Elektrotechnik, Informatik und Mathematik, Universität Paderborn, Verlagsschriftenreihe des Heinz Nixdorf Instituts, Band 380, Paderborn, 2018 – ISBN 978-3-942647-99-1

Bd. 381 PLACZEK, M.: Systematik zur geschäftsmodellorientierten Technologiefrühaufklärung. Dissertation, Fakultät für Maschinenbau, Universität Paderborn, Verlagsschriftenreihe des Heinz Nixdorf Instituts, Band 381, Paderborn, 2018 – ISBN 978-3-947647-00-2

Bd. 382 KÖCHLING, D.: Systematik zur integrativen Planung des Verhaltens selbstoptimierender Produktionssysteme. Dissertation, Fakultät für Maschinenbau, Universität Paderborn, Verlagsschriftenreihe des Heinz Nixdorf Instituts, Band 382, Paderborn, 2018 – ISBN 978-3-947647-01-9

Bd. 383 KAGE, M.: Systematik zur Positionierung in technologieinduzierten Wertschöpfungsnetzwerken. Dissertation, Fakultät für Maschinenbau, Universität Paderborn, Verlagsschriftenreihe des Heinz Nixdorf Instituts, Band 383, Paderborn, 2018 – ISBN 978-3-947647-02-6

Bd. 384 DÜLME, C.: Systematik zur zukunftsorientierten Konsolidierung variantenreicher Produktprogramme. Dissertation, Fakultät für Maschinenbau, Universität Paderborn, Verlagsschriftenreihe des Heinz Nixdorf Instituts, Band 384, Paderborn, 2018 – ISBN 978-3-947647-03-3

Bd. 385 GAUSEMEIER, J. (Hrsg.): Vorausschau und Technologieplanung. 14. Symposium für Vorausschau und Technologieplanung, Heinz Nixdorf Institut, 8. und 9. November 2018, Berlin-Brandenburgische Akademie der Wissenschaften, Berlin, Verlagsschriftenreihe des Heinz Nixdorf Instituts, Band 385, Paderborn, 2018 – ISBN 978-3-947647-04-0

Bd. 386 SCHNEIDER, M.: Spezifikationstechnik zur Beschreibung und Analyse von Wertschöpfungssystemen**.** Dissertation, Fakultät für Maschinenbau, Universität Paderborn, Verlagsschriftenreihe des Heinz Nixdorf Instituts, Band 386, Paderborn, 2018 – ISBN 978-3-947647-05-7

Bd. 387 ECHTERHOFF, B.: Methodik zur Einführung innovativer Geschäftsmodelle in etablierten Unternehmen. Dissertation, Fakultät für Maschinenbau, Universität Paderborn, Verlagsschriftenreihe des Heinz Nixdorf Instituts, Band 387, Paderborn, 2018 – ISBN 978-3-947647-06-4

Bd. 388 KRUSE, D.: Teilautomatisierte Parameteridentifikation für die Validierung von Dynamikmodellen im modellbasierten Entwurf mechatronischer Systeme. Dissertation, Fakultät für Maschinenbau, Universität Paderborn, Verlagsschriftenreihe des Heinz Nixdorf Instituts, Band 388, Paderborn, 2019 – ISBN 978-3-947647-07-1

Bd. 389 MITTAG, T.: Systematik zur Gestaltung der Wertschöpfung für digitalisierte hybride Marktleistungen. Dissertation, Fakultät für Maschinenbau, Universität Paderborn, Verlagsschriftenreihe des Heinz Nixdorf Instituts, Band 389, Paderborn, 2019 – ISBN 978-3-947647-08-8

Bd. 390 GAUSEMEIER, J. (Hrsg.): Vorausschau und Technologieplanung. 15. Symposium für Vorausschau und Technologieplanung, Heinz Nixdorf Institut, 21. und 22. November 2019, Berlin-Brandenburgische Akademie der Wissenschaften, Berlin, Verlagsschriftenreihe des Heinz Nixdorf Instituts, Band 390, Paderborn, 2019 – ISBN 978-3-947647-09-5

Bd. 391 SCHIERBAUM, A.: Systematik zur Ableitung bedarfsgerechter Systems Engineering Leitfäden im Maschinenbau. Dissertation, Fakultät für Maschinenbau, Universität Paderborn, Verlagsschriftenreihe des Heinz Nixdorf Instituts, Band 391, Paderborn, 2019 – ISBN 978-3-947647-10-1

Bezugsadresse:
Heinz Nixdorf Institut
Universität Paderborn
Fürstenallee 11
33102 Paderborn